EXPERIMENTAL AND NUMERICAL INVESTIGATION OF CHLORIDE INGRESS IN CRACKED CONCRETE

EXPERIMENTAL AND NUMERICAL INVESTIGATION OF CHLORIDE INGRESS IN CRACKED CONCRETE

Proefschrift

ter verkrijging van de graad van doctor
aan de Technische Universiteit Delft,
op gezag van de Rector Magnificus prof. ir. K. C. A. M. Luyben,
voorzitter van het College voor Promoties,
in het openbaar te verdedigen op maandag 27 oktober 2014 om 12:30 uur

door

Branko ŠAVIJA

Graduate Civil Engineer aan de Universiteit van Belgrado, Servië
geboren te Belgrado, Servië

Dit proefschrift is goedgekeurd door de promotor:

Prof. dr. ir. E. Schlangen

Samenstelling promotiecommissie:

Rector Magnificus,	voorzitter
Prof. dr. ir. E. Schlangen,	Technische Universiteit Delft, promotor
Prof. dr. R.B. Polder,	Technische Universiteit Delft
Prof. dr. ir. L.J. Sluys,	Technische Universiteit Delft
Prof. dr. M.R. Geiker,	Norges teknisk-naturvitenskapelige universitet, Noorwegen
Prof. dr. ir. G. De Schutter,	Universiteit Gent, België
Dr. ir. L. Pel,	Technische Universiteit Eindhoven
Dr. I. Ignjatović,	University of Belgrade, Servië
Prof. dr. ir. K. van Breugel,	Technische Universiteit Delft, reservelid

The work reported in this thesis is part of the STW project "Measuring, Modeling, and Monitoring Chloride ingress and Corrosion initiation in Cracked Concrete (M3C4)" (code No.10978), which is a part of an STW Perspectief Program "Integral Solutions for Sustainable Construction (IS2C)"

Keywords: Chloride ingress, Autogeneous healing, Corrosion induced cover cracking, X-ray computed tomography, Nanoindentation, Lattice fracture model, Lattice transport model

Printed by: Haveka B.V.

Front & Back: by Branko Šavija

ISBN 978-94-6186-377-5

An electronic version of this dissertation is available at
http://repository.tudelft.nl/.

Za sve moje ljude

ACKNOWLEDGMENTS

Somebody once said that no man is an island. In case of a PhD student, nothing can be more true. In fact, life of a PhD student (especially one who has moved to a new country to pursue his degree) more resembles sailing in a medieval ship. Trying to find a new route to India, not knowing that America might be in the way...
A PhD student is but a captain on this ship, trying to reach that lighthouse in India. However, embarking on an expedition is never easy. I would like to express my sincere gratitude to STW (the Dutch Science Foundation) for funding this risky and unpredictable voyage. Eddie Koenders, the head of IS2C (Integral Solutions for Sustainable Construction) program, under which this work was undertaken, is gratefully acknowledged.
Every captain needs good staff to work with, and probably the most important person on a ship is the navigator. That would be the supervisor. I was incredibly lucky to work with Prof. Erik Schlangen, probably the best in the business. He made it look so easy to find the way, and it was as if he never needed a map! We've visited many fun places in three continents together. It is a great pleasure working with him, and seeing him have so much fun doing his job made me hope that in the future I enjoy mine at least half as much. Thanks Erik!!!
Furthermore, a word of gratitude is due to Prof. Klaas van Breugel, head of the *Materials & Environment* section, for giving me an opportunity to give this project a try.
I am also very grateful to Prof. Rob Polder. Even with his extremely busy schedule, he always managed to find time to discuss my work. Also to Rob and his wife Lise - thanks once again for your great support.
I am very thankful to all the members of my doctoral committee for taking the time and effort to carefully review the preliminary version of this work. Their comments and suggestions have helped me significantly improve this thesis.
Some of the most important (and often underrated) people during a PhD research are the office mates. I was extremely lucky to share the office with my project colleague, and a good friend, José Pacheco! José, thanks for everything! Special thanks also goes to José's wife Karla, for sharing a lot of great moments with me. You've introduced me to a beautiful and exotic (at least for me) Mexican culture, which is the greatest gift anyone can receive! Thanks!
I should not forget my current office mate, Ma Xu! Thanks for your friendship both at and outside of work!
I would like to thank another guy who can almost be classified as an office mate (well, his computer shared an office with me for six months)-Caner, and his wife Neşen. Thanks for your friendship, for your ever lasting effort to have us move to Rotterdam, and for all the great parties. And once again congratulations to you both!
Special thanks is due to those that make our lab work possible: Ger (I don't even want to think about the time when he retires!), Arjan, and John of the Microlab have all helped me a lot and contributed to this work. Furthermore, I would like to thank Ton of the

Stevinlab for his help and the fun moments in the "big" lab.
Every long journey is tough at times. Luckily, there were a number of fellow sailors on the way that helped me get through the bad days (and shared with me the good ones!): Oğuzhan, Jon (even though he jumped ship while we were passing by Iceland - couldn't resist the song of the sirens), Henk, Reneé (thanks for all the "gratis" Dutch lessons!), Jeannette, Rene, Maria, Lourdes, Natalie, Rita (and Giorgio!), Damian, Jure, Virginie, Eirini (and Kostas!), Lupita, Neven, Senot, Farhad, Agus, Jiayi, Hua, Xuliang, Nynke, Hao, Hooman, Haoliang, Ennery (+ Amarelis!), Balqis, Emiel, Bei, Zhengxian, Ye, Zhuqing, Paco, Marco Pepe, Pedro, Daša, and many, many more... Thanks a lot to each and every one of you for making me enjoy the ride!
I would also like to acknowledge several student's I've worked with during my PhD: Sajjad Hosseini (you contributed a lot to chapter 4!), Nikiforos Pavlatos, and Fernando França de Mendoça Filho. I hope they have learned from me just as much as I have learned from them.
One of most important informal groups for me here in the Netherlands has been a small group of Serbians. I would like to thank Dimitrije and Andrija for many, many fun moments, and I hope there are more to come! Thanks guys! I would like to thank many others: Marko Mihailović (*el jeffe* of Delfćani), Violeta, Steva Rudinac, Steva Nađ-Perge, Aleksandar Jović, Darko Simonović, Vahid Ibrović (een echte Amsterdammer)... Thanks for the barbecues, parties, sports events (we've "won" many grand slams, water polo, and basketball medals together-lets continue!), and more!
Big thanks to Sale Milenković (momak) who, as an experienced "Nederlander", has helped me a lot during these four years in this beautiful, but at times confusing, country. Thanks for showing me that "alles komt goed", even if it doesn't always look that way!
Gratitude is also due to the Soldo family (Igor, Kaća, my great, great friend Sofija, and little Iris) for their friendship and many precious moments!
I am very thankful to all my friends back in Belgrade for their continuous love and support. Every time I went back, they made me feel as if I had never left! Some of them have already visited me in Delft, but I'm looking forward for more to come!
I am very much indebted to my extended family for showing me support at all times. My cousins, aunts, uncles, kumovi (English anyone?), my in-laws, and my grandmother are all a part of this accomplishment. Thank you all!
I would like to thank my parents and my sister, Milena, for supporting me from day one. Your love, patience, and continuous support gives me the power to always go further in life! Given our humble beginnings, we've indeed come far together!
And my final acknowledgement goes to Mladena, my wife, my colleague, my best friend, and my worst critic. Thank you very much for all of your love, for your support, for all the beautiful moments we shared and trips we've taken, for putting up with me when no one else would... Most of all, thank you for letting me believe that *I* was the captain of this ship...

Branko Šavija
Delft, October 2014

CONTENTS

LIST OF FIGURES

LIST OF TABLES

1

INTRODUCTION AND LITERATURE REVIEW

Before beginning, prepare carefully.

Marcus Tullius Cicero

In this chapter, some background and research motivation is given. Main terms related to service life of reinforced concrete with respect to chloride ingress are described. Sources and mechanisms which lead to chloride ingress into concrete are reviewed. The impact of cracking on chloride ingress is further emphasized, and different influencing factors are discussed. In the end, a critical study of literature dealing with chloride ingress in cracked concrete is performed. Finally, the aims of the thesis, together with used methodology, are stated.

Parts of this chapter have been published in Advances in Modeling Concrete Service Life: Proceedings of the 4^{th} International RILEM PhD Workshop held in Madrid, Spain, November 19, 2010 [1]

1

1.1. INTRODUCTION AND RESEARCH SIGNIFICANCE

1.1.1. DEFINITION OF SERVICE LIFE WITH RESPECT TO STEEL CORROSION IN CONCRETE

SERVICE life of a structure can be defined as the period of time after construction during which all properties exceed minimum acceptable values when routinely maintained. For most reinforced concrete structures, corrosion of reinforcing steel is the governing parameter for service life design. The most widely accepted service life modeling concept dealing with this issue is the one proposed by Tutti in 1982 [2]. According to it, the service life can be divided in two phases: the initiation phase, and the propagation phase (figure 1.1).

The corrosion initiation phase is a period from construction until the onset of active

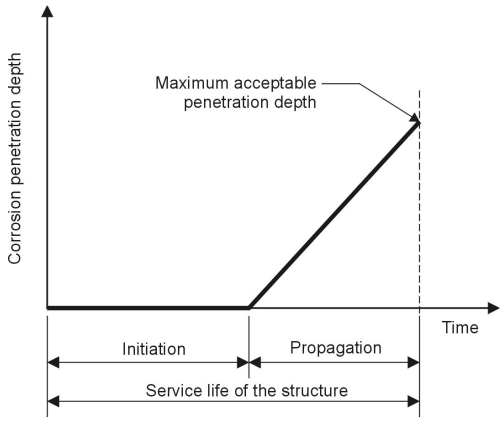

Figure 1.1: Service life model for reinforced concrete according to Tutti [2]

corrosion. The propagation phase then begins, and lasts until the maximum acceptable damage level is achieved. Since modeling and prediction of the propagation phase is associated with high levels of uncertainty, a majority of service life models adopt a conservative approach, and define the actual service life of a structure as the end of the initiation phase. This approach may result in a (very) conservative prediction of the service life. When a structure is cracked, the initiation phase could be very short, and such a conservative approach could be impractical. In such cases, the propagation phase could be considerably longer [3].

When embedded in concrete, steel forms a protective passivity layer on its surface because of the high alkalinity of the concrete pore solution (in general, pH>13). This layer (sometimes also called a passive film or an oxide film) forms spontaneously around the steel in an alkaline environment. It protects the steel by preventing contact with moisture and oxygen [4]. It is several nanometers thick, and consists of $\gamma - Fe_2O_3$ adhering tightly to the steel. It is immune to mechanical damage of the steel surface [5].

However, during the service life of the structure, this protective layer can break down. This could happen due to either:

1. Carbonation: When carbon dioxide (CO_2) from the environment penetrates the

hardened concrete, the pH of the concrete pore solution can significantly decrease (to a value around 9), where the passive film is no longer stable.

2. Penetration of chloride ions from the environment: The chloride ions can penetrate from the environment and reach the reinforcing steel. When chloride concentration at the surface of the steel reaches a certain value (threshold level, or critical chloride content), the protective layer breaks down locally.

1.1.2. BASIC THEORY OF CHLORIDE INDUCED STEEL CORROSION IN CONCRETE

If the concrete is very permeable, carbonation can be a cause of reinforcing steel corrosion. However, modern reinforced concrete structures in aggressive environments are usually highly impermeable, and carbonation is rarely a cause of concern. In marine environment, and structures exposed to deicing salts during the winter season, chloride ingress is a decisive factor for service life design. Chloride attack on reinforced concrete is different from other common deterioration mechanisms (such as alkali silicate reaction or sulfate attack), since it doesn't affect the concrete itself. Instead, it causes corrosion of steel reinforcement, and only as a consequence of it is concrete affected [6]. It is, therefore, not a concern in unreinforced concrete.
Corrosion of steel in concrete is an electrochemical process. When the passivity of steel is broken, the electrochemical potential becomes more negative locally, i.e. the area becomes anodic with respect to the rest of the steel which remains passive and acts as a cathode. The anodic and cathodic regions are connected by an electrolyte - the concrete pore solution. At the anode, the positively charged ferrous ions (Fe^{2+}) pass into the solution while the negatively charged free electrons (e^-) flow through the reinforcement are absorbed by the constituents of the electrolyte and combine with water and oxygen to form hydroxyl ions (OH^-) [4]. The reactions taking place during the process are [4, 6]:

- Anodic reaction:
$$Fe \rightarrow Fe^{2+} + 2e^- \tag{1.1}$$
- Cathodic reaction:
$$O_2 + 2H_2O + 4e^- \rightarrow 4OH^- \tag{1.2}$$

The hydroxyl ions move through the pore solution and combine with the ferrous ions to form ferrous hydroxide. It is converted to rust by further oxidation:

$$Fe^{2+} + 2OH^- \rightarrow Fe(OH)_2 \tag{1.3}$$
$$4Fe(OH)_2 + 2H_2O + O_2 \rightarrow 4Fe(OH)_3 \tag{1.4}$$

Here $Fe(OH)_2$ is ferrous hydroxide and $Fe(OH)_3$ ferric hydroxide. A scheme of the process is shown in figure 1.2: From the chemical reactions involved in the process, it is clear that two additional requirements must be met for significant steel corrosion to take place: first, a continuous supply of water and oxygen at the cathode is needed; and second, the concrete needs to be electrically conductive. Concrete conductivity increases

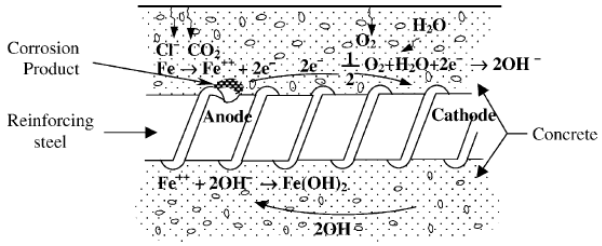

Figure 1.2: Electrochemical mechanism of reinforcement corrosion in concrete [7]

with the saturation, while in dry concrete electrical resistivity (i.e. reverse of conductivity) is very high. This is the reason why there is no significant steel corrosion in dry concrete. The optimum relative humidity for corrosion is 70-80% [6], and the corrosion rate becomes negligible when humidity is less than that of equilibrium with an atmosphere of 40-50 % RH [5]. If the water content is higher than that (near saturation), the conductivity is high, but the oxygen diffusion is slow. The controlling process then becomes the cathodic reaction, and the corrosion rate decreases as the water content increases. It almost stops completely in conditions of saturation, and fully saturated structures are therefore hardly affected by it.

Differences in electrochemical potential can occur from concentration differences in gases and ions in the vicinity of the steel. For example, this can happen when there is a variation of salt concentration in the pore water or due to a non-uniform access of oxygen. Another possible cause is when a part of the concrete member is submerged permanently in sea water, and the other part is subjected to wetting and drying. This is why structures exposed to wetting and drying cycles, such as marine structures, can be severely affected by corrosion of reinforcement.

Structures exposed to chloride are exposed to a particular form of steel corrosion - pitting corrosion. As pointed out earlier, the precondition for corrosion initiation is that the passive film which protects the steel is broken down. When a sufficient amount of chloride ions reaches the steel surface, they break down the passive film *locally* to form an anode, while the passivated surface acts as a cathode. This means that chloride induced corrosion is highly localized at a small anode, with pitting of steel taking place. A non-uniform expansion thus takes place. The reactions involved in the process are [4, 6]:

$$Fe^{2+} + 2Cl^{-} \rightarrow FeCl_2 \tag{1.5}$$

$$FeCl_2 + 2H_2O \rightarrow Fe(OH)_2 + 2HCl \tag{1.6}$$

The soluble complex of iron chloride ($FeCl_2$) increases the acidity of the anodic area (the pit) by lowering the pH value, which encourages further oxidation of the iron. Chloride ions are regenerated (equations 1.5 and 1.6) [4], and the rust contains no chloride. These chloride ions increase the corrosion rate in the pit (auto-catalytic mechanism of pitting). Depending on the oxidation state of iron, the volume of rust products formed by corrosion can be up to 6 times larger than the volume of the parent metal (figure 1.3). In corroding reinforced concrete structures, however, the most expansive corrosion product

detected in reinforced concrete structures exposed to chlorides *to date* is ferric hydroxide, with a specific volume around 4 times larger than that of iron [8]. This increase in

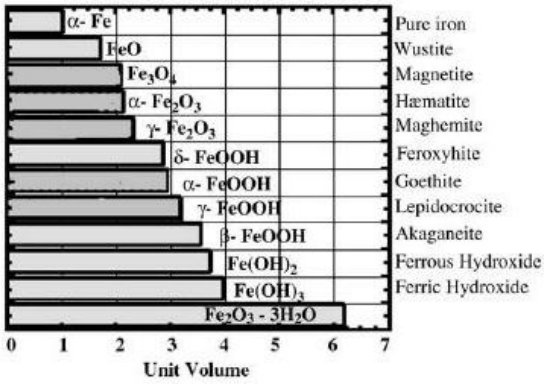

Figure 1.3: Possible corrosion products of iron [8]

volume is confined inside the concrete. It, therefore, leads to a build up of internal pressure, which eventually leads to concrete cover cracking. Investigations have shown that a steel radius loss of 20-200 μm (depending on the radius vs. concrete cover ratio) is sufficient to cause cracking the concrete cover (e.g. [9, 10]). This may sometimes be preceded by corrosion stains, but cover cracking makes corrosion of reinforcement visually detectable.

1.1.3. CRITICAL CHLORIDE CONTENT

In order for steel in concrete to start corroding, a certain amount of chlorides must be exceeded. This amount is commonly referred to as the critical chloride content or the chloride threshold concentration. Knowledge of this parameter is crucial for reliable service life predictions. Unfortunately, there is no single value for all concrete types and exposure conditions [11]. Some of the factors causing scatter in reported findings are pH of the concrete (the concentration of hydroxyl ions in the pore solution), the potential of the steel, and the presence of voids at the steel/concrete interface [5, 11]. The content of hydroxyl ions in the pore solution depends mainly on the cement type and additions (i.e. cement chemistry). Voids on the steel/concrete interface could be caused by poor compaction or debonding of steel and concrete caused by cracking. Therefore, cracking could have a significant influence on the critical chloride content.

There is no consensus on the value of the critical chloride content. This is partially due to lack of a standardized testing method, so a huge scatter in the results is present. Other parameters which could influence the results are temperature, the surface roughness of the steel reinforcement, moisture, etc.

Study of the critical chloride content is part of a related research project (see paragraph 1.5), so an in depth review of the topic is not given here. However, as a rough guideline, maximum allowed chloride (i.e. critical chloride) content as defined by various codes is given in table 1.1

Table 1.1: The critical chloride content as defined by various codes [12]

Code	Total chloride content (% weight of binder)
BS8110 [13]	0.4
ACI 222 [14]	0.2
Eurocode [15]	0.2-0.4 reinforced concrete 0.1-0.2 prestressed concrete

1.1.4. SOURCES OF CHLORIDE

Chloride ions in concrete can be of two origins[16]:

- Chlorides incorporated in the (fresh) concrete during mixing, e.g. contaminated mixing water, salty aggregates, or admixtures.
- Chlorides penetrating into the (hardened) concrete from the environment, e.g. from seawater, salty groundwater, deicing salts, industrial processes (i.e. slaughterhouses), etc.

Chlorides can be added to the concrete as impurities or accelerating admixtures. Calcium chloride was commonly used as an accelerating admixture in the past. Chloride additions ranging from 0.5% to over 2% by mass of cement have caused extensive corrosion damage [5]. However, chloride content in admixtures is limited today. Ingress of chloride ions from the environment is thus a primary concern.
Seawater and brackish water are aggressive against reinforcing steel in concrete. The typical salt content in sea water is 3.5% per weight (35 grams per liter), and the principal ions are Na^+, Mg^{2+}, Cl^-, $(SO_4)^{2-}$. Marine structures (e.g. jetties, piers, bridges) can be affected by reinforcement corrosion.
In mild climates, bridge decks and road structures are commonly exposed to deicing salts during the winter. Not all deicing salts contain chloride. However, the deicing salt containing chloride is the cheapest and the most efficient.Most commonly used deicing salt is sodium chloride ($NaCl$). When ice is removed from a structure using deicing salts, the structure is exposed to melt water. The melt water often contains a high concentration of chloride, and can be transported by vehicles from the roads to e.g. multistory car parks. These structures are then very vulnerable, because they can be exposed to dynamic loads and chlorides, which can increase the ingress of chlorides in cracked concrete [17], as will be elaborated later.
Other sources of chloride, such as PVC fire and some industrial processes [16], can contribute to attack on reinforced concrete structures, but these are of minor importance.

1.2. MECHANISMS OF CHLORIDE TRANSPORT IN CONCRETE

CHLORIDES penetrate into concrete by transport of water containing them. They penetrate the concrete through a system of capillary pores, voids, defects, and cracks. Various physical and chemical transport mechanisms contribute to chloride ingress, and

they depend on the concrete pore structure, (micro) environmental conditions, temperature, moisture content in concrete, among other factors. Cracking of the concrete cover, due to e.g. loading or shrinkage, can alter the (local) mechanism of chloride ingress significantly.
Transport mechanisms of chloride in concrete can be categorized as [16]:

1. *Capillary suction*, where the chloride transport is caused by a difference in moisture content (pressure). In non-saturated concrete, water containing chloride ions moves towards zones with lower moisture content due to surface tension in the capillary pores.

2. *Diffusion*, where ionic transport is driven by a concentration difference in various zones. Chloride ions move from zones with higher concentration to zones with lower concentration.

3. *Permeation*, where a difference in hydraulic pressure in various zones drives the movement of chloride ions.

4. *Migration*, where the transport of ions is driven by a difference in electrical potential. Chloride ions migrate to zones with lower electrical potential. This is typical for accelerated tests, such as NT Build 492 [18].

In practice, any of these mechanisms (or their combined action) can govern the ingress of chloride ions into concrete. The various mechanisms are presented schematically in figure 1.4.

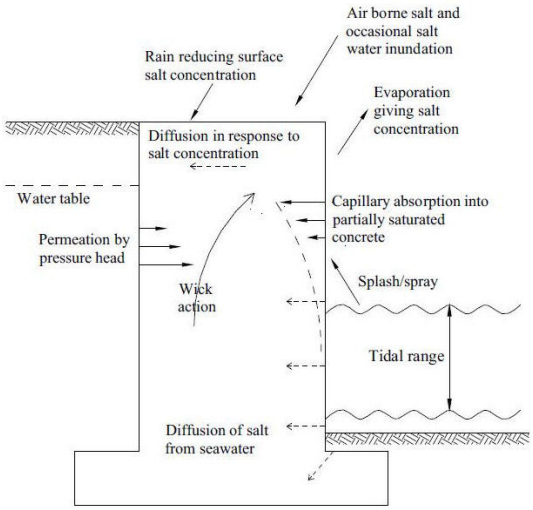

Figure 1.4: Some possible transport mechanisms of chloride into concrete in different aggressive environments (Concrete Society 1996, from [12])

1.2.1. CAPILLARY SUCTION

Capillary suction occurs in dry or partly saturated porous materials. If a liquid comes into contact with a porous material, it is absorbed rapidly by the under-pressure in the pores caused by capillary action. The action depends on the surface tension, viscosity, and density of a liquid, contact angle between the liquid and solid phases, and on the pore radius. It can be described by the Young-Laplace equation, assuming an idealized (round) pore:

$$P = -\frac{2\gamma cos\theta}{r} \tag{1.7}$$

where P is the pore pressure pulling chloride contaminated water, γ liquid-vapor surface tension of fluid, θ the contact angle between liquid and solid phases, and r the pore radius. Capillary suction is an important mechanism leading to ingress of chloride ions into non-saturated concrete.

1.2.2. DIFFUSION

For diffusion of chloride ions in concrete to occur, the concrete must have a continuous liquid phase and there must be a chloride concentration gradient. Degree of pore saturation is thus an important parameter influencing diffusion of ions in concrete; the diffusion process is most effective when the concrete is fully saturated, although it can also take place in partially saturated concrete. Therefore, ionic diffusion of chloride is the governing transport process when concrete is fully saturated; in a partially saturated condition, chlorides are transported by means of several combined mechanisms. However, it is usually assumed that diffusion is the predominant transport mechanism of chloride ions in concrete in uncracked concrete, even though in the outermost zone (several mm), capillary suction can play a major role.
The theory of diffusion is based on Fick's laws of diffusion [19]. Chloride diffusion into concrete can be described by Fick's first law, which relates the diffusive flux to the concentration field. It assumes that the flux goes from regions of high concentration to regions of low concentration, with a magnitude proportional to the concentration gradient (spatial derivative). For a one-dimensional diffusion, this is [16]:

$$J = -D\frac{\partial C}{\partial x} \tag{1.8}$$

where

- J is the diffusion flux in dimensions of [*(amount of substance)* $length^{-2}$ $time^{-1}$], e.g. $(mol/m^2 s)$.
- D is the diffusion coefficient in dimensions [$length^2$ $time^{-1}$], e.g. (m^2/s)
- C is the chloride concentration in dimensions [*(amount of substance)* $length^{-3}$], e.g. (mol/m^3)
- x is the position in dimensions [$length$], e.g. (m)

Fick's first law is used to derive the relevant equation (for derivation see e.g. Poulsen and Mejlbro [16]) for a case when concentrations are time dependent, i.e. Fick's second law:

$$\frac{\partial C}{\partial t} = \frac{\partial}{\partial x}\left(D\frac{\partial C}{\partial x}\right) \tag{1.9}$$

If the diffusion coefficient (D) is constant (i.e. independent of space and time), equation 1.9 can be simplified as:

$$\frac{\partial C}{\partial t} = D\frac{\partial^2 C}{\partial x^2} \tag{1.10}$$

Equation 1.10 can be solved analytically for a semi-infinite medium and the following initial and boundary conditions:

- $C = 0$ at $x > 0$ at time $t = 0$ (initial condition)
- $C = C_S$ at $x = 0$ and $t > 0$ (boundary condition)- surface chloride concentration is a constant

Then, the chloride concentrations as a function of x and t can be obtained [20]:

$$C(x,t) = C_s\left[1 - erf\left(\frac{x}{2\sqrt{Dt}}\right)\right] \tag{1.11}$$

where C_S is the surface chloride concentration, and *erf* is the mathematical error function.

Concrete is a composite, porous material, comprising both solid and liquid phases, in which the diffusion process through the solid is negligible compared to the diffusion through the pores. The rate of the chloride diffusion is therefore not only controlled by the diffusion coefficient through the pore solution but mostly by the physical characteristics and the connectivity of the capillary pore structure. These effects are usually implicitly considered, and the diffusion coefficient D is replaced by the effective diffusion coefficient, D_{eff}, which considers the diffusion of chlorides into concrete as a whole. It also considers (albeit implicitly) the effects of chloride binding.

Diffusion of chloride in cementitious materials is further complicated, as it strongly depends on the maturity age (degree of hydration), time, temperature, chloride concentration, binding, relative humidity (degree of saturation, as stated earlier), etc. However, equations presented in this chapter assume that concrete is homogeneous in structure, and that D (or D_{eff}, to be precise) is independent of the humidity of concrete, the chloride concentration and temperature. For certain cases, such as relatively short laboratory experiments, they can be considered as a good approximation of the process [21].

1.2.3. PERMEATION

Permeation is penetration of a permeate (such as liquid or a gas) (e.g. water containing chloride ions), through a porous material under a hydrostatic head. Permeability of concrete characterizes the ease with which a fluid will pass through it, under the action of a pressure differential. It can be described using Darcy's law:

$$\frac{\partial q}{\partial t}\frac{1}{A} = k_p\frac{\partial h}{\partial x} \tag{1.12}$$

where $\partial q/\partial t$ is the flow rate per unit area, A, k_p is the permeability coefficient, and ∂h is the pressure difference across the specimen thickness, x.
Permeability coefficient is affected by the porosity, pore network connectivity, and the viscosity of the permeate. Chloride ions can also penetrate with water into the concrete by permeation.

1.2.4. MIGRATION

Migration is the transport of ions under an electrical field. The ion velocity is proportional to the strength of the electric field and the charge and size of the ion. The ion mobility (u_i), which describes the ion movement under an electric field, is directly related to the diffusion coefficient D, which describes the movement under a concentration gradient:

$$D_i = \frac{RTu_i}{z_i F} \tag{1.13}$$

where R is the gas constant ($J/(K \times mol)$), T the temperature (K), F is the Faraday constant (96 490 C/mol) and z_i is the valence of ion i. Temperature has a marked effect on ion migration, more than on the diffusion mechanism.
The same principles hold for ionic migration in concrete. Positive ions migrate in the direction of the current, while the negative ions (e.g. Cl^-) migrate in the opposite direction. As in the case of ionic diffusion, ionic migration in concrete only takes place in water-filled pores. It is thus highly dependent on the porosity and pore network connectivity of the system.
Ion migration of concrete is often used as a measure of its resistance to chloride penetration. For example, a standardized test Nordtest NT Build 492 [18] measures non-steady-state chloride migration, expressed as the depth of penetration of chloride ions into a specimen under an electric field.

1.2.5. CHLORIDE BINDING

As chloride ions penetrate into the concrete cover, a portion of them is captured by the cement hydration products. This phenomenon is called chloride binding. It is defined as the interaction between the porous concrete matrix and chloride ions which results in their effective removal from the pore solution [22]. Chloride binding needs to be considered in the service life predictions of concrete structures because [23]:

- Reduction of the free chloride content in the vicinity of the reinforcing steel reduces the probability of corrosion.
- Removal of chloride ions from the diffusion flux slows down the penetration of chloride.
- Formation of Friedel's salt results in a less porous structure and slows down the transport of chloride ions [24, 25].

Chloride ions in concrete exist either as free or bound chlorides. In general, it is accepted that only free chloride is relevant for corrosion of the reinforcing steel, although some authors consider that bound chlorides also present a significant corrosion risk [22].

Chlorides can be bound either chemically or physically [6]. Chemical binding of chloride in cementitious materials is a result of reaction between chloride ions and C_3A to form chloroaluminate (Friedel's salt), $Ca_3Al_2O_6 \cdot CaCl_2 \cdot 10H_2O$, or the reaction with C_4AF to form a Friedel's salt analogue. Physical binding occurs due to the adsorption onto the amorphous calcium silicate hydrate (CSH) gel [26]. Bound chlorides can later be released by sulfate attack or carbonation of the hardened cement paste [6].
Chloride binding is dependent on many parameters [23, 26]. Studies have confirmed that the higher chloride concentration of external chloride leads to higher chloride content in the pore solution, and higher chloride binding [23]. Another important factor is the cement composition. It is considered that tricalcium aluminate (C_3A) and tetracalcium aluminoferrite (C_4AF) content in cement have the biggest impact on the amount of bound chlorides - as their content in cement increases, so does the chloride binding. Tang and Nilsson [27] concluded that the chloride binding capacity of OPC concrete is dependent on the amount of CSH gel in concrete and independent of the water-cement ratio and aggregate addition. CSH gel dominates the physical binding of chloride [23]. The higher the content of C_3S and C_2S is, the more chloride can be physically bound. Supplementary cementitious materials also affect chloride binding. Use of fly ash or blast furnace slag increases the level of chloride binding, while use of silica fume decreases it [28]. Sulfate resisting Portland cement (SRPC) also has a reduced binding capacity. Among other parameters that influence the chloride binding are the cation of chloride salt ($CaCl_2$ and $MgCl_2$ result in more bound chlorides than $NaCl$), temperature (higher temperature decreases the amount of bound chloride), chloride source (more chloride binding is observed when chlorides are added to the mix, than when they penetrate from the outside), sulfate ions (decrease chloride binding), etc.
The relationship between free and bound chlorides over a range of chloride concentrations at a given temperature is commonly described using chloride binding isotherms [23]. It gives the amount of bound chlorides as a function of free chlorides. Different types of chloride binding isotherms have been proposed:

- Linear binding isotherm

$$C_b = \alpha C_f \tag{1.14}$$

- Langmuir isotherm

$$C_b = \frac{\alpha C_f}{(1+\beta C_f)} \tag{1.15}$$

- Freundlich isotherm

$$C_b = \alpha C_f^b \tag{1.16}$$

- Brunauer, Emmett, Teller (BET) isotherm

$$\frac{C_b}{C_{bm}} = \frac{\alpha \frac{C}{C_S}\left[1-(1-\beta)\left(1-\beta\frac{C}{C_S}\right)^2\right]}{\beta\left(1-\beta\frac{C}{C_S}\right)\left(1-\beta\frac{C}{C_S}+\alpha\frac{C}{C_S}\left(1-\beta\frac{C}{C_S}+\frac{C}{C_S}\right)\right)} \tag{1.17}$$

The unknown parameters α and β are empirical constants and need to be determined by experiments for a given concrete. It seems that none of the binding isotherms fits the experimental data well over the whole concentration range. In general, it is considered that the linear binding isotherm is an oversimplification between free and bound chloride. As far as non-linear binding is concerned, Tang and Nilsson [27] found that Langmuir isotherm fits the experimental data well for chloride concentrations lower than 0.005 M. For higher chloride concentrations (from 0.01 to 1 M), they concluded that the chloride binding is better described by the Freundlich isotherm. Langmuir binding isotherm was used in a study by Glass and Buenfeld [22]. However, in many long-term field studies, a linear relationship between free and bound chloride was observed [23, 29, 30].
As shown by Martín-Peréz et al.[31], it is necessary to take binding into account when calculating the service life of a reinforced concrete structure. If binding is neglected, or linear binding is assumed, the service life might be grossly underestimated.

1.3. CONCRETE CRACKING

MOST of the existing literature regarding chloride ingress in concrete deals with uncracked (i.e. sound) concrete. The majority of service life models are based on Fick's second law of diffusion, with some of them taking into account different exposure conditions, material compositions, concrete maturity (age), etc. For example, a limit state equation for the depassivation of the reinforcement given by the fib Model Code for Service life design [32] states:

$$C_{crit} = C(x = a, t) = C_0 + \left(C_{S,\Delta x} - C_0\right) \cdot \left[1 - erf \frac{a - \Delta x}{2 \cdot \sqrt{D_{app,c} t}}\right] \tag{1.18}$$

where C_{crit} is the critical chloride content (% weight of cement); $C(x = a, t)$ is the content of chlorides at a depth x (structure surface: $x = 0\ m$) and time t; C_0 is the initial chloride content in concrete (% weight of cement); $C_{s,\Delta x}$ is the chloride content at a depth Δx and a certain point of time t (% weight of cement); x is the depth with a corresponding content of chlorides $C(x, t)$ (mm); a is the concrete cover (mm); Δx is the depth of the convection zone (concrete layer, up to which the process of chloride penetration differs from Fick's second law of diffusion) (mm); $D_{app,C}$ is the apparent coefficient of chloride diffusion through concrete $(mm^2/years)$; and t is time $(years)$. This model is based on the Duracrete model [33]. Other (similar) models have also been proposed (e.g. [34, 35]). While the fib Model Code [32] does include a reference to concrete cracking, it does not give a possibility to take into account the effects of (expected) cracking on service life prediction. Instead, it is stated (in chapter 3.3. of the Model Code) that "the minimum structural reliability of a cracked reinforced concrete structure has to be of comparable magnitude as the minimum reliability of a comparable exposed uncracked structure". Apart from suggestions for use of special protective measures in certain situations (e.g. car parks, which are simultaneously exposed to deicing salts and dynamic loads), no guideline is provided on how to include the effect of cracking on the structural reliability.

1.3.1. CAUSES OF CRACKING

Cracking of concrete is caused by tensile stress: once the tensile strength of the concrete is exceeded, cracking occurs. Because concrete is relatively weak in tension (i.e. its tensile strength is around 10 % of its compressive strength [36]), this happens already at moderate stress levels. This is the reason why concrete is usually reinforced by steel - once the concrete has cracked, steel takes over the tensile stresses. Some possible causes of concrete cracking are shown in figure 1.5.

Cracks in figure 1.5 are caused by [37]:

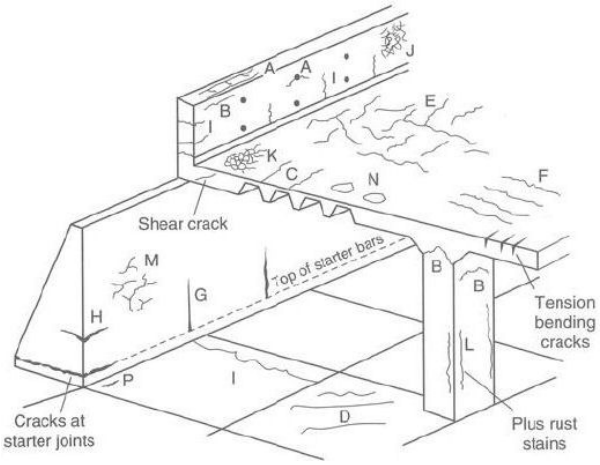

Figure 1.5: Examples of intrinsic cracks in a hypothetical concrete structure (from [37])

- Plastic settlement cracking (*A*-over the reinforcement; *B*-arching at column tops; *C*-changes in cross-sectional depth)
- Plastic shrinkage cracks (*D*-diagonal cracking of slabs; *E*-random cracking; *F*-over slab reinforcement)
- Thermal contraction (shrinkage) cracks (*G*-external restraint; *H*-internal restraint)
- Long term drying shrinkage cracking (*I*)
- Crazing (*J*-against the formwork; *K*-over troweling)
- Cracking due to the corrosion of steel reinforcement (*L*)
- Alkali-silica reaction (*M*)
- Blistering of slabs caused by trapped bleed water (*N*)
- D-cracking due to freeze-thaw damage (*P*)
- Load induced cracking (tension and bending cracking, shear cracking)

Clearly, there are many possible causes of concrete cracking. Time of cracking is also of importance. Based on the time of crack occurrence , two categories are distinguished: cracks developing from distress at either early age (before hardening), or later age (after hardening).

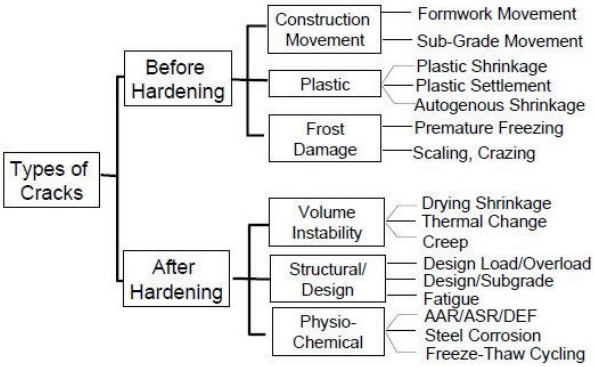

Figure 1.6: Types of cracking that may be expected in a concrete structure [38]

Table 1.2: Typical times of appearance of defects [39]

Type of defect	Typical time of appearance
Plastic settlement cracks*	Ten minutes to three hours
Plastic shrinkage cracks*	Thirty minutes to six hours
Construction defects*	On removal of framework
Crazing	One to seven days - sometimes much later
Early thermal contraction cracks*	One day to two or three weeks
Long-term drying shrinkage crakcs	Several weeks or months
Chemical attack (including sulfate attack)	Few months up to several years depending on the materials
Freeze-thaw damage	After first severe winter
Damage due to structural loading	Probably several months, possibly much later
Damage due to temperature movement (seasonal)	Probably up to a year, possibly much longer
Materials-related	Several years
Reinforcement corrosion	Several years, but may be sooner
Fire damage*	After severe fire

*Once these have formed, they do not develop further.

Most of the aforementioned cracks can be avoided or minimized through proper construction practices, such as good concrete mixture design, placement, compacting, finishing, and curing. However, load induced cracks are inevitable in a reinforced concrete

structure. It is therefore important to investigate the effect that cracks have on the durability of reinforced concrete structures.

1.3.2. CONCRETE CRACKING AND DURABILITY

While cracking in reinforced concrete structures is to be expected, it needs to be controlled in terms of crack width and/or frequency. Therefore, structural design codes prescribe certain crack width limits. Wide cracks can reduce the capacity of the concrete cover to protect the reinforcing steel. Design codes provide relatively simple tools which enable the structural designer to limit the (load induced) surface cracks width by appropriate design and detailing. Along with the good construction and execution on site, it seems that minimizing cracking in reinforced concrete is a simple task. However, it is not so: apart from possible (and maybe controllable) macrocracks, concrete always contains microcracks, very fine cracks which occur within the cement matrix due to restraint of shrinkage deformations of the cement paste. If these microcracks connect and form a continuous network, they could contribute to increased permeability of concrete, thus increasing ingress of aggressive and deleterious substances, such as carbon dioxide (CO_2) and chloride. This could have serious implications on durability of reinforced concrete structures with respect to corrosion of reinforcing steel.
Cracking in reinforced concrete structures should be minimized or limited at least for the following reasons:

- Cracks provide fast routes for ingress of deleterious substances, such as chloride contaminated water, CO_2 and oxygen.
- Cracks reduce the protection of reinforcement with respect to the environment provided by the concrete cover, increasing the probability of fast corrosion initiation.
- Cracks create differences in (micro) environmental conditions within concrete, which can result in differences in electrochemical potential and may lead to a formation of an electrochemical cell.
- Cracks are undesirable for aesthetic reasons, and may possibly reduce confidence of users in structural safety and integrity of a structure.

Clearly, there is a need for limiting cracking in reinforced concrete structures. However, structural code limits on cracking are often criticized as not being scientifically based: there is no consensus on whether cracks within these limits have long term or only short term implications on the corrosion of the reinforcing steel. Also, the prescribed limits are based on surface crack width, which, according to some researchers, is not the main parameter affecting the increased ingress of moisture and chloride [40–42].
Structural codes of practice prescribe maximum allowable surface crack widths according the environmental conditions (i.e. exposure class) in which the reinforced concrete structure is built. In general, these limits are in a range from 0.1 to 0.4 mm, depending on the environment. Salt water (sea water and deicing salts) environment is considered as severe for reinforced concrete structures, and has the lowest allowed crack width. Different national and international codes provide different limits. Those are, in general,

based on experience. An overview of different national and international codes is given in table 1.3.

A general perception is that the impact of a crack on chloride ingress is proportional to

Table 1.3: Maximum crack widths allowed by different codes for aggressive environmental conditions (from [12])

Code	Maximum crack width (mm)
ACI Committee 224 Report [43]	0.15
CEB/FIB Model Code [44]	0.30
BS 8110 [13]	0.30
Eurocode [15]	0.30

its width, which is reflected in the codes. This means that wider cracks provide faster access for ingress of deleterious species. However, the crack width controlled in structural codes is the surface crack width. Instead of the surface crack width, some authors (e.g. Tammo and Thelandersson [45]) suggested use of crack width near the bar, or even steel stress in the crack, as an indication of potential risk for reinforcing steel in the cracked section. Others (e.g. Gowripalan et al. [46]) suggested a durability design criterion based on the ratio of the surface crack width and the concrete cover thickness.

It is considered that fluid flow in a fracture is proportional to the third power of its width (following the cubic law for laminar fluid flow in cracks [47]). Aldea et al. [48] found that, while water penetration through cracks is proportional to the cube of crack width, chloride diffusion coefficient is less affected-it seems to be proportional to the crack width. The implications of this increased and faster ingress are not clear; the effects on long time performance of reinforced concrete structures, especially with respect to corrosion of reinforcing steel, are still under debate. When the effect of cracking on corrosion of reinforcing steel is concerned, there are two schools of thought: while some researchers consider cracking to accelerate both the onset of corrosion and its propagation [49, 50], others argue that, even though cracks could shorten the initiation phase, the propagation of corrosion is not affected [40, 51]. Some researchers also claim that, by defining a service life of a structure as the initiation phase, the actual service life of a cracked concrete structure is grossly underestimated. The reported findings of a 17-year long study by François and Arliguie [40] suggest that the propagation phase could be longer than the initiation phase. According to the authors, it is necessary to model the propagation phase and to be able to define the end of serviceability. Some possible mitigating mechanisms, such as autogenous healing (self-healing) or blocking of cracks by corrosion products, may be responsible for this.

1.4. REVIEW OF LITERATURE ON CHLORIDE INGRESS IN CRACKED CONCRETE

MOST studies on the influence of cracking on chloride ingress have been performed in laboratory conditions. The first step in the research is the preparation of the specimens. After casting and curing, the specimens need to be cracked. Afterwards, they are exposed to chlorides. After the exposure, specimens are examined for chloride penetration. In the following, different test methods used in the literature are discussed.

1.4.1. CRACKING METHODS

Researchers have used a variety of different methods to induce cracking. These can be roughly divided in two groups: methods used to induce cracks of controlled widths, and methods used to produce non-controlled-width cracks. Also, a distinction should be made between real cracks (induced by destructive methods) and artificial cracks (produced by "non-destructive" methods). The most important tests are performed on specimens with realistic cracks of controlled width: they aim to identify a correlation between the crack width and the chloride ingress, and to determine whether the maximum surface crack width values prescribed by the codes of practice should be changed.
The main destructive methods used to produce controlled width cracks are:

- *Splitting method.* Splitting test (Brazilian splitting test) is commonly used to assess tensile strength of concrete. The test is performed on cylindrical or disc samples. Specimens are compressed in a diametrical direction, usually through plywood strips placed between the specimen and the loading machine, to prevent crushing at the contact points. In this way, tensile stresses are imposed in the specimen, and it cracks in direction of the loading. In order to obtain controlled cracks, feedback-controlled tests are used. Two LVDT (linear variable displacement transducer) sensors, one on each side of the specimen, are used to measure the displacement perpendicular to the loading axis, and their average is used to control the load. After the target COD (crack opening displacement) is obtained, the specimen is unloaded, with the crack partially closing. As stated by the authors of one study [52], cracks produced in this way may be identical in widths on the inside as on the outside (parallel walled), while the crack widths adopted by the codes are based on flexure induced (i.e. V shaped) cracks. Specimen used for the splitting test are, typically, not reinforced.

- *Bending method.* Concrete beams are usually used. Three or four point bending can be used, depending on whether a single crack or multiple cracks are sought. The load is applied until bending cracks appear. Crack width can be controlled by using LVDTs to monitor and control the CMO (crack mouth opening). Alternatively, the load needed to produce certain crack width can be estimated and applied (e.g. [12]). Beams are exposed to chlorides in loaded condition. Specimens are typically reinforced.

- *Direct tension.* Some authors used direct tension to induce cracking in the specimens. Gérard et al. [54] devised a setup which enabled uniaxial and biaxial tension and cracking of the specimens. Another way to induce direct tension is the

following: a prismatic or cylindrical reinforced specimen is made, with reinforcement protruding on both sides of it. Reinforcement is then loaded in tension until cracking. A study by Tammo and Thelandersson [45] used this setup, and concluded that crack width on the surface is typically wider than that near the reinforcement, i.e. that the cracks are tapered. In the study by Konin et al. [55], specimens under direct tension were exposed to chloride environment in loaded state. However, when using this setup, it might be difficult to control the induced (surface) crack widths. They induced different damage levels, as opposed to creating single controlled cracks. Similar setup was used by Kim et al. [56] to preload prismatic specimens to 0, 30 and 60 % of their ultimate strength, and then expose them to a Rapid Chloride Migration test while loaded. These tensile loads induced microcracks, and a single crack of a certain width could be difficult to obtain.

- *Wedge splitting method.* This method is commonly used in fracture mechanics to determine fracture properties of concrete and rock. A prismatic specimen is provided with a groove and a notch [57]. The wedge is installed in the groove and loaded in compression in the vertical direction. Rollers turn the vertical load into two horizontal loads, which move away from each other and crack the starter notch. Using LVDTs, the CMO can be measured, and the width of the crack can be controlled. A modification of this method was used in the study by Yoon et

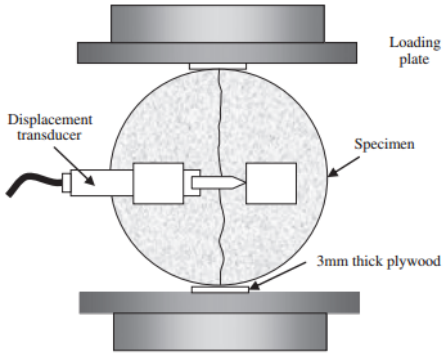

Figure 1.7: Specimen cracking using the splitting test [53]

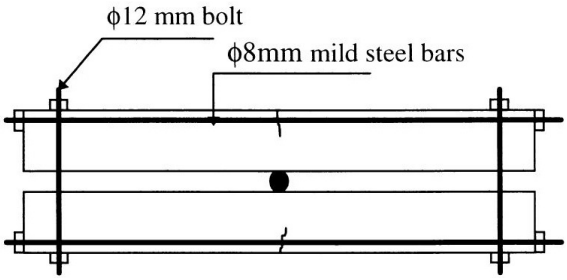

Figure 1.8: Specimen cracking using three point bending [46]

al. [58]. In their study, cylindrical specimens were used. First, steel plates were glued to a notch, and then loaded in tension. After the target CMO was achieved, the specimen was unloaded. Effective CMO (after unloading) was measured and recorded. Cracks created in this manner are V-shaped cracks, and can be considered realistic for bending loads. Unloaded specimens are exposed to chlorides. These specimens typically are not reinforced. Another modification of this cracking method was developed by Yi et al. [59]. The geometry of their specimens was that of the Brazilian test (see figure 1.7). However, instead of having a top plywood strip they made a notch, and used a wedge to load it. This way, during the loading process, a crack starts from the wedge, and develops to the lower part of the specimen. After the cracking, they used steel bands to fasten and reassemble the parts of the cracked cylinder.

- *Expansive core method.* This innovative method was used in studies by Ismail et al. [60, 61] to produce cracks of controlled widths in brick and mortar specimens. The specimens used were doughnut shaped discs (50 mm height, internal diameter 50 mm, and external diameter 100 mm). They were loaded using a mechanical expansive core and external steel confinement ring. The pressure imposed on the intrados by the expansive core and the confinement pressure applied by the external steel ring can be adjusted, and cracks with selected openings produced. The cracks obtained in this way are parallel walled, and therefore not directly compa-

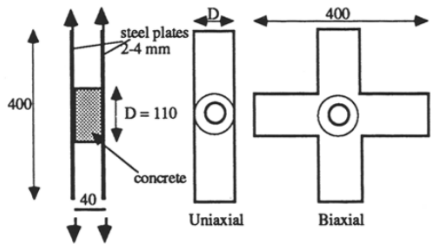

Figure 1.9: Setup for uniaxial and biaxial tension for controlled specimen cracking, developed by Gérard et al. [54]

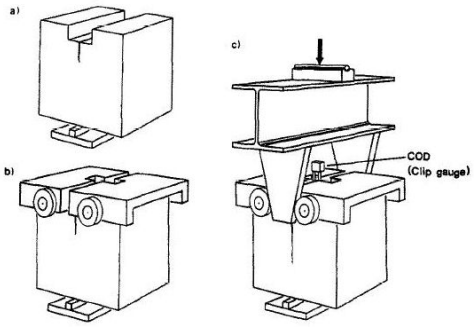

Figure 1.10: The wedge splitting test for specimen cracking [57]

rable to bending cracks. The chloride exposure can be performed under load. The method was used to produce cracks in both non-reinforced [60, 61] and reinforced [62] specimens.

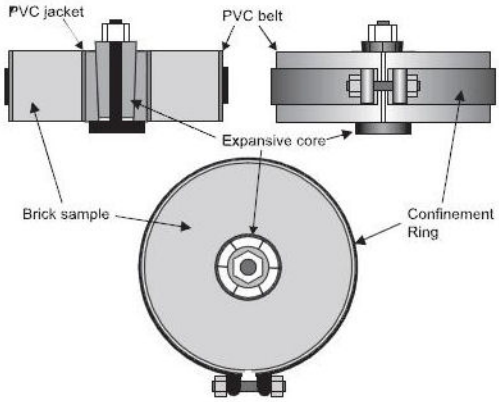

Figure 1.11: Schematic view of the specimen and the expansive core used for cracking [60, 61]

Apart from these methods, several studies used "artificial" cracks. In the study by Garces Rodriguez and Hooton [63], artificial smooth cracks were produced by saw cutting of concrete cylinders longitudinally. "Cracks" were created by clamping the cut cylinder parts back together and using brass shims of various thicknesses at the edges to keep the gap open. In studies by De Schutter [64], Marsavina et al. [65], and Audenaert et al. [66], artificial cracks were produced by placing copper sheets in hardening concrete specimens during casting, and removing them after approximately 4 hours. Different sheets were used for different crack widths and depths. The same method was used to create specimens with multiple cracks in a study by Mu et al. [67]. Artificial cracks are, in general, parallel walled, and their shape does not resemble the shape of bending cracks. While these artificial cracks can be used to study the influence of different parameters affecting the chloride ingress, they lack the tortuosity, connectivity, and roughness of real cracks. It is also possible that transport properties are altered by the wall effect in the cracks (studies [65–68]), and that lack of contact between the surfaces prevents possible autogeneous healing of cracks [69], which could be an important mitigating mechanism for chloride transport. Nevertheless, this method might be a useful tool to study the influence of different crack depths and widths on chloride ingress. It might be also a good starting point for modeling the phenomenon. Apart from these methods, which, in general, aim to create controlled cracks (i.e. cracks of pre-determined widths), some researchers induced non-controlled (micro)cracking in their specimens. Jacobsen et al. [70] used freeze-thaw cycles to induce damage (cracking), prior to subjecting the specimens to water (for autogenous healing) and chloride exposure afterwards. In a similar manner, freezing action was used to induce (micro) cracking in a study by Litorowicz [71]. Taheri-Motlagh [72] exposed beams to hygral and thermal cycles (in addition to chloride exposure) to induce surface cracking and simulate harsh environmental conditions in the Persian Gulf. Several authors [73–75] induced microcracks by means of

compressive loading. Individual crack width is not controlled; rather, the damage level (load level) is used as a control variable, and microcracking is examined as its consequence.
In table 1.4, methods for controlled cracking are listed and compared. A number of studies which have used it for either chloride or moisture (water) penetration or corrosion studies are listed.
Based on the literature review, a cracking method based on the wedge-splitting test was

Table 1.4: Overview of different cracking methods used in the literature

Setup	Reinforced	Realistic (flexural) cracks	Crack held open	Used by
Brazilian splitting	No	No	No	[48, 52, 53, 63, 76–79]
Bending	Yes	Yes	Possible	[3, 8, 12, 40, 41, 46, 49, 51, 80–86]
Direct tension	Possible	No	Possible	[54, 55]
Wedge splitting	No	Yes	Possible	[42, 58, 59, 87, 88]
Expansive core	Possible	No	Yes	[60–62]

selected for this study. It was chosen based on its relative simplicity, compact specimen size (compared to e.g. beam specimens), and realistic cracking behavior. The original test was modified to include reinforcement, and is further described in chapter 2.

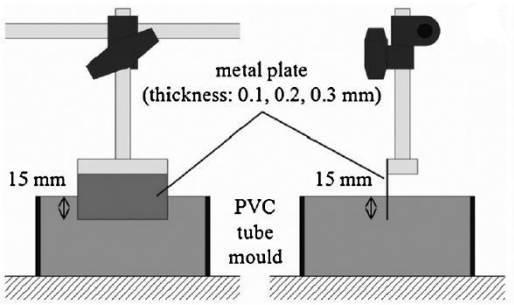

Figure 1.12: Specimen with a cast in insert (artificial crack) [68]

1.4.2. CHLORIDE EXPOSURE TESTING

As stated, chlorides penetrate concrete by several mechanisms: diffusion, migration, capillary suction, permeation, etc. Most studies assume that the mechanism governing the chloride transport is diffusion (or migration in case of accelerated testing). However, some authors (e.g. [41]) suggest that capillary suction has an influence which is greater than the diffusion mechanism, and therefore should not be ignored. Several testing methods (some of these have been standardized) have been developed for testing chloride transport in uncracked (sound) concrete. Some of these methods, or their variations, have been used by researchers to assess the effects of cracking on transport properties of concrete. These methods are further discussed, while a comprehensive description of different methods used in the literature for sound concrete can be found elsewhere (e.g. [89]).

Diffusion tests Test methods which utilize diffusion as a dominant driving mechanism agree reasonably well with natural exposure conditions. They can, therefore, be considered as directly applicable for service life predictions. However, these experiments are very time consuming.
Several researchers have used immersion tests to study the effects of cracking on chloride ingress behavior. A specimen is cracked, and then immersed in salt water for a period of time, before it is examined for chloride penetration. The sides of the specimen are usually sealed with epoxy, and only the cracked face is available for chloride penetration. In the study by Adiyastuti [12], cracked beams were immersed in 3 % $NaCl$ solution for two years. Yoon and Schlangen [88] immersed cracked specimens in chloride solution with $NaCl$ and $MgCl_2$ for 472 days, and compared the results with those of a migration (short term) test. Different chloride concentrations (3-7 % $NaCl$) were used in the study by Win et al. [41], for exposure times of 7 days and 1 month. A standardized immersion method is, for example, NT Build 443 [90], which was used in the study by Garces Rodriguez and Hooton [63]. Ismail et al. [60, 61] used steady-state diffusion test to study the effects of cracking on chloride transport in brick and mortar specimens.

Electrical migration tests Chloride penetration can be greatly accelerated by applying an electrical field as a driving force to move chloride ions into the exposed concrete. This provides a fast method to determine chloride ion transport in concrete. However, it is not directly applicable to real structures, and caution should be taken in interpreting the results. NordTest NT Build 492 [18] is a standardized non-steady state migration test. Several authors have used a modified version of the test to assess the effects of cracks. Yoon et al. [58] used it to quantify the effects of different crack widths on chloride penetration. Audenaert et al. [66] and Marsavina et al. [65] used it to assess the penetration resistance of concrete with different artificial (cast in) cracks. Apart from this rapid method, some studies utilized the steady state migration tests to study the effects of cracking. Djerbi et al.[79] used this method to study migration of chloride ions in cracked specimens. Jang et al. [53] used it to investigate the influence of w/b ratio, binder type, and crack width on the chloride migration.
Other test methods exist (e.g. electrical conductivity test- ASTM C1202 [91], used by Ja-

cobsen et al. [70]), but they are not so widely described in the literature.

1.4.3. FACTORS INFLUENCING CHLORIDE INGRESS IN CRACKED CONCRETE

A number of factors influence chloride ingress in cracked concrete. These factors include, but are not limited to:

- Concrete quality - mix proportion, cement content and cement type, supplementary cementitious materials, water/binder ratio, aggregate type and size, porosity, cover depth, execution, curing, etc.
- Environmental conditions - chloride content in the environment, exposure duration, relative humidity, temperature, wind exposure, rainfall, etc.
- Loading condition - flexural, tensile, or compressive loading, static or dynamic (cyclic) loading, etc.

Cracking of the concrete cover has a potential to significantly alter ingress behavior: if a crack is wide enough, its effect dominates the chloride penetration, and a sharp penetration front is observed at the crack location (e.g. [58]).
While influence of some factors is thoroughly examined in studies on sound concrete (exposure condition, exposure duration), similar results are reported for cracked concrete. For example, Win et al. [41] reported that higher $NaCl$ concentrations lead to deeper penetration and higher chloride content. Also, it is reported that longer test duration leads to deeper chloride penetration [12, 65, 66, 74]. However, some influencing parameters only affect chloride ingress in cracked concrete, or the effects might be different than in case of sound concrete. These are further discussed.

Crack width Crack width is considered to be a most important factor governing the ingress of deleterious substances in cracked concrete. This perception may be imposed on engineers by the design codes which limit the surface crack width, in order to achieve certain durability (table 1.3). Therefore, this is the parameter which has received the most attention when it comes to research on chloride ingress and corrosion in cracked concrete.
The main aim of researchers was to find a so called threshold crack width, below which the penetration of chlorides is similar to that of uncracked concrete. Varying findings can be found in the literature. Yoon and Schlangen [88] determined that this value is 0.012 mm for the short term (RCM) exposure, and 0.05 mm for the long term (immersion) test. They have attributed this difference to autogeneous healing. Jang et al. [53] found this value to be 0.08 mm, and Ismail et al. [60] 0.053 mm. Also, some researchers assume that there is a certain crack width above which the penetration of chloride is independent of the further increase of the crack width. Djerbi et al. [79] observed that the diffusion coefficient of cracked specimens (including transport trough a parallel walled crack and the uncracked material) increased with the increasing crack width and was almost constant for crack widths for cracks wider than 0.08 mm. A value of 0.2 mm was proposed by Ismail et al. [60]. Other authors, however, saw no correlation between the crack width and the chloride penetration: in their study on specimens with cast-in cracks, Audenaert

et al. [66] and Marsavina et al. [65] observed no significant influence of the crack width on chloride penetration in parallel-walled cracks (notches). It has to be noted however, that the crack widths examined in these studies were in the range of 0.2-0.5 mm, and therefore larger than the "limit" values found in other studies. Similar findings were reported by Garces Rodriguez and Hooton [63], with smaller crack widths, ranging from 0.08-0.68 mm. They have stated that the conclusions are not necessarily applicable to smaller crack widths.
Numerous studies have focused on the impact of different crack widths on subsequent corrosion of the reinforcing steel [3, 40, 49, 51, 80, 86]. Consensus on this has not been achieved. For example, Otieno et al. [86] concluded that it is not possible to set a threshold crack width, without taking binder type, w/c, and cover depth into account. These studies show that an integrated research approach which includes structural performance, concrete cracking and corrosion of reinforcing steel is needed to thoroughly examine risks for durability of reinforced concrete structures. Since corrosion of steel in cracked concrete is not the main topic of this work, these will not be thoroughly elaborated.

Crack depth Marsavina et al. [65] found that crack depth has a more pronounced influence on chloride ion penetration than crack width. Similar results were reported in a related study by Audenaert et al. [66], who concluded that this effect is more pronounced for longer test duration. Both of these studies utilized the artificial crack method, with cast in cracks, which have parallel walls and constant crack width. They have examined, therefore, cracks with same widths and different depths. In reality, however, crack width and crack depth are not independent quantities; they are interdependent, and should be treated as such.

Water-to-binder ratio In general, higher water-to-binder ratio leads to deeper chloride penetration. Djerbi et al. [79] studied the effect of water-to-binder ratio on the diffusion of chloride ions in a steady state migration test. Three concrete types were included in the investigation- two CEM I concrete mixes with w/b ratios of 0.5 and 0.32 (named in the study OC and HPC, respectively), and one CEM I mix with 6% silica fume replacement (named HPCSF). The conclusion was that the chloride ion penetration occurs more easily in OC than in HPC or HPCSF, mainly because of the higher diffusion coefficient for uncracked OC, which is related to its more porous and permeable microstructure. Konin et al. [55] also found that low water-to-cement ratio reduces the chloride penetration. Win et al. [41] studied chloride penetration in cracked ordinary Portland cement reinforced concrete beams with different water-to-cement ratios (0.25, 0.45, and 0.65), and found that the specimens with low water-to-cement ratio (0.25) showed lower concentration profiles both from the exposed surface and around the crack for cracks of 0.2 and 0.5 mm (see figure 1.13).

Several investigations focused on the influence of water-to-binder ratio on corrosion of reinforcing steel in cracked concrete. Schießl and Raupach [51] found that the water-to-binder ratio does influence the steel mass loss in the crack zone. While this influence

was pronounced in the first 24 weeks of the study, it was smaller after two years. However, other studies [49, 80, 86] all agree that the increase of water-to-binder ratio leads to increased corrosion rate. Mohammed et al. [80] also stated that this influence on the corrosion rate is far more significant than the influence of the crack width.

Cement content and cement type Audenaert et al. [66] and Marsavina et al. [65] found that an increase in cement content (in their case, from 300 to 400 kg/m^3) at a constant water-to-cement ratio, leads to a decrease in chloride penetration depth around the crack.

It is generally considered that the addition of supplementary cementitious materials increases the resistance of concrete to chloride penetration. Konin et al. [55] found that the addition of silica fume reduces chloride penetration in cracked specimens. Jang et al. [53] found that the same holds for the addition of fly ash. Similarly, Garces Rodriguez and Hooton [63] found that the 25% replacement of cement by blast furnace slag makes the concrete more resistant to ingress of chloride ions when compared to 100% OPC. Also, Otieno et al. [86] concluded that Corex slag concretes exhibit lower corrosion rates compared to OPC concretes, and are less sensitive to changes in water-to-binder ratio. From all of these studies, it is reasonable to believe that the addition of supplementary cementitious materials (fly ash, silica fume, blast furnace slag), should improve the resistance of concrete to chloride ingress, even in the cracked condition.

These effects agree well with studies on sound concrete and can be, partly, attributed to

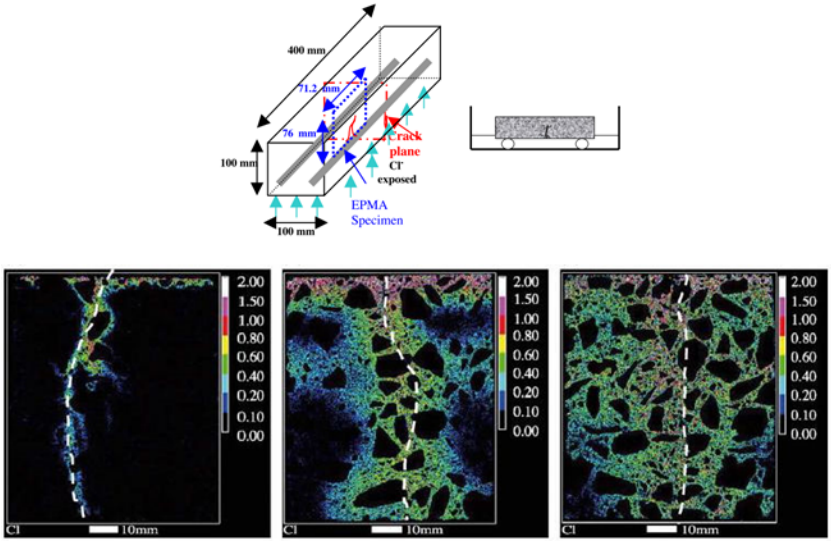

Figure 1.13: Top - Geometry and sampling procedure used by Win et al. [41]; Bottom - EPMA images of chloride ion concentrations for w/c ratios (left to right) of 0.25, 0.45 and 0.65, after one month of exposure (the dashed line indicates crack position, crack width 0.2 mm) [41]. Note chloride penetration parallel to the reinforcement (bottom middle) due to damage at the steel/concrete interface.

increased binding ability of such cement types, as well as denser and a more refined pore structure of concretes with supplementary cementitious materials (see e.g. [5]).

Loading conditions Most of the studies so far have been performed on unloaded specimens. However, as cracks partially close upon unloading (e.g. [45, 53, 73, 76, 82, 84]), and this might alter the ingress behavior of chloride, it is important to test chloride resistance of loaded specimens.

Most studies have focused on static loading. Gowripalan et al.[46] studied the influence of (sustained) flexural load on chloride ingress. They found that the apparent diffusion coefficient in the compression zone of the beam was lower than in the tension zone, and attributed this to the damage at the aggregate-paste interface in the tension zone which can expedite chloride diffusion, while in the compression zone a reduction of porosity occurs, which can slow down the diffusion. Samaha and Hoover [73] studied the effects of compressive load induced damage on chloride resistance. The specimens were preloaded to 0.0-1.0 of their compressive strength, and then unloaded. Slices (50 mm) were taken from the specimens and tested for chloride transport by means of rapid chloride permeability test [91]. They concluded that microcracks caused by compressive loading did not affect mass transport properties at load levels below roughly 75% of the maximum capacity of the concrete. However, when the load was increased beyond that point, the concrete became 15 to 20% less resistant to fluid and ion movement. Similar experiments by Lim et al. [74] concluded that a critical (compressive) stress level exists above which an increase in chloride penetration is to be expected. When this critical stress in a specimen is not exceeded, the increase in the charge passed is marginal in spite of the large increase in microcracks. However, they have clearly stated that there is a possible influence of the test condition, i.e. whether the test was carried out under load or after unloading the specimens. Chloride penetration tests under sustained compressive loads were performed by Antoni and Saeki [75] on fiber reinforced concrete specimens. Under low static compressive loading, they found a reduction in the chloride penetration depending on the type of concrete. At higher static compressive loading, an increase in chloride penetration was found. The same was observed by Jiang et al. [92].

Although the majority of research to date has focused on static loading conditions, several studies investigated the effect of repeated loading on chloride penetration in cracks. Küter et al. [17] studied the effect of cyclic flexural loading on chloride ingress in cracks, and concluded that it is far more severe than in the case of static loading conditions. They attributed this to pumping of chloride containing water into the concrete due to opening and closing of cracks. Similar findings were reported by Wang et al. [93]. Antoni and Saeki [75] found an increase of chloride penetration when a fiber reinforced concrete specimen is subjected to cyclic compressive loading above a certain level, when compared to static compressive loads of the same magnitude. The conclusion was that small and insignificant damage in the concrete material could accumulate under cyclic loading and increase the chloride penetrability. Otieno et al. [86] studied the effect of reloading and crack widening on corrosion rate of reinforcing steel in flexural beams. They found that reloading (crack reopening) of corroding reinforced concrete structures accelerates corrosion by reactivating (reopening) self-healed cracks, widening existing

ones, increasing the load level (i.e. stress in the steel), damaging the concrete/steel and/or aggregate/paste interfaces or a combination thereof. However, the effect of reloading of beams in their study was more significant if the RC structure was actively corroding before reloading. Jaffer and Hansson [8] studied the effects of different loading conditions on corrosion products of steel in cracked beam specimens. Significant differences were found between static and dynamic loads, which suggests that dynamic loads could be potentially more detrimental for durability of concrete structures.
The loading condition seems to influence both the initiation phase (chloride penetration to the reinforcing steel) and the propagation phase (active corrosion of the reinforcing steel). Loading conditions might affect self-healing of cracks [86], and disable this mitigating mechanism when it comes to chloride ingress in cracks. It is also possible that the loading conditions might significantly influence the spatial distribution of corrosion products within and around the crack [8], which might cause crack blocking and reduce the chloride penetration needed to sustain growth of corrosion pits.

1.4.4. MITIGATING MECHANISMS

Autogenous (self) healing It has been long known that concrete cracks have a certain ability to heal under favorable conditions. This mechanism is called autogenous (self) healing, sometimes referred to as self closing, since no significant recovery in mechanical characteristics is achieved. Several mechanisms are thought to govern self healing (figure 1.14) [94]:

- *Physical causes*: The main physical cause is swelling of hydrated cement paste (HCP) near the crack surfaces. This is a minor cause contributing to self closing of cracks.
- *Chemical processes*: There are three chemical processes which contribute to autogenous healing. The first one is the hydration of unhydrated cement particles. This might be a significant contribution when crack widths are small (less than 0.1 mm) and concrete is young. The second chemical process is the formation of calcium carbonate and the growth of crystals on the crack faces. Calcium ions originating from the concrete pore solution react with carbonate ions in the water and form $CaCO_3$, which precipitates in the crack. This mechanism has been thoroughly examined by Edvardsen [95], and is considered to be the most important mechanism leading to autogenous healing of cracks. In seawater, a third process occurs: due to the presence of $Mg(SO)_4$ in sea water, ettringite and brucite form in the crack [96].
- *Mechanical causes*: It is considered that mechanical causes, such as clogging of the cracks by fine particles originally present in water, or by particles broken off from fracture surface, constitute a minor mechanism in autogenous closing of cracks.

Presence of water inside the crack is the most important factor for autogenous healing of cracks. When there is no water, autogenous healing is not possible, because water is involved in chemical reactions and it is needed for transport of fine particles.
This innate ability of concrete to repair cracks to a certain extent may have significant implications for their ability to resist chloride ingress. Several investigations have been

undertaken in recent years to study the effect of autogenous healing on water permeability [77, 95, 97, 98], using different additional experimental methods to quantify it. The most common technique used is measuring the water penetration through cracked concrete, and quantifying autogenous healing by recording its decrease over time [77, 95, 98]. Some investigations dealt with the strength recovery of (young) healed concrete [69] and Engineered Cementitious Composite (ECC) [99–101], and quantified healing by measuring the strength or stiffness recovery.
It was also noted that under certain conditions (i.e. tight crack width), autogenous healing can slow down chloride penetration in cracked concrete/mortar (see table 1.5) [3, 61, 70, 84, 86, 88]. It is, therefore, important to study the effect and extent of autogenous healing on chloride penetration, under various exposure conditions (e.g. submerged, wet and dry, temperature variations, etc.).

Crack blocking by corrosion products Another mitigating mechanism which is reported in the literature is crack blocking by corrosion products. Marcotte and Hansson [81] found, in their study, that crack blocking by corrosion products occurred in concrete made using 10% silica fume replacement. This phenomenon is also mentioned elsewhere in the literature, although not widely studied. Further research is needed to assess and quantify these effects and implications on the corrosion propagation, since it is postulated that crack blocking might prevent further chloride ingress, necessary to sustain the growth of corrosion pits.

1.5. SUMMARY AND OUTLINE OF THE THESIS

IN chapter 1, the motivation and background of the research project are given. In sections 1.1-1.2, the basic theory of chloride ingress and steel corrosion in reinforced concrete is given. Transport mechanisms and important parameters related to the phenomenon are explained. This part is intentionally brief, as there are many excellent textbooks for the interested reader, e.g. [4, 5, 16, 102]. Section 1.3 briefly reviews the

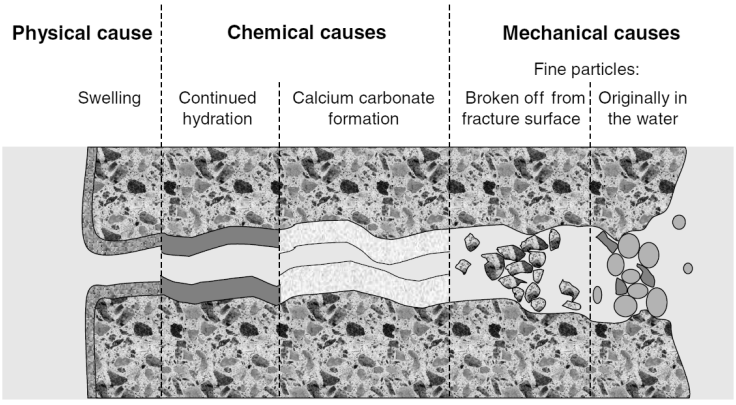

Figure 1.14: Possible causes of autogeneous crack healing in concrete [94]

phenomenon of concrete cracking, its causes and perceived impact on durability of reinforced concrete. It is followed by section 1.4, which gives a literature study of chloride ingress in cracked concrete. Experimental methods, influencing factors, and main findings are addressed. Section 1.4 is accompanied by appendix A, in which around 40 studies on chloride ingress in cracked concrete are analyzed.

The objective of this work is studying the influence of concrete cracking on ingress of chloride ions. Furthermore, cracking of the concrete cover due to ongoing reinforcement corrosion, a related phenomenon, is also studied. To achieve the study goals, both experimental and numerical approaches are used. The thesis is organized in a way that it follows these approaches.

The introductory chapter is followed by three chapters on the experimental side of the research and three chapters on the modeling side of the research. The emphasis is on the influence of damage at the steel/concrete interface, and autogeneous healing on chloride ingress in cracked concrete. Chapters 2, 3, and 4 are related to the experimental part of the thesis. Chapter 2 deals with chloride ingress in cracked concrete under wet-dry conditions. Chapter 3 is focused on the effect of autogeneous healing on chloride ingress in cracks. Chapter 4 deals with an experimental study of a closely related phenomenon - cracking of the concrete cover due to reinforcement corrosion. Chapters 5, 6, and 7 deal with numerical modeling. Chapter 5 presents a meso-scale model for chlo-

Table 1.5: Autogenous healing in the literature related to chloride ingress in cracked concrete

Reference	Exposure	Concluding remark
[70]	3 months submerged in lime saturated water (autogenous healing measured by UPV)	Reduction in rate of chloride migration: 28-35%, compared to migration in newly cracked specimens
[61]	Chloride penetration cell (autogenous healing not measured)	Reduces chloride diffusion along the crack path.
[3]	Salt fog cycles (17 years) (autogenous healing not measured)	Autogenous healing is possible.
[86]	Weekly wet-dry cycles (autogenous healing not measured)	Autogenous healing expected to have occurred for smaller crack widths.
[84]	$NaCl$ ponding (AASHTO T259-80) (autogenous healing not measured)	Autogenous healing of cracks smaller than 50 microns. $CaCO_3$ presence confirmed by X-ray diffractiogram.
[88]	Submerged condition (472 days)	Autogenous healing quantified as a reduction of crack width by optical microscopy.

ride diffusion in sound and cracked concrete. The model is extended to study chloride migration in chapter 6. Chapter 7 presents a meso-scale model of corrosion induced cracking of concrete.

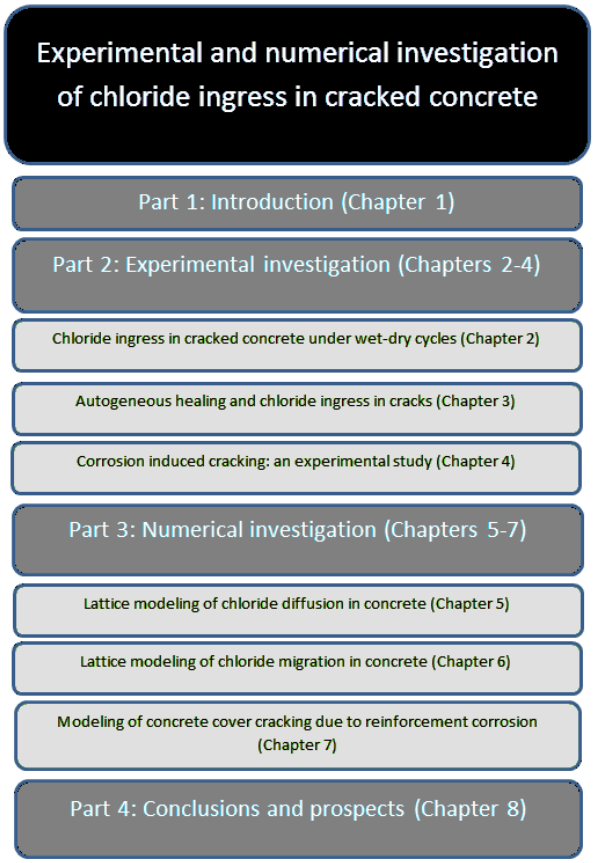

Figure 1.15: Outline of the thesis

This work was performed within a framework of a larger project entitled "Measuring, modelling, and monitoring chloride ingress and corrosion initiation in cracked concrete (M3C4)", funded by the Dutch Technology Foundation STW. Within this project, three PhD students were working on different topics (see figure 1.16). PhD students 1 and 3 were based at Delft University of Technology, while PhD student 2 was based at Eindhoven University of Technology.

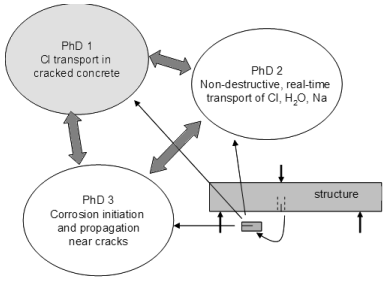

Figure 1.16: Schematic of the collaboration between the three PhD projects

As works of PhD students 1 (this thesis) and 3 were complementary in many aspects, several experimental studies presented in this thesis were done in collaboration with PhD 3. For example, in chapter 2, a study of chloride ingress in cracked reinforced concrete specimens is presented. Corrosion of reinforcement in the same specimens was monitored by PhD 3 as a part of his work. Even though those results are not presented in this thesis, the findings are sometimes used in discussions and conclusions. For more details about steel corrosion aspects of the project, the reader is referred to work of PhD 3 (José Pacheco, [103]). The work of PhD 2 (Jinping Han) focuses on non-destructive measurement of chloride ingress in porous materials by means of nuclear magnetic resonance (NMR) and is ongoing.

2

CHLORIDE INGRESS IN CRACKED CONCRETE UNDER WET-DRY CYCLES

Experimental observations are only experience carefully planned in advance, and designed to form a secure basis of new knowledge.

Sir Ronald Fisher

This chapter deals with the long term study of chloride ingress in cracked concrete. Two series of concrete specimens (Portland cement concrete and Blast furnace slag cement concrete) were prepared, cracked, and exposed to salt water cycles. After a prolonged chloride exposure, the specimens were analyzed for chloride content. Chloride profiles were determined using LIBS (Laser Induced Breakdown Spectroscopy), in cooperation with BAM institute, Berlin. To study the cracking behavior inside the specimen, the Delft lattice model was used. This study shows that cracking has a marked influence on chloride ingress, which is not independent on the concrete quality. Also, the importance of damage occurring at the steel/concrete interface was found. Furthermore, it was found that the use of fine-scale experimental techniques, such as LIBS, provides detailed chloride distributions, which are necessary in heterogeneous and (especially) cracked materials.

2.1. INTRODUCTION AND RESEARCH SIGNIFICANCE

CRACKING is inevitable in reinforced concrete structures. Although not a structural problem, it could potentially be a durability issue, as discussed in chapter 1. Numerous studies in the past two decades have been devoted to ingress of chloride and reinforcement corrosion in cracked concrete (for an overview, see appendix A). However, there is no consensus on the issue yet. This chapter aims at broadening the knowledge regarding the impact of cracks on chloride ingress.

First, a cracking procedure and specimen geometry needs to be selected. In chapter 1.4, advantages and disadvantages of different cracking procedures proposed in the literature have been discussed. It was concluded that the cracks in laboratory specimens should resemble those in structural elements (beams) if the results of a study are to be applicable in engineering practice. Therefore, specimen geometry and cracking procedure should be selected to achieve this goal.

Most studies have been performed on plain (unreinforced) concrete specimens (chapter 1.4). However, reinforced concrete has somewhat different cracking behavior than plain concrete. As tension is applied in the reinforcing steel, microcracks form in the steel/concrete interface [104]. Also, debonding of the steel/concrete interface occurs, possibly creating a fast pathway for fluid penetration. This was proven in an investigation by Wittmann et al. [105], who studied the water penetration in reinforced cracked specimens using neutron radiography. Rapid moisture penetration along the damaged steel/concrete interface was observed. Pease [42] also suggested that damage created in the steel/concrete interface might be much more detrimental with regard to chloride ingress and steel corrosion than cracking of the concrete cover itself. Similar findings were reported by François et al. [62].

A convenient way of creating controlled cracks in compact concrete specimens is the wedge-splitting method. The wedge-splitting method has long been used in fracture mechanics of concrete. Brühwiler and Wittmann [57] used the test to determine fracture mechanics parameters of concrete, such as the specific fracture energy and the fracture toughness. Similar setups have been used in some durability studies. Reinhardt et al. [87] used it as a way of creating controlled cracks in specimens which were subsequently subjected to fluid penetration. The penetration front through the specimen was monitored visually. It was observed that the penetration *in front* of the crack tip is slower than in the undisturbed zone. This essentially means that a bending crack cannot be treated as free surface, when it comes to fluid ingress. Furthermore, they concluded that concrete with crack widths below 0.03 mm behaves like uncracked concrete. Yoon et al. [58] used a similar setup to prepare cracked specimens to be subjected to Rapid Chloride Migration tests. In their investigation, a threshold crack width for chloride migration was found, and said to be dependent on the concrete composition, among other things. Pease et al. [106] also used the method to create controlled cracks in their investigation. Cracked specimens were then subjected to water penetration. The penetration front was monitored using X-ray absorption. The investigation showed that only a portion of the total crack length contributes as a free surface to water sorption, while the remaining part of the crack length inhibits sorption. These investigations emphasize the impact of crack width variations and crack shape on the ingress behavior.

However, in the standard wedge-splitting setup, plain concrete specimens are used. In

the current study, a modified wedge-splitting method is used. Reinforcement is placed in the specimens to mimic the cracking behavior of reinforced concrete beams, which somewhat alters the mechanical behavior of the specimens. Also, monitoring reinforcement corrosion was a part of a related study (PhD 3, see chapter 1). To examine the effect of the proposed modifications on the mechanical and cracking behavior of the wedge-splitting specimens, a numerical lattice type model is used [107].
In order to determine chloride ion distribution around the cracks, a meso-scale measurement technique (i.e. with spatial resolution in the mm range) should be used. Some of the techniques used in the literature are electron probe micro analysis (EPMA) [41], laser ablation inductively coupled plasma mass spectrometry (LA-ICP-MS) [108], and laser induced breakdown spectroscopy (LIBS) [109, 110]. In the current study, a LIBS setup at the BAM Federal Institute for Materials Research and Testing in Berlin, Germany, was used to determine chloride distribution in cracked specimens, as explained further.

2.2. MATERIALS AND METHODS

2.2.1. MATERIALS

TWO concrete mixes with w/c ratio of 0.45 were used in this study: a mix prepared with CEM I 52.5 R cement (designated OPC mix), and a mix prepared with CEM III/B 42.5 N cement (designated slag mix). Mix proportions for both mixes are given in table 2.1.
The mixing procedure was as follows: first, fine aggregate was mixed for one minute.

Table 2.1: Concrete mixes used in the study

Mix	Water	Cement	Sand	Gravel	Superplasticizer
(kg/m^3)	(kg/m^3)	(kg/m^3)	(kg/m^3)	(kg/m^3)	(% cement)
OPC	166	366	842	1027	1.4
Slag	157	350	1055	844	1.4

Then, cement was added, and mixing was continued for one more minute. After that, water (with superplasticizer) was added and mixed for four minutes. The mixing was then stopped for one minute. Finally, coarse aggregate was added and mixed for three minutes. The total mixing time was about ten minutes. The specimens were then cast and compacted using a vibrating table. Three standard cube specimens ($150 \times 150 \times 150$ mm^3) per mix were tested to determine the compressive strength at 28 days. The average concrete strength at 28 days was 55.4 MPa (standard deviation $\sigma = 3.53$ MPa) for the OPC mix and 46.9 MPa for the slag mix (standard deviation $\sigma = 2.58$ MPa).

2.2.2. SPECIMEN PREPARATION, CRACKING, AND EXPOSURE

The wedge-splitting method has long been used in fracture mechanics of concrete [57]. The test was briefly described in chapter 1.4. A specimen is prepared by casting or saw-

ing a groove and a notch. In the testing machine, the specimen is placed on a linear support. Two rollers and a wedge are used to transfer the vertical load (i.e. machine movement) into a horizontal load. Two LVDTs are placed at the bottom of the notch, and their average is used as a feedback signal to the machine. This way, the average crack width is controlled. The setup is schematically shown in figure 1.10. This method is used in chapter 3, where plain concrete specimens are studied.

As discussed in chapter 2.1, cracking behavior of reinforced concrete is somewhat different. Cracks form parallel to the reinforcing steel, with additional microcracks around the reinforcement [104]. This effect could possibly be more important for chloride ingress [42] and reinforcement corrosion than traversing cracks only [111]. In order to study this effect, two ribbed reinforcing steel bars were placed in the specimens (figure 2.1 right). This modification enables crack branching around the steel rebar, with cracks forming parallel to the steel, in addition to being perpendicular to it.

For the specimen preparation, cubic moulds of $150 \times 150 \times 150\ mm^3$ are used. Inside the mould, two reinforcing bars of 12 mm diameter and about 120 mm in length are placed (figure 2.1). They were positioned using plastic spacers. Prior to casting the specimens, a PVC profile with a cross section of $40 \times 40\ mm^2$ is mounted on the mould, in order to create a recess. This PVC profile is removed around 2 hours after casting. This way, the desired specimen geometry is obtained. After the curing period (28 days in a curing chamber at 20 °C and 95 % relative humidity), a notch (5 mm thick) is sawn in the specimen using a water cooled saw. The purpose of the notch is to guide the fracture process; namely, the crack should typically start from the notch. The depth of this notch can also be adjusted in order to achieve certain concrete cover depth. It should not be too shallow, however, since the crack then might initiate outside the notch.

Wedge-splitting specimens were taken out of the climate chamber after 28 days and

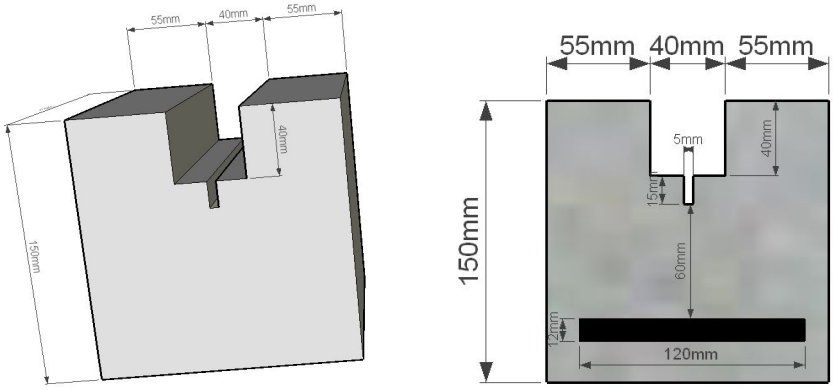

(a) (b)

Figure 2.1: Geometry of the proposed (MWST) specimen in 3D (a) and a cross-section through the reinforcing bar (b)

thereafter stored at room temperature in the lab until testing. At the age of 36 days, the cracking procedure was performed. In order to control the obtained crack width, LVDTs are placed on both sides of the specimen at the bottom of the notch, where the crack is

expected to initiate. Their average is used as a feed-back signal for the machine, and controls the whole loading process. In this way, a stable cracking procedure is performed. The final (unloaded) crack width was recorded and this crack width was used in subsequent discussions. It has to be noted that these crack widths could reduce over time due to e.g. creep, however this was taken into account in this study.
After cracking, the specimens were stored in lab conditions for more than 7 days prior to exposure (hence, they were not water saturated). Then, they were exposed to weekly wet-dry cycles consisting of 48 hours of 3.3% $NaCl$ solution contained in the recess and 5 days of drying at 20 °C and 50% RH. The solution was poured in a pond formed by the recess and two rubber sheets glued to the sides of each specimen. The OPC and the slag series were exposed to 45 and 36 weekly cycles, respectively. The exposure duration of slag series was shorter due to time constraints presented by the PhD project. At the end of the exposure to chlorides, the OPC specimens were cut longitudinally (parallel to the reinforcement) into three pieces, and the middle piece was analyzed using LIBS (figure 2.2a). For the slag series, the top part (i.e. the recess) was cut off first, to enable easier handling of the specimens. Then the specimens were cut in half, and one half was analyzed using LIBS (figure 2.2b). Both series were cut without use of water, in order to avoid washout of chloride ions from specimens. For cutting of the OPC series, no liquid was used. As this resulted in heating up of the saw, oil was used as cooling liquid for cutting the slag series.

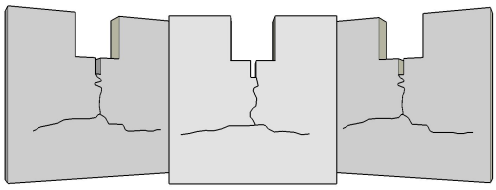

(a) OPC

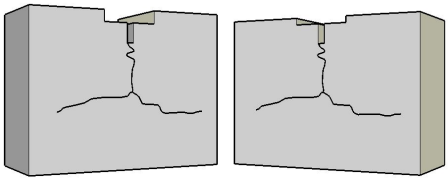

(b) Slag

Figure 2.2: Cut specimens prior to LIBS analysis

2.2.3. MECHANICAL MODELING OF THE MWST

To study the influence of proposed modification (i.e. addition of the steel rebars) on the mechanical behavior of specimens, a lattice model is used. This type of model has been adopted by various authors to simulate concrete fracture (e.g. [107, 112]). The Delft lattice model [107, 113] is extensively used in the chapters related to modeling (in chapters

5,6, and 7), where it is explained in more detail. It is used in this chapter merely to try to capture the effects of the proposed modified wedge-splitting test.

Reinforcing bars can be included in a lattice model by either explicitly meshing the rebars [114] or by introducing additional rebar elements in the lattice mesh which are linked to the initial random mesh through prescribed kinematic relations [112]. The first method was selected herein, i.e. part of the mesh was defined as a reinforcement bar, with its mechanical properties.

In figure 2.3a, the geometry, loading and boundary conditions of the test are shown. Figure 2.3b shows the initial lattice mesh. The only difference between the wedge-splitting mesh (designated as WST) and the modified wedge splitting mesh (designated MWST) was the presence of the two reinforcement bars and interface elements in the latter, according to the geometry of tested specimens (figure 2.1).Figures 2.3c and 2.3d show the rebars and interface elements connecting concrete and steel. The mesh size (before creating the recess and the notch) was $150 \times 150 \times 150\ mm$, with $60 \times 60 \times 60$ nodes with cell size of 2.5 mm. Element properties were as follows: concrete - $f_t = 3.6\ MPa$ (tensile strength), $f_c = -36\ MPa$ (compressive strength), and $E = 30\ GPa$ (Young's modulus); steel - $f_t = 500\ MPa$ and $E = 200\ GPa$; and interface - $f_t = 2\ MPa$, $f_c = -4\ MPa$, and $E = 30\ GPa$. All elements were assigned with a brittle failure law, and could fail in either tension or compression when the strength was achieved. At the left and the right side of the recess, horizontal external forces were applied (figure 2.3a). At the middle of the bottom surface, a linear support was simulated by constraining displacement in all directions (figure 2.3a). Note that only the loading phase is simulated, while the experimental results show also the unloading phase. During the simulation, relative displacement of two nodes at the bottom of the notch is monitored, similar to the experiment. This is designated as crack opening displacement (COD). As the aim of these simulations was not to replicate experimentally observed results, but merely to compare MWST and WST responses, the selected input is reasonable.

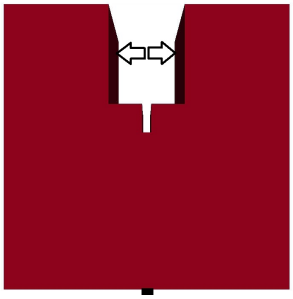

(a) Geometry and loading conditions

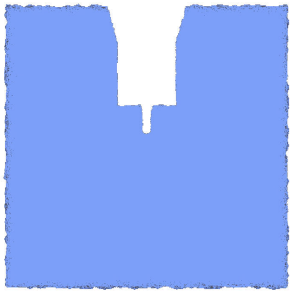

(b) Lattice mesh

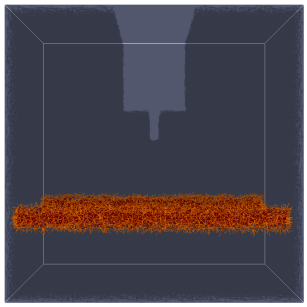

(c) Side view of the rebar and interface elements in MWST lattice

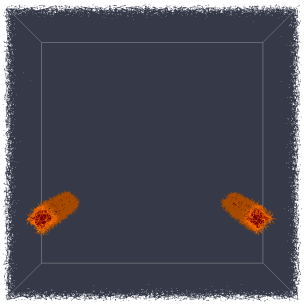

(d) Front view of the rebar and interface elements in MWST lattice

Figure 2.3: WST/MWST specimens used in the lattice simulation

2.2.4. LASER INDUCED BREAKDOWN SPECTROSCOPY (LIBS)

Laser induced breakdown spectroscopy (LIBS) is a powerful and reliable optical technique for detection of trace elements present in a solid, liquid or gaseous sample [115]. It is based on atomic emission spectroscopy where analyses are performed by monitoring intensities and wavelengths of the emission lines. A highly energetic laser pulse is focused to form a plasma on the surface of the specimen. The plasma excites and atomizes just a very small part of the specimen, and the atomic emission spectrum is recorded. In principle, all elements can be detected by LIBS, since all elements emit characteristic frequencies when excited to sufficiently high temperature. In practice, this is limited by the power of the laser, the focusing conditions, the sensitivity and the wavelength range of the detector and the spectrometer.

Compared to wet chemical analyses, specimen preparation for LIBS is simple. A split or cut concrete surface is examined, and no grinding/crushing of concrete is needed. Also, multiple elements can be traced with a single LIBS analysis, unlike in titration analyses (e.g. Volhard's titration for chloride) which are limited to a single element.

LIBS can be used for determination of trace elements, such as chloride and sulfur, in cement based materials [109, 110, 115–117]. It can be considered as a meso-scale technique, with spatial resolution in mm range. Also, chloride ions are (usually) present only in the cement paste and not in the aggregate particles, and LIBS, with help of software tools, can discriminate between these locations based on other elements, such as Ca, Si, or O.

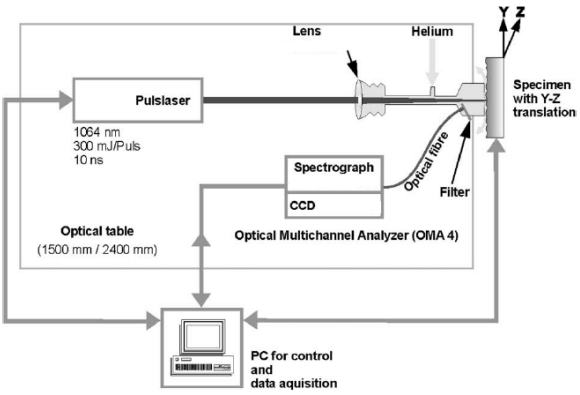

Figure 2.4: Experimental set-up for laser induced breakdown spectroscopy (LIBS) [109]

The setup enables scanning the exposed surface in a grid-like fashion. In the current study, the OPC series was scanned using a grid of 140×140 locations, and the slag series using a grid of 150×110 locations, both with a spacing of 1 mm. After processing the results, two dimensional element distributions on the analyzed surface are obtained.

After the LIBS analysis was performed in Berlin, the specimens were shipped back to Delft for examination of the cracks. They were impregnated under vacuum with fluorescent low viscosity epoxy, which enabled visual examination of cracks under UV light.

After the impregnation, the exposed surface was polished to remove excess epoxy. Then, photos of the specimens were taken with UV light. These were processed and included in the results section, together with corresponding element profiles. Unfortunately, several specimens broke during shipping, so they were not impregnated and examined.

2.3. RESULTS AND DISCUSSION

2.3.1. CRACKING

IN a MWST specimen, a vertical crack typically develops starting from the notch. As the crack widens, it reaches the reinforcing steel, branches horizontally, parallel to the reinforcement and around it. This behavior was observed and studied non-destructively (using concrete resistance measurements) and destructively (using fluorescent epoxy impregnation) in a related study [118]. This branching is similar to the behavior of reinforced concrete beams subjected to bending loads, as shown by Pease [42]. In his study, the concrete cover was cut off in order to expose the steel rebar for visual monitoring. Then, photogrammetric assessment was used to study cracking behavior in the steel/concrete interface of RC beams.

A typical vertical load-average COD (crack opening displacement) curve is shown in figure 2.6. The first part of the curve includes elastic deformation and occurrence of nonlinearity close to the peak load. It is followed by a descending branch, as the stiffness of the specimen is reduced due to cracking. Once a target COD is achieved (denoted as *Loaded crack width* in figure 2.6), the specimen is unloaded, and the crack partially closes. The final crack width (denoted as *Unloaded crack width* in figure 2.6) is noted and used in further analyses. Crack widths of all analyzed specimens are shown in table 2.2. As will be further shown, this crack branching around the reinforcement is reflected in chloride and sodium distributions in exposed specimens.

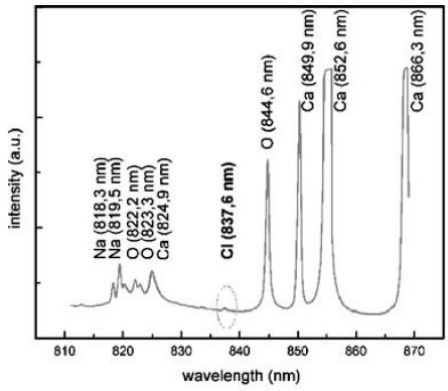

Figure 2.5: Typical concrete spectrum in the chlorine wavelength range, with identification of the spectral lines. [110]

Table 2.2: Surface crack widths of specimens used in the study. Specimens are marked as mixture name-unloaded crack width.

Specimen	Loaded crack width (μm)	Unloaded crack width (μm)
OPC-55	100	55
OPC-80	151	80
OPC-115	203	115
OPC-165	249	165
OPC-186	299	186
OPC-190	300	190
OPC-217	292	217
OPC-305	400	305
Slag-55	96	55
Slag-162	289	162
Slag-212	386	212
Slag-313	482	313
Slag-424	579	424

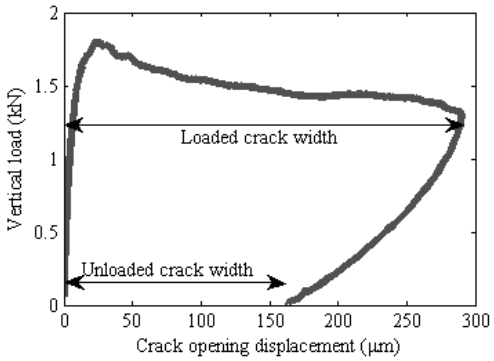

Figure 2.6: A typical load-displacement curve for MWST

2.3.2. MODELING

In figure 2.7a, a comparison of load-COD (crack opening displacement) curves of WST and MWST is given. It can be seen that the pre-peak behavior is similar, while the post-peak response differs. The WST exhibits somewhat more brittle behavior, while MWST is more ductile due to the presence of reinforcement. Figure 2.7b gives a comparison of load-COD curves of WST and MWST obtained by the model. As in the experiment, the pre-peak behavior of both specimens is similar. However, they exhibit a significantly different post-peak response. The response of the WST is brittle (in fact, more brittle than experimentally observed), and exhibits a steeper softening curve compared to the experiment. This is expected in a lattice model with no material heterogeneity (except the mesh randomness)[107]. The MWST on the other hand shows hardening after the peak load due to presence of reinforcement. This approach seems to somewhat overestimate the mechanical effect of the reinforcing steel in current tests. This could be due to the relatively large size of interface elements in the present simulation (around 2.5 mm, same as other lattice elements), while in reality the interface is very thin. This coarse discretization was necessary herein due to very large computational cost associated with the analysis. Given the modeling assumptions and limitations, it can be said that the model can reasonably reproduce the global behavior of WST and MWST. The output of this simulation will be used in chapter 5 as input for modeling of chloride ingress.

Figure 2.8 shows a side view of the development of cracks during the simulation in both

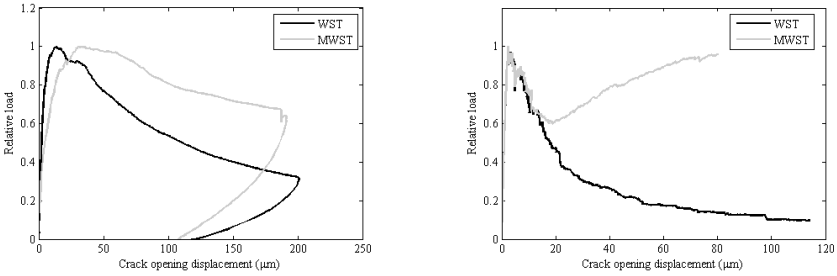

(a) Experiments (WST from chapter 3) (b) Simulation

Figure 2.7: Comparison of load-COD curves for WST and MWST

WST and MWST specimens. In the beginning, the behavior of both tests is the same. A vertical crack starts at the notch and develops. This crack develops all the way through the specimen in the WST test. In the MWST specimen, however, crack branching occurs at the level of the reinforcement, which was also observed in experiments. A horizontal crack parallel to the reinforcing steel then develops, together with a further development of the vertical crack.

More insight into the cracking process can be obtained by observing the development of cracks inside the specimen (figure 2.9). While cracks in the WST specimen develop uniformly along the thickness of the specimen, in the MWST specimen cracks form also around the rebar and in the steel/concrete interface. Debonding of the steel/concrete

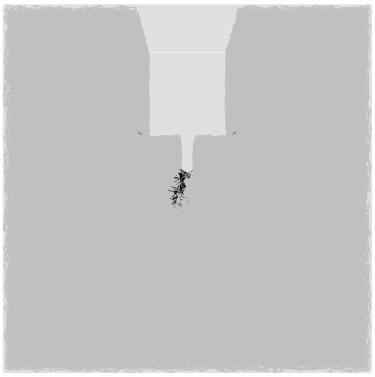

(a) WST after 2000 steps (COD=5.9 μm)

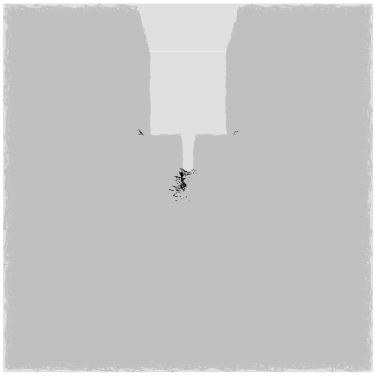

(b) MWST after 2000 steps (COD=4.9 μm)

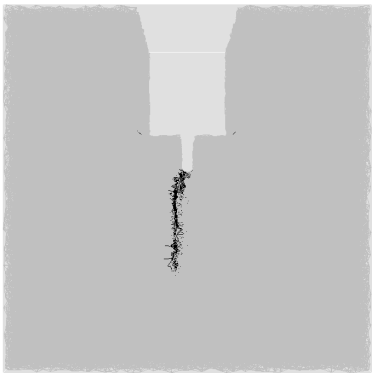

(c) WST after 6000 steps (COD=15.5 μm)

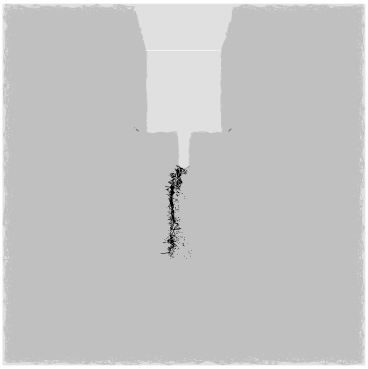

(d) MWST after 6000 steps (COD=15.5 μm)

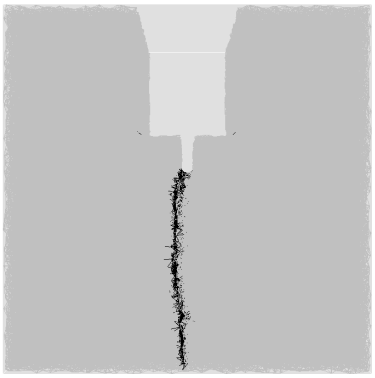

(e) WST after 12000 steps (COD=107.3 μm)

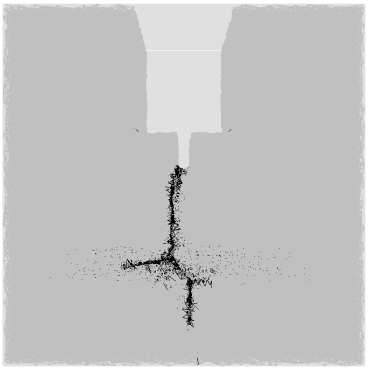

(f) MWST after 17500 steps (COD=78.4 μm)

Figure 2.8: Cracked lattice in the WST and MWST setup

interface occurs, and is related to the surface crack width for the selected geometry. This behavior was also observed in experiments, and has significant implications for durabil-

ity of reinforced concrete.

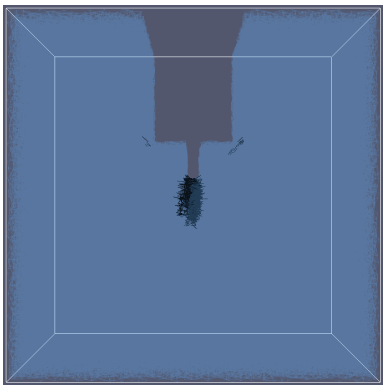

(a) WST after 2000 steps (COD=5.9 μm)

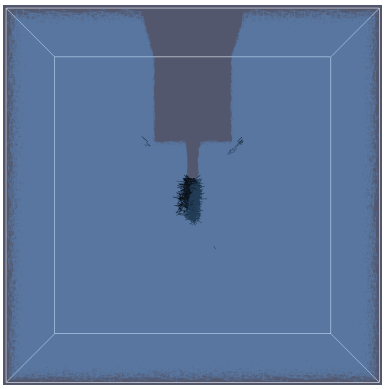

(b) MWST after 2000 steps (COD=4.9 μm)

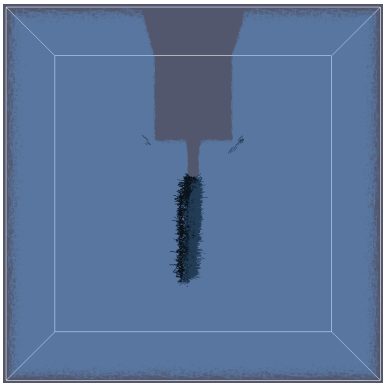

(c) WST after 6000 steps (COD=15.5 μm)

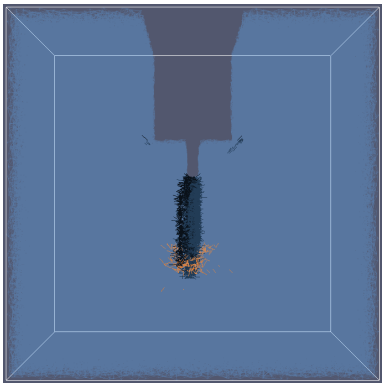

(d) MWST after 6000 steps (COD=15.5 μm)

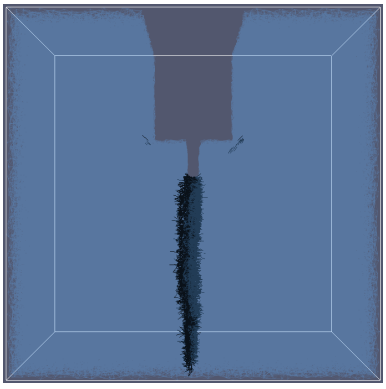

(e) WST after 12000 steps (COD=107.3 μm)

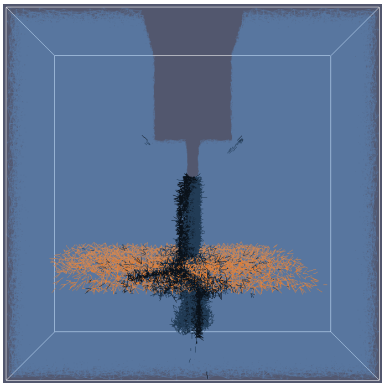

(f) MWST after 17500 steps (COD=78.4 μm)

Figure 2.9: Cracked lattice in the WST and MWST setup (only cracks are displayed). Black- concrete cracks; orange - interface cracks

2.3.3. LIBS

In figures 2.10-2.17, chloride and sodium profiles are shown for the OPC series specimens. In figures 2.18-2.22, chloride and sodium profiles are shown for the slag series specimens. Where available (note that some of the specimens broke during shipment), also the images of cracks obtained from impregnation are shown. The distribution of Cl and Na on the whole analyzed surface of the specimen OPC-55 is shown in figure 2.10. Then, the aggregate particles are excluded, since they present impermeable inclusions and therefore obstacles to chloride penetration, and contain no chloride. Aggregate particles are discriminated based on a Ca to O ratio, because the aggregate particles contain no Ca, while on the contrary cement paste contains plenty of Ca. More details on how the aggregate particles are discerned can be found in Weritz et al. [110]. Results of all other specimens are displayed only for the case without coarse aggregates. In the slag series, also areas rich in iron are excluded. Because the iron peak in the spectrum is close to the chlorine peak in the spectrum (838.77 nm for Fe, compared to 837.59 nm for chlorine), iron rich areas could be misinterpreted as chloride rich areas in the images, and are therefore not taken into account. Note that with LIBS does not enable distinction between free and bound chloride, i.e. the total chloride content is measured.

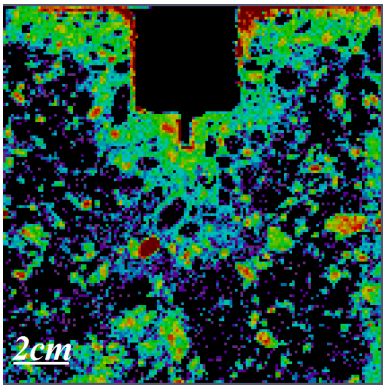

(a) *Cl* (aggregates included)

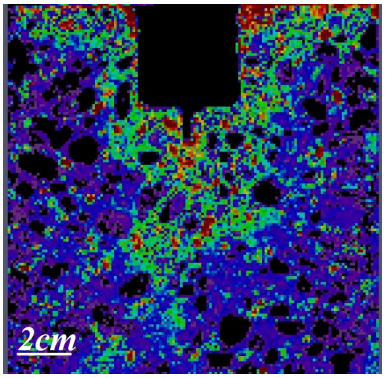

(b) *Na* (aggregates included)

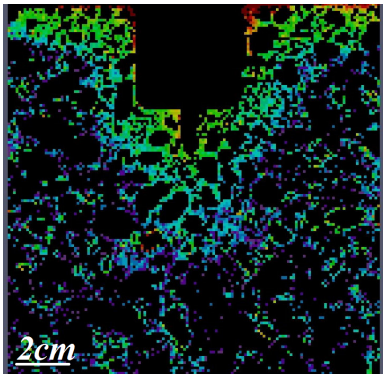

(c) *Cl* (aggregates excluded)

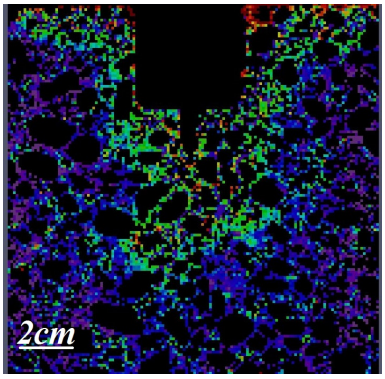

(d) *Na* (aggregates excluded)

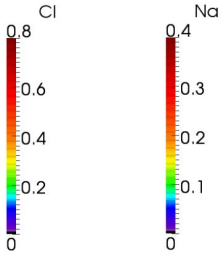

(e) Legend for element distributions (in % of mortar weight)

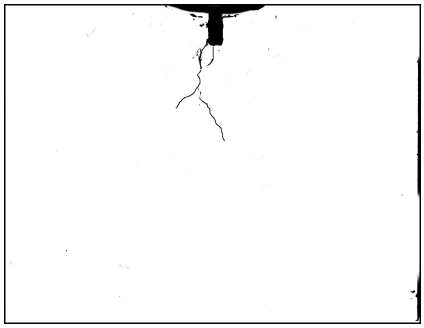

(f) Crack

Figure 2.10: Chloride (*Cl*) and sodium (*Na*) distributions determined by LIBS analysis (a-d); legend (e); and crack (f) in OPC-55 specimen

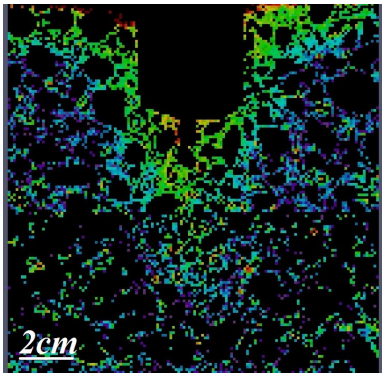

(a) Cl (aggregates excluded)

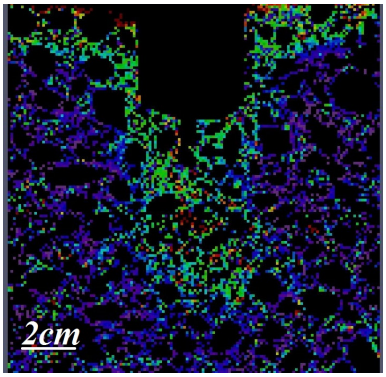

(b) Na (aggregates excluded)

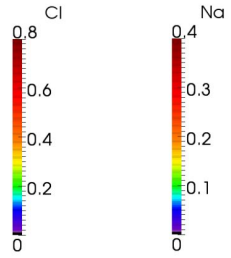

(c) Legend for element distributions (in % of mortar weight)

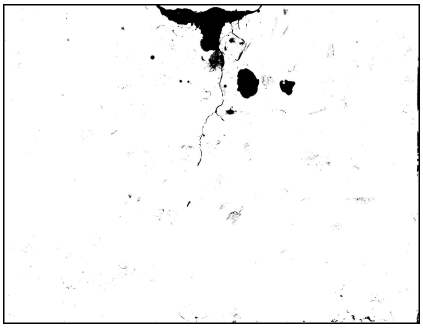

(d) Crack

Figure 2.11: Chloride (Cl) and sodium (Na) distributions determined by LIBS analysis (a,b); legend (c); and crack (d) in OPC-80 specimen

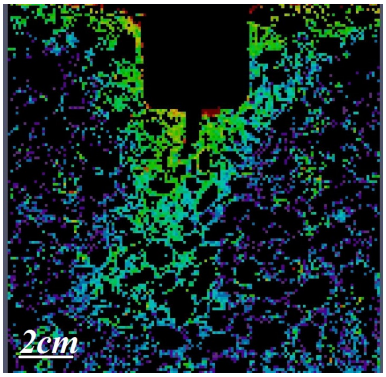

(a) Cl (aggregates excluded)

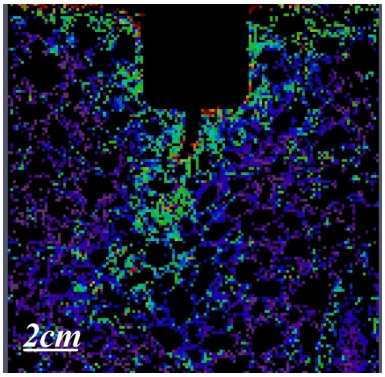

(b) Na (aggregates excluded)

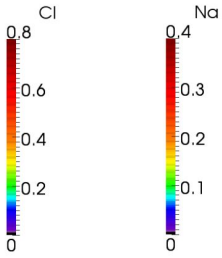

(c) Legend for element distributions (in % of mortar weight)

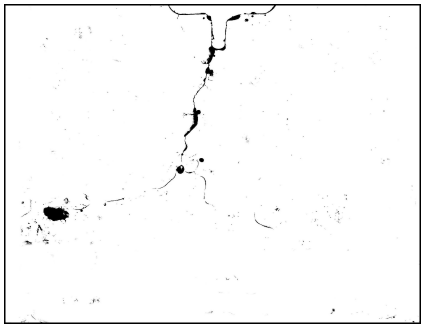

(d) Crack

Figure 2.12: Chloride (Cl) and sodium (Na) distributions determined by LIBS analysis (a,b); legend (c); and crack (d) in OPC-115 specimen

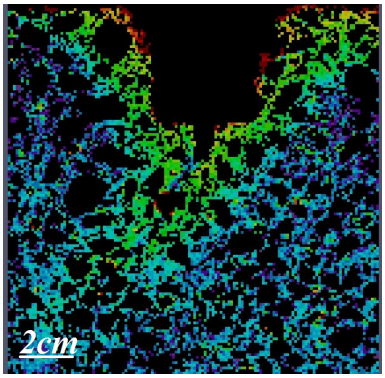

(a) Cl (aggregates excluded)

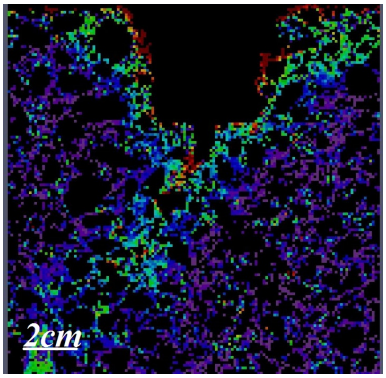

(b) Na (aggregates excluded)

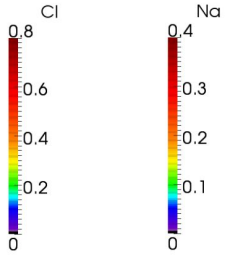

(c) Legend for element distributions (in % of mortar weight)

Figure 2.13: Chloride (Cl) and sodium (Na) distributions determined by LIBS analysis (a,b); and legend (c) in OPC-165 specimen

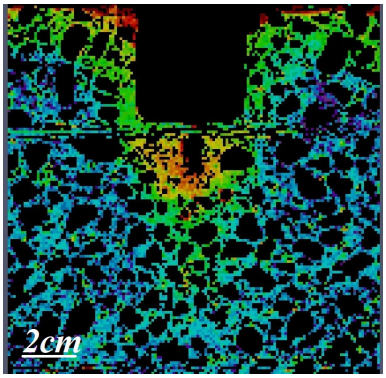

(a) Cl (aggregates excluded)

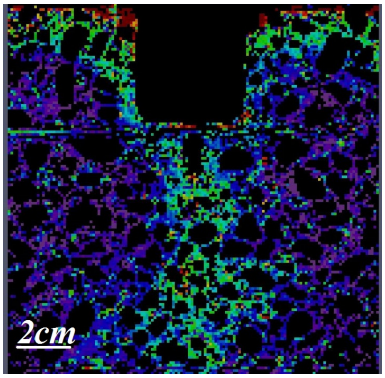

(b) Na (aggregates excluded)

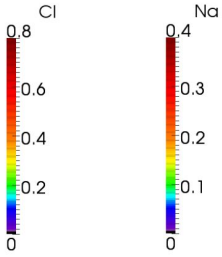

(c) Legend for element distributions (in % of mortar weight)

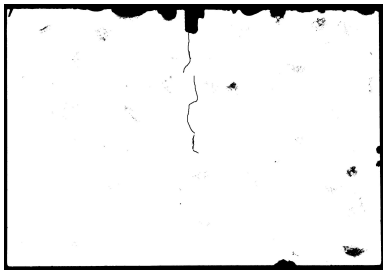

(d) Crack

Figure 2.14: Chloride (Cl) and sodium (Na) distributions determined by LIBS analysis (a,b); legend (c); and crack (d) in OPC-186 specimen

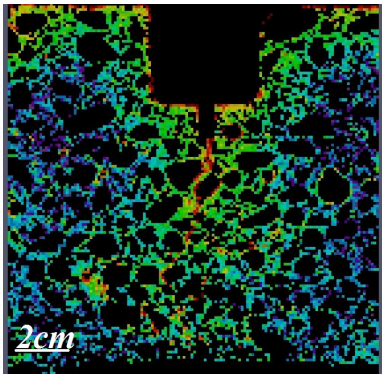

(a) *Cl* (aggregates excluded)

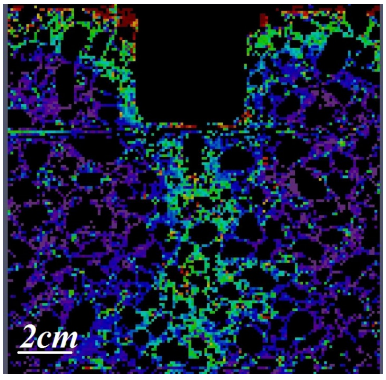

(b) *Na* (aggregates excluded)

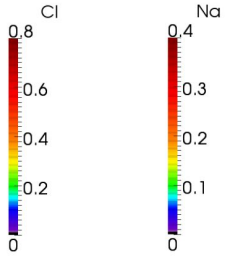

(c) Legend for element distributions (in % of mortar weight)

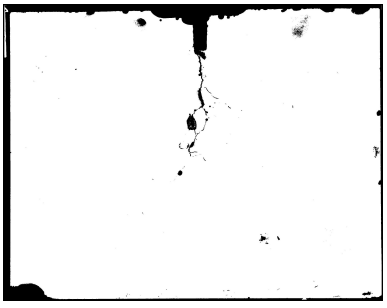

(d) Crack

Figure 2.15: Chloride (*Cl*) and sodium (*Na*) distributions determined by LIBS analysis (a,b); legend (c); and crack (d) in OPC-190 specimen

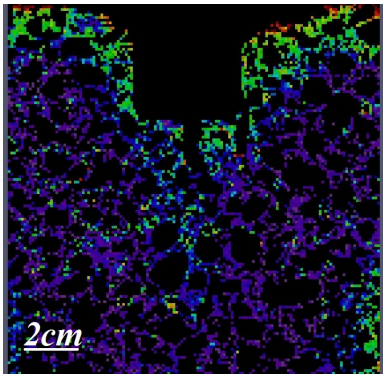

(a) Cl (aggregates excluded)

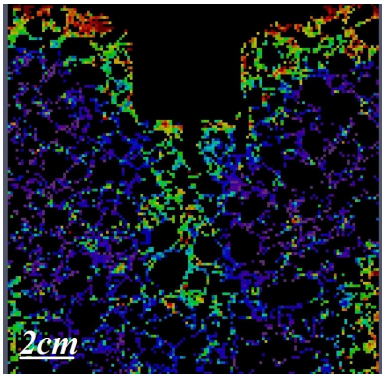

(b) Na (aggregates excluded)

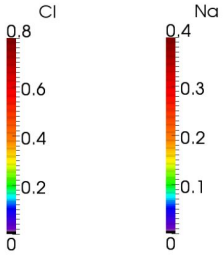

(c) Legend for element distributions (in % of mortar weight)

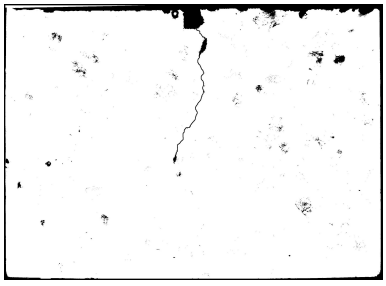

(d) Crack

Figure 2.16: Chloride (Cl) and sodium (Na) distributions determined by LIBS analysis (a,b); legend (c); and crack (d) in OPC-217 specimen

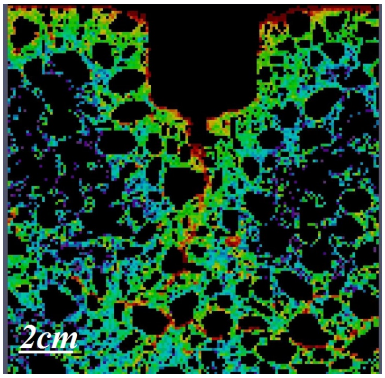

(a) Cl (aggregates excluded)

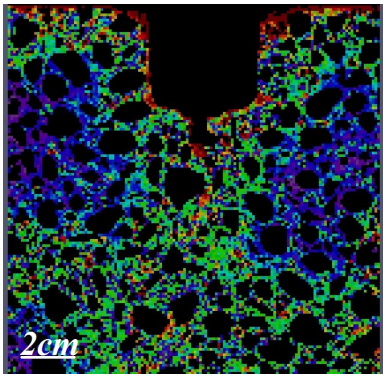

(b) Na (aggregates excluded)

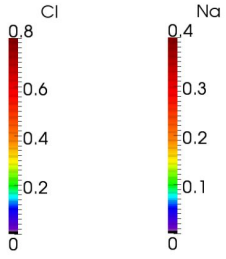

(c) Legend for element distributions (in % of mortar weight)

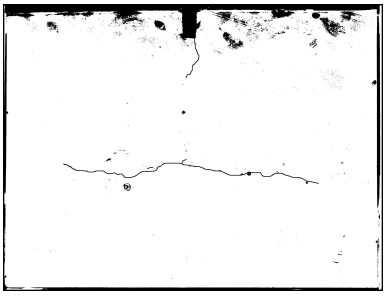

(d) Crack

Figure 2.17: Chloride (Cl) and sodium (Na) distributions determined by LIBS analysis (a,b); legend (c); and crack (d)in OPC-305 specimen

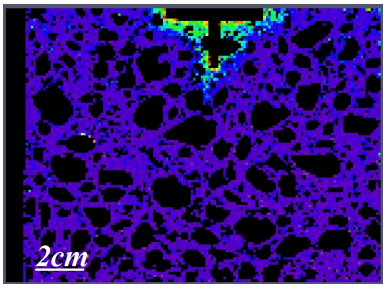

(a) Cl (aggregates and Fe rich areas excluded)

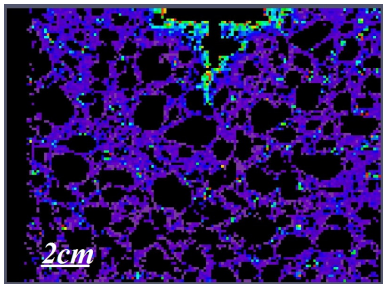

(b) Na (aggregates and Fe rich areas excluded)

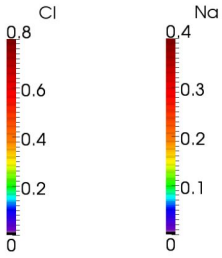

(c) Legend for element distributions (in % of mortar weight)

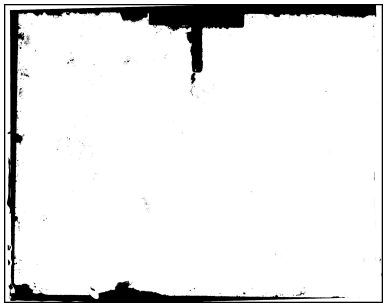

(d) Crack

Figure 2.18: Chloride (Cl) and sodium (Na) distributions determined by LIBS analysis (a,b); legend (c); and crack (d) in Slag-55 specimen

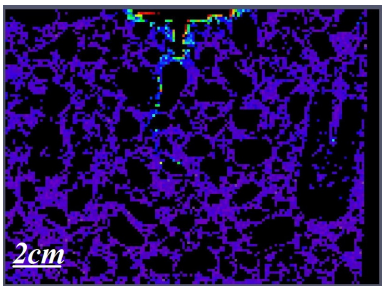

(a) Cl (aggregates and Fe rich areas excluded)

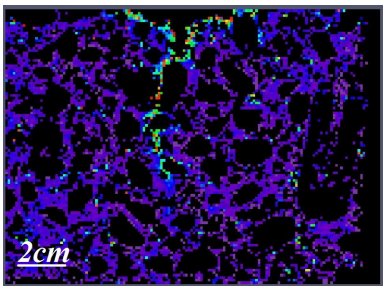

(b) Na (aggregates and Fe rich areas excluded)

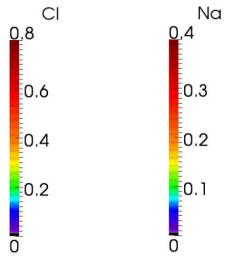

(c) Legend for element distributions (in % of mortar weight)

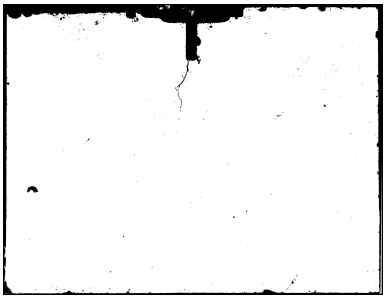

(d) Crack

Figure 2.19: Chloride (Cl) and sodium (Na) distributions determined by LIBS analysis (a,b); legend (c); and crack (d) in Slag-162 specimen

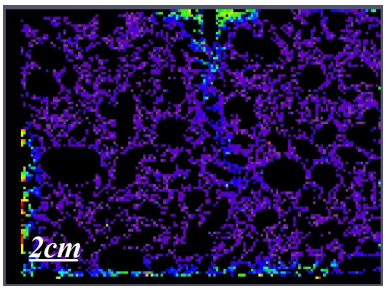

(a) Cl (aggregates and Fe rich areas excluded)

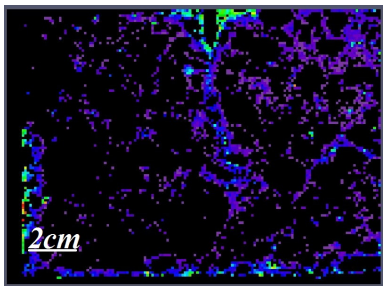

(b) Na (aggregates and Fe rich areas excluded)

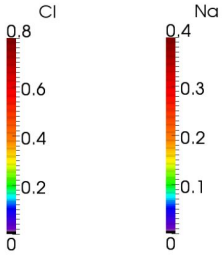

(c) Legend for element distributions (in % of mortar weight)

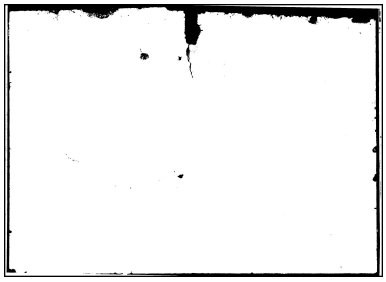

(d) Crack

Figure 2.20: Chloride (Cl) and sodium (Na) distributions determined by LIBS analysis (a,b); legend (c); and crack (d) in Slag-212 specimen

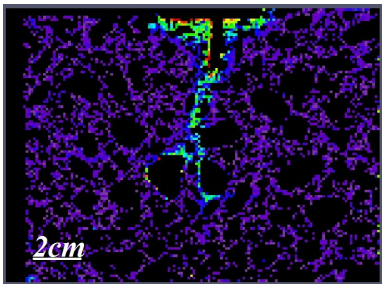

(a) Cl (aggregates and Fe rich areas excluded)

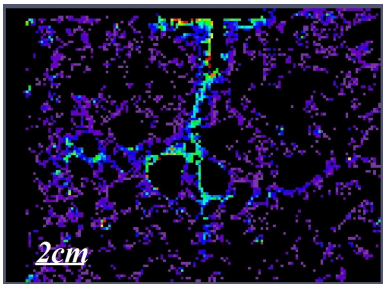

(b) Na (aggregates and Fe rich areas excluded)

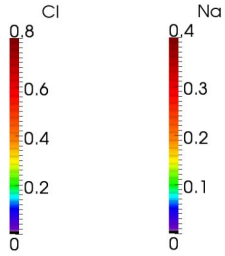

(c) Legend for element distributions (in % of mortar weight)

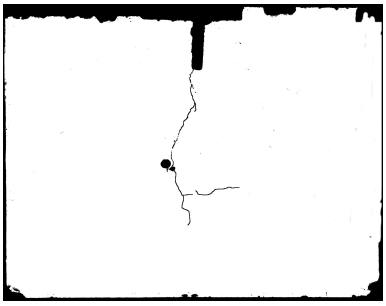

(d) Crack

Figure 2.21: Chloride (Cl) and sodium (Na) distributions determined by LIBS analysis (a,b); legend (c); and crack (d) in Slag-313 specimen

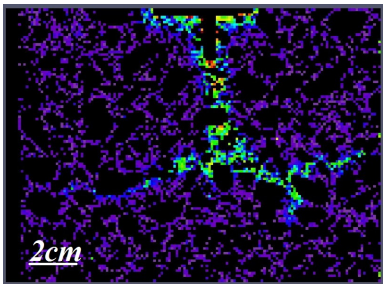

(a) Cl (aggregates and Fe rich areas excluded)

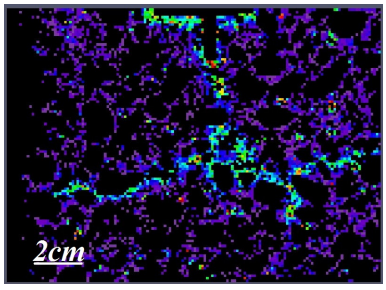

(b) Na (aggregates and Fe rich areas excluded)

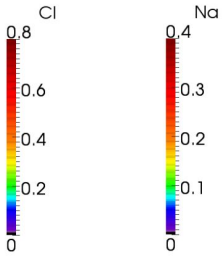

(c) Legend for element distributions (in % of mortar weight)

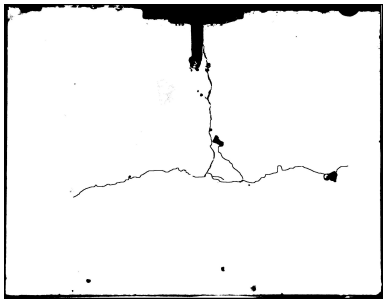

(d) Crack

Figure 2.22: Chloride (Cl) and sodium (Na) distributions determined by LIBS analysis (a,b); legend (c); and crack (d) in Slag-424 specimen

It is clear that the ingress profiles follow the cracks. In cases where cracks develop horizontally (parallel to the reinforcement), the ingress profiles change accordingly. Similar behavior was observed by Michel et al. [119] in their study. As a consequence, corrosion behavior is somewhat different in these cases [103]. Namely, if there was debonding at the steel/concrete interface, corrosion pits did not occur in the middle of the rebar. If there was no debonding, the pits did occur in the middle of the rebar, i.e. where the vertical crack is [103].
Much more significant chloride penetration was observed in the OPC series. Apart from the longer exposure time for this series (45 vs. 36 weekly cycles for slag), there is also a significant difference in chloride diffusion coefficient between the two mixes. As shown in chapter 3 (see table 3.1), the non-steady state migration coefficient of the OPC mix measured at 28 days according to NT Build 492 [18] is (9.76-12.80)$\times 10^{-12}$ m^2/s, while for the slag mix it is (3.23-4.83)$\times 10^{-12}$ m^2/s.
Typically, chloride ion distributions are obtained by wet chemical analysis of the concrete material. Grinding of consecutive layers (typically in the order of 1-5 mm each) provides powdered samples to be analyzed. These samples give essentially averaged values of chloride content in a certain layer. While this provides relatively reliable data for one-dimensional chloride ingress (even though concrete is then treated as a homogeneous medium), it may not be sufficient for a case of cracked concrete. Even so, it is commonly used in the literature due to convenience and widespread availability. For example, Gowripalan et al. [46] drilled holes around cracks using a dry 20-mm diameter rotary impact drill. Powdered samples from these cores were then analyzed. In order to mimic and assess such approach here, two different subsets are analyzed. First, a vertical subset (with a width of 20 mm) is obtained by averaging out the chloride concentrations in the horizontal direction (figure 2.23a). Similarly, a horizontal subset is obtained for all analyzed specimens (figure 2.23b). In this way, a one-dimensional chloride profile is obtained, without taking into account the crack shape and the width of the contaminated zone around the crack. Aggregate particles are excluded from these considerations, i.e. only the mortar phase is considered.

It can be seen in figure 2.24a that, in OPC specimens with crack widths between 55 μm and 165 μm, a very small increase in chloride content is observed in this way. It is somewhat higher in specimens with cracks wider than 186 μm. In all cases, the maximum values of chloride content seem to be relatively low (compared to figure 2.10-2.17) due to the "averaging" over a zone of 20 mm (roughly 10 mm of each side of the crack).
A similar trend is observed for the vertical average in slag specimens (figure 2.24b). A minor increase in chloride content is observed in this way, except for the specimen with the widest crack (424 μm), where it is somewhat higher. This way of testing would grossly underestimate maximum values of chloride content in such concrete (i.e. with low diffusivity) due to low penetration of chloride to the sides of the crack (see figures 2.18-2.22).

In figure 2.25a, presence of a crack is notable in all OPC specimens when horizontal averaging (as shown in figure 2.23b) is performed. The trend clearly shows a peak in the middle of the profile which is higher the wider the crack is. However, similar to the vertical profiles, the averaging "smears out" the chloride content, so maximum values are

lower than found in figures 2.10-2.17.
Similar to the OPC series, the presence of a crack can be observed in horizontally averaged profiles in slag specimens (figure 2.25b). Also here, the peak in the middle of the profile is higher when the crack is wider. But, again, maximum values of the chloride content are underestimated (figures 2.18-2.22).

When comparing different experimental techniques for determining chloride distribution/profiles in concrete, it has to be noted that it is not the average chloride content at the level of the reinforcement that causes its depassivation (i.e. beginning of the corrosion process), but the maximum value [120]. In a study by Angst and Polder [121], a difference of 20-70% was found between a "microscopic" and "macroscopic" chloride content in a homogeneously exposed area, attributed solely to heterogeneity of concrete. In fact, it seems that the larger the aggregate particles in the concrete mix, the higher the deviation from the "ideal" (i.e. uniform) chloride profile [120]. The deviation is even higher in the presence of cracks, as shown here. This implies that a "macroscopic" technique would underestimate the chloride content around the crack and at the level of the steel, in comparison with a meso-scale technique such as LIBS. A large scatter in experimental results would then be expected. It is therefore advised to use meso- or micro-scale techniques (e.g. LIBS, LA-ICP-MS [108], EPMA [41] or EDS (Energy-dispersive X-ray spectrometry) [122]) when dealing with problems that require high spatial resolution, such as chloride distribution in cracked concrete or critical chloride content analyses.

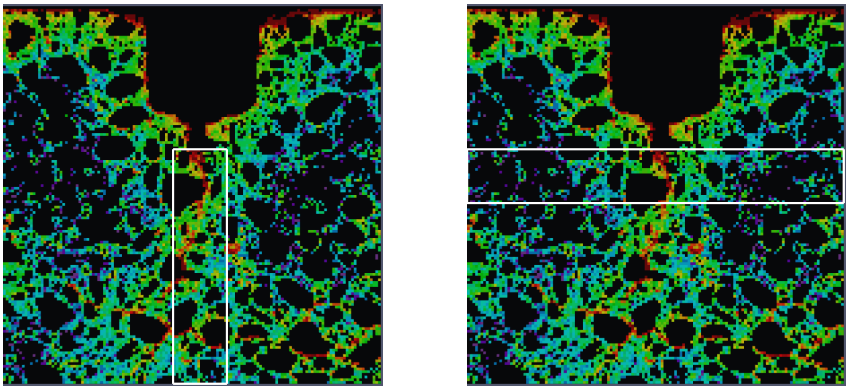

(a) Vertical subset (b) Horizontal subset

Figure 2.23: Definition of subsets for averaging of chloride content

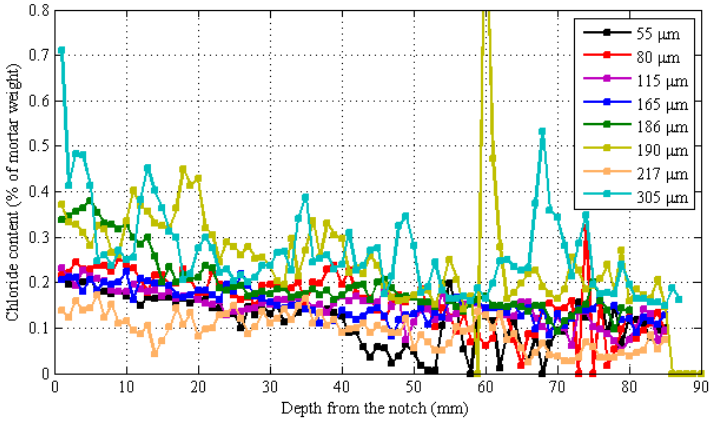

(a) OPC

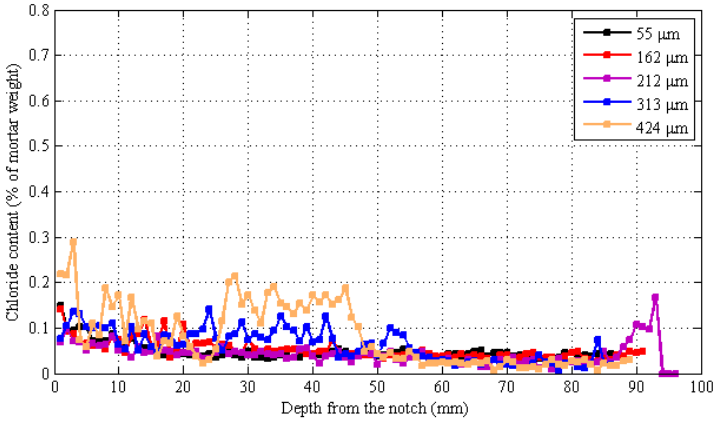

(b) Slag

Figure 2.24: Vertical averaged chloride contents over the subset width

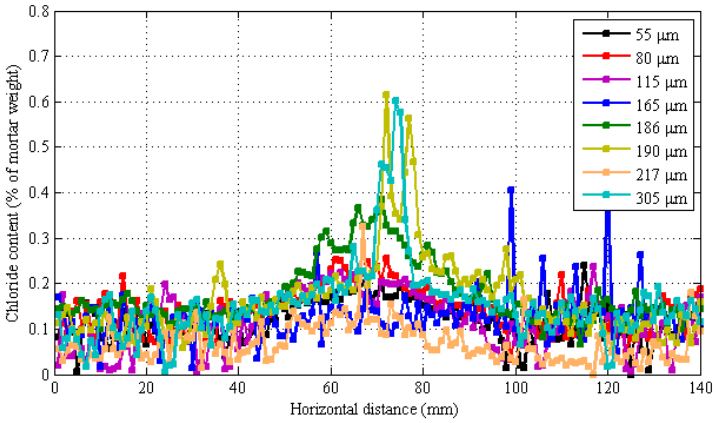

(a) OPC

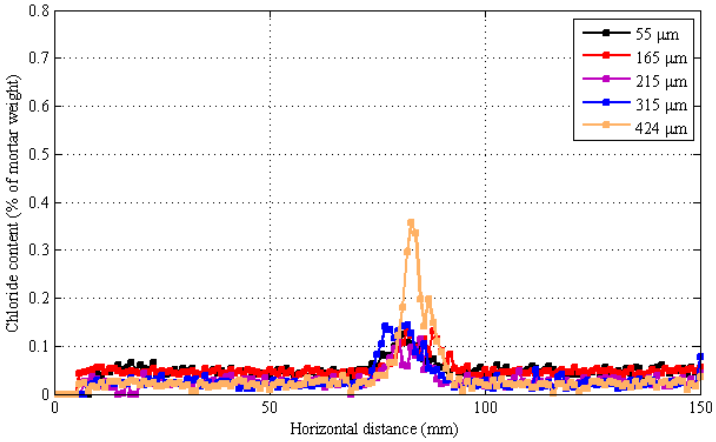

(b) Slag

Figure 2.25: Horizontal averaged chloride contents over the subset width

2.4. SUMMARY AND CONCLUSIONS

IN this chapter, influence of cover cracking on chloride ingress into concrete under wet-dry cycles is investigated. First, a method for specimen preparation and cracking, which mimics the cracking behavior of reinforced beam elements subjected to bending, is proposed. The proposed setup was also examined numerically, using the Delft lattice model. Secondly, specimens prepared with two concrete mixtures (using Portland cement and blast furnace slag cement) were exposed to wetting and drying cycles with $NaCl$ solution for a prolonged time period. Afterwards, they were cut and chloride ingress was examined. For chloride profiling, Laser Induced Breakdown Spectroscopy (LIBS), a meso-scale technique, was used. Based on this study, the following conclusions can be drawn:

- The proposed cracking method and specimen design enable creating bending-type cracks, with debonding occurring at the steel/concrete interface. This is similar to the behavior of reinforced concrete beams.
- The Delft lattice model can reasonably mimic the mechanical behavior and cracking of the WST (plain concrete specimen). However, with the Delft lattice model, the influence of the reinforcing steel in MWST (reinforced concrete specimen) is overestimated compared to the experiment, and the post peak behavior is strain-hardening instead of a strain-softening.
- LIBS can be used as a tool for two-dimensional element mapping with high spatial resolution on the meso-scale. Multiple elements can be measured in the same analysis, which is an advantage over titration based chemical techniques.
- Chloride ingress is affected by cracking. The wider the surface crack, the more chloride penetration occurs. In wide cracks, penetration of chloride ions parallel to the steel occurs, due to the damage in the steel/concrete interface.
- Chloride penetration depth, both at the exposed surface and around the cracks, is much higher in OPC than in slag specimens, due to its higher diffusivity. This is also true for cracks which propagate around the steel/concrete interface.
- Macro-scale techniques for chloride profiling (such as powder grinding and wet chemical analysis) may underestimate chloride contents around cracks, especially in concrete with low diffusion coefficients. Therefore, use of meso- or micro-scale techniques (such as LIBS herein) is advised when high spatial resolution of element distributions is sought.

When studying chloride ingress in cracked concrete, it is important to use reinforced specimens, since their cracking behavior is different from plain concrete. This is important, as chloride ingress is not an issue in plain concrete. From this chapter, it is clear that cracking has a marked influence on chloride ingress, and therefore the initiation period of reinforcement corrosion. However, the impact of chloride ingress on long-term durability of cracked concrete cannot be assessed by only studying chloride ingress. It is important to monitor the corrosion behavior of reinforcement steel, which is part of

a related study [103]. Finally, the impact of cracking on short- and long-term durability (i.e. the initiation and the propagation period) can be found only through synergy of these studies.

3

AUTOGENEOUS HEALING AND CHLORIDE INGRESS IN CRACKS

Never let anyone define what you are capable of
by using parameters that don't apply to you.

Chuck Close

In this chapter, an experimental study of the influence of autogeneous healing on chloride ingress in cracked concrete is presented. In the study, two concrete mixtures (a Portland cement mix and a ground granulated blast furnace slag mix), two healing regimes (submerged and fog room regime), two cracking ages (14 and 28 days), and multiple crack widths are used as parameters. An adapted Rapid Chloride Migration testing procedure is used after the healing period to assess the effectiveness of healing. It was found that small bending-type (i.e. tapered) cracks can heal fully, and larger cracks partially under tested conditions. The obtained results provide a good starting point for further study of the influence of autogeneous or self healing on concrete durability. Furthermore, the results are directly applicable to engineering practice in humid environmental conditions.

3.1. INTRODUCTION AND RESEARCH SIGNIFICANCE

IT has been known for a long time that concrete has an inherent ability to "heal" itself: under favorable conditions, small cracks in the material can close. Multiple factors are thought to be responsible for this phenomenon: swelling of the cement paste near the crack faces, clogging of the cracks by fine particles from the environment, continued hydration, and formation of calcium carbonate in the crack (for more details, see chapter 1.4.4). In recent years, different smart systems have been developed in order to aid in repair of cracks: bacteria-based systems in which bacteria produce calcium carbonate and close cracks [123, 124]; porous network concrete in which cracks can be closed by various viscous healing agents [125]; concrete in which self-healing is aided by a combination of super absorbent polymers and microfibers [126], and other systems. As with autogeneous healing, most of these systems do not aim to restore the mechanical properties of cracked concrete; rather, the aim is to maintain the durability or water tightness of an uncracked structure.

Autogeneous healing was first noticed to occur in water retaining structures and pipes. Leakage of water through small cracks was shown to stop due to crack healing. Accordingly, multiple studies have dealt with the relation between autogeneous healing of cracks and water permeability: Ramm and Biscoping [98] studied autogeneous healing of cracks and reinforcement corrosion in deionised and acidic water; Edvardsen [95] performed a systematic study on healing of cracks under hydraulic pressure; Reinhardt and Jooss [127] studied the influence of temperature on healing. Although these studies show somewhat contradictory results on the influence of some parameters, all of them agree that autogeneous healing can significantly reduce the water permeability of cracked specimens. The findings are of importance for design of water retaining structures and reservoirs.

Apart from water permeability, other techniques have been used to characterize and quantify effects of crack healing [94]: air permeability, optical and electron microscopy, capillary water absorption, ultrasonic measurements, computed tomography, and others. These techniques are a good way to characterize and quantify the extent of crack healing, but cannot be directly used to assess the effect that crack healing has on durability of reinforced concrete.

It is expected that autogeneous healing can reduce chloride ingress in cracks. Several studies have dealt with the issue: Jacobsen et al. [70] found a 28-35 % reduction in rate of chloride migration in specimens which were stored in lime water for 4 months, compared to newly cracked specimens; Şahmaran [84] observed autogeneous healing of small cracks in specimens subjected to a $NaCl$ ponding test; Ismail et al. [61] found that autogeneous healing reduced chloride ingress along the crack path in specimens cracked after 28 days compared to those cracked after 2 years; Yoon and Schlangen [128] found a significant difference between chloride ingress in cracks in a short term (rapid) and long term test, and attributed it to crack healing. Even though most studies suggest that a submerged condition is needed for autogeneous healing (e.g.[69]), Yang et al. [99] showed that cracks in engineered cementitious composites can heal also under wetting and drying cycles. Similar findings were reported by Ferrara et al. [129].

Apparently, crack healing could have an important impact on chloride ingress in cracked concrete. With that in mind, a research program was designed to try to quantify the

extent of autogeneous healing on chloride ingress in cracks. Concrete specimens were prepared, cracked, exposed to promote healing, and tested using a modification of the Rapid Chloride Migration test [18]. The results reflect an influence of different healing regimes on chloride ingress in cracks, and can be used when assessing the influence of cracks on the long term durability of concrete structures. It has to be noted that the aim was not to study the mechanisms of autogeneous healing [130, 131], but rather its effect on the chloride transport.

3.2. MATERIALS AND METHODS

3.2.1. MATERIALS

TWO concrete mixes with w/c ratio of 0.45 were used in this study: a mix prepared with CEM I 52.5 R cement (designated OPC mix), and a mix prepared with CEM III/B 42.5 N cement(designated slag mix). These are the same mixes which were used in chapter 2 (table 2.1). The mixing procedure was also the same.

3.2.2. SPECIMEN PREPARATION AND EXPOSURE

For cracking of the specimens, the standard wedge-splitting procedure was used [57]. The adopted specimen geometry and loading were identical to that used in chapter 2, except that no reinforcing bars were placed inside the concrete. Therefore, only a vertical crack should form (see figure 2.9).

In total, five series of specimens were tested per concrete mixture. The series had different curing regimes: series 1 was cracked at 14 days and cured afterwards in a fog room (20 °C and 95% relative humidity), series 2 was cracked at 28 days and cured in a fog room, series 3 was cracked at 14 days and cured in water, series 4 was cracked at 28 days and cured in water, and series 5 was cracked only prior to chloride testing to prevent any healing. The nomenclature used for different series is given in table 3.1. For each series, slump, air void content, and non-steady-state migration coefficient at 28 days (D_{NSSM} according to NT Build 492 [18]) were measured (table 3.1). All series (except series 5) were cured after cracking as stated for more than 70 days prior to chloride exposure. As previously stated, series 5 was tested shortly after cracking.

Prior to chloride testing, a 100 mm diameter core was drilled from each specimen (figure 3.3). The cores were further cut in such a way that cylindrical specimens with about 90 mm thickness are obtained for chloride exposure.

The specimens were tested in a modified Rapid Chloride Migration test [18]. The modifications were the test duration, and the specimen thickness, which is 50 mm in the standard test. A trial-and-error procedure was employed to obtain a reasonable test duration and voltage for each concrete mixture.The OPC specimens were tested using a voltage of 25 V for 12 hours, while the slag specimens were tested using a voltage of 50 V for 4 hours. After the chloride exposure, the specimens were split in the direction perpendicular to the crack, and then sprayed with $AgNO_3$ solution. The penetration depth was measured. The maximum penetration depth (penetration through the crack) was designated as P_{max}, and the average penetration depth (average of five measurements) in the uncracked part as P_0.

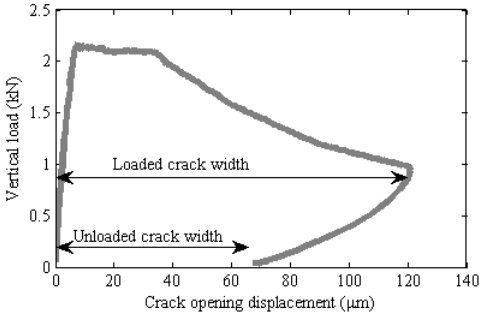

Figure 3.1: A typical load-displacement curve for wedge-splitting test (WST)

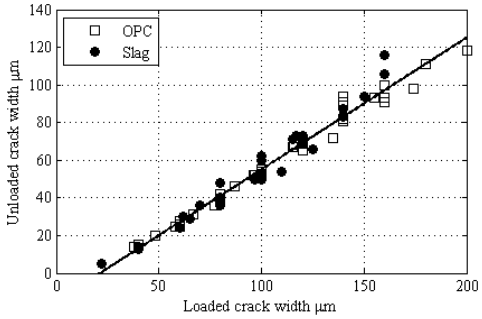

Figure 3.2: Loaded vs. unloaded crack width for all tested specimens

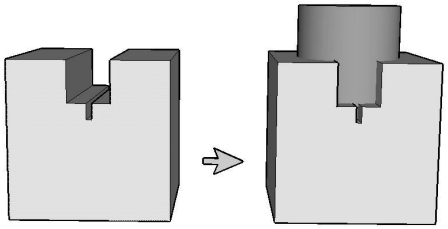

Figure 3.3: The coring procedure prior to the chloride exposure

3.3. RESULTS AND DISCUSSION

IN figure 3.4, a relationship between the loaded crack width and the maximum penetration depth (P_{max}), and the average penetration depth in the uncracked part of the specimen (P_0) is given for OPC and slag series, respectively.

As the crack partially closes upon unloading (figure 3.2), it might be more important to see how the unloaded crack width influences the penetration depth. This relationship is shown in figure 3.5.

Table 3.1: Properties of different mixes used in the study

Series	Slump (cm)	Air void content (%)	28 days D_{RCM} ($\times 10^{-12}$ m^2/s)
14DaysFogOPC	8	3.1	9.76
28DaysFogOPC	7	2.75	12.54
14DaysWaterOPC	6	3	9.84
28DaysWaterOPC	5.5	1.35	12.03
NoHealingOPC	6	1.7	12.80
14DaysFogSlag	22	2.5	3.51
28DaysFogSlag	18	2.5	4.83
14DaysWaterSlag	21.5	1.9	3.68
28DaysWaterSlag	22	2.5	3.23
NoHealingSlag	19	3	4.25

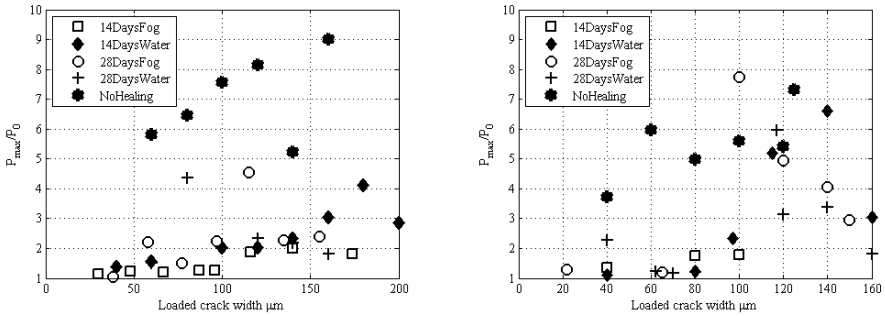

(a) OPC (b) Slag

Figure 3.4: Influence of crack width on autogeneous healing (crack width before unloading)

The NoHealing series of both mixtures exhibit the expected behavior: the penetration depth increases with the increase in crack width. This has to do with both the crack width and the crack depth (which was not measured): as the crack becomes wider, it also becomes deeper in the present setup. The obtained cracks are V shaped, similar to bending cracks. It is therefore expected that this trend would also increase for cracks larger than those studied. This would not be the case for parallel-walled cracks, e.g. obtained by Brazilian splitting.

There is a marked difference between the NoHealing series and all others: namely, the maximum penetration depth is significantly lower in other series. This can probably be attributed to autogeneous healing of cracks. From figures 3.4 and 3.5, the maximum crack width which seems to have healed is about 60 μm in the unloaded state (about 100 μm in the loaded state) for all series subjected to healing. Chloride penetration in these cracks seems to be of the same order of magnitude as in the uncracked material. Similar

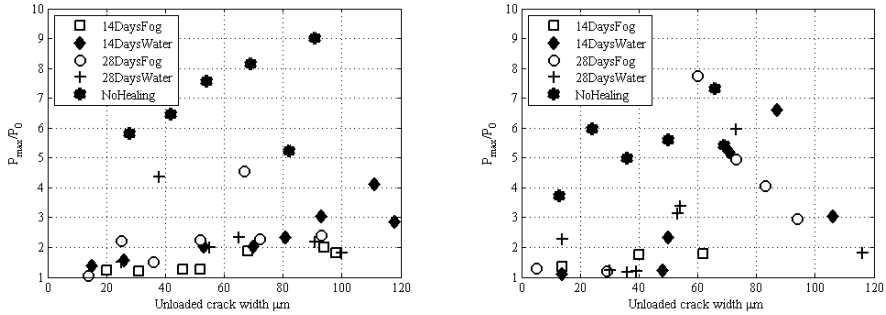

(a) OPC (b) Slag

Figure 3.5: Influence of crack width on autogeneous healing (crack width after unloading)

was observed by Ismail et al. [61]: they found that "in the case of fine cracks (<60 μm), the age at which the crack is induced influences the ability of self-healing to impede chloride diffusion - when the crack openings are 60 μm or more, the age at which the cracks were induced appears to have no significant effect on the ability of self-healing to impede chloride diffusion along the crack path". In the same study, larger cracks showed no autogeneous healing, due to their parallel walled shape. In the current study, it can be seen that larger cracks have partially recovered the transport properties, due to their tapered shape, which enabled the narrow part to heal (figure 3.6). Also, it seems that the transport properties of small cracks have recovered not only when cured under water, which was expected [69], but also when specimens were cured in the fog room. This means that autogeneous healing of these cracks could be possible in real structures in humid climate, and not only in submerged conditions.

The age at which concrete cracks could also potentially have an influence on the extent of autogeneous healing. Ter Heide [69] studied crack healing in young concrete, and found that cracking age is a significant contributing factor. In her study, strength recovery of specimens cracked between 20 and 72 hours was studied. In the current study, two cracking ages were compared for both mixtures and healing conditions. The effect of cracking age on the P_{max}/P_0 ratio is given in figure 3.7 for the OPC mix and in figure 3.8 for the slag mix.

There is not much difference between specimens cracked at 14 and at 28 days in terms of autogeneous recovery of transport properties, judging by figures 3.7 and 3.8. A slight difference can be observed for specimens cured in the fog room (figures 3.7a and 3.8a), where it seems that specimens cracked at 14 days show somewhat lower relative chloride penetration in the crack compared to those cracked at 28 days. This is probably due to higher autogeneous healing capacity of the specimens cracked at an earlier age. However, for specimens cured under water (figures 3.7b and 3.8b), such trend is not observed.

Curing/healing conditions are another important factor. Ter Heide [69] found that healing only occurred in specimens stored under water. Yang et al. [99] observed crack heal-

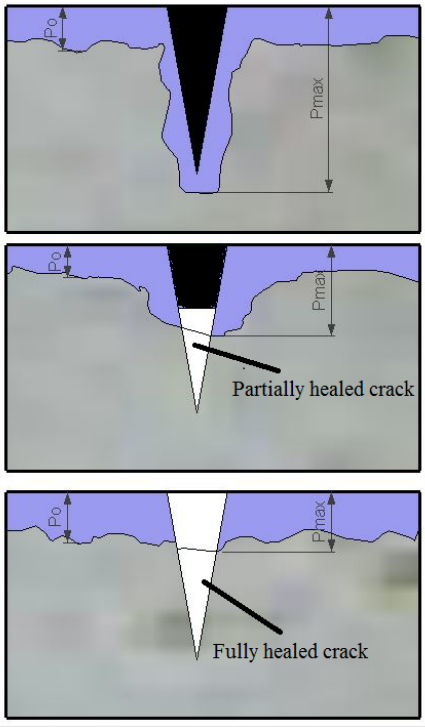

Figure 3.6: Schematic representation of partial and full healing of tapered cracks

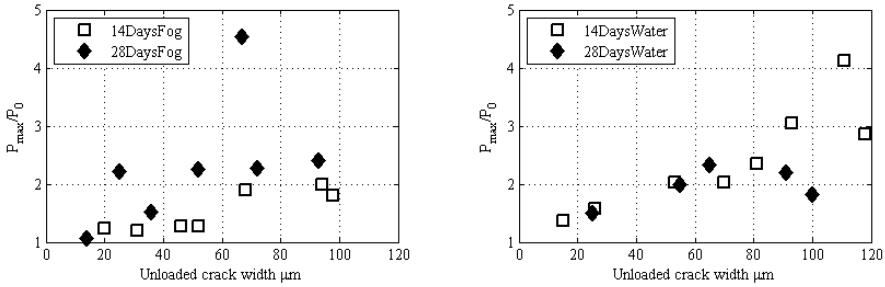

(a) (b)

Figure 3.7: Influence of cracking age on autogeneous healing (OPC mixture)

ing in SHCC also under wet-dry cycles. In these studies, autogeneous healing was defined as recovery of mechanical properties. In the current study, however, recovery of transport properties is sought. The comparison is given in figures 3.9 and 3.10 for OPC and slag mixtures, respectively.

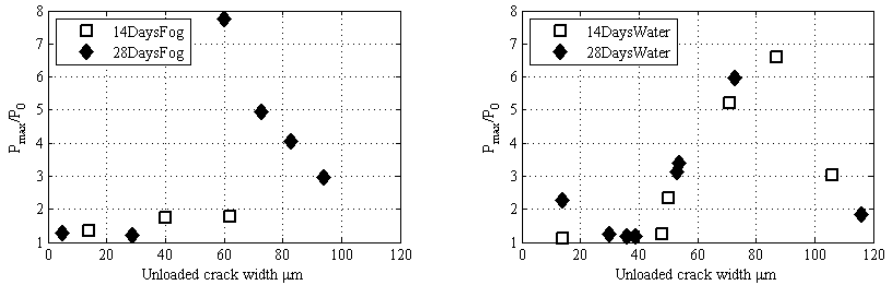

(a) (b)

Figure 3.8: Influence of cracking age on autogeneous healing (slag mixture)

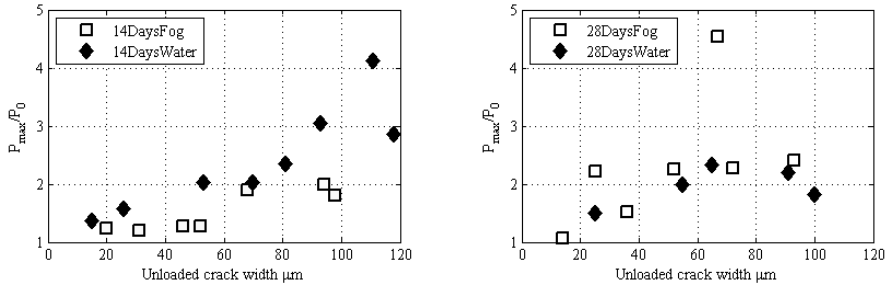

(a) (b)

Figure 3.9: Influence of curing/healing conditions on autogeneous healing (OPC mixture)

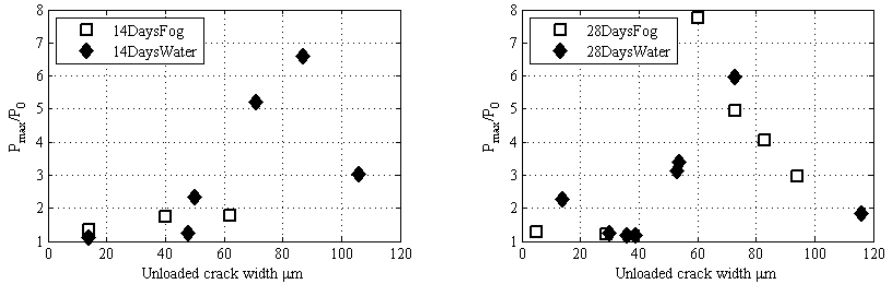

(a) (b)

Figure 3.10: Influence of curing/healing conditions on autogeneous healing (slag mixture)

No clear trends are observable here. It seems that there is no significant difference between specimens cured under water and those cured in the fog room. This seems to be the case for both specimens cracked at 14 days (figures 3.9a and 3.10a) and those cracked at 28 days (figures 3.9b and 3.10b). It seems that curing in the fog room provides a sufficiently moist environment for crack healing with respect to chloride transport. Pro-

longed curing under water is, therefore, not necessary.
It has to be noted that the observed absolute values for D_{max}/D_0 ratio are *specific* for tested mixtures, crack geometries and testing conditions (applied voltage and exposure duration). Studies by Marsavina et al. [65] and Yoon and Schlangen [128] yielded somewhat different ratios, due to different experimental conditions. This is a limitation of the adopted accelerated setup, and one which limits its direct use in practice. This is further elaborated in chapter 6, which deals with numerical modeling of the Rapid Chloride Migration test. Consequently, diffusion coefficients of cracked zones are not calculated here according to NT Build 492 [18]. Also, since different parameters were used for two tested mixtures (due to a significant difference in their transport properties), the results cannot be directly compared. The proposed test is, however, useful for comparative purposes. Its short duration enables it to discriminate between the autogeneous healing, which occurs prior to the chloride exposure, and its effect on the chloride ingress. In a long term (diffusion) experiment, these two would be coupled, since crack healing would occur during the chloride exposure (e.g. [61, 84]). The diffusion test thus simulates well the conditions in submerged structures. The proposed test, however, mimics a case when a structure is built and loaded (cracked), and only after a certain period of time exposed to chloride load, such as deicing salt exposure.

3.4. CONCLUSIONS

IN chapter 3, an experimental study dealing with the relation between chloride ingress in cracks and autogeneous crack healing is presented. The study considered two concrete mixtures, two different cracking ages, two different curing/healing regimes (and a control mixture), and a range of crack widths. Based on the results presented in chapter 3.3, several conclusions can be drawn:

- For the NoHealing (control) series of both concrete mixtures, a nearly linear relation exists between the crack width (loaded or unloaded) and the relative maximum chloride penetration (i.e. P_{max}/P_0 ratio). This probably has to do with the increase of crack depth which follows the increase of crack width.
- For all series subjected to conditions suitable for autogeneous crack healing, a decrease in P_{max}/P_0 ratio is observed, compared to the control series. For cracks smaller than 60 μm (in the unloaded state), this ratio is close to unity, meaning that the cracks have fully recovered their transport properties (full crack healing, figure 3.6) . For wider cracks, this ratio is higher, but still lower than that of the NoHealing series. This implies that wider cracks have partially recovered their transport properties (partial crack healing, figure 3.6).
- Cracking age in the tested range (14 and 28 days) does not seems to influence the ability of cracked specimens for autogeneous healing of their transport properties. A larger influence of cracking age could be expected for very early age (e.g. 3-7 days) and for very mature concrete. However, such ages were not studied.
- Both healing/curing regimes tested in this study (i.e. submerged and fog room conditions) enabled similar recovery of transport properties.

In this study, a potential of ordinary concrete mixes (i.e. mixes not engineered for self-healing) for autogeneous recovery of transport properties of cracks is proven. In the future, a wider range of healing/curing conditions should be studied, in order to determine which are the minimum conditions needed for crack healing (e.g. relative humidity and temperature and duration of curing). Also, a wider range of concrete mixtures could be studied (e.g. different w/c ratios and cement types). Furthermore, this study deals only with consequences of autogeneous healing (i.e. decrease in chloride ingress), and not with the mechanisms of autogeneous healing itself. This is beyond the scope of the current project.

4

CORROSION INDUCED CRACKING: AN EXPERIMENTAL STUDY

Our doubts are traitors and make us lose the good
we oft might win by fearing to attempt.

William Shakespeare

In this study, several experimental techniques are utilized to study different aspects of cracking of the concrete cover due to reinforcing steel corrosion. Firstly, microcomputed X-ray tomography technique (CT-scanning) is used for monitoring rust formation during accelerated corrosion of reinforcement, and subsequent cover cracking. Secondly, the nanoindentation technique is employed to determine mechanical properties of the rust layer, which is an important input parameter for numerical models. Finally, Energy Dispersive X-Ray Spectrometry (EDS) is used for elemental mapping around the steel-concrete interface. Also, as a part of the study, the resistance of a strain hardening cementitious composite (SHCC) to corrosion induced cover cracking is examined. It was found that CT-scanning can be successfully utilized in non-destructive monitoring of the corrosion process in reinforced specimens. The nanoindentation study showed that the Young's modulus of rust is highly dependent on the level of confinement provided to the rust layer by the surrounding concrete. And, finally, SHCC proved to be an excelent alternative to brittle cementitious materials when corrosion induced cracking of the cover is a concern.

Parts of this chapter have been published in Materials and Structures, 2014 [132]

4.1. INTRODUCTION

CORROSION of steel in reinforced concrete structures is a common cause of deterioration, resulting in unforeseen maintenance and repair costs. The steel in concrete is initially protected from active corrosion by a passive layer, which forms on its surface in the alkaline environment provided by the concrete. However, this protective layer can break down, either due to carbonation or chloride ingress [5]. An electrochemical process of steel corrosion, which causes the dissolution of iron and formation of iron oxides, then takes place. The resulting rust occupies a larger volume than its parent steel and exerts internal pressure on the surrounding concrete. Cracking of the cover occurs during the pressure buildup, due to the relatively low tensile strength of concrete. Cracking of the concrete cover is usually the first visible sign of the ongoing deterioration. It also speeds up the corrosion deterioration, as cracks enable faster ingress of chloride, carbon dioxide, and moisture .

A number of analytical and numerical models have been proposed in order to assess the mechanical consequences of the corrosion process [133–137]. Initial models, such as those by Bažant [133] and Molina et al. [134], only took into account the expansion of corroding steel, which eventually causes the surrounding concrete to crack. However, the time-to-cracking was underestimated by these models. It was later observed that part of the oxides accumulates close to the steel-concrete interface, without causing expansive pressure [135]. A porous layer [135] (or a corrosion accomodating region [138]), which exists around the reinforcement, was claimed to provide this buffer. Its existence has been experimentally confirmed by using electron microscopy [139] and x-ray attenuation [138, 140]. By considering this layer in models, improved results were obtained [141]. Some investigations also detected that iron oxides are transported into open cracks, hence further relieving the stress [8, 139]. This has been implemented in recent models of Ožbolt et al. [136] and Šavija et al. [137], leading to even better predictions. However, more experiments are needed in order to determine to which extent these mechanisms occur.

Very little research has focused on non-destructive and continuous monitoring of the cracking process caused by reinforcement corrosion. Early studies measured surface deformation of specimens by means of strain-gages [9, 10]. Lately, non-destructive techniques, such as acoustic emission [142], x-ray attenuation [138], and digital image correlation [140], have been used. Another non-destructive technique, micro-computed tomography (CT scanning), has been used recently for studying concrete fracture (e.g. [143]) and corrosion processes [144, 145]. Computed Tomography enables qualitative and non-destructive measurements of volume quantities (e.g. void location [146] or porosity [147]), which are not accessible to other methods. The nature of the technique enables its use for monitoring of corrosion product formation and subsequent cracking of concrete, which is one aim of this study.

Another important parameter used in numerical models is the Young's modulus of iron oxides. A wide range of values has been proposed in the literature. Molina et al. [134] tested values of 2-4 GPa, with no significant influence on the simulation result. In her model, Lundgren [148] used a non-linear stress dependent stiffness of the corrosion layer, with a maximum value of 14 GPa. Others proposed values as low as 40-87 MPa [141], or as high as 47-86 GPa [149]. Depending on the model used, this value can have a

significant impact on the result. To determine mechanical properties on the microscale, nanoindentation can be used. Nanoindentation has so far been used for determining properties of different phases in hydrated cement paste [150], interfaces in concrete repair systems [151] and fiber reinforced mortar [152]. An investigation into properties of corrosion products has been published by Zhao et al. [149]. Hence, another aim of the presented investigation is to study the elastic modulus of corrosion products using nanoindentation technique. It is accompanied by scanning electron microscope (SEM) imaging, together with element maps of relevant elements.
In this work, also the benefit of using a fiber reinforced cementitious material, in this case strain hardening cementitious composite (SHCC), is studied. SHCC is characterized by formation of narrow microcracks and strain hardening behavior [153]. When subjected to reinforcement corrosion, SHCC exhibits a significant anti-spalling ability compared to conventional mortar [154]. It is reasonable to believe that this improved performance can be proven by using non-destructive testing, namely micro-computed tomography. This hypothesis is also tested in the presented study.

4.2. EXPERIMENTAL APPROACH

4.2.1. MATERIALS AND SPECIMEN PREPARATION

MATERIALS used were Ordinary Portland Cement (CEM I 42.5N), limestone powder, blast furnace slag (BFS), water, superplasticizer, and polyvinyl alcohol (PVA) fibers. Two variations of the mixture were used for specimen fabrication: one with PVA fibers (SHCC mixture), and one without fibers (control mixture). Corrosion was initiated and accelerated by applying an electrical current as described in chapter 4.2.2. The mixture proportions are given in table 4.1. Note that the control mixture is the same as the SHCC mixture, but without the PVA fibers. As reinforcement, a smooth carbon steel rod with a diameter of 6 mm was used. In order to minimize beam-hardening effect (defined in chapter 4.2.3) due to the presence of dense steel, a hole was drilled in the steel bars. Hence, bars used in the study had an inner diameter of 4.2 mm and the outer diameter of 6 mm. This inside of the bars was filled with epoxy resin, in order to prevent the additional formation of rust there (see figure 4.1).
Two cylindrical specimens were fabricated, one using the SHCC, and the other using

Table 4.1: SHCC mix proportions (weight %) (developed by Zhou et al. [155])

CEM I 42.5N	Limestone powder	Blast furnace slag	Water/powder ratio	Superplasticizer	PVA fiber (by volume, %)
0.6	2	1.4	0.26	0.02	2 or 0

the control mixture. The specimens had a diameter of 34.1 mm and length of about 58 mm, with the steel rod positioned in the middle of each cylinder (figure 4.1). About 10

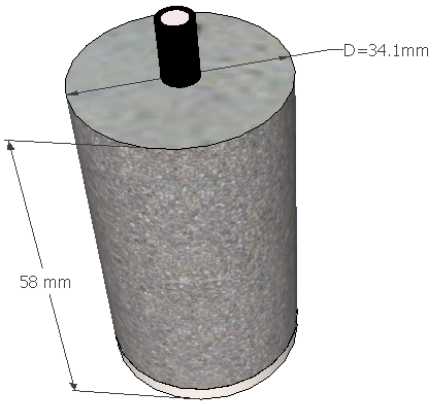

Figure 4.1: Geometry of the specimen used in this study

mm of steel was protruding from one side of each specimen, in order to enable connection with a direct current (DC) power supply used in the accelerated corrosion test. The steel rod was fixed in place using epoxy resin 24 hours prior to casting, and hence the bottom 3mm of each cylinder was made out of epoxy. The freshly cast specimens were consolidated using a vibrating table. The specimens were sealed and left in a climate room (20°C and more than 95% relative humidity) for 10 days, before being demolded and prepared for the accelerated corrosion test.

4.2.2. ACCELERATED CORROSION TEST

For the micro-computed tomography (CT) tests, two specimens were used (one SHCC specimen and one control mixture specimen, i.e. without PVA fibers). Each specimen was connected to a DC regulator to enforce corrosion. A titanium mesh was wrapped around each specimen in order to act as a counter electrode. During the exposure, each specimen was immersed in a container with saturated calcium hydroxide ($Ca(OH)_2$) solution. The applied voltage was varied during the test, in order to cause increase of damage between scans (figure 4.2).

4.2.3. MICRO-COMPUTED TOMPGRAPHY TECHNIQUE

Internal structure of specimens after different exposure times were monitored by using three dimensional micro-computed tomography (CT scanning). While mostly used in diagnostic medicine, CT scanning is increasingly used in non-destructive measurements, also of cementitious materials. Previous studies showed promising results [143, 144]. The aim of CT scanning is to obtain information regarding the nature of material occupying exact positions inside the body [156]. CT images are 3D maps of X-ray absorption in the material [143]. Multiple X-ray images of a specimen are taken at different angles. Using a reconstruction algorithm, a 3D image of the internal structure of a specimen is produced. The measurement principle is shown in figure 4.3. When used

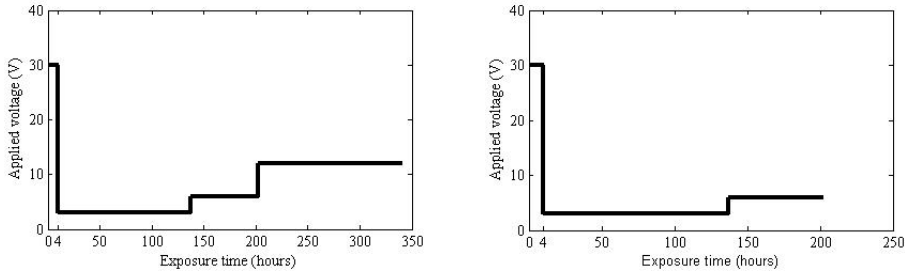

(a) SHCC (b) Control

Figure 4.2: Variation of applied voltage with time for both specimens

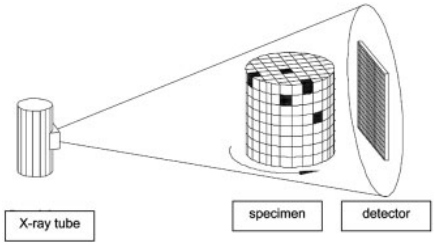

Figure 4.3: Measurement principle of computed tomography [144]

on specimens with large differences in X-ray attenuation coefficients, such as reinforced concrete/mortar, *beam hardening* is a concern. When an X-ray beam passes through the body, its attenuation at any point depends on the material at that point and on the energy distribution (spectrum) of the beam. In CT, the spectrum is made up from many energy levels (polychromatic) and it changes (hardens) as the beam passes through the object. Thus, the attenuation at any point may vary with the direction of the beam passing through it [156]. Two types of artefacts could result [157]:

1. *Cupping artefacts*: X-rays passing through the middle portion of a uniform cylindrical specimen are hardened more than those passing through the edges because they are passing through more material. As the beam hardens, the rate at which it is attenuated decreases, so the beam is more intense when it reaches the detectors, than would be expected if it had not been hardened. Therefore, the resultant attenuation profile differs from the ideal profile that would be obtained without beam hardening. An X-ray absorption map across the specimen displays a characteristic cupped shape. This is easy to see when an X-ray CT image of a steel rod is observed (see examples in Česen et al. [145]).

2. *Streaks and dark bands:* In very heterogeneous cross-sections (in terms of their attenuation coefficients), streaks or dark bands can appear between two dense objects in an image. They occur because the portion of the beam that passes through one of the objects at certain tube positions is hardened less than when it passes

through both objects at the other tube positions. This would be the case if, for example, a concrete specimen with two steel rods would be scanned.

Specimens in this study were prepared to fully utilize the benefits of CT scanning. During the exposure period of the samples, they were periodically removed from the corrosion cell in order to perform a CT scan. Each sample was first scanned prior to the accelerated corrosion testing. Than, the SHCC specimen was scanned in total five times during the corrosion test, while the control mixture specimen was tested only four times, because excessive damage had already occurred at that point (Table 4.2).

Table 4.2: A scheme of performed scans and exposure times

Scan	Exposure duration (h)	Cumulative exposure duration (h)	Voltage (V)	Current density ($\mu A/cm^2$)	SHCC	Control
0	0	0	/	/	+	+
1	4	4	30	120	+	+
2	90	94	3	12	+	+
3	43	137	3	12	+	+
4	65	202	6	24	+	+
5	138	340	12	48	+	-

A Phoenix Nanotom X-ray system was used for data acquisition. During the scan, a specimen is positioned on a rotating stage. A marker was placed on each specimen, in order to try to fit the specimen at almost the same position during every scan. During each scan, 1440 tomographic images were taken over a complete 360° rotation. A $0.2mm$ copper filter was used to decrease the beam hardening effect. A single scan took about 90 minutes to perform. Achieved voxel size was about $16\mu m$. Total scanned height of the sample was about $36mm$.

4.2.4. NANOINDENTATION AND EDS ELEMENT MAPPING

SPECIMEN PREPARATION

After the last CT scan, both specimens were vacuum impregnated using low viscosity fluorescent epoxy. They were then carefully cut perpendicular to the steel bar. A slice from each specimen was selected and prepared for nanoindentation testing. The specimens were ground with grade #120, #220, #320, #600, #1200 grinding sandpaper (Silcone Carbide) and polished with $6\mu m$, $3\mu m$, $1\mu m$ and $0.25\mu m$ polishing (Diamond) paste on a lapping table. Prior to nanoindentation testing, specimens were kept in a dessicator, in order to avoid carbonation and further corrosion of the steel.

NANOINDENTATION STUDY

The local mechanical properties of the tested points can be determined from the indentation load and displacement measurement [150, 152].The elastic modulus of the indented material can be calculated using the following formula:

$$\frac{1}{E_r} = \frac{1-\nu_s^2}{E_S} + \frac{1-\nu_i^2}{E_i} \tag{4.1}$$

where, ν_s is the Poisson's ratio of the tested material, ν_i is the Poisson's ratio of the indenter (0.07), E_s is the Young's modulus of the sample and E_i is the Young's modulus of the diamond indenter (1141 GPa). During unloading, it is assumed that only the elastic displacements are recovered, and therefore, E_r (reduced elastic modulus) can be obtained from the slope of the unloading curve:

$$S = \frac{dP}{dh} = \frac{2}{\sqrt{\pi}} E_r \sqrt{A} \tag{4.2}$$

where, S is the elastic unloading stiffness (or contact stiffness) defined as the slope of the upper portion of the unloading curve during the initial stages of unloading, P is the load, h is the displacement relative to the initial undeformed surface, and A is the projected contact area at the peak load.
An Agilent Nano Indenter G200 with a diamond Berkovich tip (i.e. a three-sided pyramidal diamond) was used for nano-indentation tests. A quartz standard was indented before and after each test series to check the calibration values. Several series of indents were performed on a tightly spaced grid, with spacing of 20 μm (for all tested locations). The indentation depth was set to 2000 nm. Three indentation areas were tested, perpendicular to the steel-cementitous material interface, in order to study the change of elastic modulus across the rust layer. Additionally, since penetration of rust into a large crack was visually observed in the SHCC specimen, this area was also tested. The Continues Stiffness Method (CSM), developed by Oliver and Pharr [158], which provides continuous results as a function of indentation depth, was used for the analysis of the results. The average E modulus was determined in the loading range between 1000 and 1800nm depths. In the E modulus calculation, Poisson's ratio of the indented material (steel, rust, and cementitious material) was set to 0.25 in the calculations.

EDS ELEMENT MAPPING

After the nanoindentation study, element mapping of indented areas was performed using a EDS unit (EDX system by EDAX) of the Environmental Scanning Electron Microscope (Philips XL30 ESEM). Main elements examined were carbon, oxygen, and iron. Element map for iron should clearly show the distribution of corrosion products, while the map for carbon should emphasize the areas where the fluorescent epoxy has penetrated. Oxygen should be present only in the rust layer, and not in the intact steel. Backscatter images (BSE) of indented areas were captured as well.

4.3. RESULTS AND DISCUSSION

4.3.1. CT SCANNING RESULTS

As the difference in density between cementitious material and steel is large, resulting in large difference in X-ray attenuation coefficients, unprocessed CT images are dark, with steel being very bright. Therefore, a number of CT images have been processed manually in order to reveal the most interesting features. The aim was to emphasize four different phases, namely air voids and cracks, cementitious material, corrosion products, and non-corroded steel. They are displayed as white, black, red, and blue, respectively. Due to beam hardening effects, the inside of the hollow steel rebar is affected. Hence it has been filled with blue colour for clarity in the displayed CT images.

SHCC SPECIMEN

As shown in table 4.2, the SHCC specimen was scanned in total six times, including an initial scan before the accelerated corrosion exposure. A single horizontal slice was selected, and its processed CT image during each of the scans is shown in figure 4.4. The selected slice also shows a large air void close to the steel-concrete interface, presumably available for deposition of dissolved corrosion products. Already in scan 1, several cracks are clearly visible. Subsequent scans show the formation of new cracks, without formation of a single major crack. The rust layer around the steel bar is of relatively uniform thickness, with the exception of the contact with the large air void. These scans also suggest that the corrosion products, indeed, penetrate into open spaces (in this case, an air void) thereby relieving some of the pressure which would otherwise be exerted onto the concrete.

In figure 4.5, a zoomed-in image of the steel-cementitious material interface is shown (from scan 5) The penetration of dissolved rust into the large air void is clearly visible. The rust layer is, at this stage, not uniform. It seems that the corrosion affects the steel more at the contact with the air void, resulting in a sort of a pit. Although the reason for this is not clear, it could be due to local differences in the current flow caused by the high conductivity of the water-filled void. Some penetration of rust into a crack is also observed.

Figure 4.6 shows a number of processed CT slices from scan 5, clearly displaying movement of corrosion products into an open crack.

CONTROL MIXTURE SPECIMEN

The control mixture specimen was scanned in total five times, including the initial scan before the accelerated corrosion exposure (table 4.2). Again, a single slice was selected, and the processed CT images during each of the scans are displayed in figure 4.7. Already in scan 1, one large crack formed, accompanied by three smaller cracks. The largest crack was also clearly visible from the outside of the specimen, while the smaller cracks didn't reach the surface of the specimen at this stage. Scan 2 shows widening of already existing cracks, accompanied by formation of a new crack. These cracks are wider at scan 3, and at scan 4, a large piece of the cementitious material has spalled. At this point, the

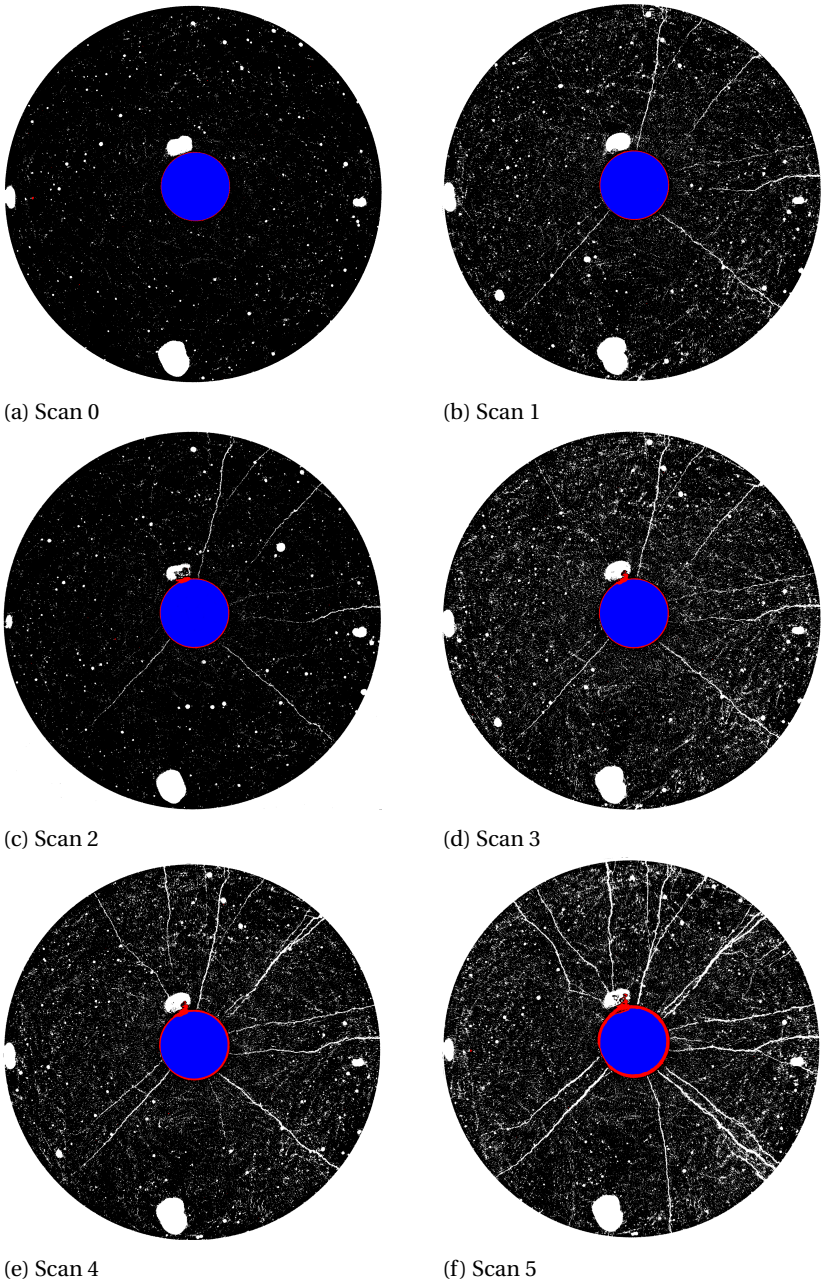

(a) Scan 0 (b) Scan 1

(c) Scan 2 (d) Scan 3

(e) Scan 4 (f) Scan 5

Figure 4.4: Processed CT images of the cracking sequence in the SHCC sample (black-cementitious matrix; red-rust; blue-steel; white-cracks and voids)

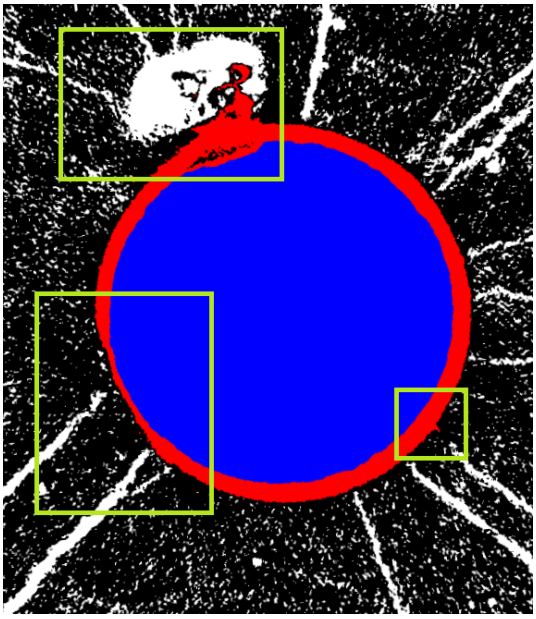

Figure 4.5: Steel-cementitious material interface from scan 5 of the SHCC sample. Top-penetration of rust into an air void; left: non-uniform rust layer; right: penetration of rust into a crack (black-cementitious matrix; red-rust; blue-steel; white-cracks and voids)

accelerated corrosion exposure was stopped.
What is interesting to see is that the rust layer around the steel bar is non-uniform already at scan 1. At this point already, excessive cracking has occurred. The same trend is observable in scans 2-4. Also, a discontinuity seems to form between the rust layer and the cementitious material. It seems to increase with exposure, i.e. with the increase in damage. This is probably due to partial leaching out of dissolved corrosion products through open cracks, as discussed later.

Figure 4.8 shows a zoomed-in image of the steel-cementitious material interface at scan 4. The gap which forms between the rust layer and the material matrix is visible. The corrosion layer seems to be of a non-uniform density at this stage, resulting in a seemingly layered structure (shown as black spots within the red layer). Some penetration of rust into a crack is also observed here.

DISCUSSION OF CT SCAN RESULTS

Presented results demonstrate the applicability of the X-ray computed tomography technique for studying corrosion induced cracking in cementitious materials. The sequence of cracking over time can be followed, as demonstrated in figures 4.4 and 4.7. This is an improvement compared to conventional X-ray attenuation measurements [138, 140], where averaging of X-ray attenuation coefficients in one direction is present, making it impossible to observe and monitor, for example, discrete voids and cracks. The size of

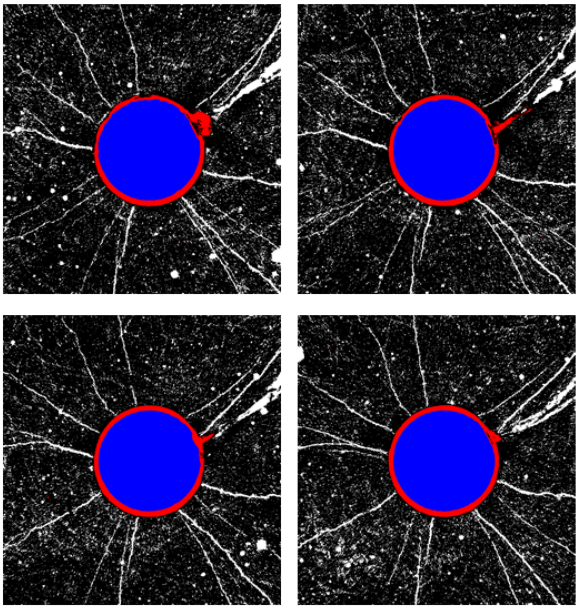

Figure 4.6: Penetration of corrosion products into an open crack in the SHCC sample- different horizontal slices from scan 5 (black-cementitious matrix; red-rust; blue-steel; white-cracks and voids)

cracks which can be detected by the CT scanning technique is limited by its resolution (about $16\mu m$ per voxel in the current research). This, of course, means that some very small cracks may remain unnoticed. The same holds for pores and air voids. Also, due to the finite pixel size, some averaging is present. This results in, for example, a thin red layer around the steel in figures 4.4a and 4.7a, which suggests a 1 pixel wide layer of corrosion even prior to the exposure. This is certainly not the case. Nevertheless, the increase in the corrosion layer thickness over time can be monitored, as shown in figure 4.4 and 4.7. These scans also suggest that the corrosion products, indeed, penetrate into open spaces, such as air voids and cracks, thereby relieving some of the pressure which would otherwise be exerted onto the concrete. This is, especially, clear in figures 4.5 and 4.6. In addition, figures 4.7 and 4.8 suggests that a discontinuity forms at the steel-cementitious material interface after cracking occurs, especially close to large cracks. Also, close to large cracks, there is a pronounced non-uniformity of the corrosion layer thickness, which is especially noticeable in the control mixture specimen. This would go to suggest that some of the corrosion products dissolved in the calcium hydroxide ($Ca(OH)_2$) solution and leached out. It is possible that this process was aided by the presence of the cathode (i.e. the counter electrode) wrapped around the specimen. Therefore, the observed behavior could be somewhat different than that occurring under "real" corrosion conditions. In that sense, A modeling approach of Ožbolt et al. [136], who simulated the movement of red rust as a diffusion problem, seems promising. The higher "diffusivity" of large cracks, with respect to rust transport, indeed explains the observations. The quantification of this effect, however, remains an issue. Even so, the

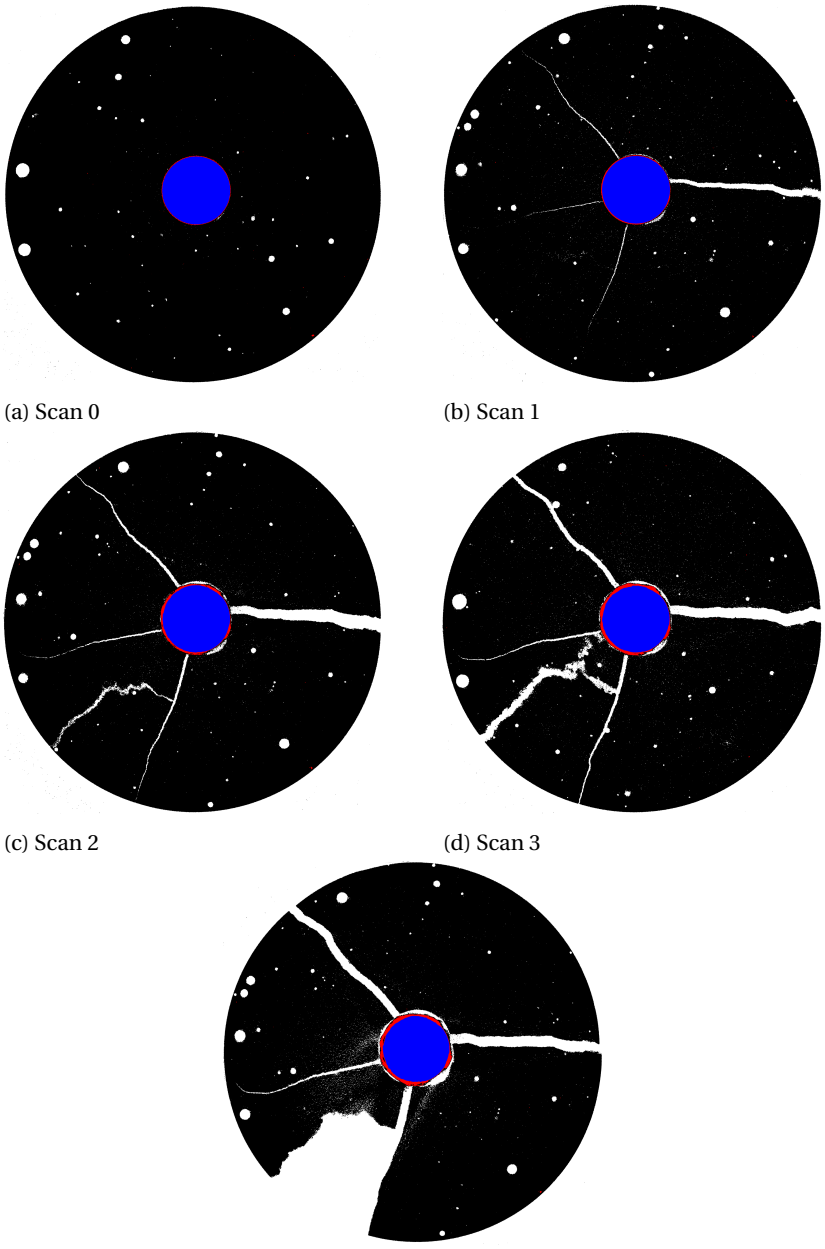

(a) Scan 0

(b) Scan 1

(c) Scan 2

(d) Scan 3

(e) Scan 4

Figure 4.7: Processed CT images of the cracking sequence in the control mixture sample (black-cementitious matrix; red-rust; blue-steel; white-cracks and voids)

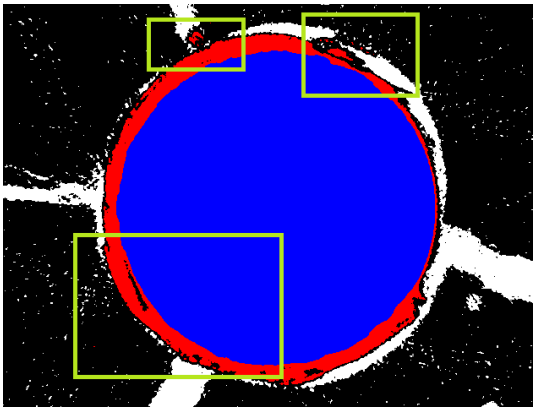

Figure 4.8: Steel-cementitious material interface at scan 4 of the control mixture sample. Top left-penetration of rust into into a crack; top right and bottom: non-uniform density within the rust layer (black-cementitious matrix; red-rust; blue-steel; white-cracks and voids).

importance of taking this relief mechanism into account in numerical models is clear [136, 137].

When comparing the two tested specimens, it is clear that the control mixture specimen exhibits more brittle behavior. Already at an early stage of the test, a large crack has occured in the specimen. On the other hand, the SHCC specimen showed high resistance to the pressure caused by steel bar corrosion. Even at the end of the exposure, no single crack has localized. Instead, the number of cracks kept increasing, and to a lesser extent their width. This can be atributed to its high deformational capacity compared to the brittle control mixture [153]. Also, due to its small crack widths, the SHCC specimen keeps the rust layer confined together, unlike the control mixture specimen (figures 4.6 and 4.8). This would also suggest that the SHCC specimen was subjected to more internal pressure, although this was not measured. The performance of the SHCC specimen was superior in terms of cracking resistance, similar to the study of Şahmaran et al. [154].

4.3.2. NANOINDENTATION AND EDS RESULTS

SHCC SPECIMEN

In total, four locations were tested in the nanoindenter: 3 locations on the interface between steel and cementitious material (locations 1a, 2a and 3a), and one location in a large crack (location 4a), where the presence of corrosion products was visually observed. For the locations 1a-3a, a 25×8 grid of indents was used. For location 4a, a 20×8 grid was used. Images taken in the nanoindenter after the test are shown in figure 4.9.

In figure 4.10, the distribution of elastic modulus values for locations 1a-3a is shown. A distinct difference can be seen between the indents positioned in the sound steel, the rust layer, and within the cementitious matrix.

Averaged E modulus values for locations 1a-3a are shown in figure 4.11. Each point

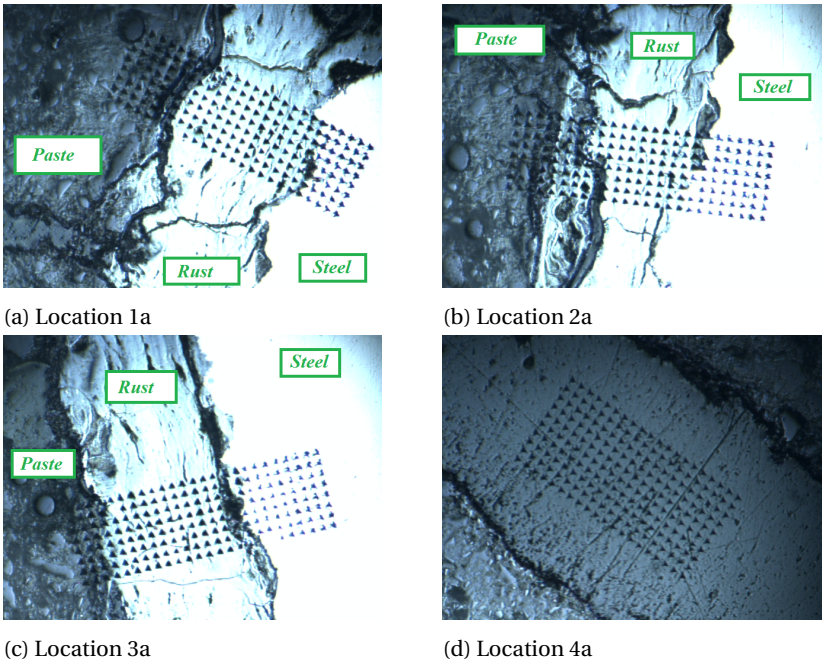

(a) Location 1a

(b) Location 2a

(c) Location 3a

(d) Location 4a

Figure 4.9: Optical micrographs of indented locations in SHCC sample

in the plot is an average of 8 points along the short side of the grid. Because the indentation grid is not precisely perpendicular to the steel-cementitious material interface, large error bars can be used to distinguish three areas (with distinctly different E modulus values): intact steel, corrosion products, and material matrix.

In figure 4.10a and 4.10b, a clear distinction between different materials can be noticed, depending on their E modulus values. This is somewhat more difficult in figure 4.10c. Accordingly, a gradient in the E modulus values can be observed in figure 4.11. If only the indents that are within the rust layer (as designated in figure 4.11 are averaged, the following values are obtained: 67.9 GPa, 64.3 GPa, and 49.4 GPa, for locations 1a, 2a, and 3a, respectively. At location 4a, a uniform distribution of E-modulus values was obtained, ranging from 2.9-3.5 GPa. This very low value suggests that iron oxide particles are dissolved in the epoxy resin, and provide little to no additional stiffness to the composite. In fact, these values are quite close to the Young's modulus of the epoxy itself. This further indicates that the assumption that dissolved corrosion products "diffuse" through open cracks is valid.

In the SHCC sample, penetration of rust into an open crack was also observed in the BSE mode of the ESEM. Element maps and BSE images for this location are shown in figure 4.12. It seems that iron oxides are mixed with the epoxy in the crack, resulting in lower intensities of oxygen and iron (figure 4.12b and 4.12c) overlapping and mixing with carbon (figure 4.12d). This is yet another proof of movement of iron oxides into open cracks.

In figures 4.13-4.15, BSE images and element maps of oxygen, iron, and carbon for lo-

cations 1a-3a are shown. Presence of oxygen is observed in the corrosion layer and, to a lesser extent, in the material matrix. Iron is present in the steel, and in the rust layer. No precipitation of iron oxides in the material matrix around the reinforcement is observed. Carbon is observed in cracks and voids, due to presence of carbon in the epoxy used for impregnation.

CONTROL MIXTURE SPECIMEN

In total, three locations on the steel-cementitious material interface (locations 1b,2b, and 3b), were tested in the control mixture sample. For each location, a 30×7 grid of indents was used. Images taken in the nanoindenter after the test are shown in figure 4.16.

Unlike the SHCC specimen, in figures 4.17 and 4.18 it is difficult to clearly distinguish the indents belonging to the rust based on their E modulus value. Here, the layer between the intact steel and the cementitious material is composed of rust layers and epoxy resin.
In figures 4.19-4.21, BSE images and element maps of oxygen, iron, and carbon for locations 1b-3b are shown. Here, the corrosion layer is not as uniform as in the SHCC specimen: although predominantly composed of iron and oxygen, presence of carbon is observed. This is due to existence of micro gaps and defects within the rust layer itself, which created empty space, subsequently filled by epoxy resin during the impregnation process. Here too, no precipitation of iron oxides in the material matrix around the reinforcement is observed.

DISCUSSION OF NANOINDENTATION AND EDS RESULTS

In a study by Zhao et al. [149], it was suggested that the rust around the reinforcing steel is composed of two distinct layers, based on their mechanical and chemical properties: an inner rust layer, with an E modulus between 47-86 GPa, and an outer rust layer, with an E modulus between 98-122 GPa. The scatter of E modulus values within each layer was attributed to different exposure conditions in different samples. It was also suggested that only the inner rust layer is responsible for concrete cracking. In the present study, different layers of rust have not been identified. E modulus values for confined rust (i.e. SHCC specimen) are found to be between 49.4-67.9GPa, somewhere in the range of the inner rust values of Zhao et al. [149]. In the control mixture specimen, the (tested) rust layer is composed of layers of iron oxide intertwined by epoxy, which penetrated into the inter-layer cracks, which makes it difficult to determine a single value for the E modulus.
These can be clearly seen in the EDS maps of locations 1b-3b of the control mixture (figures 4.19-4.21), where iron and oxygen are separated by layers of carbon from the epoxy resin. It is likely that more cracks are present within the rust layer, which cannot be seen at this magnification. The loss of cohesion in the rust layer itself is probably caused by the lack of confinement of the rust layer due to cracking of the surrounding material. It is perhaps also aided by partial leaching of corrosion products through open cracks. This results in lower E modulus values of the "rust" indents in the control mixture sample (figure 4.17) compared to the SHCC sample (figure 4.10). In the SHCC sample, the

amount of cracks within the rust layer is insignificant (figures 4.13-4.15), compared to the control mixture sample. This is probably caused by confinement of the rust layer, whose pressure was successfully accommodated by the ductile SHCC material, with relatively minor damage and narrow cracks. As a consequence, the rust layer in the SHCC sample is relatively uniform both in mechanical (figure 4.10) and chemical sense (figure 4.13-4.15). The observed behavior seems to be in accordance with the statement that "the steel corrosion is supposed to grow layer by layer, so there are micro gaps and defects between rust layers" [149]. Results presented herein suggest that the size of these micro gaps is dependent on the deformation of the rust layer, i.e. the level of confinement provided to it by the surrounding cementitious material.

No accumulation of corrosion products into the surrounding cementitious matrix has been observed. This is not in accordance with previous studies [138–140]. It is probable that, due to relatively early occurrence of cracking in both specimens, there simply was no need for corrosion products to accumulate at the interface - large open cracks were already available. This, also, is in agreement with the modeling approach of Ožbolt et al. [136]. However, it is expected that, in natural conditions (i.e. with lower current density), a part of the corrosion products would accumulate in pores close to the steel-concrete interface. Further research is needed to confirm and quantify this behavior.

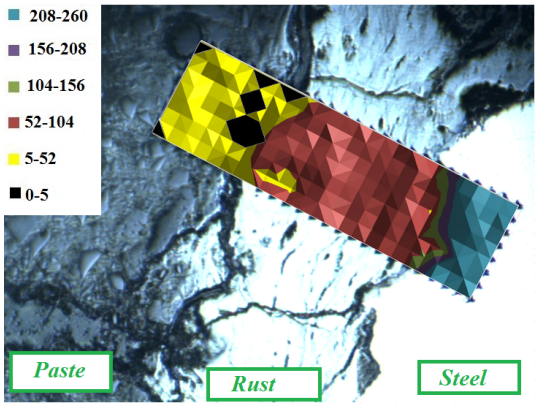

(a) Location 1a

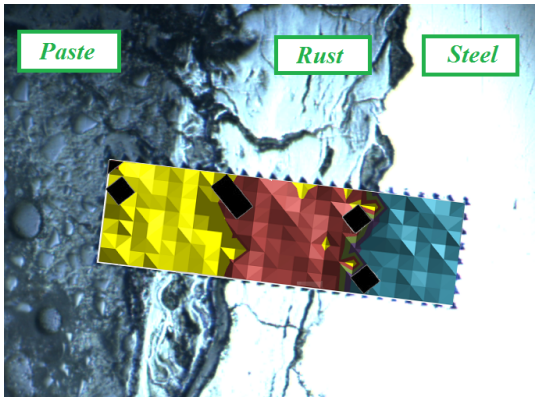

(b) Location 2a

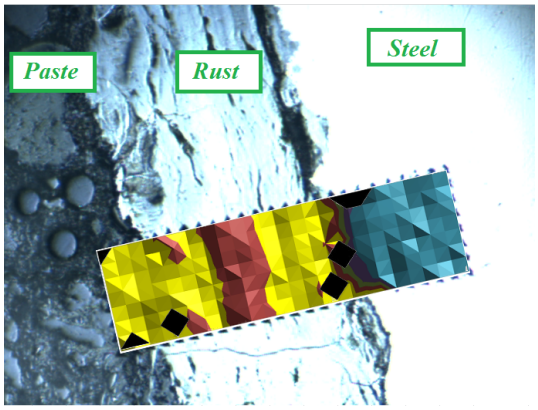

(c) Location 3a

Figure 4.10: Young's modulus distributions in the steel-cementitious material interface of the SHCC sample (overlayed on the optical micrographs)

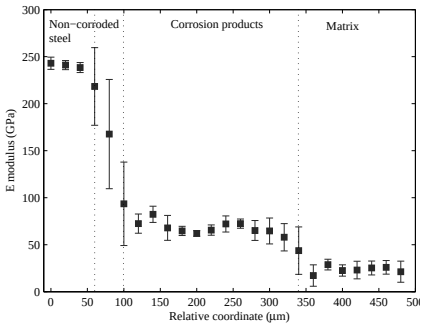

(a) Location 1a

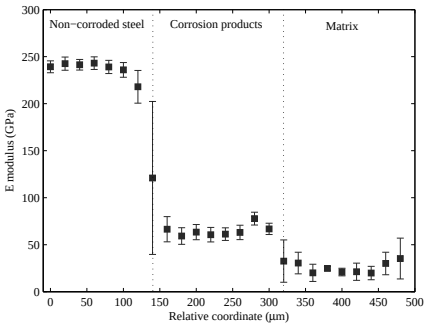

(b) Location 2a

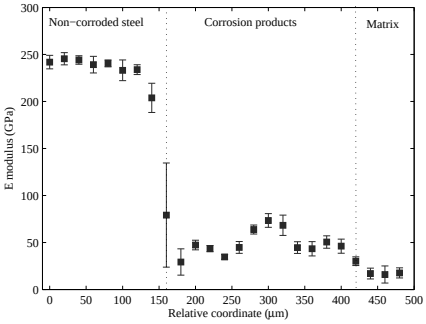

(c) Location 3a

Figure 4.11: Young's modulus profile of the steel-cementitious material interface zone in SHCC sample

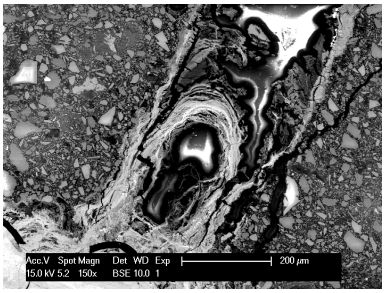

(a) BSE image

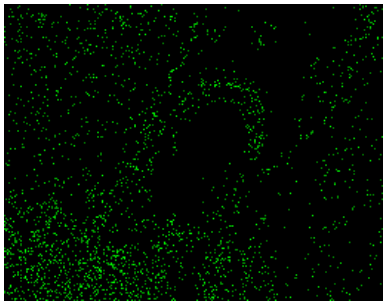

(b) *O* element map

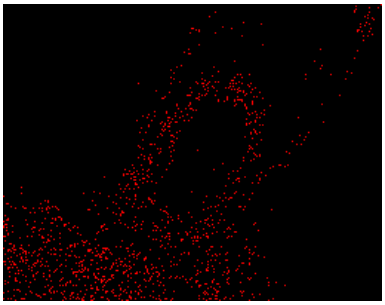

(c) *Fe* element map

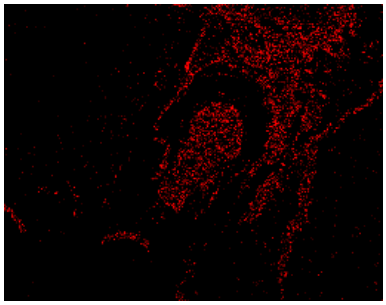

(d) *C* element map

Figure 4.12: Penetration of rust into a crack in the SHCC sample, shown by BSE imaging (a) and element maps (b-d)

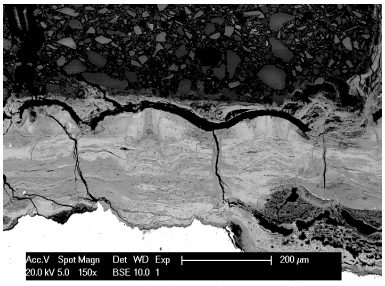

(a) BSE image

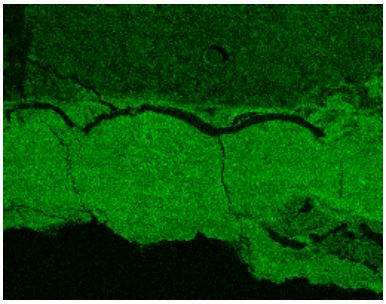

(b) *O* element map

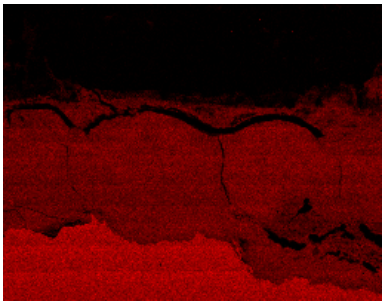

(c) *Fe* element map

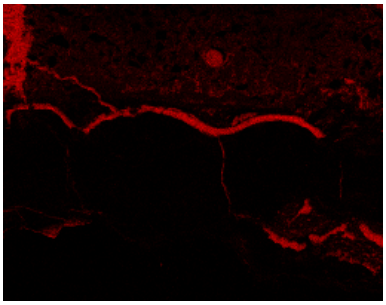

(d) *C* element map

Figure 4.13: BSE image (a) and element maps (b-d) of the location 1a in SHCC sample

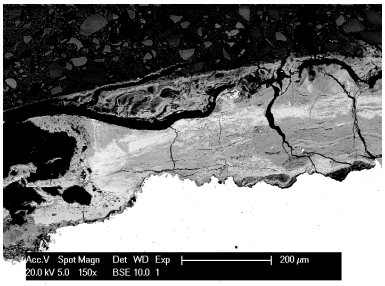

(a) BSE image

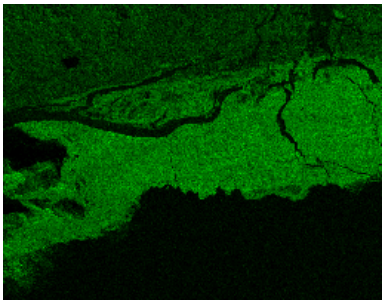

(b) *O* element map

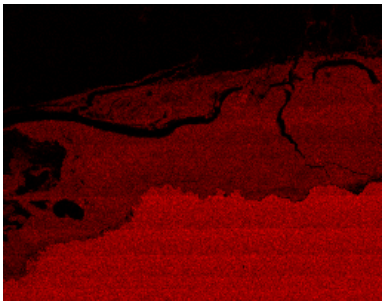

(c) *Fe* element map

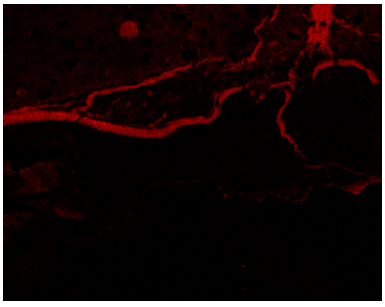

(d) *C* element map

Figure 4.14: BSE image (a) and element maps (b-d) of the location 2a in SHCC sample

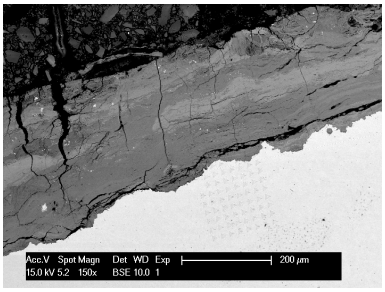

(a) BSE image

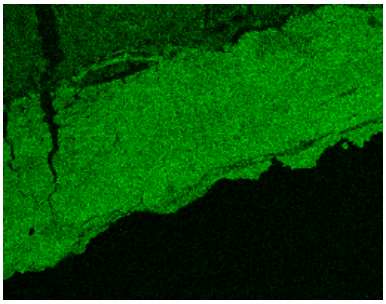

(b) *O* element map

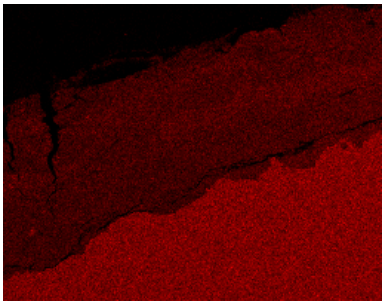

(c) *Fe* element map

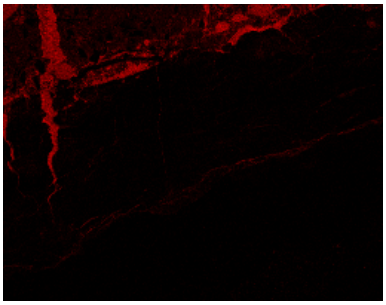

(d) *C* element map

Figure 4.15: BSE image (a) and element maps (b-d) of the location 3a in SHCC sample

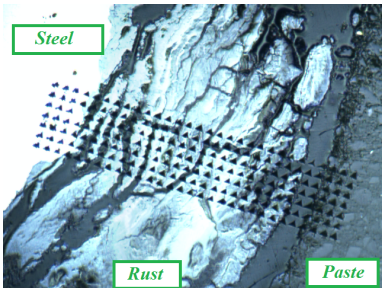

(a) Location 1b

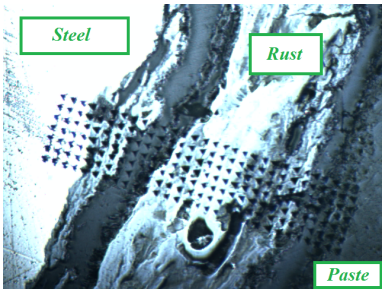

(b) Location 2b

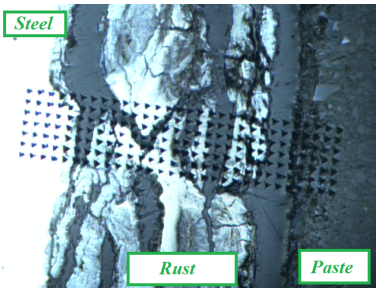

(c) Location 3b

Figure 4.16: Optical micrographs of indented locations in control mixture sample

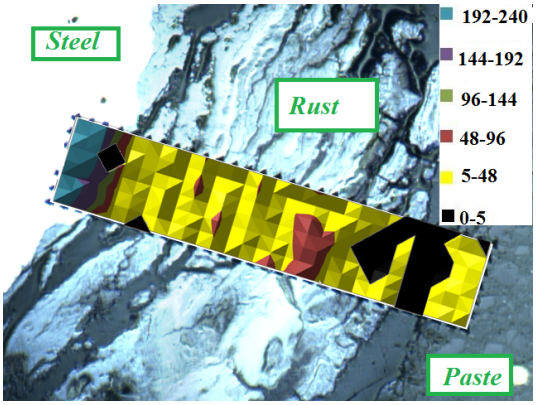

(a) Location 1b

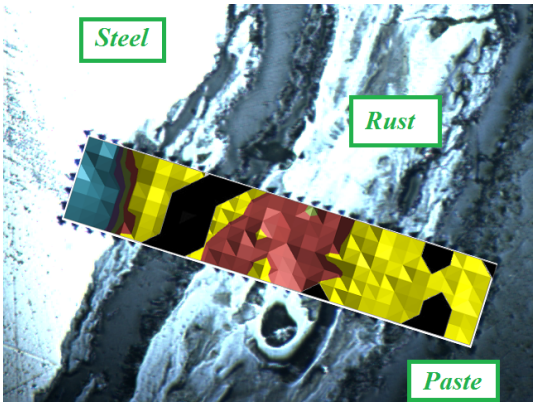

(b) Location 2b

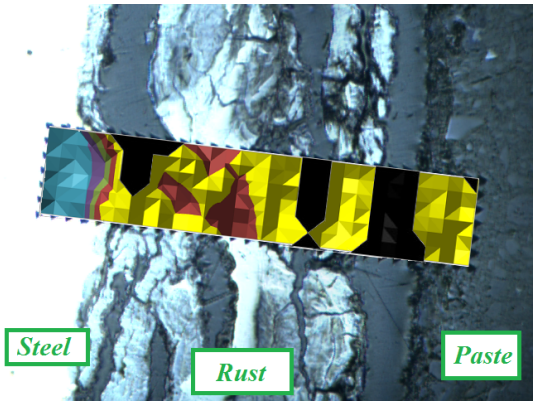

(c) Location 3b

Figure 4.17: Young's modulus distributions in the steel-cementitious material interface of the control mixture sample (overlayed on the optical micrographs)

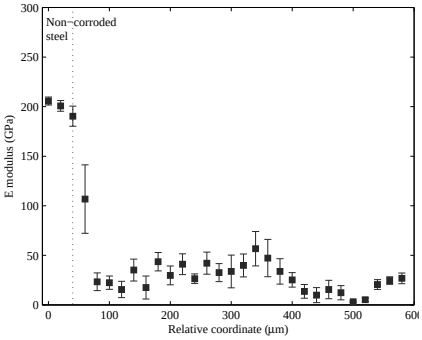

(a) Location 1b

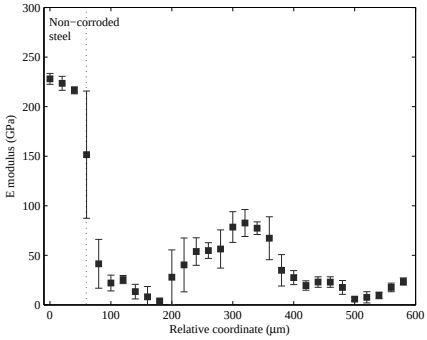

(b) Location 2b

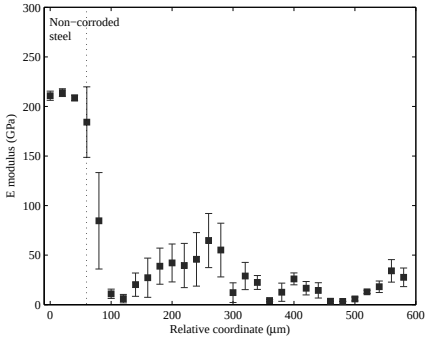

(c) Location 3b

Figure 4.18: Young's modulus profile of the steel-cementitious material interface zone in control mixture sample

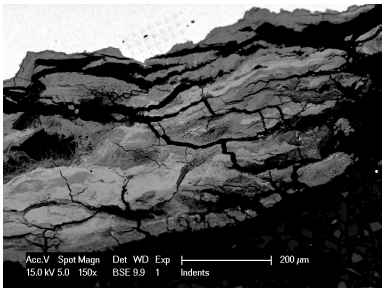

(a) BSE image

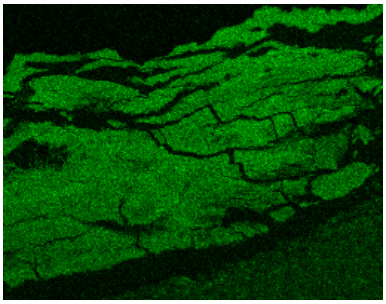

(b) *O* element map

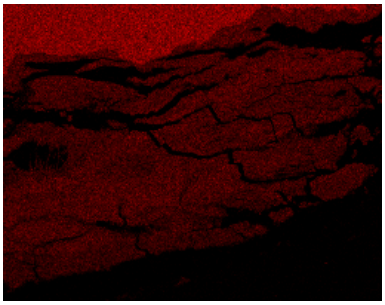

(c) *Fe* element map

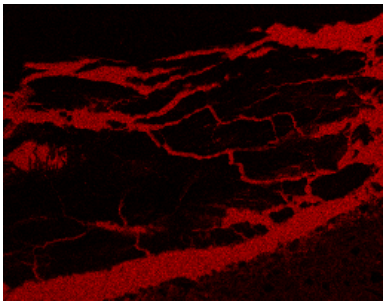

(d) *C* element map

Figure 4.19: BSE image (a) and element maps (b-d) of the location 1b in control mixture sample

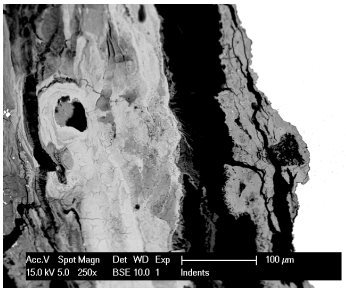

(a) BSE image

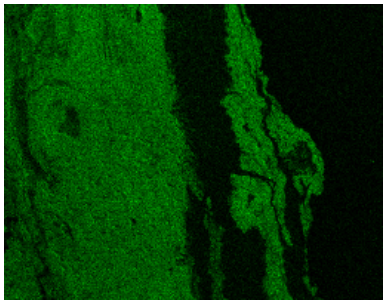

(b) *O* element map

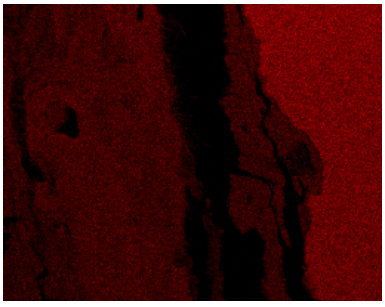

(c) *Fe* element map

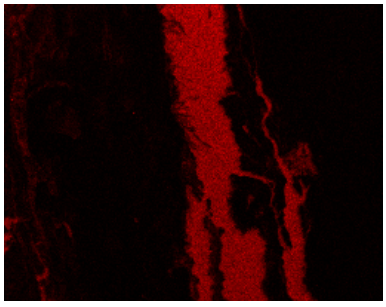

(d) *C* element map

Figure 4.20: BSE image (a) and element maps (b-d) of the location 2b in control mixture sample

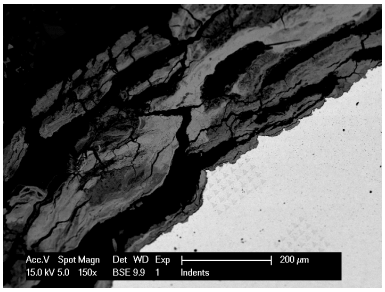

(a) BSE image

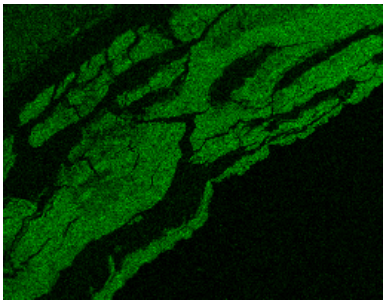

(b) *O* element map

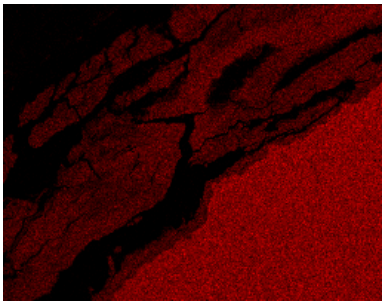

(c) *Fe* element map

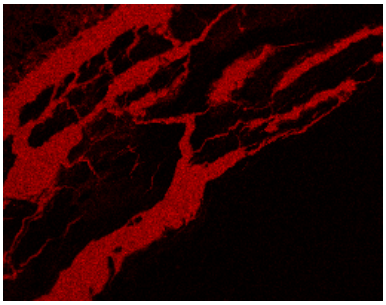

(d) *C* element map

Figure 4.21: BSE image (a) and element maps (b-d) of the location 3b in control mixture sample

4.4. SUMMARY AND CONCLUSIONS

In this study, the applicability of X-ray micro-computed tomography to monitor corrosion induced cracking of concrete was tested under electrochemically accelerated corrosion conditions. Also, nanoindentation technique and EDS mapping were used to characterize corrosion products. Furthermore, the efficiency of SHCC in suppressing the damage caused by corrosion induced expansion was examined. This research has led to following conclusions:

1. Micro-computed X-ray tomography (i.e. CT scanning) is a valuable tool for non-destructively studying fracture in cementitious materials. Findings regarding initiation and propagation of cracking in specimens subjected to internal pressure due to rust expansion are valuable for validation and fine-tuning of numerical models.

2. Differences in X-ray attenuation coefficients between the cementitious matrix, corrosion products, and intact steel, enable one to resolve the distribution of each of these phases in space. As a consequence, formation of a rust layer around the steel, discrete cracking, and movement of rust into open cracks and air voids have all been observed.

3. Penetration of rust into open spaces causes a non-uniform rust layer to occur. This is especially noticeable close to large cracks and air voids. Dissolved rust seems to migrate into open spaces, without causing expansive pressure on the concrete.

4. The Young modulus of the rust layer changes depending on the level of confinement provided to it by the surrounding material. In the confined state, the rust layer exhibits relatively uniform mechanical and chemical properties. The Young modulus of confined rust was found to be between 49.4-67.9 GPa. Once extensive cracking occurs, the rust layer is no longer of uniform density. This is caused by lack of confinement provided by the surrounding cementitious material, which leads to occurence of micro gaps within the rust layer itself, and also results in lower Young modulus values of the layer as a whole.

5. SHCC specimen showed higher resistance to corrosion induced cracking compared to the control mixture specimen. Even at the end of the test, no single wide crack has formed. Instead, a large number of relatively narrow cracks has formed. In contrast, the control mixture specimen had already failed completely at that stage.

When using the CT scanning technique, one has to be aware of its drawbacks and limitations. First, specimen size is a limiting factor for the resolution, since the larger the specimen, the lower the resolution. Second, the thickness of the reinforcing bar has to be carefully selected, due to the beam-hardening effect. This is the reason why a hollow bar was used in this research. Also, studying interaction of multiple corroding steel bars would be affected by the beam-hardening effect. Third, a large difference between densities of steel and cementitious material result in relatively dark unprocessed images, with steel being very bright. This makes the imaging of reinforcing steel within the concrete

more challenging than imaging of a steel bar extracted from concrete (e.g. [144, 145]). This would make identification of different iron oxides (with different densities) in the CT images quite a task, even if a calibration curve [159] for different rust products was available. Finally, in the present study, specimens were moved in and out of the CT scanner for accelerated corrosion exposure. This inevitably resulted in slight vertical movements of specimens between subsequent scans. A better solution would be to carry out the test in-situ, which was not possible during this research. This would also enable the use of advanced post-processing techniques, such as digital volume correlation [160], to resolve the state of strains and stresses within the specimen during the test.

One needs to be aware of the limitations of the presented experiment. Corrosion was greatly accelerated compared to natural conditions, resulting possibly in somewhat different corrosion products and affecting their mobility. Also, effects of concrete creep are not taken into account in such an experiment, but could allow for more corrosion products to form prior to cracking of concrete. Further research is, therefore, needed to quantify these effects.

5

LATTICE MODELING OF CHLORIDE DIFFUSION IN CONCRETE

If the facts don't fit the theory,
change the facts.

Albert Einstein

Reinforced concrete structures are frequently exposed to aggressive environmental conditions. Most notably, chloride ions from sea water or de-icing salts are potentially harmful since they promote corrosion of steel reinforcement. Concrete cover of sufficient quality and depth can ensure protection of the steel reinforcement. However, it is necessary to study the effects of material heterogeneity and cracking on chloride ingress in concrete. This is done herein by proposing a three-dimensional lattice model capable of simulating chloride transport in saturated sound and cracked concrete. Means of computationally determining transport properties of individual phases in heterogeneous concrete (aggregate, mortar, and interface), knowing the concrete composition and its averaged transport properties, are presented and discussed. Based on numerical experimentation and available literature, a relation between the effective diffusion coefficient of cracked lattice elements and the crack width was adopted. The proposed model is coupled with a lattice fracture model to enable simulation of chloride ingress in cracked concrete. The model was validated on data from the literature, showing good agreement with experimental results.

Parts of this chapter have been published in Cement & Concrete Composites **42**, (2013) [161].

5.1. INTRODUCTION

In understanding the mechanism and parameters influencing chloride ingress in cracked concrete, numerical simulations can be of great use. Compared to experiments, it is a lot easier to control and study the effect of individual parameters. Therefore, in recent years, a number of numerical models have been proposed in the literature for modeling chloride ingress in cracked concrete. Some of them model the effect of cracking in a smeared way, by introducing an increase of the diffusion coefficient in the whole domain (e.g.[162]). Others model cracks as notches or faults in concrete, without the mechanical analysis (e.g. [12, 163]). Very few have made a step further, and coupled the mechanical and transport analyses (e.g.[164]). Most of these models treat concrete as a quasi-homogeneous continuum, i.e. mechanical and transport properties are constant for the whole domain. On the other hand, a truss-network approach proposed by Wang and Ueda [165], considers concrete as a three-phase composite, consisting of coarse aggregate, mortar, and ITZ. Both of these approaches (homogeneous and heterogeneous) are applicable within the lattice framework as presented here.

In the following, a three dimensional lattice model for simulating chloride penetration in sound and cracked concrete is presented. Governing equations and discretization procedure are addressed. The focus of the paper lies on determination of transport properties of different phases in concrete (aggregate, mortar, and the interface), and cracks. The model is validated using experimental results from the literature. Finally, these results are discussed and evaluated, and some conclusions are drawn.

5.2. METHOD

5.2.1. CHLORIDE TRANSPORT IN CONCRETE

Different physical and chemical transport mechanisms can contribute to chloride ingress, and they depend on the concrete pore structure, (micro) environmental conditions, temperature, moisture content in concrete, etc. These mechanisms are described in detail in chapter 1.2. It was stated that it is the diffusion mechanism that is considered to be most important in concrete. The degree of pore saturation is an important parameter influencing ionic transport in concrete; the diffusion process is most effective when the concrete is fully water saturated, although it can also take place in partially saturated concrete. It can be considered that chloride diffusion is the governing transport mechanism when concrete is fully saturated; in a partially saturated condition, chlorides are transported by means of several combined mechanisms.

Transport of chloride ions in non-saturated sound concrete is a complicated issue and is still an important topic of research. Therefore, in order to simplify studies of chloride ingress in cracked concrete, laboratory specimens are usually water saturated. For all analyses performed in this chapter, the concrete pore system is assumed to be fully saturated with water. Under this assumption, ionic diffusion is considered to be the sole mechanism governing the transport of chloride ions, both in the crack and in the sound material.

5.2.2. MODEL DESCRIPTION

Lattice models have long been used in fracture mechanics of concrete [107]. Recently, the use of lattice (or rather discrete) models has been extended to simulating transport processes in concrete [165–170]. Coupling of the mechanical and transport simulations, while taking into account the effect of cracking on the transport mechanism, was performed by [167–170]. In the mechanical lattice approach, concrete is discretized as a set of truss or beam elements. In the transport lattice approach, concrete is treated as an assembly of one-dimensional "pipes", through which the flow takes place. While some authors use "dual" lattices (one for the mechanical simulation, and the other for the flow simulation- for details see [168–170]) the approach proposed here uses the same lattice network for both simulations. In this approach, mechanical simulation is performed first; its output is then used as an input for simulating chloride ingress. Therefore, it is actually a one-way coupling - mechanical degradation does affect the chloride penetration, while, on the other hand, there is no influence of the chloride penetration on the mechanical behavior.

SPATIAL DISCRETIZATION

For the spatial discretization of the specimen in three dimensions, the basis is the prismatic domain. Discretization of the domain is performed according to the following procedure: first, the domain is divided into a number of cubic cells. As an input value, the number of cells in x, y and z direction, and cell size, are specified. Then, a network of cubic cells is generated, and a sub-cell can be defined within each cell. A node is randomly placed in every sub-cell using a (pseudo) random number generator (figure 5.1). Voronoi tessellation[1] of the prismatic domain with respect to the specified set of nodes

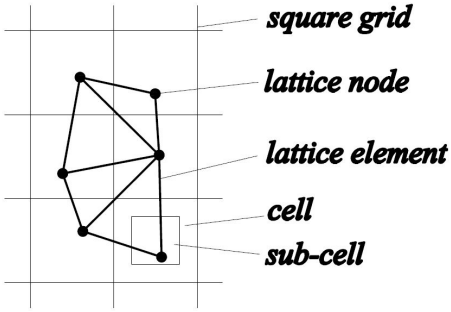

Figure 5.1: Random node-placement procedure for each cell, used for formation of a lattice mesh (shown in 2D, for simplicity)

is performed. Nodes with adjacent Voronoi cells are connected by lattice elements (figure 5.2). Since Voronoi diagrams are dual with Delaunay tessellation, this approach is equivalent to performing a Delaunay tessellation of the set of nodes, as outlined by Yip

[1] In mathematics, Voronoi tessellation is a way of dividing space into a number of regions. A set of points (called seeds, sites, or generators) is specified beforehand and for each seed there will be a corresponding region consisting of all points closer to that seed than to any other. The regions are called Voronoi cells [171].

et al. [172]. The length ratio of the sub-cell to the cell defines the degree of randomness

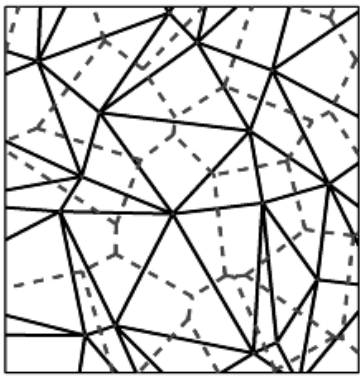

Figure 5.2: Lattice meshing procedure for a given set of nodes (shown in 2D, for simplicity). Solid- lattice mesh; dashed- Voronoi tessellation.

of the lattice. The degree of randomness can be between 0 and 1. When it is 0, the node is placed at the center of each cell. When it is 1, the sub-cell is identical to the cell. However, there is a small probability then that two nodes of neighboring cells are identical. Consequently, it is advised to use a value smaller than 1. In all presented simulations, the degree of randomness was set to 0.99.

In order to take material heterogeneity into account, the particle overlay procedure (schematically shown in figure 5.3) is employed: it is in this manner that different transport (or mechanical) properties are assigned to different phases. For this purpose, either a computer-generated material structure [173], or a material structure obtained by micro-CT scanning [113, 174] can be used. Each node is assigned a voxel from the used microstructure . Element properties depend on the voxel value of its end nodes (see figure 5.3). What has to be noted here is that interface, as used in the present model, does not exactly coincide with the interfacial transition zone (ITZ). Its thickness is between 30 and 80μm [175], while on the other hand interface elements in the present model take up also a piece of aggregate and a piece of mortar (figure 5.3). Their actual size in the model depends on the characteristic element size (voxel size). Therefore, the transport properties of this "phase" are slightly altered, as explained later.

It is important to note that, in general, nodes are not placed on the boundary of the analysed domain (see figure 5.3). This creates some error in the boundary-condition application. Due to the relatively small voxel size usually used in the simulation, generally it can be discarded.

MECHANICAL MODEL

Concrete is a heterogeneous and multiscale material, which shows complicated fracture behavior related to its microstructure. Linear elastic fracture mechanics approaches can

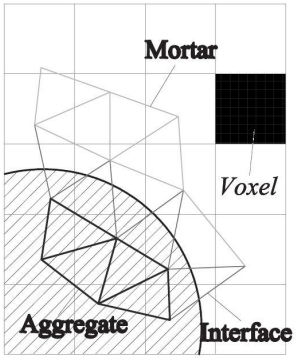

Figure 5.3: Particle overlay procedure for determining lattice element type ((shown in 2D, for simplicity).

hardly be used on concrete, since fracture pattern usually consists of a main crack with branches, bridges, secondary cracks and microcracks.
Lattice type models have been first used by theoretical physicists to model fracture mechanisms in heterogeneous materials (e.g. [176]). This type of model has been adopted by various authors to simulate concrete fracture (e.g. [107, 112]). Fracture processes in other anisotropic or heterogeneous materials have been successfully simulated by lattice models as well (e.g. wood [177] or porous reactor core graphite [178]).
In these models, material is discretized as a set of small truss or beam elements which can transfer forces (Figure 5.4). In the Delft lattice model as used herein, all individual elements exhibit linear elastic behavior. The fracture simulation is achieved by performing a linear elastic analysis of the lattice under loading, and removing an element which exceeds a prescribed fracture criterion (e.g. strength, strain, or energy) from the mesh. This analysis is then repeated in a step-wise manner, removing a single element in each step. Thus, a non-linear analysis is performed by actually performing a number of linear analyses. Using this method, realistic crack patterns are found. Furthermore, even though individual elements all behave brittle, a ductile global response is achieved [107, 179].
Heterogeneity of the material can be implemented using various methods [107]: (1) using a distribution (e.g. normal distribution) of strengths and stiffness of individual lattice elements; (2) using a digital image (2D) or a micro-CT image (3D) of the concrete and assigning different properties to elements representing different material phases. Alternatively, computer generated concrete micro-structure can be used; (3) using a random orientation of lattice elements. Most realistic results are, of course, obtained when the implemented heterogeneity resembles closely the real material microstructure.
Details about the underlying elastic equations as well as the full computational procedure of the model are available in the literature [107, 113, 173].
In the present work, a fracture criterion based on the tensile stress in beams is adopted. Normal force and bending moments are both taken into account by the following general relation:

$$\sigma = \alpha_N \frac{N}{A} + \alpha_M \frac{max(M_X, M_Y)}{W} \; [MPa] \tag{5.1}$$

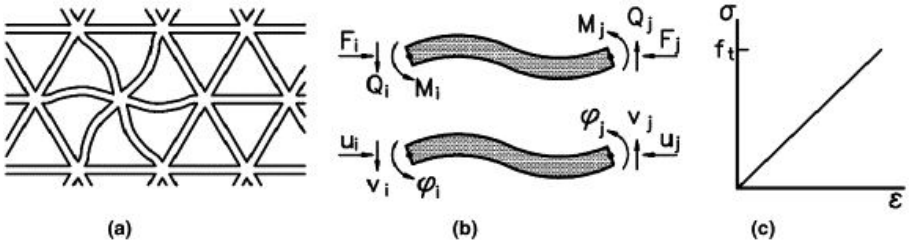

Figure 5.4: Lattice of beam elements (a), definition of forces and degrees of freedom (b), stress-strain relation of beam element (c)

where A is the beam cross-sectional area, W the cross sectional moment of resistance, α_N and α_M are the normal force influence factor and the bending influence factor. Their values are most commonly adopted as 1.0 and 0.05, respectively. These values have also been adopted herein. The influence of different values of these parameters on the concrete fracture response is discussed elsewhere [180].

5

After the mechanical analysis is performed, crack width is calculated by subtracting the initial element length from its end-node distance in the loaded configuration for each cracked element. This crack width is used as input for the chloride diffusion simulation, as further explained. It needs to be emphasized that such a procedure for crack width calculation is, to a certain extent, dependent on the lattice mesh used in the simulation. Cell size (figure 5.1) has a significant influence: a smaller cell size results in smaller crack widths and a somewhat more brittle response, as shown by Schlangen and Garboczi [179]. This is due to the fact that, in a lattice-type model, the cracked area localizes into the narrowest band permitted by the lattice discretization (which is, dependent on the structure of the lattice mesh, often one element wide) [181]. More complex approaches are available in the literature (e.g. the approach of Grassl and Jirásek [182]), in which an isotropic damage constitutive model is used (instead of the linear elastic-brittle, as used herein), and the resulting crack openings are independent of the length of the element. However, in these approaches, the simplicity of lattice models (i.e. simple constitutive laws and a small number of input parameters) is lost. Cell size also has some effect on the fracture criterion (equation 5.1). A larger cell size makes the bending moment in beam elements higher compared to the normal force, and therefore has a higher contribution in the fracture criterion. This causes smaller beams to break faster. However, this effect is minimized by the selected value of α_M (0.05).

CHLORIDE DIFFUSION MODEL

The proposed model treats concrete as an assembly of one-dimensional “pipe” elements, through which chloride diffusion takes place. An assembly of these elements in 3 spatial dimensions enables the simulation of chloride penetration in 3D. As stated, chloride diffusion is assumed to be the only parameter governing chloride transport. The scope of the current study is, therefore, limited to water saturated conditions only.

The governing equation for the chloride diffusion simulation is Fick's second law [16]:

$$\frac{\partial C}{\partial t} = D\frac{\partial^2 C}{\partial x^2} \tag{5.2}$$

for the whole domain, Ω. Here, C is the chloride content, D the chloride diffusion coefficient, and x the spatial coordinate. The boundary conditions for this type of problem are [183]:

$$C = C_b \quad \text{on} \quad \Gamma_b \tag{5.3}$$

$$q = -D\frac{\partial C}{\partial t} \quad \text{on} \quad \Gamma_q \tag{5.4}$$

where $\Gamma_b \cup \Gamma_q = \Gamma$ and $\Gamma_b \cap \Gamma_q = 0$ is the whole boundary of the domain. In the above equation, q is outward flux normal to the boundary (i.e. in direction n), and C_b is the prescribed chloride content at the boundary. The initial condition for the problem is:

$$C = C_0 \quad \text{at} \quad t = 0 \tag{5.5}$$

The chloride content is discretized in space as:

$$C = \sum_{i=1}^{n} N_i C_i \tag{5.6}$$

where N_i are the shape functions, n the number of nodes in an element, and $C_i(t)$ the time dependent nodal chloride contents. The Galerkin approximation of equation 5.2 is [183]:

$$\int_\Omega N_i \left(\frac{\partial}{\partial x} D \frac{\partial C}{\partial x} - \frac{\partial C}{\partial t} \right) d\Omega = 0 \tag{5.7}$$

Employing integration by parts on the first term of equation 5.7 yields:

$$-\int_\Omega \left(D\frac{\partial N_i}{\partial x}\frac{\partial C}{\partial x} + \frac{\partial C}{\partial t} \right) d\Omega + \int_{\Gamma_q} N_i D \frac{\partial C}{\partial x} n d\Gamma_q = 0 \tag{5.8}$$

From equation 5.4 it holds:

$$\int_{\Gamma_q} N_i D \frac{\partial C}{\partial x} n d\Gamma_q = -\int_{\Gamma_q} N_i q d\Gamma_q \tag{5.9}$$

On substituting the spatial discretization from equation 5.6, equation 5.8 becomes:

$$\int_\Omega \left(D\frac{\partial N_i}{\partial x}\frac{\partial N_j}{\partial x} C \right) d\Omega + \int_\Omega N_i N_j \frac{\partial C}{\partial t} d\Omega - \int_{\Gamma_q} N_i q d\Gamma_q = 0 \tag{5.10}$$

or, in matrix form:

$$M\frac{\partial C}{\partial t} + KC = f \tag{5.11}$$

Here, M is the element mass matrix, K the element diffusion matrix, and f the forcing vector. For one-dimensional linear elements, as used here, the shape functions (N_i, N_j) and their derivatives (B_i,B_j) are [183]:

$$\begin{bmatrix} N_i \\ N_j \end{bmatrix} = \begin{bmatrix} 1-\frac{x}{l} \\ \frac{x}{l} \end{bmatrix} \tag{5.12}$$

$$\begin{bmatrix} B_i \\ B_j \end{bmatrix} = \begin{bmatrix} \partial N_i/\partial x \\ \partial N_j/\partial x \end{bmatrix} = \begin{bmatrix} -\frac{1}{l} \\ \frac{1}{l} \end{bmatrix} \tag{5.13}$$

The relevant elemental matrices (equation 5.11) for a one-dimensional element are:

$$K = \int_{\Omega} B^T D B d\Omega = DA \int_{l} B^T B dx = \frac{DA}{l} \begin{bmatrix} 1 & -1 \\ -1 & 1 \end{bmatrix} \tag{5.14}$$

$$M = \frac{1}{\omega} \int_{\Omega} N^T N d\Omega = \frac{A}{\omega} \int_{l} N^T dx = \frac{Al}{6\omega} \begin{bmatrix} 2 & 1 \\ 1 & 2 \end{bmatrix} \tag{5.15}$$

$$f = -\int_{\Gamma_q} q N^T d\Gamma_q = \begin{bmatrix} -q_i A \\ -q_j A \end{bmatrix} \tag{5.16}$$

Note that $d\Omega$ in equations 5.14 and 5.15 is replaced by Adx. Here, A is the uniform cross-sectional area of a one-dimensional element. Further, l and D are the length and the diffusion coefficient of each element, respectively. In equation 5.16 q_i and q_j are the prescribed nodal fluxes at nodes i and j. Cross sectional areas of individual elements are assigned using the so-called Voronoi scaling method [167] - cross section of an element is equal to the area of a facet of a Voronoi cell which is common to its end nodes (see chapter 5.2.2). Element mass and diffusion matrices (equations 5.14 and 5.15) are the same as those of regular one-dimensional linear elements [183], except the non-dimensional correction parameter ω in the mass matrix (equation 5.15). This parameter is added to convert the volume of a Voronoi cell to the volume of lattice elements, due to overlap volume of adjacent lattice elements (figure 5.5): It can be determined as [170]:

$$\omega = \frac{\sum_{k=1}^{m} A_k l_k}{V} \tag{5.17}$$

where m is the total number of elements, A_k and l_k cross sectional area and length of each lattice element, k element number, and V the volume of the specimen. It was shown that ω can be set as 2 for a two-dimensional and 3 for three-dimensional cases, respectively, without loss of accuracy [167, 170]. Using the Crank-Nicholson procedure [183], the system of linear equations 5.11 is discretized in time, and the following equation results (if no flux boundary conditions are applied):

$$\left(M + \frac{1}{2}\Delta t K\right) C^n = \left(M - \frac{1}{2}\Delta t K\right) C^{n-1} \tag{5.18}$$

This equation is then solved for each discrete time step (Δt) and chloride profiles are obtained.

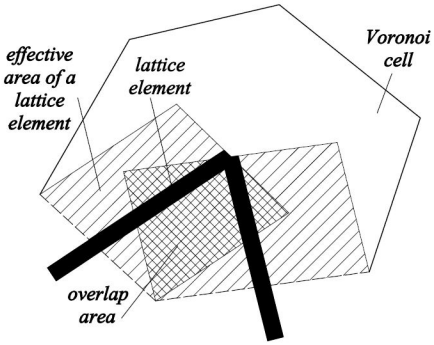

Figure 5.5: Definition of overlap area for determination of correction parameter ω for the mass matrix 5.15 (adapted from [170])

Saturated concrete was assumed in all analyses, since the purpose of this work was to validate the approach by comparing the results with experimental data, not to develop a fully functional service-life modeling tool. Therefore, Fick's second law (equation 5.2) was assumed to be valid, and diffusion was the only transport mechanism considered. For elements which are cracked, D in the diffusion matrix (equation 5.14) is replaced by D_{CR}, an effective diffusion coefficient dependent on the local element crack width. Dependence of D_{CR} on the element crack width is elaborated in chapter 5.2.4.

5.2.3. PHASE TRANSPORT PROPERTIES

In order to determine transport properties of individual phases within the heterogeneous concrete, the approach developed by Caré and Hervé [184](the so-called n-phase model) was used. This analytical model takes into account the characteristics of different phases of concrete on the effective diffusion coefficient of the composite material. The material is treated as a three-phase composite, consisting of a mortar phase, aggregate phase, and an interface transition phase. This model considers an n-layered spherical inclusion embedded in a matrix. In case of concrete, the aforementioned 3 phases are distinguished. Hence, the model assumes that, at mesoscopic scale, the effective diffusion coefficient of concrete (D_{eff}) is a function of the volume fraction and the diffusion coefficient of different phases (here: aggregate, mortar, and interface phase). This model was developed with spherical particles in mind, so for any other particle shape (e.g. the *Anm* material model developed by Qian [173]) can be considered as only an approximation. The following formulae were used (assuming impermeable aggregates):

$$D_{eff}/D_M = N/D \tag{5.19}$$

Here, the following are:

$$\begin{aligned} N &= 6D_M(1-C_A)(C_A+C_I)+2C_I(D_I-D_M)(1+2C_A+2C_I) \\ D &= 3D_M(2+C_A)(C_A+C_I)+2C_I(1-C_A-C_I)(D_I-D_M) \end{aligned} \tag{5.20}$$

Here, D_M, and D_I are the diffusion coefficient of the mortar phase, and the diffusion coefficient of the interface phase, respectively. Also, C_A and C_I are volume fractions of the aggregate and the interface phases, respectively. If the aggregates are porous, a different set of formulas, which take the diffusivity of the aggregate particles into account, can be used [184]. This approach enables one to determine the diffusion coefficient of individual phases (mortar and interface) in concrete, given the volumetric contents of each phase, and the effective diffusion coefficient of concrete. All these are usually available from the experimental data. Therefore, in order to determine this, it is necessary to determine the ratio between the diffusion coefficient of the interface and the diffusion coefficient of mortar.

To estimate the magnitude of this ratio, a set of experimental data provided by Oh and Jang [185] was used (Table 5.1). Here, transport properties of concrete are compared to corresponding mortars. Concrete used in the experiments contained about 35% coarse aggregate by volume. Rapid chloride migration test was used to determine the non-steady state migration coefficient (D_{NSSM}) of concretes and mortars. From these, diffusion coefficients (D) were calculated.

Table 5.1: Experimental results of Oh and Jang [185] (C-concrete, M-mortar)

	D_{NSSM} ($\times 10^{-12}$ m^2/s)			D ($\times 10^{-12}$ m^2/s)		
ID	C	M	M/C	C	M	M/C
NI-0	6.56	8.80	1.34	2.43	5.53	2.28
NI-PFA15	3.54	4.55	1.29	1.47	3.18	2.17
NI-BFS15	5.77	6.79	1.18	2.16	4.31	2.00
NI-BFS30	5.42	4.93	0.91	2.00	3.09	1.54
NV-0	9.43	11.94	1.27	3.35	7.20	2.15
NV-PFA30	3.43	5.04	1.47	1.19	2.94	2.47
NV-BFS30	4.68	5.49	1.17	1.70	3.39	2.00
LI-0	15.7	11.23	0.71	5.48	6.74	1.21
HI-0	3.76	5.40	1.44	1.49	3.56	2.40
HI-BFS30	3.54	2.92	0.82	1.42	1.96	1.37

Note: L, N, H mark series with w/c of 0.55, 0.45 and 0.35, respectively. I and V mark series using ASTM Type I Cement (Ordinary Portland Cement) and ASTM Type V Cement (sulfate-resisting cement, respectively). PFA and BFS indicate supplementary cementitious material content by binder percentage (fly ash and slag, respectively).

By careful observation of the results (table 5.1), it is clear that the ratio of mortar to concrete diffusion coefficient (M/C) changes dramatically when the diffusion coefficients are calculated. It even states that, in some cases, the diffusion coefficient of mortar is higher than that of concrete, even though its non-steady state migration coefficient is lower. This is unlikely to be the case. In order to correct this, diffusion coefficients of concrete were calculated using a suggestion from [186]: it is stated that there exists a linear relationship between the non-steady state migration coefficient (D_{NSSM}) and the diffusion coefficient of concrete (D). Similarly, Yang and Wang [187] found that there is a linear relationship between the non-steady state diffusion coefficient obtained from the accelerated chloride migration test ($ACMT$), and the diffusion coefficient obtained from the ponding test, irrespective of the concrete composition. Linear regression of the

data provided by [186] yields the following tentative equation:

$$D = 0.97 D_{NSSM} - 2.64 \tag{5.21}$$

where D and D_{NSSM} are in $10^{-12}\ m^2/s$. Furthermore, by employing the M/C ratio from the migration experiment, the diffusion coefficient of mortar is calculated (Table 5.2). It has to be noted that equation 5.21 is used here merely as a tool to calculate the diffusion coefficient from the non-steady state migration coefficient.

Table 5.2: Diffusion coefficients calculated using equation 5.21 from experimental results of Oh and Jang [185]

	D ($\times 10^{-12}\ m^2/s$)		
ID	C	M	D_I/D_M
NI-0	3.70	4.97	2.79
N-PFA15	0.78	1.01	3.06
NI-BFS15	2.94	3.46	3.57
NI-BFS30	2.60	2.36	5.23
NV-0	6.48	8.21	3.14
NV-PFA30	0.68	1.00	2.24
NV-BFS30	1.88	2.21	2.46
LI-0	12.56	8.98	7.16
HI-0	1.00	1.44	2.39
HI-BFS30	0.78	0.65	5.94

In order to determine the ratio between the diffusion coefficient of the interface and the diffusion coefficient of mortar (D_I/D_M ratio), a concrete material structure with about 35% of coarse (spherical) aggregates was generated using a simple packing algorithm. Diameters of the coarse aggregate particles were in range of 4-24 mm. A lattice with characteristic elements size (voxel size) of 1 mm was projected on top of it, and volume of lattice elements of each phase was calculated (58.41% mortar, 29.35% aggregate, and 12.24% interface). Then, using formulae 5.19 and 5.20, the ratio between the diffusion coefficient of the interface and the diffusion coefficient of mortar was calculated for each mixture (Table 5.2). In order to achieve the desired effective concrete properties, these vary in the range 2.24-7.16. This seems to be in accordance with the variability of the diffusion coefficient of ITZ, which is stated to be somewhere in the range 2-8 times that of the cement paste [175].

The variability of this parameter can also be taken into account in a statistical manner; however more experimental results are needed to justify this approach. Based on presented analysis, a deterministic value of 3 for the D_I/D_M ratio was selected. This value is used in further analyses.

It has to be emphasized once again that the interface zone as modeled here does not correspond directly to the ITZ. As stated before, thickness of the ITZ is 30-80μm [175], while in the presented model the interface thickness is dependent on the cell size (figure 5.1). As the fitting procedure in this paragraph was performed for a lattice with a cell size of $1mm$, the obtained values are generally applicable only for such a lattice. Strictly speaking, the procedure would need to be repeated if a significantly different lattice resolution

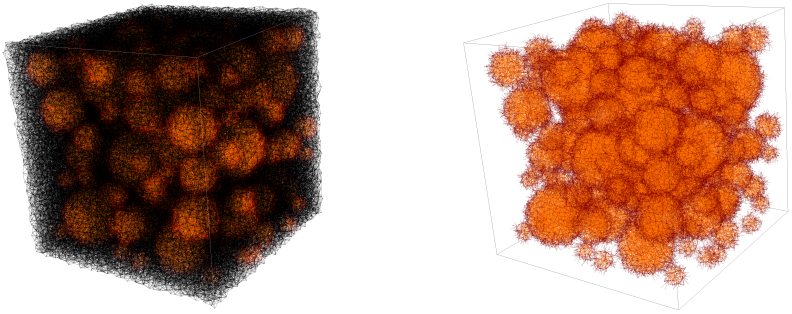

(a) (b)

Figure 5.6: Lattice mesh used for determination of the D_I/D_M ratio ((a)-the whole lattice; (b)-only aggregate and the interface).

is used. This might not be important for finer meshes, as experiments also show a wide range of D_I/D_M values (2-8 [175]), but it might be an issue for coarser meshes.

5.2.4. CRACK TRANSPORT PROPERTIES

Two sets of experiments performed by Ismail et al.[60, 61] are used for determining transport properties of a single crack. They used the expansive core method to create parallel-walled cracks in doughnut shaped specimens. Due to a large variety of smaller crack widths, these experiments are suitable for the procedure employed here. First set of experiments [60] was performed on cracked brick samples, while the second set [61] used cracked mortar samples. In both instances, cracked samples were placed in a chloride penetration cell, with chloride loading on both sides of the sample. After the exposure period, using the grinding technique, two types of chloride profiles were determined: perpendicular to the exposed surface, and perpendicular to the crack walls. The second type of profiles were determined by grinding the material in the middle part of the specimen height, in order to ensure that powder samples would contain only chloride ions penetrating from the crack plane, and not from the sample surface (figure 5.7).

Here, the approach proposed by Wang and Ueda [165] was used. In order to determine the effective crack transport properties, numerical simulation results are fitted to experimental data. For the simulations, the geometry of the test (figure 5.7) was simplified: a prismatic 3D lattice of $50 \times 5 \times 50$ mm was used, with a total number of 12500 nodes and 85095 lattice elements (figure 5.8). To simplify the process at this stage, the mechanical analysis is not performed here; rather an artificial "crack" is created in the middle of the analysed specimen (red lattice elements in figure 5.8). Different transport properties of "cracked" elements (D_{CR}) are needed to reproduce experimental results for different crack widths. A trial-and-error approach was then taken: transport properties of these lattice elements (i.e. red elements in figure 5.8) were adjusted in order to obtain a good match between simulation results and experiments. The fitting procedure was

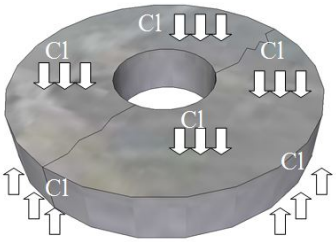

Figure 5.7: Brick/mortar specimen used for chloride diffusion experiments in studies of Ismail et al. [60, 61]

performed for every crack width, providing a range of values of D_{CR} for different crack widths. The results are discussed below.

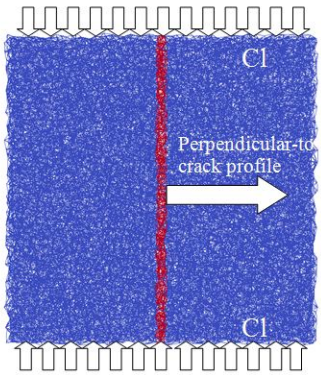

Figure 5.8: Lattice mesh used for determining transport properties of a crack. Blue-brick/mortar, red-"crack"

First, experimental results of cracked brick specimens are reproduced [60]. After cracking, these were fitted in the chloride penetration cell, and exposed for 10 hours. Regression analysis of the chloride profile perpendicular to the exposed surface (uncracked sample) yielded the diffusion coefficient of $156.71 \times 10^{-12}\ m^2/s$, and the surface chloride concentration of 0.37% per weight of sample (figure 5.9). These were used as input for all analyses of this experiment.
In order to obtain results close to experimental values, a trial-and-error procedure was followed. This means that the effective diffusion coefficient of "cracked" elements was adjusted until the calculated perpendicular-to-crack profile corresponded well to the experimental one. Values of the fitted effective diffusion coefficients for different crack widths are shown in figure 5.10.

For large cracks ($60\mu m$ and $128\mu m$), the effective diffusion coefficient is 3 orders of magnitude higher than the diffusion coefficient of chloride ions in free bulk water (which is around $2.03 \times 10^{-9}\ m^2/s$ at 20 °C [188, 189]). An ionic diffusion coefficient this high is impossible to achieve in liquid water. However, these results seem to be in good ac-

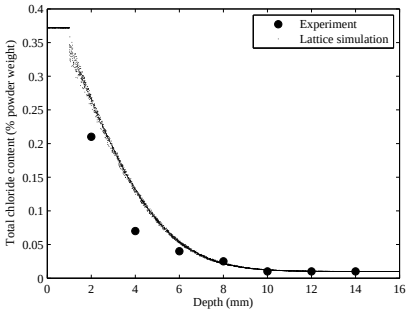

Figure 5.9: Experimental and simulated chloride profile for the exposed surface in an uncracked brick specimen.

cordance with values proposed by Wang and Ueda [165]. They also suggested that the effective diffusion coefficient in large cracks in brick samples is very high, much higher than that in free bulk water. They attributed this to additional transport mechanisms which may occur in the crack, e.g. "convection current due to the small temperature gradient and/or small hydraulic pressure gradient" [165], and further used these values to model chloride diffusion in cracked concrete. However, it seems also possible that, even though the experiment aimed at determining local diffusion coefficient of chloride ions in cracks, the brick specimens had not been completely saturated when the experiment begun. Therefore, capillary suction might have played a significant role, if by accident. Due to high porosity of brick samples, this could strongly influence the chloride ingress behaviour, and explain these high diffusion coefficients. The validity of these assumptions is addressed later on. Nevertheless, based on the present tests, the following (tentative) linear relation can be proposed:

$$\begin{aligned} D_{CR} &= (23.84\,w + 8.37) \times 10^{-11} \quad m^2/s \quad \text{for } 21\mu m \leqslant w \leqslant 55\mu m \\ D_{CR} &= 1.4 \times 10^{-6} \quad m^2/s \quad \text{for } w > 55\mu m \end{aligned} \tag{5.22}$$

The lower bound of $21\mu m$ in equation 5.22 represents the smallest tested crack width [60]. When the crack is smaller than this, it can be considered that no increase in the diffusion coefficient occurs. The value of $55\mu m$ in equation 5.22 was selected based on the recommendation of Ismail et al. [60]. It was found, after performing a deformation-controlled uniaxial tension test on the material, that the critical crack opening of about 50-55μm is where the mechanical interaction between crack surfaces ceases to exist, so there can be no reduction of the chloride diffusion in larger cracks. This value is higher for concrete, where, due to material heterogeneity, more crack bridging and branching occurs.

In order to check whether these results are directly applicable to cement based materials, the same experiment, but this time on cracked mortar samples (CEM I 52.5R, w/c=0.5), was simulated [61]. In this work, two series of mortar specimens were cracked at different ages (28 days and 2 years). These were tested in order to check also the influence of cracking age on autogeneous healing of cracks. Regression analyses (i.e. fitting of

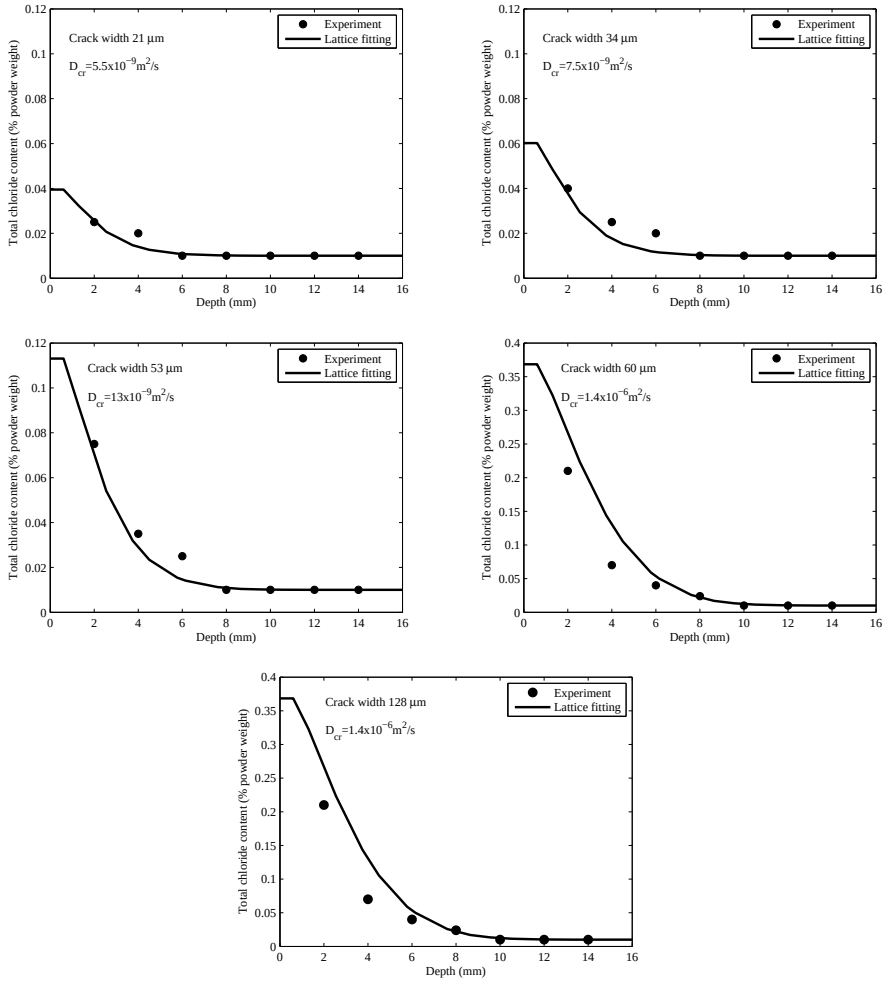

Figure 5.10: Experimental and simulated perpendicular-to-crack chloride profiles for different crack widths in brick specimens.

equation 1.11 to experimental data) of perpendicular-to-surface profiles yielded the following data: diffusion coefficient of 8.66×10^{-12} m^2/s (bulk mortar), surface chloride concentration of 0.32% mortar weight; and the diffusion coefficient of 7.51×10^{-12} m^2/s, surface chloride concentration of 0.32% mortar weight, for 28 days and 2 years series, respectively. In both instances, specimens were exposed to chloride loading for a total of 14 days.

Based on equation 5.22, effective diffusion coefficients for different crack widths were calculated. After the analyses were performed, the results indicated that equation 5.22 overestimated the perpendicular - to -crack diffusion in cracked mortar (figure 5.11). A different relation, proposed by Djerbi et al. [79], was also used to check whether it gives

better results when applied to cement-based materials (note that w is in μm):

$$D_{CR} = 2 \times 10^{-11} w - 4 \times 10^{-10} \quad m^2/s \quad \text{for } 30\mu m \leqslant w < 80\mu m$$
$$D_{CR} = 1.4 \times 10^{-9} \quad m^2/s \quad \text{for } w \geqslant 80\mu m \tag{5.23}$$

Clearly, values obtained from equation 5.22 overestimate the perpendicular-to-crack

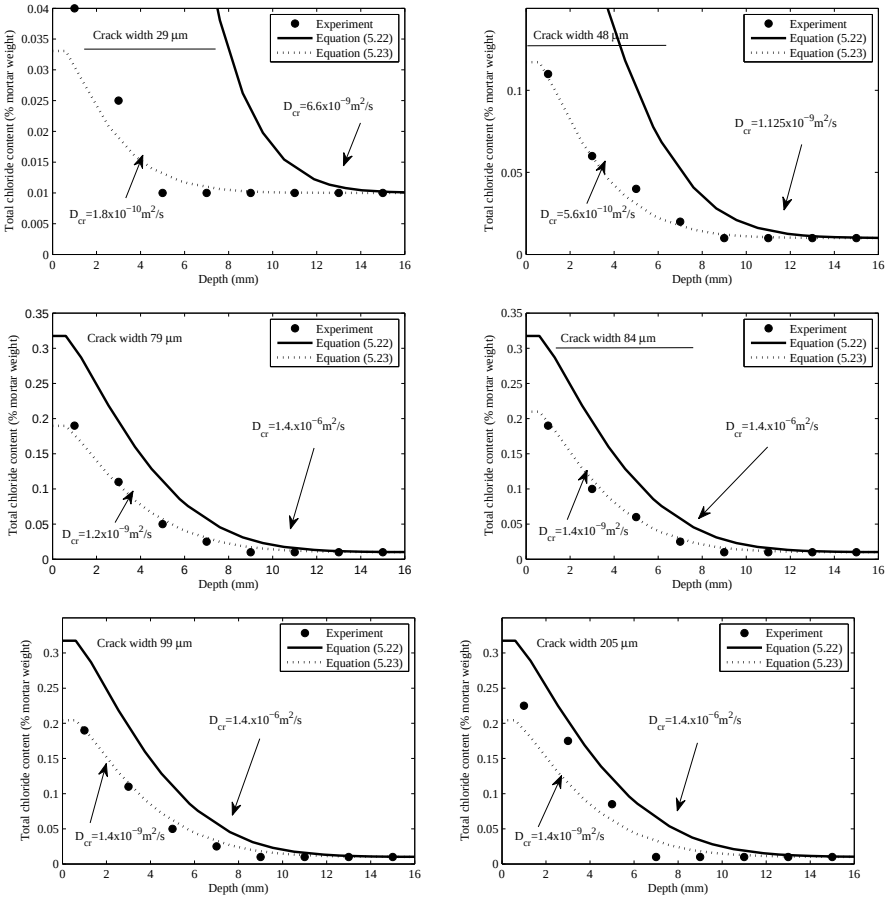

Figure 5.11: Experimental and simulated perpendicular-to-crack chloride profiles for different crack widths in mortar specimens. Not underlined-cracked at 28 days. Underlined- cracked at two years.

chloride penetration in this case. On the contrary, results for D_{CR} obtained using 5.23 are in good agreement with the experiments. It seems, then, that the values for D_{CR} which hold for cracked brick specimens overestimate the chloride penetration in cracked mortar. Since brick is much more brittle and homogeneous, less crack branching and bridging occurs when it cracks, compared to mortar. This potentially slows down chloride ingress through cracks in heterogeneous materials, like mortar and concrete. Also, it is most probable that capillary suction played a significant role in brick experiments

[60], thereby altering the effective transport properties of a crack. Moreover, whether results from tests on different materials can be applied directly to mortar and concrete is questionable. In the mechanical lattice model with embedded aggregate particles, crack branches and bridges will be found automatically, and are slowing down the diffusion process. It can be, therefore, concluded that equation 5.23 can be used to simulate chloride penetration in cracked cement based materials using the proposed lattice approach.

5.3. VALIDATION AND DISCUSSION

5.3.1. HETEROGENEOUS MATERIAL

IN order to validate the approach developed in section 5.2.3, experimental results provided by Yang and Wang [187] were used. A 90-day ponding test was used to determine the diffusion coefficient of different concretes. All concrete mixes used in their study had a volumetric content of coarse aggregates of about 30%, with maximum grain size of 10mm. For the simulation, a concrete material structure with about 30% of coarse aggregate particles was generated, with coarse aggregate particle diameters ranging from 4-10 mm. A lattice with characteristic elements size (voxel size) of 1 mm was projected on top of it, and volume of lattice elements of each phase was calculated (61.60% mortar, 22.50% aggregate, and 15.90% interface). Note that the thickness of the interface in the model is determined by the characteristic element size (i.e. in this case it was around 1mm). The total size of the mesh was 50 × 50 × 50mm, with 125000 nodes and 938156 lattice elements. This particular mix was made using ASTM Type I Portland cement as a binder.

Regression analysis of experimental data yielded the following: diffusion coefficient of $47.614 \times 10^{-12}\ m^2/s$, and surface chloride content of 0.51%. Using equations (18) and (19) and the D_I/D_M value of 3, diffusion coefficients of the mortar and the interface phases were calculated as $48.35 \times 10^{-12}\ m^2/s$, and $145.06 \times 10^{-12}\ m^2/s$, respectively.

An analysis was performed using both the homogeneous and the heterogeneous lattices, using the input data as provided above.

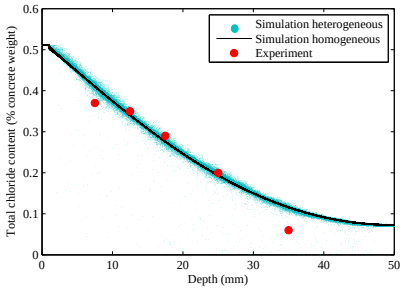

Figure 5.12: Comparison of chloride profiles obtained by homogeneous and heterogeneous lattice analyses and the experiment (aggregate particles excluded from the plot).

Figure 5.12 shows that the results of both homogeneous and heterogeneous lattice analyses correlate well with experimentally obtained data. Zero values in the hetero-

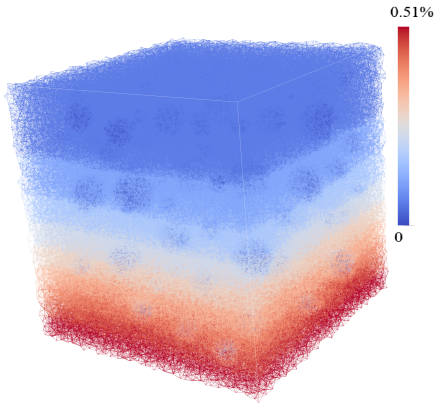

Figure 5.13: Chloride distribution obtained from the heterogeneous lattice analysis (% of concrete weight).

geneous lattice analysis correspond to lattice nodes which are inside the impermeable aggregate particles; therefore, no chloride ions can be present. Other points below the maximum penetration band show that, in a heterogeneous material as modeled here, there is no clear front of chloride penetration. Instead, a three-dimensional profile is presented, with variable chloride content at a certain depth. It can also be seen that there exists a difference between the maximum total chloride content at a certain depth (the one obtained from the heterogeneous analysis), and the value which is obtained if concrete is considered to be a homogeneous medium. By performing similar analyses (but considering concrete as a two-phase medium, comprising mortar and coarse aggregates), this phenomenon also occurred in other studies [120, 190]. They suggested that this could be one of the factors contributing to large discrepancy in values of critical chloride contents reported in the literature. It is possible that a threshold value of chloride is reached in certain points on the reinforcing steel, thus depassivating it and creating local corrosion pits. However, chloride content elsewhere along the steel could be lower, due to material inhomogeneity. Due to the usual experimental procedure (i.e. grinding the material close to the reinforcing steel and performing chemical analysis to determine the chloride content), the value obtained would be lower than the actual value which caused the local depassivation of the steel. This phenomenon justifies the use of more advanced material models, such as the presented one, in order to get more insight into the process of steel depassivation and corrosion pit locations in concrete. Also, it encourages the use of more sophisticated experimental techniques, such as laser-induced breakdown spectroscopy (LIBS) [110] (used in chapter 2) or electron probe microanalysis (EPMA) [41], especially when determining the value of critical chloride content in concrete.

5.3.2. CRACKED MATERIAL

The approach presented in chapter 5.2.3 was verified on experimental results of Şahmaran [84]. Mortar prisms ($355.6 \times 50.8 \times 76.2\ mm^3$), made using Portland (ASTM-Type I) cement and reinforced with three levels of steel mesh reinforcement were cast. The prisms were reinforced to enable creation of cracks of varying controlled widths. No details are given on positioning of the reinforcing mesh or its mechanical interaction with the mortar matrix, so it was omitted from the simulations here, even though it could affect the cracking behavior. After the curing period, they were cracked using a 4-point bending test to obtain different crack widths. After loading, one single crack occurred in each of the specimens. Cracks formed in bending are tapered (V-shaped). Upon unloading, some crack closure occurred, so their width was measured in the unloaded state. Then, the samples were exposed to $NaCl$ solution for 30 days. After the exposure period, the area around the crack was drilled, ground, and analyzed for chloride [84].
Regression analysis of the experimental data gave the following (for the uncracked sample): diffusion coefficient of $20.3 \times 10^{-12}\ m^2/s$, and surface chloride content of 0.39% by weight of mortar. The analyzed sample had a size of $355 \times 50 \times 75\ mm^3$, with a characteristic element size of 2.5mm. Steel mesh reinforcement was neglected in the simulation. First, a mechanical analysis was performed. Using a four-point bending setup, cracks of different widths were produced. As in the experiments, one single crack formed in the fracture analysis. The output of the mechanical analysis was used as input for the chloride diffusion analysis. Equation 5.23 was used for defining the effective diffusion coefficients of cracks. Every “local” cracked element has its own value of the diffusion coefficient, depending on its crack width (as the cracks are, in this case, "V" shaped).

At loading levels at which cracks are similar to those from experiments [84], diffusion analyses were performed. Surface crack widths achieved in the simulations were not exactly the same as the experimental ones, due to the sequentially-linear solving procedure of the lattice model (chapter 5.2.2). The surface chloride contents for each analysis were adjusted to match those in experiments with a similar crack width. Both experimental and simulation results are shown in figure 5.15.

As expected, chloride penetration depth increases with the increase of surface crack width. The effect is less pronounced than in the case of a parallel-walled crack, though. This is due to the fact that bending cracks are V-shaped, being wider at the surface than on the inside of the prism. According to equation 5.23, cracks wider than $80\mu m$ all have the same effective diffusion coefficient. However, since wider bending cracks also run deeper, the effect of widening is still pronounced with large cracks. This means that widening of the cracks above the $80\mu m$ threshold does increase chloride penetration further, since they become deeper in the process.
Comparing the experimental and simulation results (figure 5.15), evidently there is a difference. Experimental results for wider cracks (more than $210\mu m$) show a more pronounced influence of cracking, compared to simulation results. There are two reasons for this: first, the crack width was measured in the unloaded state. This means that the crack was larger during the loading and some damage was created, which is not accounted for in the model. Secondly, some cracks have probably formed alongside the steel mesh reinforcement, speeding up the lateral chloride penetration. This was disregarded in the model. Overall, the simulation results seem to be in relatively good agree-

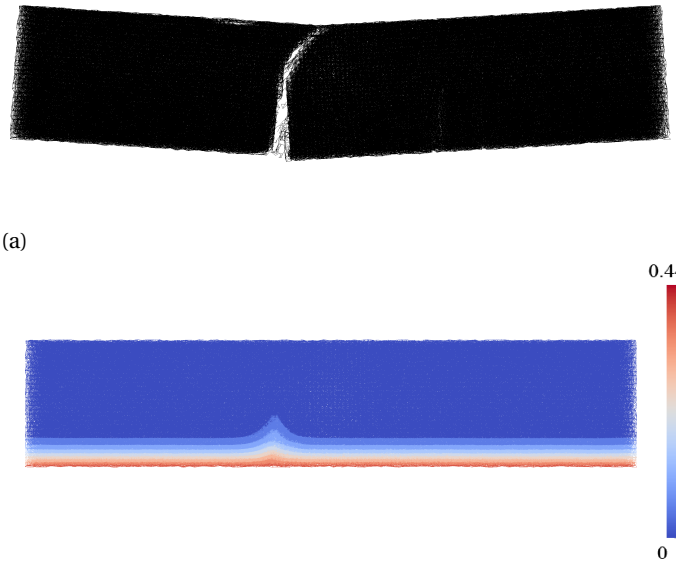

(a)

(b)

Figure 5.14: Mortar sample with surface crack width of 369μm. (a)- crack pattern (side view). (b)- total chloride profile (% of mortar weight) after 30 days of exposure.

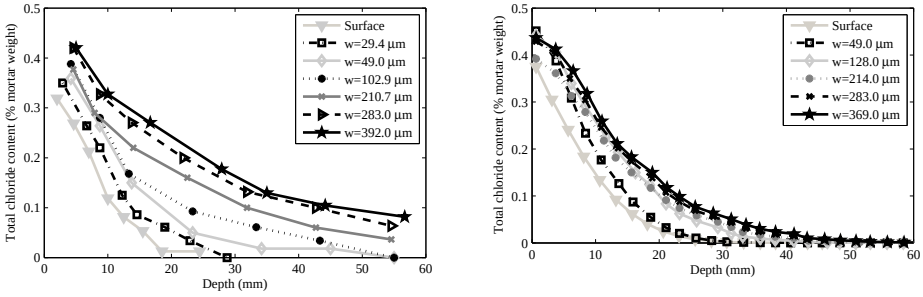

(a) (b)

Figure 5.15: Total chloride profiles for different crack widths after 30 days of exposure. (a)- experiment; (b)- simulation.

ment with experimental data.

5.3.3. PROSPECTS

In experiments performed in chapter 2, diffusion was not the only mechanism governing chloride ingress. As specimens were not fully saturated, the contribution of capillary suction cannot be ignored. To make matters more complicated, the specimens were exposed to wet-dry cycles. Such severe exposure conditions were selected in order to speed-up the chloride ingress and subsequent corrosion initiation. It is, therefore, not possible to correctly simulate the performed experiments with the current model. For that to be done, the model should be extended to consider non-saturated conditions and effects of wetting and drying. Even though computationally this would be relatively straightforward, many experimental parameters still need to be determined. Nevertheless, an example simulation is performed here, using the geometry of the experiment from chapter 2 (i.e. the mechanical simulation performed in that chapter), and the assumption of full saturation. The results for uncracked and cracked specimens are shown in figure 5.16.

Clearly, the trend observed in experiments of chapter 2 can be qualitatively captured. As noted previously, the model should be extended to obtain quantitatively good results.

5.4. SUMMARY AND CONCLUSIONS

As cementitious materials are highly heterogeneous and often cracked, their transport properties show significant local variations. More advanced models than presently available are needed for studying these effects. In view of this, a three-dimensional lattice model for simulating chloride ingress was developed. The proposed framework described here enables:

1 Simulating chloride ingress in heterogeneous concrete, i.e. taking into account the presence of aggregate particles and porous interface surrounding them.

2 Taking into account presence of cracks on chloride ingress, by coupling the simulation with the mechanical analysis.

In order to focus on these two issues, saturated concrete was assumed in all analyses. The procedures developed were tested and validated using data from the available literature. The following conclusions can be reached from the presented numerical simulations:

- When neglecting the material heterogeneity, simulation results are very close to experimental ones. The reason for this lies in the usual experimental procedure (grinding and chemical titration), which gives an averaged value of the chloride content at a certain depth.
- The heterogeneous model shows some deviation from the perfect diffusion profile, which is observed in experiments where penetration depth is determined by silver

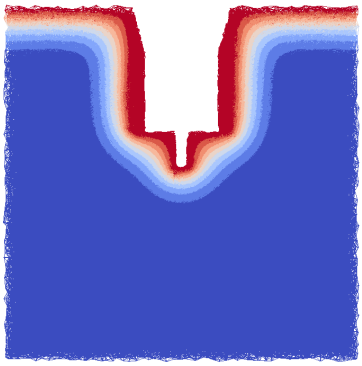

(a) Side view uncracked

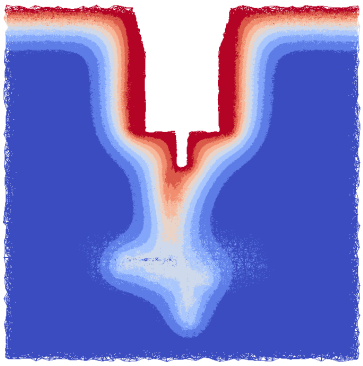

(b) Side view cracked

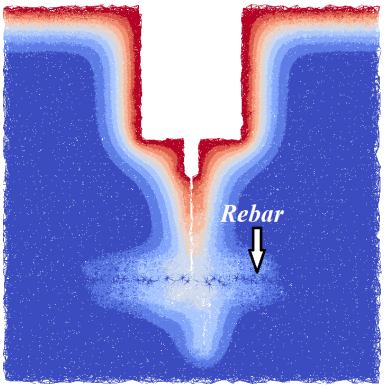

(c) Slice through the steel bar (cracked)

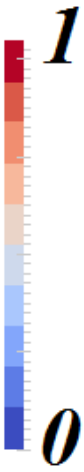

(d) Relative Cl content (legend)

Figure 5.16: Chloride contents in an example simulation of chloride diffusion in modified wedge splitting test (MWST) specimens (as analyzed in chapter 2)

nitrate spraying or the grinding and chemical titration procedure. More importantly, maximum chloride contents at a certain depth are higher than the averaged ones. This should be kept in mind, especially when studying the critical chloride content in concrete. Use of more advanced experimental methods is therefore encouraged.

- Mechanical cracks do promote chloride ingress into concrete, depending on their width. This is observed also in the model. However, even though commonly addressed only by their surface widths, not all cracks are created equal. Bending cracks are V-shaped, meaning that a part of the crack close to its tip remains inaccessible for rapid chloride penetration. Thus, parallel walled cracks of a certain surface width are more detrimental than flexural cracks of the same surface crack width. Coupling of the mechanical and transport model, as proposed here, enables studying this behavior in more detail.

In all the analyses presented here, it was assumed that concrete was fully saturated. Consequently, capillary suction was not considered. Also, effects of chloride binding have not been explicitly taken into account [31], and no distinction was made between free and bound chloride ions. Rather, the effective diffusion coefficient of the material was used in the simulations. For the laboratory experiments simulated, performed in controlled conditions and short term, these are valid assumptions. However, for engineering service-life analyses, these effects should not be neglected.
Finally, it can be concluded that the presented model can be successfully employed in simulating chloride penetration in both sound and cracked cement based materials. Presence of coarse aggregates in concrete (both in the mechanical and transport simulations) can be included in the model, and gives more insight on the transport behavior.

6

LATTICE MODELING OF CHLORIDE MIGRATION IN CONCRETE

The eye sees only
what the mind is prepared to comprehend.

Robertson Davies

Test methods which use external voltage are commonly used to assess resistance of concrete to chloride ion penetration. In order to facilitate fast chloride ingress, an electrical voltage (typically 10-60 V) is applied across the concrete specimen. These methods have also been used on microcracked and cracked specimens in order to study the influence of cracking on chloride ingress. The chloride migration transport mechanism is fundamentally different from the diffusion process usually occurring in practice. To study the behavior during the test, a model is proposed, based on the transport lattice modeling framework. First, the accuracy and computational aspects of the proposed model are discussed. Then, the model is applied to study the transport in heterogeneous concrete (i.e. on the meso-scale). Also, chloride migration in microcracked, notched, and cracked concrete is simulated. The findings show that the proposed model can successfully reproduce experimentally observed behavior.

Parts of this chapter have been published in Cement and Concrete Research **61-62**, (2014) [191].

6.1. INTRODUCTION

NUMEROUS laboratory tests are in use for chloride penetration resistance. Test procedures which involve artificial acceleration of the process by means of an electrical voltage are commonly used due to their relatively short duration (for example [192, 193]). Even though reliable from an engineering point of view, research is still needed to fully understand these rapid tests and how their results correspond to naturally occurring diffusion.

Better understanding of these testing procedures is to be found through synergy between experiments and numerical modeling. Numerous models have been proposed recently, aiming to provide more insight into the underlying processes. Most of these models have focused on studying transport of different ions present in the pore solution (e.g. Na^+, K^+, OH^-, in addition to Cl^-) during a migration experiment. These so-called multi-species models use complex formulations based on the Nernst-Planck [194, 195] and Poisson-Nernst-Planck equations [196], which take into account the effect of applied voltage and ionic interactions. Using finite difference [195] and finite element methods [194, 196], spatial distribution of ionic species is resolved in time. However, all of these models are one-dimensional, and do not take heterogeneity of concrete into account. A step further in this respect was made by Liu et al. [197], who modeled ionic transport of multiple species in concrete, allowing for its heterogeneous nature. They considered concrete as an assembly of impermeable spherical inclusions (aggregates) and mortar. Their two-phase model revealed some features which cannot be found from one-dimensional models.

The model developed herein aims to further enrich the understanding of these experiments. A single-species model is used [198], as the emphasis of the study lies on the chloride migration in heterogeneous and cracked/notched specimens. First, main mechanisms driving chloride ingress into concrete and some testing methods are briefly addressed and discussed. Then, a description of the developed model is given. The proposed model is then validated against the analytical solution and experimental data. Finally, some conclusions are drawn.

6.2. METHOD

6.2.1. CHLORIDE PENETRATION INTO CONCRETE

TESTING OF CHLORIDE PENETRATION RESISTANCE OF CONCRETE

Performance based approach to service life design is increasingly replacing the prescriptive approach. This means that, instead of the deemed-to-satisfy demands for concrete composition (minimum cement content or maximum water-to-cement ratio), performance of each concrete mix needs to be proven by a certain test.This has lead to researchers proposing a number of tests in past two decades.

For resistance to chloride ingress, these can be divided into three groups:

1. tests based on natural diffusion, such as the salt ponding test (AASHTO 259 [199]) or the bulk diffusion test (NT BUILD 443 [90]).

2. tests which use a DC voltage to assess the chloride ion penetrability, like the Rapid

Chloride Permeability Test (ASTM C1202 [91]), or to accelerate the movement of chloride ions due to the migration transport mechanism, such as the Rapid Chloride Migration test (NT BUILD 492 [18]).

3. different indirect measurement techniques, such as electrical resistivity or sorptivity, which try to correlate these values to resistance of concrete to chloride ingress.

Due to their relatively short duration compared to the natural diffusion tests, the second group is mostly used in engineering practice and research. A comprehensive review of most common testing procedures can be found in [89].
The Rapid Chloride Migration test is commonly used in Europe as a mix design tool [32]. Initially proposed by Tang and Nilsson [198] it has been standardized as NT BUILD 492 [18]. The test uses 50 mm thick and 100 mm diameter specimens. First, the specimens are vacuum saturated with a saturated $Ca(OH)_2$ solution for 24 hours. Then, they are placed in a migration cell, where the catholyte solution is 10% $NaCl$ and the anolyte solution is 0.3 N $NaOH$ (figure 6.1). Electrical voltage (ranging from 10-60 V, depending on the concrete quality) is applied across the length of the specimen, effectively pushing the chloride ions towards the anode. Test duration is from 6 to 96 hours, again depending on the concrete quality, based on the current at $30V$.
This test is extensively used in research due to its relatively short duration. It is used to

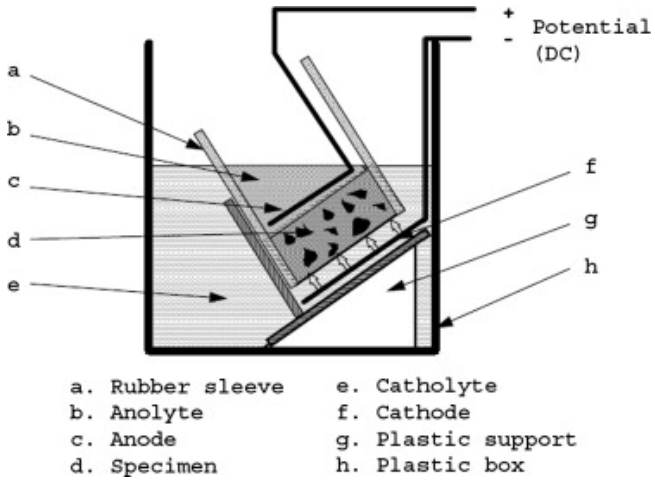

Figure 6.1: Rapid chloride migration test setup according to NT Build 492 [18]

test, for example, the effect of different binder types on chloride penetration resistance. More recently, however, it has been used to study the impact of cracking on chloride resistance of concrete [58, 65, 162, 200]. The model proposed herein aims to provide new insights on these experiments, by further explaining the mechanism behind this rapid test. The emphasis is on the influence of cracks on chloride transport. If fully understood, it will enable closer correlation of accelerated experiments with naturally occurring diffusion, which is actually the prevailing mechanism of chloride ingress in

real structures.

6.2.2. MODEL DESCRIPTION

This model can be considered as an extension of the chloride diffusion model presented in chapter 5. The spatial discretization procedure, and the mechanical part of the model are identical. The model for transport, in this case chloride migration, is different, as described further.

CHLORIDE MIGRATION MODEL

In the chloride migration model proposed herein, concrete is discretized as a set of one-dimensional "pipe" (conduit) elements, through which chloride transport takes place. An assembly of these elements in 3 spatial dimensions enables 3D modeling of chloride migration. The current model is based on the so-called single-species approach [196], hence ionic interactions are neglected.

The governing equation used to model chloride ion transport under the action of an electrical field is [198]:

$$\frac{\partial C}{\partial t} + D\alpha\frac{\partial C}{\partial x} - D\frac{\partial^2 C}{\partial x^2} = 0 \tag{6.1}$$

$$\alpha = \frac{zFE}{RT} \tag{6.2}$$

for the whole domain, Ω. Here, C is the chloride concentration (a scalar variable), D is the diffusion coefficient, x is the spatial coordinate, t the time, z the ion valence (-1 for Cl ions), F the Faraday constant (96485 $\frac{C}{mol}$), R the gas constant (8.314 $\frac{J}{Kmol}$), T the Kelvin temperature, and E constant electrical field along the specimen length ($\frac{V}{m}$). Therefore, α is considered to be constant, independent of time t and space x.

For a semi-infinite medium, the boundary condition is:

$$C = C_0, \text{ for } x = x_0 \text{ and } t > 0 \tag{6.3}$$

the initial condition is:

$$C = 0, \text{ for } x > 0, \text{ and } t = 0 \tag{6.4}$$

and the infinite point condition is:

$$C = 0, \text{ for } x \to \infty, \text{ and } t = t_M \tag{6.5}$$

where C_0 is the total chloride concentration at the exposed concrete ("upstream") surface, and t_M is a large finite number. The analytical solution of equation 6.1 is given as [198]:

$$C = \frac{C_0}{2}\left[e^{\alpha x} erfc\left(\frac{x+\alpha Dt}{2\sqrt{Dt}}\right) + erfc\left(\frac{x+\alpha Dt}{2\sqrt{Dt}}\right)\right] \tag{6.6}$$

where $erfc = (1 - erf)$ is the complementary error function.

If a Galerkin type approximation was used to discretize equation 6.1, the result would be marked with spurious spatial oscillations, if a critical value of the element Peclét number is exceeded [183]. Therefore, the *Charasteristic Galerkin (CG) scheme* is used here to deal

with spatial oscillations due to the discretization of the migration term in equation 6.1. Using the CG approach, equation 6.1 is discretized as (when no flux boundary conditions are applied)[1]:

$$[M]\frac{\Delta[C]}{\Delta t} = -[H][C]^n - [K_1][C]^n - [K_2][C]^n \tag{6.7}$$

Here, M is the mass matrix, H the convection matrix, K_1 the diffusion matrix, and K_2 the stabilization matrix. These element matrices are given as:

$$M = \frac{Al}{6\omega}\begin{bmatrix}2 & 1\\ 1 & 2\end{bmatrix} \tag{6.8}$$

$$H = \frac{D\alpha A}{2}\begin{bmatrix}-1 & 1\\ -1 & 1\end{bmatrix} \tag{6.9}$$

$$K_1 = \frac{DA}{l}\begin{bmatrix}1 & -1\\ -1 & 1\end{bmatrix} \tag{6.10}$$

$$K_2 = (D\alpha)^2\frac{\Delta t}{2}\frac{A}{l}\begin{bmatrix}1 & -1\\ -1 & 1\end{bmatrix} \tag{6.11}$$

Here, A is the uniform cross-sectional area, l the length, and D the diffusion coefficient of each element, and Δt is the time step. The cross sectional area of each element is assigned using the Voronoi scaling method [167], where the cross section of an element is equal to the area of a facet of the Voronoi cell which is common to its end nodes. All matrices are equivalent to those of regular one-dimensional linear elements [183], except the correction parameter ω in the mass matrix (equation 6.8), which was defined in chapter 5.

6.3. MODEL RESULTS

The proposed model is first compared to the analytical solution of equation 6.1. In this respect, some computational details are discussed. Further, the model is compared to experimental data from the literature, with emphasis on, firstly, the heterogeneous nature of concrete and, secondly, on cracking.

6.3.1. COMPUTATIONAL ASPECTS

If the standard Galerkin approach is used to discretize equation 6.1, the accuracy of the numerical solution is highly dependent on the element size used [183, 197]. Mathematically, this means that the Peclét number of the problem needs to be lower than one. The Peclét number for this type of problem is defined as [183]:

$$P_e = \frac{\alpha h}{2} \tag{6.12}$$

where h is the element size parallel to the direction of the applied electrical field. Clearly, this is controlled by parameter α, which depends on the temperature T and the applied electrical field E (equation 6.2). Evidently, the higher the applied voltage, the smaller the

[1] Full derivation is given in the end of the chapter

element size required for the simulation. As shown by Liu et al. [197], this can lead to very small element sizes, and hence an increased computational effort.
To test if this issue affects the proposed model, a benchmark problem is simulated. As input, concrete with a diffusion coefficient $D = 13 \times 10^{-12}\ m^2/s$ was subjected to a voltage of 50 V (i.e. electrostatic potential gradient of $E = 1000\ V/m$), with $T = 293\ K$. Specimen sides in contact with the catholyte and anolyte solution were subjected to constant chloride concentrations of $C = C_0 = 1$ and $C = 0$, respectively.
In table 6.1, some information is given about the meshes used. Figure 6.2 shows simulation results after 8 hours for different cell sizes, together with the analytical solution (equation 6.6).

Table 6.1: Meshes for different cell sizes

Cell size	Mesh size	Number of Nodes	Number of elements
1 mm	50 × 50 × 2 mm	5000	27491
0.5 mm	50 × 50 × 1 mm	20000	111165
0.25 mm	50 × 50 × 0.5 mm	80000	447562
0.1 mm	50 × 50 × 0.2 mm	500000	2809173

Note: Even though the meshes almost degenerate to two-dimensions due to computational demands, three-dimensional analyses are performed.

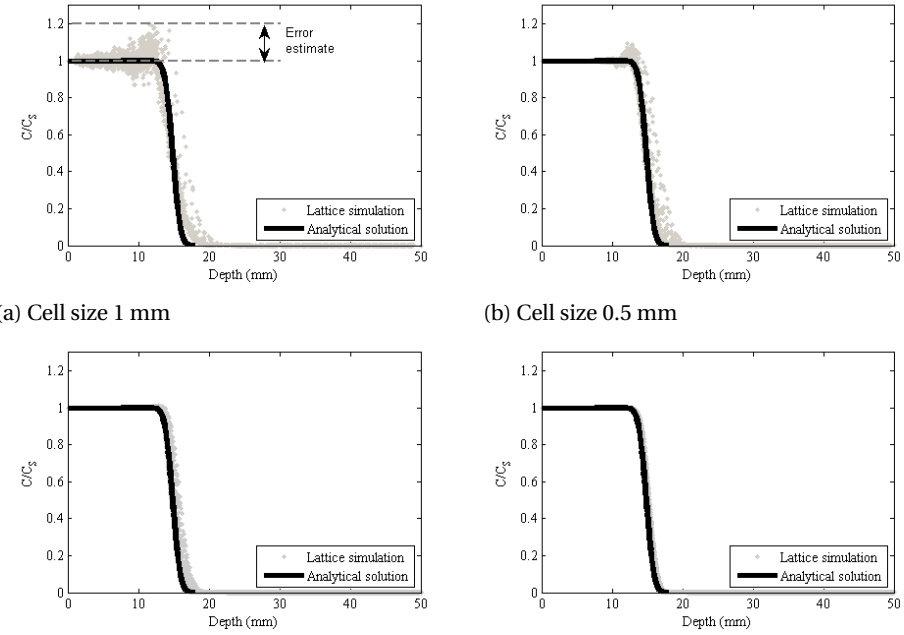

(a) Cell size 1 mm

(b) Cell size 0.5 mm

(c) Cell size 0.25 mm

(d) Cell size 0.1 mm

Figure 6.2: Simulated vs. analytical chloride profiles for different cell sizes

Clearly, the larger the cell size (i.e. element size), the higher the noise in the numerical solution. This is related to the Peclét number of the simulation (equation 6.12). When error is defined as a percentage difference between the largest numerically obtained and theoretical value of the chloride concentration (see figure 6.2a), and simulations are performed for a range of 5-60 V (and $T = 293\ K$), the result is shown in figure 6.3. In figure 6.4, a relationship between the applied voltage and the Peclét number for each mesh is shown. By examining figures 6.3 and 6.4, an appropriate mesh size for a certain simulation can be chosen. It can be seen that a Peclét number of about 4-5 can be handled by the model without loss of accuracy. This is a significant improvement compared to the standard Galerkin approach, where this number should be less than 1[197]. As a result, larger applied voltages can be simulated, or a smaller number of elements can be used, without loss of accuracy.

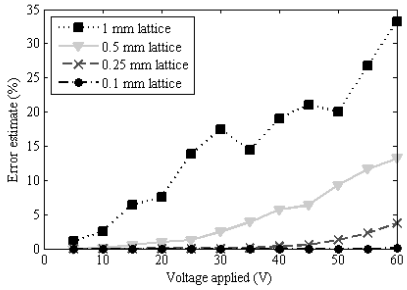

Figure 6.3: Error estimate vs. applied voltage for different cell sizes and $T = 293\ K$

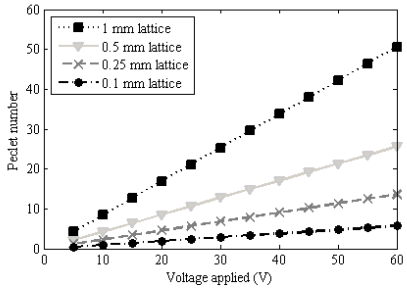

Figure 6.4: Peclét number vs. applied voltage for different cell sizes and $T = 293\ K$

Another important issue is the influence of factor ω in the mass matrix (equation 6.8). It is usually taken as 2 for two-dimensional [168, 170] and 3 for three-dimensional analysis [167] of diffusion dominated problems, without loss of accuracy. For migration dominated problems, it is important to use equation 5.17 to calculate ω, since otherwise the result will not be accurate, as shown in figure 6.5.

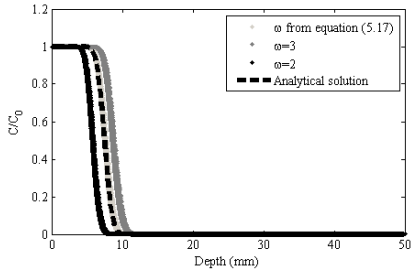

Figure 6.5: Influence of ω on the simulated chloride profile (cell size 0.125 mm, $D = 13 \times 10^{-12}\ m^2/s$, $E = -500\ V/m$, $T = 293\ K$, $t = 8$ h)

6.3.2. HETEROGENEOUS CONCRETE

In the current study, an attempt is made to try to understand the deviation of experimentally observed chloride profiles [201] from the theoretical profile, predicted by equation 6.6. Perhaps this can be, at least partly, explained by the heterogeneous nature of concrete.

On the meso-scale, concrete can be considered as a three-phase composite material, comprising coarse aggregate particles, mortar, and interface between the two. Each of these phases has different mechanical and transport properties. The Delft lattice model has been successfully used in modeling fracture processes of concrete on this scale [107]. Recently, this approach has also been used to simulate chloride diffusion in concrete by taking its heterogeneity into account (chapter 5). There, it was found that the diffusion coefficient of the interface is 2.5 - 7 times that of mortar.

Here, concrete with impermeable aggregate particles is considered. A material structure with about 35% of coarse (circular) aggregates (with diameters in the range of 2-8 mm) was generated using a simple packing algorithm. A lattice with cell size of 0.125mm ($50 \times 50 \times 0.25\ mm^3$ in total) was projected on top of it, and transport properties were assigned to each phase using the particle overlay procedure (Figure 5.3). These were as follows: mortar $D_M = 8.8 \times 10^{-12}\ m^2/s$; interface $D_I = 26.4 \times 10^{-12}\ m^2/s$ (3 times higher than the mortar); and aggregate $D_M = 8.8 \times 10^{-14}\ m^2/s$ (100 times lower than mortar, i.e. impermeable). The applied voltage was 30 V(i.e. $E = -600\ V/m$). Then, the chloride profile was averaged in the migration (z) direction, i.e. $Cl'(z) = \frac{1}{Ar} \int_{Ar} Cl(x,y)dz$, where Ar is the area of the exposed concrete surface (i.e. cross sectional area of the specimen). This emulates what typically happens in an experiment (if a chloride profile, and not only the penetration depth, is determined): consecutive layers of concrete are ground, collected, and analyzed, thereby giving an average chloride content at a certain depth; chloride content per weight of concrete is obtained as a result. For illustrative purpose, this averaged 1D profile was compared to the one obtained by using equation 6.6 for homogeneous material with $D = 8.8 \times 10^{-12}\ m^2/s$ (figure 6.6). This diluting effect of coarse aggregates on the chloride concentration may, at least in part, explain the difference between the theoretical and experimental chloride profile, which is sometimes attributed to mechanisms such as chloride binding [201]. Normalized chloride distributions are shown in figure 6.7.

Coarse aggregate particles, as modeled in here, present impermeable inclusions and therefore obstacles for chloride ingress. They need to be circumvented by chloride ions in order for ingress to take place. This is the reason why in mortar specimens chloride ingress results in a nearly-uniform front, while in concrete this is not the case (Figure 6.7). This process could be somewhat more pronounced in the model presented in this chapter, due to its two-dimensional aggregate distribution, compared to a fully three dimensional case. In their work, Nilenius et al. [202] found that effective diffusivity of a 3D model is about 1.4 that of a 2D model. Therefore, care should be taken when a homogenized diffusivity of concrete is sought after.

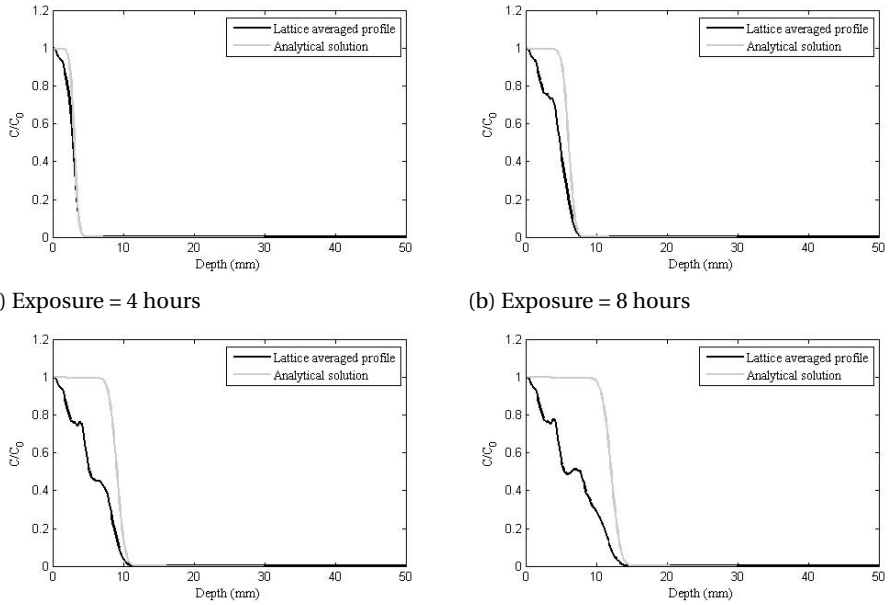

(a) Exposure = 4 hours

(b) Exposure = 8 hours

(c) Exposure = 12 hours

(d) Exposure = 16 hours

Figure 6.6: Analytical and averaged simulated (i.e. with impermeable aggregates taken into account) normalized chloride profiles at different exposure times

6.3.3. INFLUENCE OF CRACKING

Concrete cover is often cracked due to e.g. mechanical loading or shrinkage. Numerous experimental and modeling studies have been devoted to understanding the influence of these cracks on chloride penetration into concrete. In order to speed up the process, modifications of the Rapid Chloride Migration test are often used in these experiments. In the following, the implications of this are assessed. Three cases are studied: first, the case of compressive loading, where cracking can be taken into account in an averaged way (i.e. diffuse cracking); second, where a discrete artificial crack (a notch) is created; and third, where the mechanical simulation is performed first, followed by the chloride

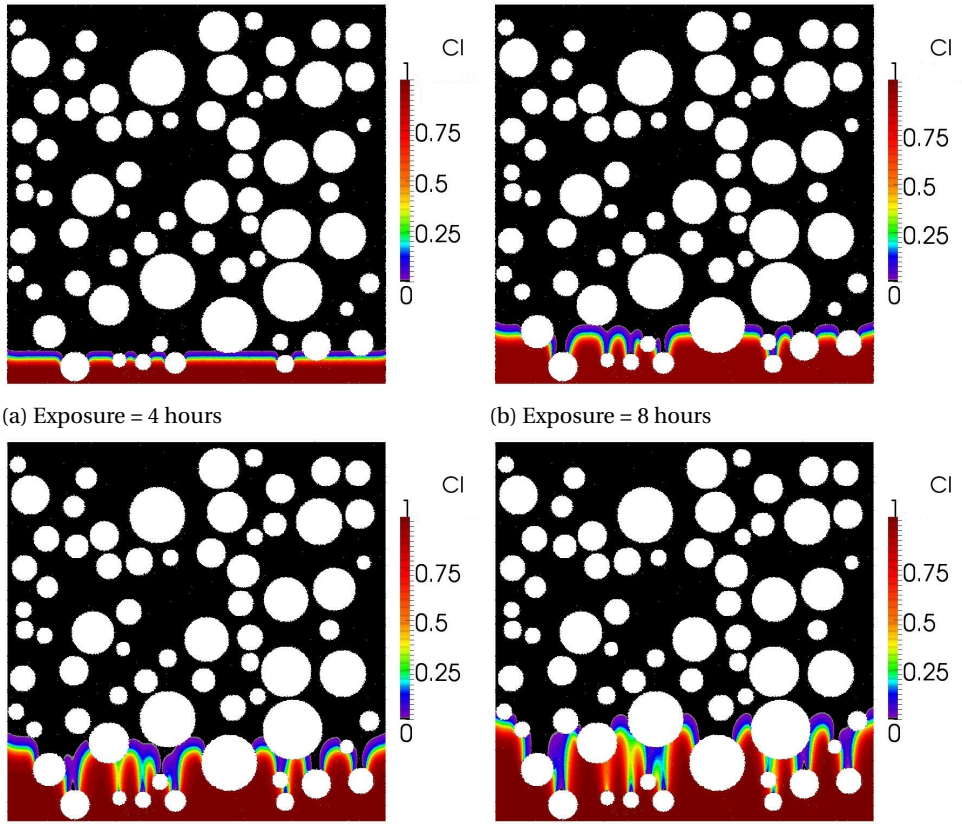

(a) Exposure = 4 hours

(b) Exposure = 8 hours

(c) Exposure = 12 hours

(d) Exposure = 16 hours

Figure 6.7: Simulated (normalized) chloride ion distributions at different exposure times (aggregate particles left out)

transport simulation.

DIFFUSE CRACKING

In case of diffuse cracking, it is reasonable to assume that the chloride diffusion coefficient increases uniformly in the whole domain, following a certain trend. This is confirmed by experiments, e.g. [162]. Following this assumption, an example is given.
In Rahman et al. [162], concrete samples were subjected to different levels of compressive stress (0-90% of their compressive strength, f_c). Following the mechanical damage, RCM tests were performed on the samples with 40 V for 24 h. Then, the diffusion coefficient (from the RCM test) of these damaged specimens was measured (Table 6.2). This was simulated using a homogeneous lattice with cell size of 0.125 mm ($50\times50\times0.25\ mm^3$ in total), and C_0 = 0.3% per weight of concrete. Experimental and simulation results for different loading levels are shown in figure 6.8.

Table 6.2: Correlation between compressive stress level and chloride diffusivity, from experiments of Rahman et al. [162]

Stress level (% f_c)	D_{eff} (10^{-12} m^2/s)
0	4
40	4.5
75	7.5
90	12

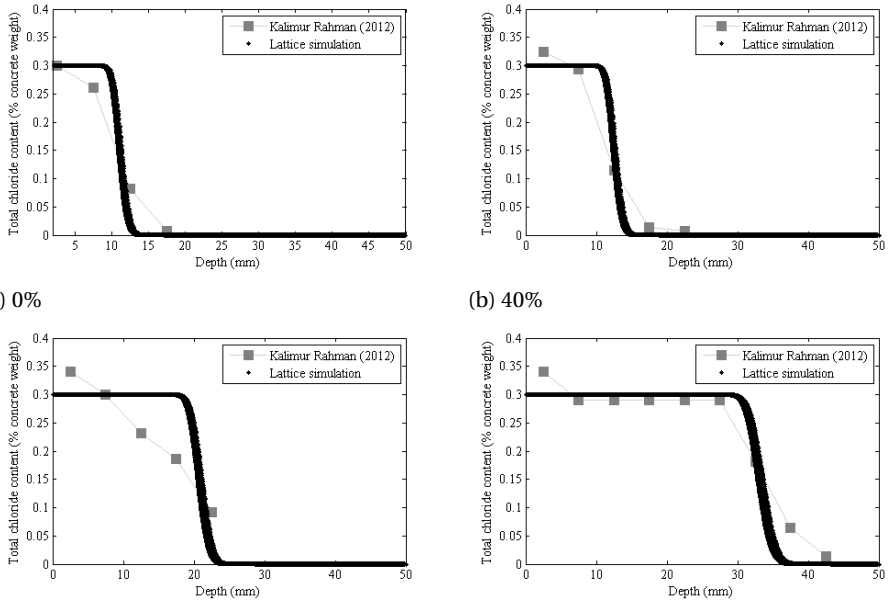

(a) 0% (b) 40%

(c) 75% (d) 90%

Figure 6.8: Experimentally observed vs. simulated chloride profiles for different compressive loading levels

As expected, the model can reproduce the experimentally observed behavior quite well. Clearly, for diffuse microcracking, this simplified approach is sufficient, given an appropriate relationship between the diffusion coefficient and applied stress is known (see table 6.2). This is not the case when discrete cracks are concerned [163].

ARTIFICIAL CRACKS

Artificial cracks (notches) are sometimes used as a simple and controllable method of simulating cracks in concrete [65, 66]. In these studies, notches were created by positioning of thin copper sheets and their removal 4 hours after casting. Notches of different thicknesses (0.2 mm, 0.3 mm, and 0.5 mm) and depths (5 mm, 10 mm, 15 mm, and 20 mm) were created. After hardening and curing, the specimens were subjected to Rapid

Chloride Migration according to NT BUILD 492 [18]. Chloride penetration depth was assessed by spraying the freshly split surface with $AgNO_3$ solution. The study, expectedly, showed that chloride ion penetration is higher at the notch tip than in the "uncracked" part of tested specimens, and that the influence of the notch depth was much more pronounced than the influence of its width.
Here, a specimen with a notch 0.3 mm wide and 20 mm deep is simulated using a homogeneous lattice with cell size of 0.125 mm ($50 \times 50 \times 0.25\ mm^3$ in total), and $C_0 = 2.2045 \times 10^{-5}\ g/mm^3$ for the exposed surface and in the notch [65], and with a voltage of $25V$. Based on the penetration depth in the sound part of the specimen tested for 10 hours, $D = 24.51 \times 10^{-12}\ m^2/s$ was selected. Simulation results for different exposure times are shown in figure 6.9.

In figure 6.9 it can be seen that the penetration front obtained by the simulation is sharp and narrow. As the exposure continues, it becomes somewhat wider. However, it is qualitatively quite different from the pure diffusion case (a simulation example is given in figure 6.10), where a smoother profile is obtained. This can clearly be attributed to the applied voltage: as it increases the mobility of ions only in the longitudinal direction, the result is a sharp penetration front in front of the notch. Clearly, the higher the applied voltage, the sharper the penetration front. This is a fundamental difference between the pure diffusion and migration experiments. As a consequence, relating experiments such as these to natural (diffusion) conditions is not straightforward. Also, modeling such experiments by using an "equivalent diffusion" concept is only an approximation of the process (e.g. [65, 200]).
In figure 6.11, chloride penetration corresponding to the concentration at which $AgNO_3$ solution changes colour (i.e. approximately $1.183 \times 10^{-5}\ g/mm^3$ [65]) is compared to experimental results of Marsavina et al [65]. As noted previously, the penetration front is very narrow in the beginning, and becomes somewhat wider during the test. This is underestimated by the model, since experimental results show a somewhat wider penetration front. One potential cause could be the wall effect, which might have caused a more porous zone close to the notch, which was not considered in the model. Also, it is possible that the crack introduces a change in the electrical field locally due to the high conductivity of the solution in the crack, resulting in somewhat higher penetration of chloride ions in the lateral direction than expected. Another cause could be the accuracy of the penetration depth measurement in the experiment, which could lead to some variations. Overall, a good agreement between the experimental and simulated values is observed.

COUPLED ANALYSIS

The last study concerns a coupled analysis. First, the mechanical analysis is performed, followed by the chloride transport analysis. Several studies have focused on studying chloride migration in cracked specimens [58, 200]. In these studies, cracks were created using a splitting procedure. After unloading, the specimens were subjected to RCM testing according to NT BUILD 492 [18]. Yoon et al. [58] found that, if cracks are wider than 12 μm, the chloride penetration is faster than in sound concrete. On the basis of this statement, the following analyses are performed.

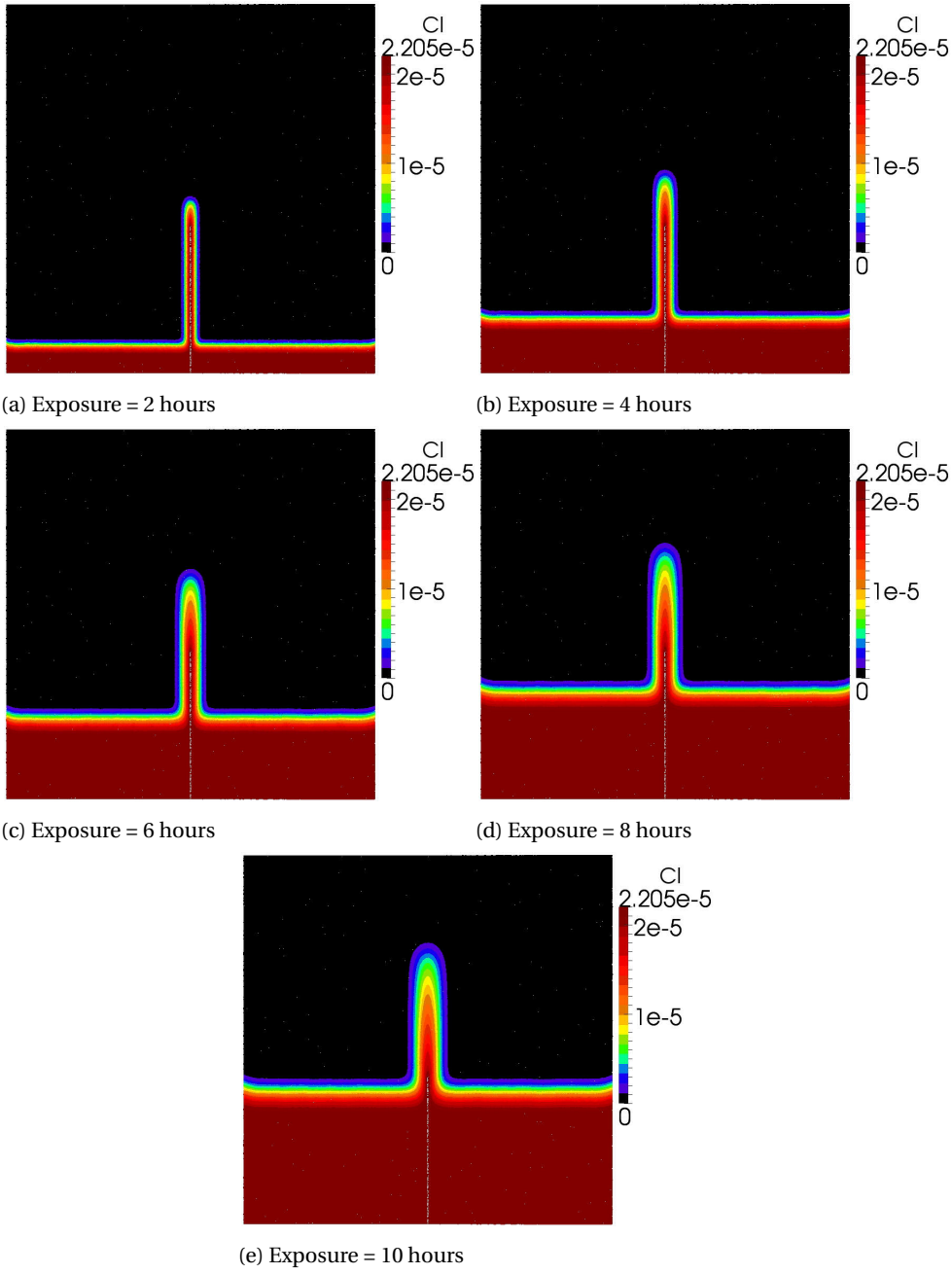

(a) Exposure = 2 hours

(b) Exposure = 4 hours

(c) Exposure = 6 hours

(d) Exposure = 8 hours

(e) Exposure = 10 hours

Figure 6.9: Simulated chloride ion distributions (in g/mm^3) for notch width of 0.3 mm and depth of 20 mm [65]

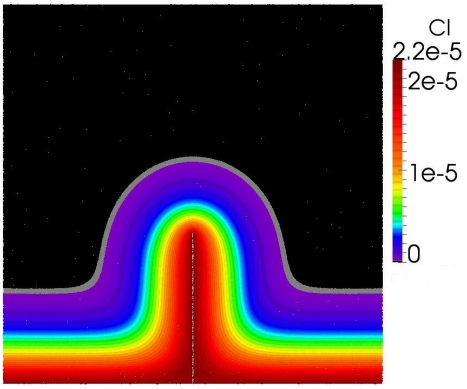

Figure 6.10: A typical chloride profile from a diffusion simulation

A material structure with about 60% of circular aggregates (with diameters in the range of 0.5-8 mm) was generated using a simple packing algorithm. A lattice with cell size of 0.125mm ($50 \times 50 \times 0.25$ mm^3 in total) was projected on top of it, and mechanical and transport properties were assigned to each phase using the particle overlay procedure. These were as follows: mortar $D_M = 8.8 \times 10^{-12}$ m^2/s, $f_t = 3.6$ MPa, $E = 30$ GPa; interface $D_I = 26.4 \times 10^{-12}$ m^2/s, $f_t = 1.8$ MPa, $E = 15$ GPa; and aggregate $D_M = 8.8 \times 10^{-14}$ m^2/s, $f_t = 8$ MPa, $E = 70$ GPa. Cracking is induced by exposing the bottom surface of the numerical specimen to splitting: the left half is subjected to displacement to the left, and the right half to displacement to the right (see figure 6.12). A crack forms, therefore, in the middle of the bottom surface.

The cracked specimen is then subjected to an RCM test with 25 V applied voltage for 6 hours. Applied surface chloride concentration was $C_0 = 2.2045$ kg/m^3 for the exposed surface and cracks wider than 12 μm, which were found to increase chloride ingress in cracks during accelerated experiments by Yoon et al. [58]. Analyses results are shown in figure 6.13.

It is clear that the presence of a crack significantly influences the chloride penetration. A sharp penetration is observed in front of the crack. Similar findings were reported in the literature [58, 200]. Also, chloride penetration in this case seems to be more influenced by the crack depth than its width (see figure 6.13d and 6.13f), which was clearly observed in simplified experiments where notches were used [65]. The findings are qualitatively in good accordance with experimental data[58, 200]. The relative influence of cracking on the penetration depth is dependent on the applied voltage and test duration, amongst other things. Therefore, care has to be taken when interpreting such experimental findings, before clear correlations with natural conditions are claimed.

6.4. CONCLUSIONS

RESISTANCE to chloride ingress is one of the most important durability parameters used in engineering practice. Currently, rapid chloride migration (RCM) test accord-

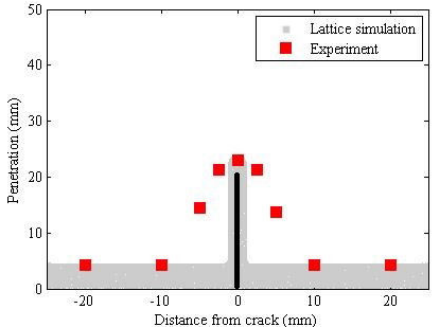

(a) Exposure = 2 hours

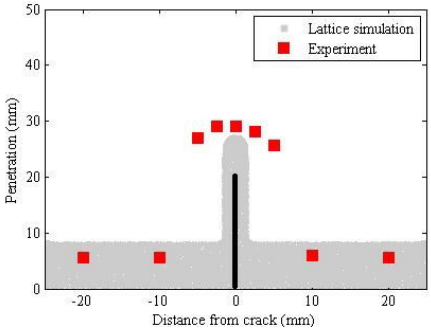

(b) Exposure = 4 hours

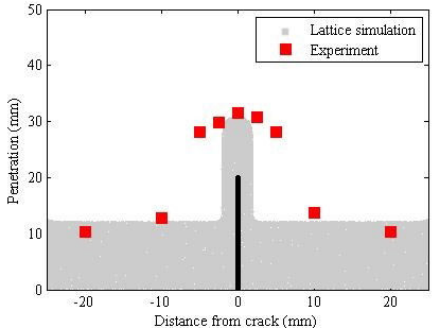

(c) Exposure = 6 hours

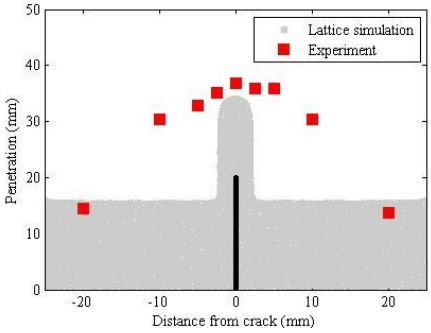

(d) Exposure = 8 hours

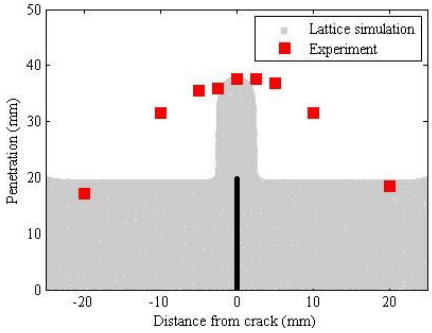

(e) Exposure = 10 hours

Figure 6.11: Simulated vs. experimental chloride profiles for notch width of 0.3 mm and depth of 20 mm [65]

ing to NT BUILD 492 [18] is frequently used in Europe for mix design of concrete mixtures. A single-species model for simulating chloride transport in concrete when subjected to an external electric field is presented herein. Using the characteristic Galerkin approach and the lattice modeling framework, modeling of chloride migration in (theoretically) 3 dimensions was made possible. Influence of concrete material heterogeneity

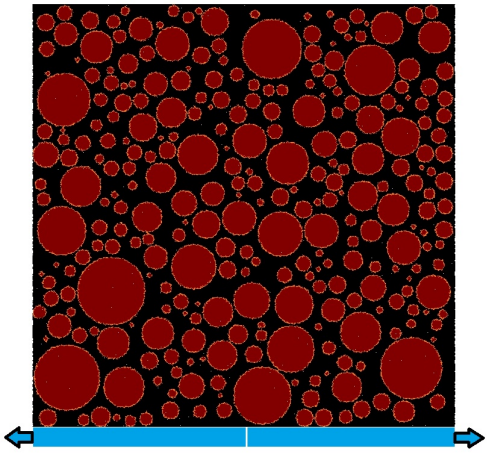

Figure 6.12: Heterogeneous lattice and loading conditions (black-mortar; dark brown-aggregate; light brown-interface).

and cracking is considered. Some computational issues are first addressed. The model is then verified with theoretical and experimental data. Since rapid chloride migration is frequently used, the developed model is used in simulating experiments and trying to (at least in part) explain some observations. From the presented work, the following conclusions can be drawn:

1. The model can successfully reproduce the analytical solution of the governing equation. However, care has to be taken when element Peclét numbers are concerned. While the standard Galerkin discretization requires that the Peclét number remains less than 1 [197], with the presented model it should be less than about 4, resulting in less computational effort.

2. The heterogeneous nature of concrete causes deviations from the theoretical migration profile by taking into account the tortuosity of concrete, in particular the effect of large impermeable aggregates. This is also observed in experiments.

3. The influence of distributed (diffuse) cracking can be simulated in a simple way by increasing the diffusion coefficient of the domain depending on the stress level. This is in good accordance with experimental observations.

4. Discrete notches or cracks cause a sharp increase in penetration in front of the defect, as shown by experimental data from the literature. How sharp this increase is, depends mainly on the applied voltage. The model can reproduce this behavior.

It has to be noted once again that a single-species model was used. Hence, the influence of ionic interactions on transport of chloride (and other ions present in the pore solution) is neglected. The model verification by experiments was thus relatively simple. Future work will focus on extending the lattice modeling framework to include

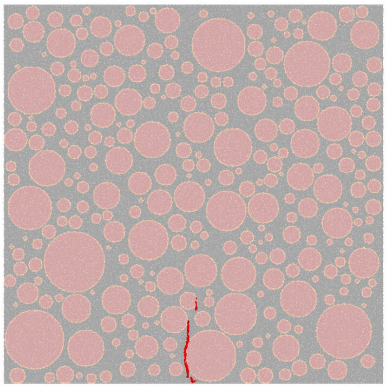

(a) $w = 32.8\ \mu m$

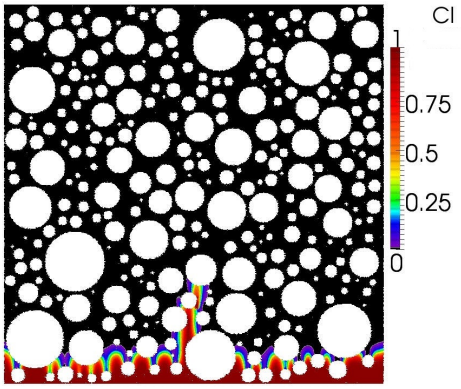

(b) Normalized Cl concentration

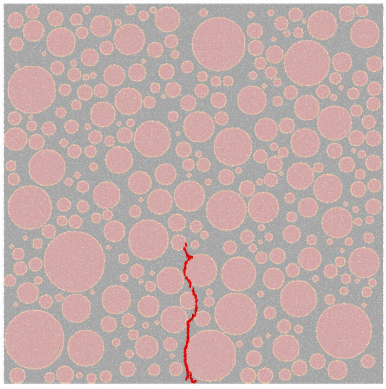

(c) $w = 61.6\ \mu m$

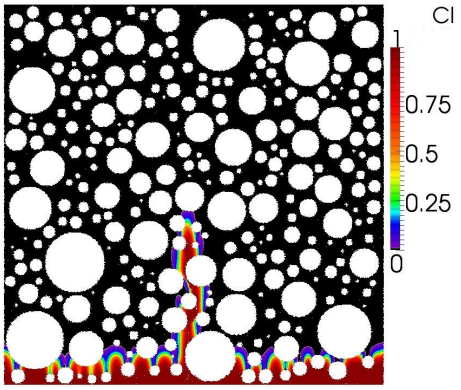

(d) Normalized Cl concentration

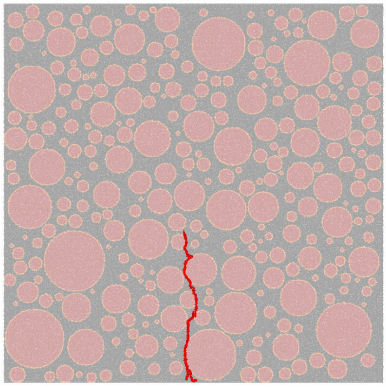

(e) $w = 84.6\ \mu m$

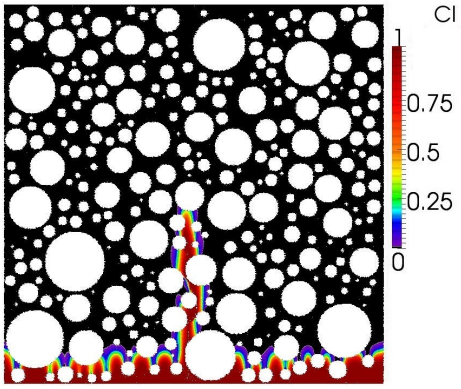

(f) Normalized Cl concentration

Figure 6.13: Simulated (normalized) chloride ion distribution for different crack widths (only cracks wider than 12 μm are depicted on the left hand side)

multi-phase modeling of ionic transport under an applied electrical field.

DERIVATION[2]:

Characteristic Galerkin (CG) approach is used to deal with spatial oscillations due to discretization of the convection-diffusion transport terms [183]. The governing diffusion-migration equation is equation 6.1 [198].

A characteristic of the flow (figure 6.14) in the time-space domain is observed. The

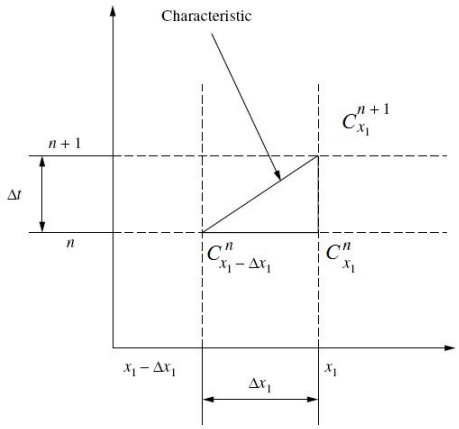

Figure 6.14: Characteristic in a space-time domain [183]

incremental time period covered by the flow is Δt from the n-th time level to the (n+1)-th time level and the incremental distance covered during this time period is Δx, from $x-\Delta x$ to x. If a moving coordinate is assumed along the path of the characteristic wave with a speed of $D\alpha$, the convection term of equation 6.1 disappears. This approach does eliminate the convection term responsible for spatial oscillation when discretized in space, but it indtroduces the complication of a moving coordinate system is, i.e. equation 6.1 assumes the following form:

$$\frac{\partial C}{\partial x}(x',t) - D\frac{\partial^2 C}{\partial x'^2} = 0 \tag{6.13}$$

In the semi-discrete form, equation 6.13 becomes:

$$\frac{C^{n+1}|_x - C^n|_{x-\Delta x}}{\Delta t} - \frac{\partial}{\partial x'}\left(D\frac{\partial C}{\partial x'}\right)^n|_{x-\delta x} = 0 \tag{6.14}$$

Here the diffusion term is treated explicitly (i.e. explicit time stepping scheme). It is possible to solve the above equation by using moving coordinates. However, it can be avoided by a single spatial Taylor series expansion in space. A Taylor series expansion is given as (figure 6.14):

[2]The derivation is largely based on Lewis et al. [183], chapter 7.4.1

$$C^n|_{x-\Delta x} = C^n|_x - \frac{\partial C^n}{\partial x}\frac{\Delta X}{1!} + \frac{\partial^2 C}{\partial x^2}\frac{\Delta x^2}{2!} + \dots \tag{6.15}$$

Similarly, the diffusion term is given as:

$$\frac{\partial}{\partial x'}\left(D\frac{\partial C}{\partial x'}\right)^n|_{x-\delta x} = \frac{\partial}{\partial x'}\left(D\frac{\partial C}{\partial x'}\right)^n|_x - \frac{\partial}{\partial x}\left[\frac{\partial}{\partial x}\left(D\frac{\partial C}{\partial x'}\right)^n\right]\Delta x \tag{6.16}$$

On substituting equations 6.15 and 6.16 into equation 6.14, the following results (higher order terms being neglected):

$$\frac{C^{n+1}-C^n}{\Delta t} = -\frac{\Delta x}{\Delta t}\frac{\partial C^n}{\partial x} + \frac{\Delta X^2}{2\Delta t}\frac{\partial^2 C^n}{\partial x^2} + \frac{\partial}{\partial x}\left(D\frac{\partial C}{\partial x}\right)^n \tag{6.17}$$

Now, all terms are evaluated at the position x and not at two positions as in equation 6.14. If the "flow" velocity is $D\alpha$, then it holds that $\Delta x = D\alpha\Delta t$. By inserting this into equation 6.17, the semi-discrete form arises:

$$\frac{C^{n+1}-C^n}{\Delta t} = -D\alpha\frac{\partial C^n}{\partial x} + (D\alpha)^2\frac{\Delta t}{2}\frac{\partial^2 C^n}{\partial x^2} + \frac{\partial}{\partial x}\left(D\frac{\partial C}{\partial x}\right)^n \tag{6.18}$$

By carrying out the Taylor series expansion, the convection term reappears in the equation along with an additional second order term, which acts as a smoothing operator that reduces the oscillations resulting from the spatial discretization of convection terms. This equation can now be discretized in space.

A one-dimensional linear element is used for the spatial discretization of C:

$$C = N_i C_i + N_j C_j \tag{6.19}$$

where $[N]$ are the shape functions and subscripts i and j indicate element nodes. If Galerkin weighing is used, the following results:

$$\int_\Omega [N]^T \frac{C^{n+1}-C^n}{\Delta t}\,d\Omega + \int_\Omega [N]^T\left(D\alpha\frac{\partial C}{\partial x}\right)^n d\Omega - \frac{\Delta t}{2}\int_\Omega [N]^T\left((D\alpha)^2\frac{\partial^2 C}{\partial x^2}\right)^n d\Omega - \int_\Omega [N]^T\frac{\partial}{\partial x}\left(D\frac{\partial C}{\partial x}\right)d\Omega = 0 \tag{6.20}$$

For a domain with a single element, it holds:

$$[N]^T = \begin{pmatrix} N_i \\ N_j \end{pmatrix} \tag{6.21}$$

If equation 6.21 is substituted into equation 6.20, we get:

$$\int_{\Omega} [N]^T [N] \frac{[C^{n+1} - C^n]}{\Delta t} d\Omega = -D\alpha \int_{\Omega} [N]^T \frac{\partial}{\partial x} ([N][C])^n d\Omega$$
$$+ \frac{\Delta t}{2} (D\alpha)^2 \int_{\Omega} [N]^T \frac{\partial^2}{\partial x^2} ([N][C])^n d\Omega + \int_{\Omega} [N]^T \frac{\partial^2}{\partial x^2} ([N][C])^n d\Omega \tag{6.22}$$

Applying integration by parts to second-order terms of equation 6.22 gives:

$$\int_{\Omega} [N]^T [N] \frac{[C^{n+1} - C^n]}{\Delta t} d\Omega = -D\alpha \int_{\Omega} [N]^T \frac{\partial}{\partial x} ([N][C])^n d\Omega -$$
$$\frac{\Delta t}{2} (D\alpha)^2 \int_{\Omega} \frac{\partial [N]^T}{\partial x} \frac{\partial [N]}{\partial x} [C] d\Omega + \frac{\Delta t}{2} (D\alpha)^2 \int_{\Gamma} [N]^T \frac{\partial [N]}{\partial x} [C] n_1 d\Gamma -$$
$$\int_{\Omega} \frac{\partial [N]^T}{\partial x} D \frac{\partial [N]}{\partial x} [C] d\Omega + \int_{\Gamma} [N] D \frac{\partial [N]}{\partial x} [C] n_1 d\Gamma \tag{6.23}$$

6

For a single element, the term on the left hand side of equation 6.23 is (note that, for a one-dimensional element of a constant cross-section, it holds that $d\Omega = A dx$, where A is the element cross-sectional area):

$$\int_{\Omega} [N]^T [N] \frac{[C^{n+1} - C^n]}{\Delta t} d\Omega = [M_e] \frac{\Delta [C]}{\Delta t} \tag{6.24}$$

$$D\alpha \int_{\Omega} [N]^T \frac{\partial}{\partial x} ([N][C])^n d\Omega = [H_e] [C]^n \tag{6.25}$$

$$\int_{\Omega} \frac{\partial [N]^T}{\delta x} D \frac{\partial [N]}{\partial x} d\Omega [C]^n = [K_{1e}] [C]^n \tag{6.26}$$

$$(D\alpha)^2 \frac{\Delta t}{2} \int_{\Omega} \frac{\partial [N]^T}{\delta x} D \frac{\partial [N]}{\partial x} d\Omega [C]^n = [K_{2e}] [C]^n \tag{6.27}$$

Here, $[M_e]$ is the element mass matrix, $[H_e]$ the element convection matrix, $[K_{1e}]$ the element diffusion matrix, and $[K_{2e}]$ the element stabilization matrix.
The boundary terms are given as:

$$\int_{\Gamma} [N]^T D \frac{\partial [N]}{\partial x} [C]^n d\Gamma = \left[f_{1e}\right] \tag{6.28}$$

$$(D\alpha)^2 \frac{\Delta t}{2} \int_{\Gamma} [N]^T \frac{\partial [N]}{\partial x} [C] d\Gamma = \left[f_{2e}\right] \tag{6.29}$$

Here, f_{1e} is the element forcing vector due to the diffusion term, and f_{2e} the element forcing vector due to the stabilization term.
The system matrices are assembled using the usual FE procedure. One has only to note that term E in equation 6.2 is electrical field along the *specimen length*. This means that, in each element matrix, $E = E_G \times cos\theta$, where E_G is the global electrical field, and θ the angle between the longitudinal axis (catholyte-anolyte) of the specimen and the lattice element.
Once global matrices are assembled, the discretized equation becomes:

$$[M]\frac{\Delta[C]}{\Delta t} = -[H][C]^n - [K_1][C]^n - [K_2][C]^n + \left[f_1\right]^n + \left[f_2\right]^n \tag{6.30}$$

After applying appropriate initial and boundary conditions, equation 6.30 is then solved for each time step.

7

MODELING OF CONCRETE COVER CRACKING DUE TO REINFORCEMENT CORROSION

Experience without theory is blind,
but theory without experience is mere intellectual play.

Immanuel Kant

Corrosion of steel reinforcement is a serious problem for durability and serviceability of reinforced concrete. As the reinforcing steel corrodes, it expands and exerts pressure on the surrounding concrete cover, causing tensile stresses in concrete. This leads to cracking and spalling of the concrete cover, further worsening the durability problems of a structure and increasing the rate of its deterioration. In order to study cracking mechanisms due to reinforcement corrosion, mechanics of the problem was implemented in a two-dimensional lattice model. The heterogeneous nature of concrete was taken into account in the mechanical analysis. Firstly, the case of uniform corrosion was tested, and successfully verified using experimental data from the literature. Also, it was found that cracking pressure is not a deterministic value, and depends on local mechanical parameters. Secondly, two pitting scenarios were tested and compared to the uniform corrosion case. Pitting results in significant reduction of cracking pressure, compared to the uniform corrosion case. Based on the proposed model, some conclusions with implications for engineering practice were drawn.

Parts of this chapter have been published in Construction and Building Materials **44**, (2013) [137]

7.1. INTRODUCTION

STEEL in reinforced concrete is protected from active corrosion by a passive layer, which forms on its surface when it is placed in the highly alkaline fresh concrete. This protective layer can break down, either due to carbonation or chloride ion penetration [5]. This marks the end of the initiation and the beginning of the propagation phase of reinforcement corrosion [2]. Although most of the accepted service life models set the end of the service life of a structure at this point [32], no significant damage actually occurs at this point. Only when the reinforcing steel actively corrodes, does the damage occur. As rust occupies a larger volume than its parent steel, internal pressure is exerted on the concrete cover. Since the tensile strength of concrete is relatively low, at a certain point in time cracking of the cover can follow. Cracking of the concrete cover due to reinforcement corrosion is usually the first visible sign of ongoing deterioration. It also serves as a catalyst of the whole corrosion process: cracks speed up the further penetration of chloride ions, moisture, and carbonation, thus expediting the deterioration.
Corrosion of reinforcing steel is a serious problem with many consequences, besides cover cracking:

1 It diminishes the effective reinforcing steel area, lowering the load bearing capacity of the composite section and increasing deflections [203]

2 it affects the steel-concrete bond properties [114, 148, 204, 205], and can change the failure mode from shear to bond failure [203]

3 It causes a change in ductility of the steel itself, leading to its more brittle behaviour [206]

Even though these are very serious structural issues, visible cover cracking is usually a warning that deterioration is taking place. It is, sometimes, reasonable to set the end of the service life of a structure at this point, because cracking can be observed with visual inspection. At the end of the initiation phase there is no visible damage yet and (mostly destructive) tests are needed to observe the change in properties. This makes the study of cracking behavior due to reinforcement corrosion a necessity.
Numerous experimental studies have been devoted to cracking of the concrete cover due to reinforcement corrosion. To speed up the corrosion process, impressed current is often used [9, 10, 207, 208] (see also chapter 4). This leads to general corrosion of reinforcing steel bars, where the whole surface of the bar corrodes uniformly. When using this method, controlling the corrosion rate is simple. Corrosion is sometimes accelerated by mixing the Cl- rich solution with water during casting of the samples [135]. While in the beginning some pits do occur, general corrosion is dominant at later stages. Due to time constraints, concrete cracking due to natural chloride induced corrosion is rarely studied [139]. External chloride penetration leads to pitting corrosion, which creates non-uniform pressure around the bar. This could potentially lead to faster cover cracking than uniform corrosion, and is one of the topics of this research.
A number of modeling efforts have also been devoted to studying the phenomenon. These can be roughly divided into two distinct categories: analytical or numerical models based on the thick-walled cylinder theory; and numerical models based on finite elements or similar methods. Analytical and numerical models based on the thick-walled

cylinder theory, with different levels of sophistication, have been used by a number of authors (e.g. [133, 141, 209, 210]). Despite their widespread use, these models have one major drawback: the effect of only one corroding steel bar on cracking can be studied. This is overcome by using numerical models: since the model of Molina et al. [134], more and more sophisticated models have been introduced (e.g. [136, 148, 207, 208, 211, 212]). All of these models have been based on the assumption that concrete is a homogeneous medium, i.e. that its mechanical or transport properties are the same in the entire analysed domain. A step further in that respect was taken by Pan and Lu [213], who included the effect of heterogeneous concrete material structure in their analyses. This should lead to improved understanding of the cracking process due to expansion of corrosion products formed on the rebar in reinforced concrete, and is another important aspect of the presented work.
The present work addresses two important aspects regarding concrete cover cracking caused by corrosion of the reinforcing steel through numerical modelling. Firstly, the effects of heterogeneity of concrete (i.e. presence of coarse aggregate, mortar, and interface in the concrete matrix) are assessed and their relative importance highlighted. Secondly, the impact of pitting corrosion on the cover cracking is investigated and compared to the uniform corrosion case. These goals are achieved by using a meso-scale micromechanical model. This study, therefore, aims to provide knowledge and understanding of the corrosion induced cover cracking process that extends beyond the current state of the art.

7.2. METHODS

7.2.1. CORROSION PRODUCTS

Depending on the level of oxidation, corrosion products of carbon steel may occupy up to six times more volume than the original steel. Different oxides that can form during the corrosion process have the following relative volume ratios, (compared to pure iron, Fe) [8, 210]: FeO=1.7 (wustite); Fe_3O_4=2.0 (magnetite); Fe_2O_3=2.1 (maghemite); $\beta - FeO(OH)$=3.5 (akaganéite); $Fe(OH)_2$=3.6 (ferrous hydroxide); $Fe(OH)_3$=4.0 (ferric hydroxide); and $Fe(OH)_3 3H_2O$=6.15. Up to date, the most expansive corrosion product detected in statically loaded and cracked reinforced concrete specimens subjected to chloride induced corrosion is akaganéite, which has a relative volume ratio of about 3.5 compared to pure iron [81]. In dynamically loaded and cracked specimens, the most expansive corrosion product found was ferric hydroxide, having a relative volume ratio of about 4 compared to pure iron [8]. Bearing in mind that the molar mass of Fe is 55.85 g, O_2 is 32 g, and H_2 is 2 g, it can be shown that the ratio r_m of molecular weight of iron to that of corrosion products for typical rust products is 0.523 (for ferric hydroxide, $Fe(OH)_3$) and 0.622 (for ferrous hydroxide, $Fe(OH)_2$). This range of r_m values has been commonly used in models [133, 135, 209, 210]. Depending on the fraction of each individual aforementioned oxide in the corrosion products, the actual volume increase due to corrosion reaction will differ. The composition of rust depends on many factors, most influential being moisture and oxygen supply, and chloride concentration. Although great experimental progress has been achieved in recent years using advanced analyt-

ical techniques, such as Raman spectroscopy and energy-dispersive X-ray microanalysis (EDX) [8, 81, 139], it is still not possible to conceivably assume the rust composition. For mechanical modelling purposes, it is common to assume that the density of rust is a fixed fraction of the iron density, i.e. $\beta = \frac{\rho_s}{\rho_r}$ lies in the range between 2 and 4 [133–135, 207, 209]. Values outside of this range are seldom used (e.g. Balafas and Burgoyne [141] used a value of 1.907). A value in this range is also assumed in this study.

7.2.2. RUST PRODUCTION

Different models exits in the literature for rust production prediction. A linear relation between the corrosion current density i_{corr} and the rebar diameter decrease, based on Faraday's law, was proposed by Andrade et al.[9]:

$$D_{rb} = D_b - 0.023 i_{corr} \Delta t \, [mm] \tag{7.1}$$

where D_{rb}(mm) is the reduced rebar diameter, D_b(mm) the initial rebar diameter, i_{corr} corrosion current intensity ($\frac{\mu A}{cm^2}$), 0.023 a conversion factor (from $\frac{\mu A}{cm^2}$ to mm per year), and Δt the time since the beginning of the propagation period (years). Now, the corresponding volume of steel consumed per unit length of anodic steel is [210]:

$$\Delta V_s = \frac{0.023}{2} \pi D_b i_{corr} \Delta t \, [mm^3/mm] \tag{7.2}$$

Some authors have suggested that the rate of rust production decreases in time (e.g. Liu and Weyers [135]). According to them, as the rust layer thickens, the iron ionic diffusion distance increases, and the rate of rust production decreases because diffusion is inversely proportional to the oxide layer thickness. Others (e.g. Balafas and Burgoyne [141]) used a combined rule: they assumed that the rate of rust production in the beginning of the corrosion process is linear (i.e. follows Faraday's law), while at later stages, as the oxide thickness increases, this rate decreases, considering the approach of Liu and Weyers [135].

For impressed current experiments, which are usually short in duration, linear rust production is usually assumed. Since results of such experiments are used herein for model validation, linear rust production (with respect to exposure time) was assumed in present work.

7.2.3. EXPANSION

If a uniform corrosion process is assumed, the rebar radius is reduced due to corrosion from R_b to R_{rb} (see equation 7.1). This reduction can be calculated based on the known volume of steel consumed per unit length of anodic steel ΔV_s (equation 7.2) [141, 210]:

$$R_{rb} = \sqrt{\left({R_b}^2 - \Delta V_s/\pi\right)} \, [mm] \tag{7.3}$$

The total radius of the rebar, including the rust layer, can be calculated now as:

$$R_r = R_{rb} + t_r \, [mm] \tag{7.4}$$

where t_r is the thickness of the oxide layer that builds up around the bar. Since the total volume of oxide generated is $\Delta V_r = \Delta V_s \rho_s / (\rho_r r_m)$, then t_r can be calculated as [141, 210]:

$$t_r = \sqrt{{R_{rb}}^2 + \frac{\Delta V_s}{\pi}} - R_{rb}\,[mm] \tag{7.5}$$

This is the free expansion of rust, i.e. the expansion if no confinement by concrete is provided. Also, it is long known that part of the rust products fills up the pores in the surrounding concrete, while the remainder exerts expansive pressure [135]. This was recently experimentally confirmed by Wong et al. [139], and lately observed in a X-ray attenuation study by Michel et al.[138] [1]. The thickness of this layer depends mainly on the porosity of concrete and compaction degree, and is assumed to be in the range of 10-100μm [135]. In the present work, it is taken into account by modifying equation 7.5 to take into account the thickness of this porous layer t_f [141]:

$$t_r = \sqrt{{R_{rb}}^2 + \frac{\Delta V_r}{\pi}} - R_{rb} - t_f\,[mm] \tag{7.6}$$

It is, therefore, assumed that no pressure is exerted on the surrounding concrete, until the porous layer around the reinforcement has been filled up by corrosion products. Although some relations have been proposed for calculating the thickness of this porous layer, in the present model its thickness is assumed in the range between 10-100μm, and the effects of different values are examined.

In some investigations it has also been detected that oxides resulting from corrosion of reinforcement are transported into open cracks, and thus relieve a part of expansion pressure [8, 139]. This has also been introduced in some recent models: Ožbolt et al.[136] modeled the transport of corrosion products into cracks and pores of concrete as a convective diffusion problem, where the "diffusion" coefficient of rust through concrete is dependent on the moisture content; Tran et al.[208] have taken it into account as a "pressure relief" buffer, i.e. open cracks are first filled up with oxides, and only then can further pressure on concrete be exerted. Although the approach proposed by Ožbolt et al.[136] is more sophisticated, some parameters in their model (e.g. the diffusion coefficient of rust) still cannot be experimentally quantified. Consequently, the approach of Tran et al.[208] is also adopted in the presented model. The penetration of corrosion products into open cracks is taken into account by subtracting the accessible crack volume (i.e. the volume open for penetration of corrosion products -V_{ac}) from the total volume of the generated oxide (ΔV_r):

$$\Delta V^* = \Delta V_r - V_{ac}\,[mm^3/mm] \tag{7.7}$$

Here, ΔV^* is the amount of corrosion product which does exert pressure. Therefore, equation 7.6 is modified, and has the form:

$$t_r = \sqrt{{R_{rb}}^2 + \frac{\Delta V^*}{\pi}} - R_{rb} - t_f\,[mm] \tag{7.8}$$

[1] Note that the existence of this layer was not observed in experiments shown in chapter 4, probably due to the high corrosion current density applied.

To summarize: two mechanisms are responsible for delaying the (further) cracking of the concrete cover in the model (Figure 7.1): firstly, the existence of the porous layer around the reinforcement, which is available for deposition of oxides; and secondly, penetration of corrosion products into open cracks, which creates additional open space for oxide deposition. Both of these mechanisms are taken into account using equation 7.8. Their influence on the cracking process is further discussed.

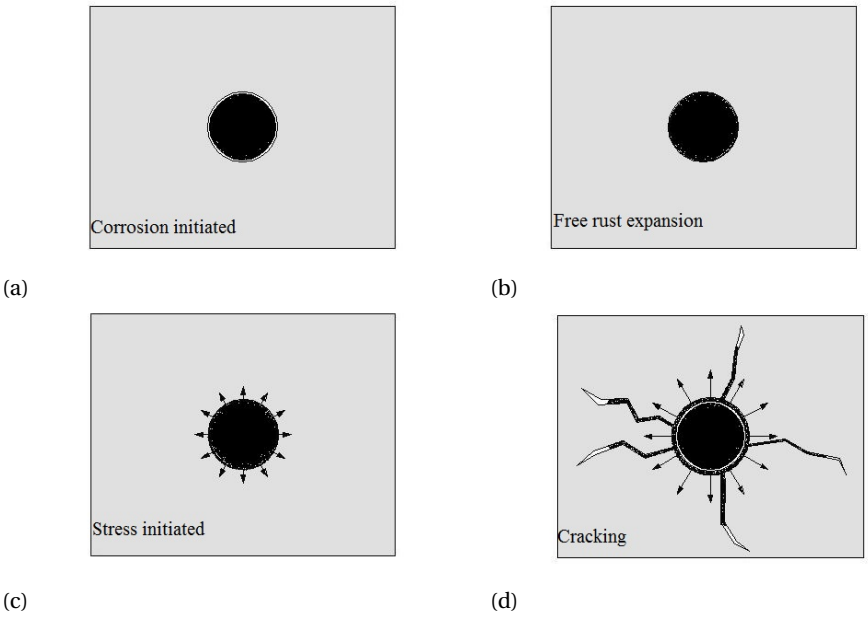

Figure 7.1: (a-d) Illustration of the corrosion process (modified from [14])

7.2.4. PRESSURE

In the presented model, expansion of the corroding reinforcement is simulated by equivalent pressure around the reinforcing steel. The free rust expansion (equation 7.8) is constrained by the surrounding concrete medium. In order to calculate the stresses induced by this confinement, the combined corrosion product and non-corroded steel are modelled as a growing composite [207].
First, non-dimensional effective mass loss can be calculated as [207]:

$$\gamma = \frac{\frac{(D_b+2t_r)^2}{D_b{}^2} - 1}{\beta - 1} \tag{7.9}$$

where $\beta = \frac{\rho_s}{\rho_r}$ is the ratio between steel and rust density. Then, the reinforcement free-expansion strain can be calculated as:

$$\varepsilon_{s,free} = \sqrt{1 + \gamma(\beta - 1)} - 1 \tag{7.10}$$

This strain is the mean strain of the corroded system with respect to the initial bar diameter, and is a function of the level of corrosion. The stress induced by restraint of the surrounding concrete can be determined by multiplying the strain of the corroded system with its average stiffness. The average stiffness of the corroded system is calculated based on the volume fraction of steel and corroded layers as [207]:

$$E_{s,eq} = \frac{1+\gamma\left(\beta-1\right)}{\left(1-\gamma/E_s\right)+\left(\gamma\beta/E_O\right)}\,[GPa] \tag{7.11}$$

where E_s is the Young's modulus of steel (200 GPa) and E_O the Young's modulus of the oxide. A large range of oxide Young's modules can be found in the literature. Molina et al.[134] tested values of 2 to 4 GPa, with no significant impact on simulation results. Lundgren [148] proposed a non-linear stress level dependent stiffness of the corrosion product, with a maximum value of 14 GPa. On the other hand, values as low as 40-87 MPa were reported by Balafas and Burgoyne [141], and as high as 47-86 GPa by Zhao et al. [149]. In the present work, a constant value of 7 GPa has been assumed [207] [2].
Finally, the internal pressure (P) caused by the concrete restraint is calculated as:

$$P = E_{s,eq} \times \varepsilon_{s,free}\,[MPa] \tag{7.12}$$

Equation 7.12 is, then, the relation between the level of corrosion and the induced pressure in the present model.

7.2.5. MECHANICAL MODEL

Although primarily used for modeling fracture of materials under external loading or deformation, the Delft lattice model has been recently used also for simulating internally caused cracking of concrete (e.g. shrinkage induced eigenstresses [214], freeze-thaw damage [215] and alkali-silica reaction [216]). Herein the attention is focused on yet another possible cause of internal distress in reinforced concrete – reinforcement corrosion. Due to large computational expense, only two-dimensional simulations are performed. Concrete material structure is obtained by using the Anm material model of Qian [173], developed for packing realistic aggregates using spherical harmonics. This model is used to pack the coarse aggregates into a concrete box of $150 \times 150 \times 150\ mm^3$, out of which 1 mm thick slices are extracted and used for the two-dimensional analysis (Figure 7.2). The concrete cube used herein contains about 30% of coarse aggregate per volume.

The Influence of the reinforcing steel on the aggregate packing was neglected for simplicity. The radial pressure (as defined in 7.2.4) is applied around a "hole" in the mesh, which is positioned where the steel should be.

[2] Note that a different value was found in chapter 4, where the Young's modulus was found to be dependent on the deformation. Here, a constant value of 7 GPa was selected for simplicity. The influence of different Young's moduli within the GPa to tens of GPa range does not have a marked effect on the pressure calculation.

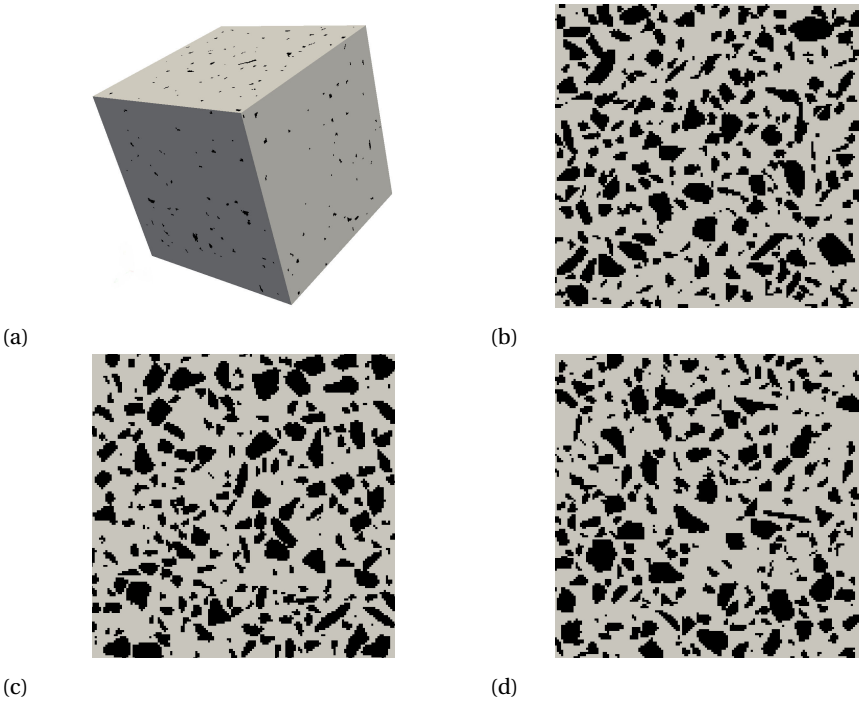

(a) (b)

(c) (d)

Figure 7.2: Concrete material structure generated by the *Anm* material model (a), and slices used in simulations (b-d)

7.3. MODEL VALIDATION

7.3.1. UNIFORM CORROSION

To validate the proposed modeling approach, a well-documented set of experiments by Andrade et al.[9] was simulated. They used the imposed current method to speed up the corrosion process, with a corrosion current density of 100 $\mu A/cm^2$. Also, 3% of $CaCl_2$ was added to the mix. A potentiostat/galvanostat was used to apply the current through a counter electrode. Prismatic specimens of 150 × 150 × 300 mm^3 were used in the study. A single rebar with a diameter of 16 mm was used in all specimens. Three different rebar placements were tested (Figure 7.3): (1) corner rebar, with a cover of 20 mm to the top and 30 mm to the side; (2) rebar in the center of the top side, with a cover of 20 mm and (3) rebar in the center of the top side, with a cover of 30 mm. These are designated henceforth as experiment 1, 2, and 3, respectively. The splitting tensile strength of the specimens was about 3.55 MPa.
As already mentioned, this type of experiment leads to general or uniform corrosion, so the expansion can be reasonably simulated by a radial uniform load. The diameter decrease was calculated using equation 7.1, assuming a 100 % current efficiency (no losses due to heat generation or other factors were considered).

In the presented model, concrete comprises three phases: coarse aggregate (gravel),

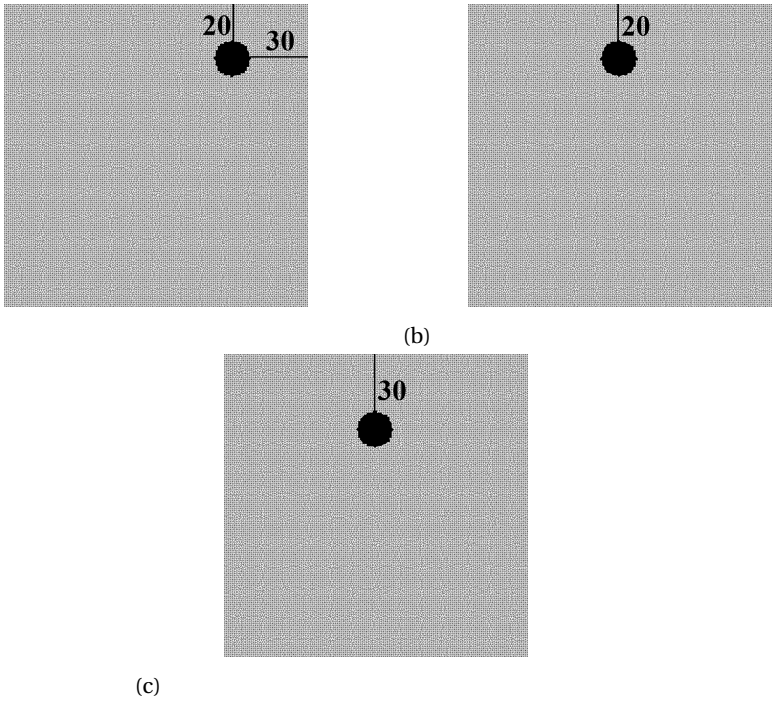

Figure 7.3: Geometry 1, 2, and 3 (a, b, and c, respectively) tested by Andrade et al. [9] and simulated herein

mortar and the interface. These phases have all been assigned with different mechan-

ical properties (Table 7.1). Mechanical properties of individual phases were chosen in order to obtain similar tensile strength as in the experiments (about 3.5 MPa in direct tension). A cross section of $150 \times 150\ mm^2$ was used in the simulations. Each experiment was simulated with three different microstructures (Figure 7.2), in order to check the influence of local mechanical properties and material heterogeneity on the cracking behavior. The names have been assigned according to the following rule: *Experiment number-Microstructure type* (e.g. 1-3 is experiment number 1 projected on a microstructure number 3, etc.).

Table 7.1: Mechanical properties used in lattice simulations

Phase	Young's modulus $[GPa]$	Tensile strength $[MPa]$
Aggregate	70	8
Mortar	25	4
Interface	15	2.5

To determine the expansion pressure (equations 7.1-7.12), parameters given in Table 7.2 are used.

Table 7.2: Parameters used in the expansion pressure calculation

Parameter	Value
Rebar diameter (mm) D_{rb}	16
Corrosion current density $(\mu A/cm^2\ i_{corr})$	100
Molecular weight of iron/molecular weight of rust r_m	0.622
Density of steel/density of rust β	2.2
Young's modulus of steel (GPa) E_s	200
Young's modulus of oxide (GPa) E_O	7

In the experiments [9], 5-8 strain-gauges were glued on each specimen, in order to follow the cracking process. They were placed on different positions on each sample, allowing monitoring deformations where cracking was anticipated. On the other hand, in the simulations crack width is calculated for each cracked element. Since two-dimensional simulations are performed here, a maximum element crack width from the simulations is compared to the maximum crack width found in the corresponding experiment (Figure 7.4).

If the existence of the porous layer is neglected and the penetration of corrosion products into open cracks does not occur, simulation results do not match the experimental results very well (Figure 7.4). In the simulation, at the beginning microcracks form on the inside of the specimen, without reaching the surface. After achieving a certain pressure (i.e. after a certain period of time), a wide crack propagates through the cover and reaches the surface. This is clearly represented by an almost vertical jump in the plots (Figure 7.4). When experiments are concerned, strain gauges measure also the elastic deformation of concrete, and only cracks wider than about 50 μm are clearly visible. It is, therefore, reasonable that the plots do not match the experimental data before the main crack penetrates through the concrete cover. However, at later stages the simulated response is too brittle, which is one of the causes of criticism of early modeling

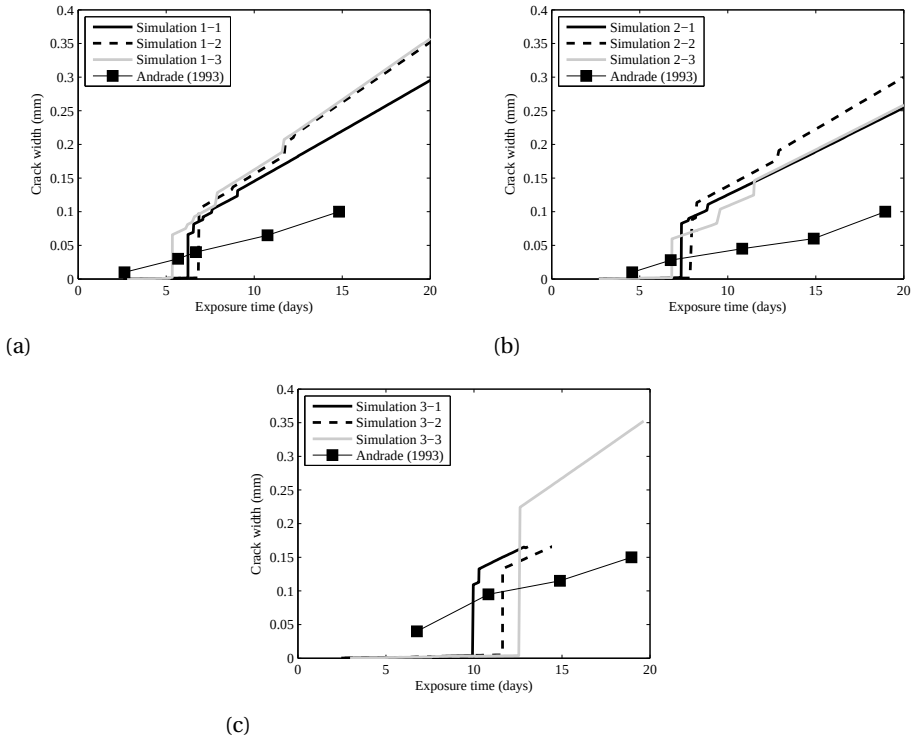

Figure 7.4: Experimental and simulated crack width vs.time, when no porous layer around the rebar exists and penetration of corrosion products into open cracks does not occur (experiment 1 (a), experiment 2 (b), and experiment 3 (c))

efforts (see e.g. [141] or [217] for detailed discussion). Clearly, it is important to take into account additional mechanisms, such are the two addressed before.
After destructively examining their samples, Andrade et al. [9] found that oxides have "partially diffused" through the concrete. In general, the existence of the porous layer around the reinforcement does not change the shape of the diagram as shown in figure (figure 7.4); it merely delays the onset of damage (figure 7.5). Even though its existence has been experimentally observed [139], some authors assume that its influence is very small and choose to omit it from their analyses for simplicity [218].

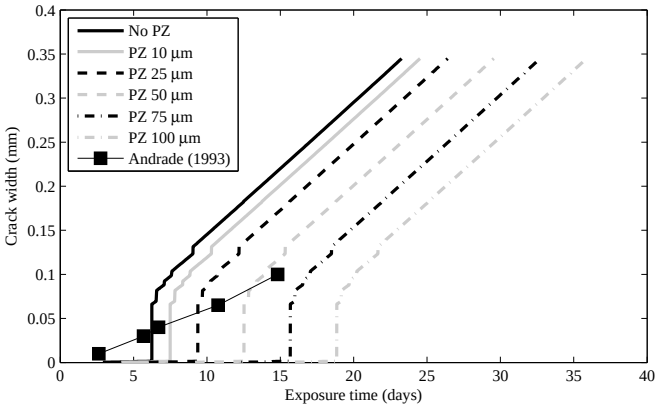

Figure 7.5: Influence of the porous zone (PZ) existence on crack development over time (simulation 1-1)

In Figure 7.5, typical influence of the porous zone (PZ) on the cracking time is shown. From Figure 7.5 it is clear that the delay in damage caused by the existence of the porous layer around the reinforcement, which can accommodate part of the oxides, does not fully explain the difference between the experimental and simulation results. Other simulations exhibit the same type of behavior.
As the pressure builds up, more and more cracking develops. As already discussed in chapter 7.2.3, these cracks create space for accommodation of oxides, thus relieving some of the pressure. This space is designated herein as the *accessible crack volume*. It is, however, impossible to surely asses which percentage of all cracks can serve as such buffer. Therefore, different assumptions are tested. It is assumed that all cracks wider than a *threshold crack width* are fully filled with corrosion products (Figure 7.6).

Evidently, the lower the threshold value for the penetration of the oxides, the more space there is for accommodation of these oxides (Figure 7.6). Typical influence of the penetration of corrosion products into open cracks is shown in Figure 7.7. This mechanism smoothens the curves, and slows down further propagation of cracking. Similar behavior was observed experimentally and included in the model of Chernin et al.[218]. However, this mechanism can also not fully explain the difference between experimental data and simulations.

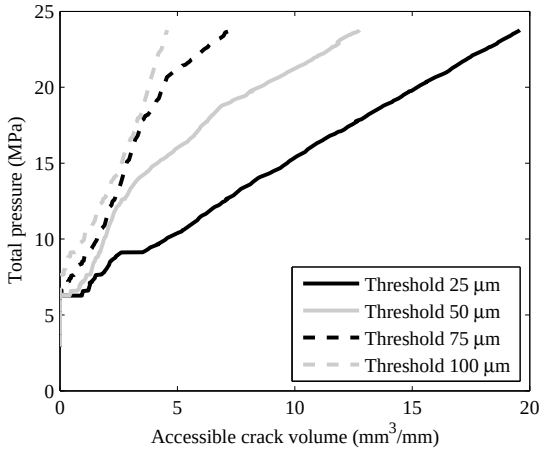

Figure 7.6: Influence of the threshold crack width on the accessible crack volume vs. total pressure (simulation 1-1)

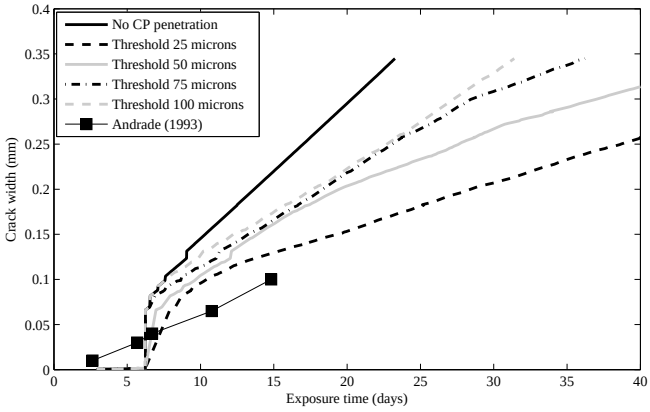

Figure 7.7: Influence of corrosion product penetration into cracks on crack development over time (simulation 1-1) (CP-corrosion products)

A combination of the two mechanisms (i.e. existence of the porous layer around the reinforcement and corrosion product penetration into open cracks) should provide a better comparison. This demonstrates the importance of experimental findings of Wong et al.[139]. Therefore, a number of scenarios were tested: for each simulation, five different thicknesses of the porous layer (range 10-100 μm – see Figure 7.5) and four different threshold values for corrosion product penetration (range 25-100 μm – see Figure 7.7) were tested.

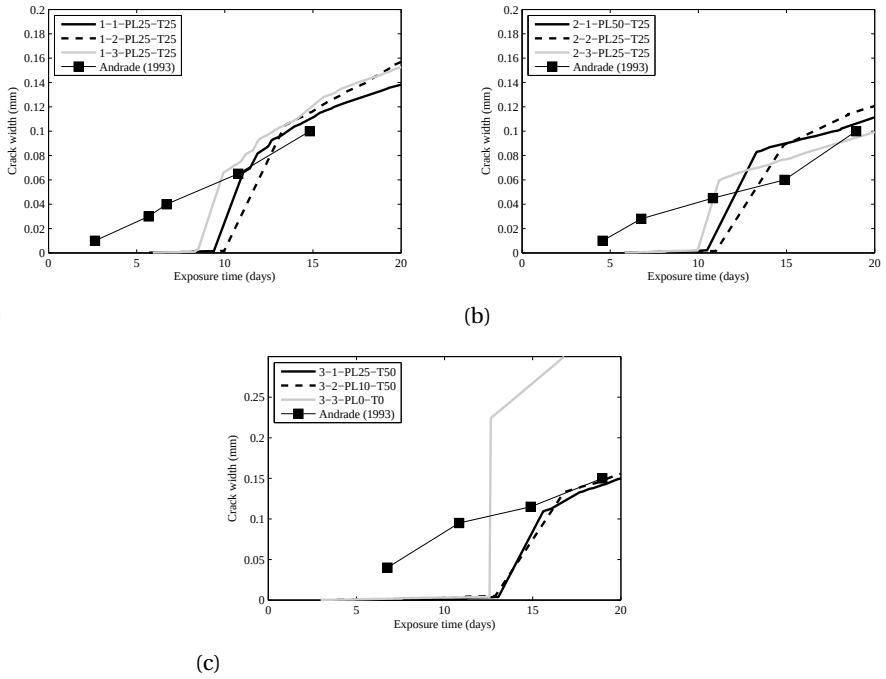

Figure 7.8: Best fit of simulations and experimental data for crack development over time for experiment 1 (a), experiment 2 (b), and experiment 3 (c). (PL – porous layer; T – threshold)

Figure 7.8 shows results which best fit the experimental data from all nine simulations (three simulations per experiment). Figure 7.10 shows crack patterns when the largest crack exceeds 100μm for all nine simulations. Depending on the crack width, cracks are plotted in different colors (see Figure 7.9).

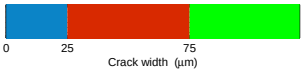

Figure 7.9: Color legend for crack widths in crack pattern plots

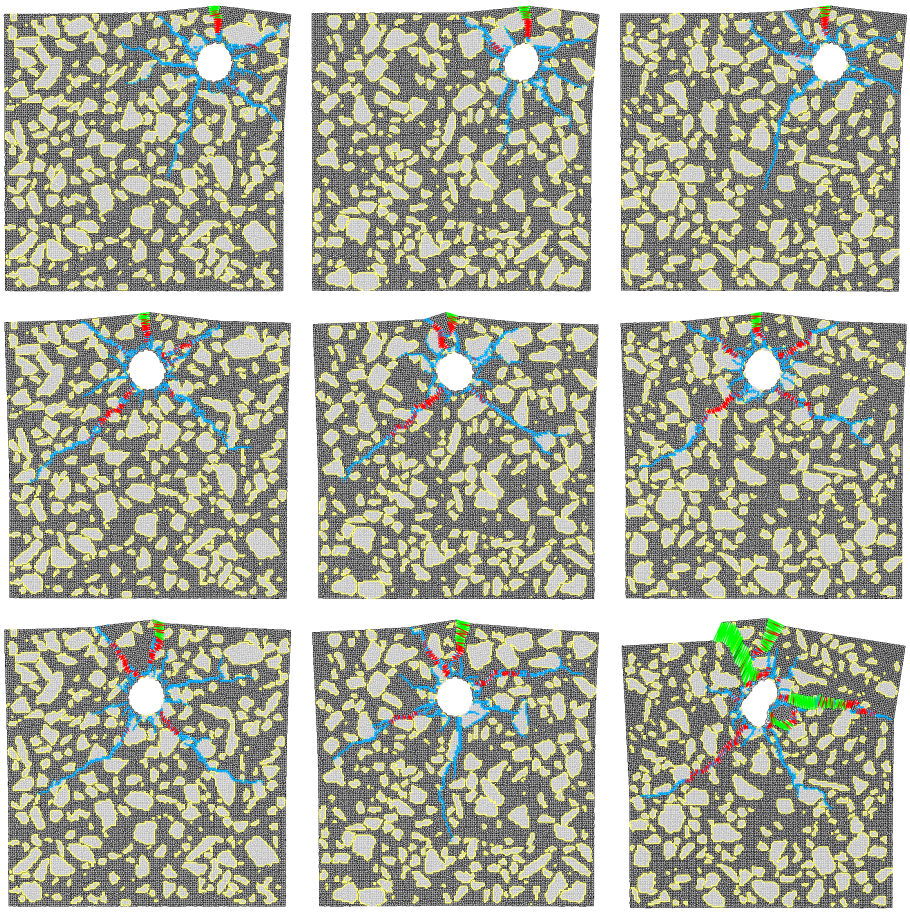

Figure 7.10: Simulated crack patterns for different microstructures and experiments 1 (top), 2 (middle), and 3 (bottom), when largest crack exceeds 100μm

For the experiment 1 (Figure 7.8), cases where the porous layer around the reinforcement is $25\mu m$ thick and the threshold crack width is $25\mu m$ best reproduce the experimental results (simulations 1-1, 1-2, and 1-3). For the experimental case 2 (Figure 7.8), simulations 2-2 and 2-3 fit the experimental results well with the porous layer of $25\mu m$ and the threshold crack width of $25\mu m$ also. For simulation 2-1, however, the porous layer should be $50\mu m$ in order to reproduce the experimental behavior. For the experimental case 3 (Figure 7.8), the results are a bit more complex. Simulation 3-1 matches the experiments well when the porous layer thickness is set to $25\mu m$ and threshold crack width to $50\mu m$. Simulation 3-2 can also match the experiment quite well if the porous layer thickness is set to $10\mu m$ and the threshold crack width is set to $50\mu m$. On the other hand, simulation 3-3 was not able to correctly reproduce the experimentally observed behavior for any set of the input parameters. In this case, a large crack (wider than 0.2 mm) occurs suddenly, followed by spalling of a piece of concrete (Figure 7.10).

7.3.2. NON-UNIFORM CORROSION

In situations when external chloride penetration is the cause of depassivation, the corrosion process may start from the outer region of a rebar, which might expand non-uniformly [139, 211]. In such a case, a model assuming uniform expansion may be used only as a very rough approximation [217]. Typically, this pitting behaviour is more detrimental to the concrete cover than uniform corrosion. For the non-uniform corrosion case, a reasonable assumption is that the corrosion depth decreases linearly from the outer region of the rebar (Figure 7.11). The value α is defined as the ratio of the depth of non-uniform corrosion to that of uniform corrosion [211]. Experimentally, it was observed that α assumes a value ranging from 4-8 in natural corrosive environment [219].

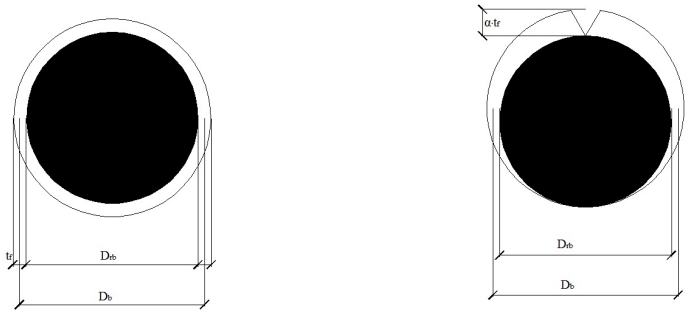

(a) (b)

Figure 7.11: Description of uniform (a) and non-uniform (b) corrosion. Adapted from [211]

A numerical study was conducted by Jang and Oh [211], who concluded that the assumption of uniform corrosion may not lead to a conservative estimate for time to cracking. Values of $\alpha = 2, 4$ and 8 were tested (Figure 7.12). A slightly non-uniform case ($\alpha = 2$) showed minor difference with the uniform case, and hence is not considered in

the present work. Values of $\alpha = 4$ and $\alpha = 8$ were tested in herein, with resulting non-uniform pressures shown in Figure 7.13. It has to be noted that the pressures for pitting cases were also calculated using equation 7.12, and then redistributed according to the scheme shown in Figure 7.13.

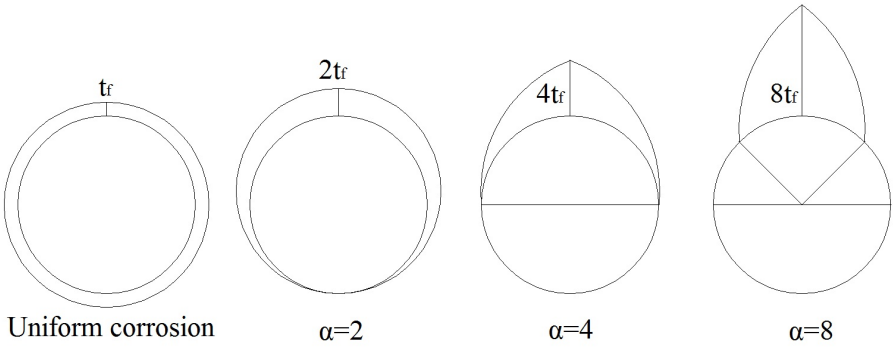

Figure 7.12: Corrosion product distribution for uniform corrosion and different pitting cases (total corrosion products = constant). Adapted from [211]

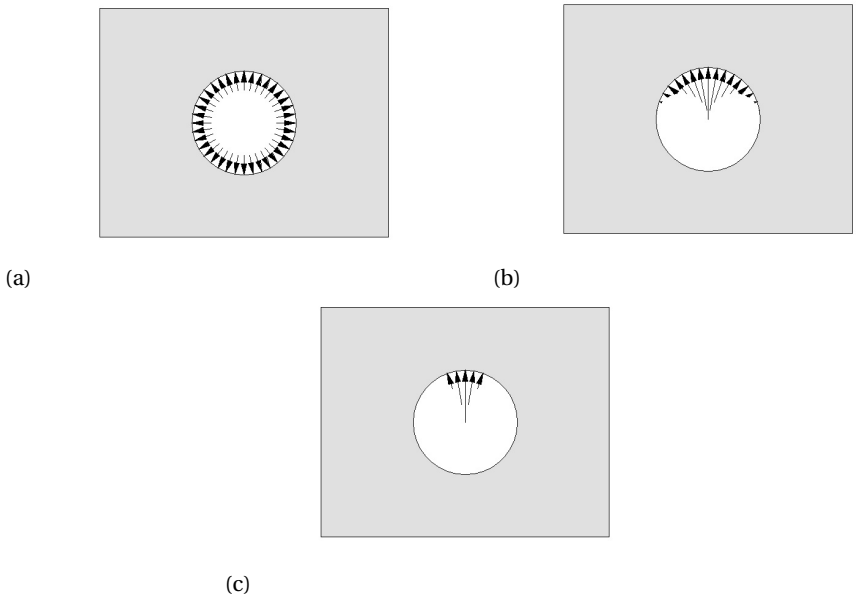

Figure 7.13: Pressure distributions caused by uniform corrosion (a) and different pitting scenarios, $\alpha = 4$ (b) and $\alpha = 8$ (c). Adapted from [211]

Experimental investigations where cracking due to external chloride attack is studied are rare. This is due to a very long duration of such a process. Therefore, it is also rarely modelled [136, 208, 211, 213]. Due to lack of experimental data, it is still not possible

to verify these models. Nevertheless, when based on sound assumptions, these efforts can provide engineers and researchers with an idea of relative influence of pitting on the cracking dynamics.

Here, an attempt is made in comparing the cracking processes of two different pitting scenarios ($\alpha = 4$ and $\alpha = 8$) to the cracking process due to uniform corrosion (presented in chapter 7.3.1). The same simulation scheme as with the uniform case is repeated: namely, each rebar geometry was simulated with three different concrete microstructures (same as in the uniform case). This was done for both pitting states ($\alpha = 4$ and $\alpha = 8$). The cracking patterns for each of the simulations is shown in Figure 7.14 ($\alpha = 4$) and Figure 7.15 ($\alpha = 8$). For comparison purposes, all snapshots are taken as soon as one of the elements had a crack width of more than $100\mu m$.

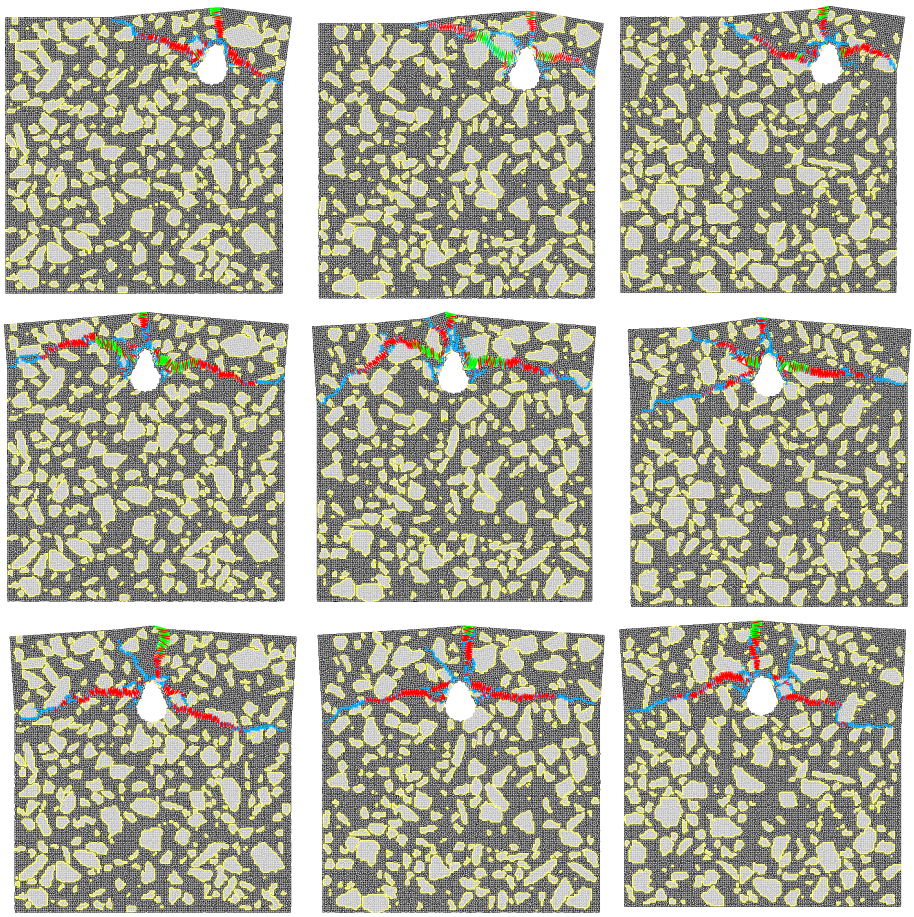

Figure 7.14: Simulated crack patterns for different microstructures, loading pattern $\alpha = 4$ and geometry 1 (top), 2 (middle), and 3 (bottom), when largest crack exceeds $100\mu m$

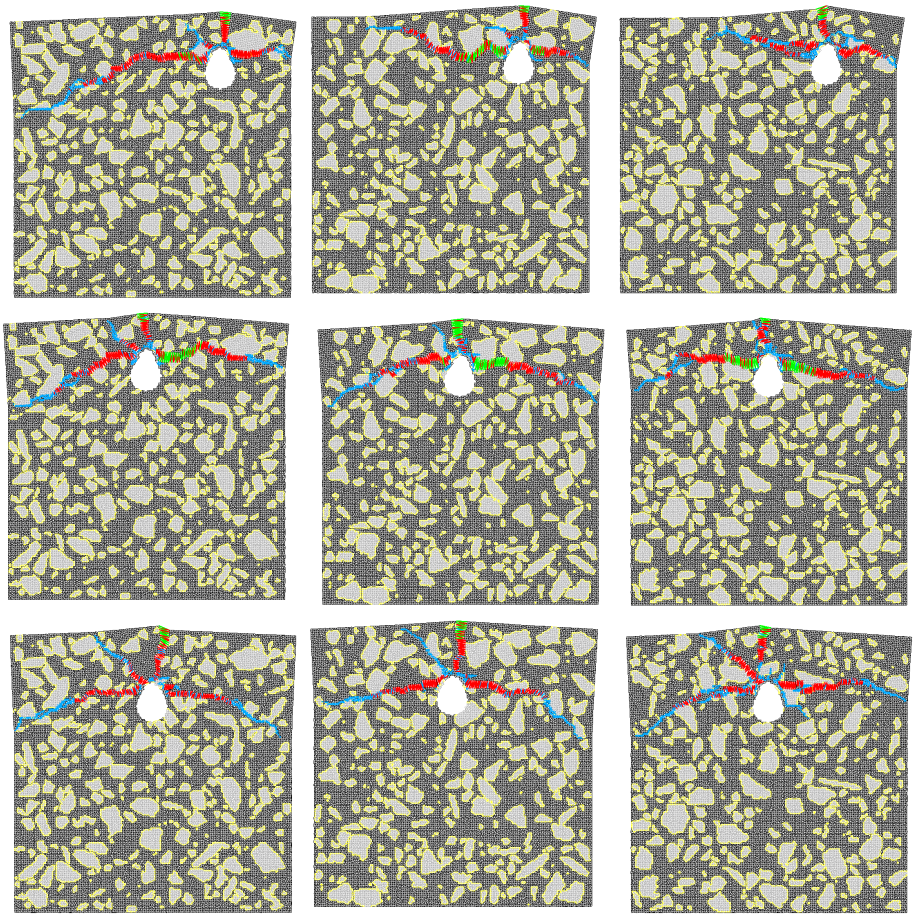

Figure 7.15: Simulated crack patterns for different microstructures, loading pattern $\alpha = 8$ and geometry 1 (top), 2 (middle), and 3 (bottom), when largest crack exceeds $100\mu m$

Besides the crack patterns, it is also interesting to compare the amount of total internal pressure needed for cracking in pitting and uniform cases (Figure 7.16). Note that internal pressure is directly proportional to the amount of oxide formed (equations 7.1-7.12).

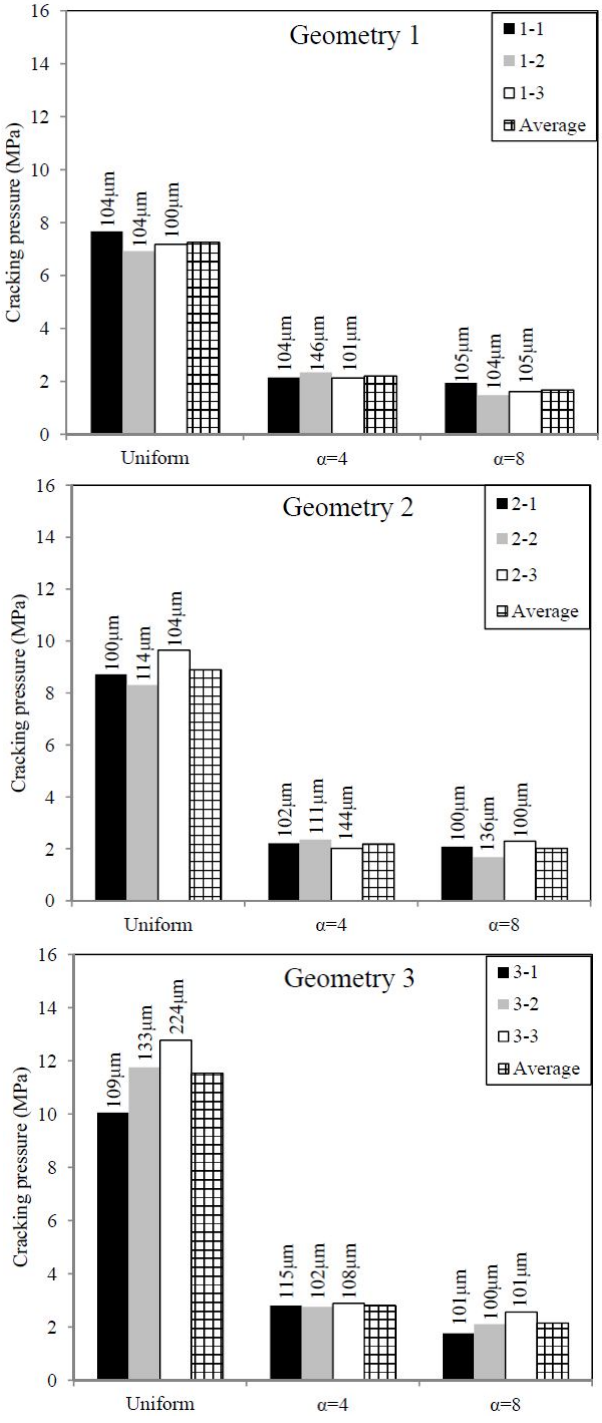

Figure 7.16: Cracking pressure for the different microstructures and loading scenarios (note: for comparison, cracking is defined as occurrence of a crack wider than 100μm) for geometry 1 (top), 2 (middle), and 3 (bottom). Labels denote the actual crack width in each simulation

7.4. DISCUSSION

It appears that the suggested model is able to reasonably simulate the process of cracking induced by corrosion of steel reinforcement. The proposed procedure for determining the relation between diameter loss and internal pressure which develops in the concrete seems to enable a sound basis for the model. Although a good basis for numerical modelling, care must be taken when interpreting the results: due to lack of precise and reliable experimental records, a number of factors needs to be assumed. These are mostly parameters related to the properties of the oxide, such as the oxide stiffness (E_O), and relationship between steel and oxide density (β). An increasing number of experimental studies conducted recently ensure that more reliable input will be available in the future [15, 28].

For the uniform pressure case, a well-documented set of experiments was available for model validation [9]. Three different microstructures were used to simulate each experiment, and showed significant differences. In all simulations, a major crack appeared first at the surface nearest to the rebar (the upper surface). This is consistent with experimental investigations [10]. It also justifies to a certain extent the use of models based on the thick-walled cylinder theory, since they assume that the thickness of the cylinder is equal to the thickness of the smallest cover. It is also clear that the crack follows the weakest route, penetrating around the aggregate particles, and through the mortar and the interface (Figure 7.10). This crack tortuosity is observed in the experiments, but is missing in models which treat concrete as a quasi-homogeneous continuum. In simulations of the experiment 1, a single major crack appears at the specimen surface, accompanied by a significant number of microcracks penetrating trough the interior of the specimen. The extent of microcracking is dependent on the concrete microstructure in each simulation. Simulations of experiment 2 showed similar tendencies. However, apart from the main crack, several larger secondary cracks appear accompanied by microcracks. Simulations of experiment 3 showed similar behaviour, except simulation 3, where a large crack followed by spalling occurred.

Comparing the numerical simulations with experimental results, it is evident that, for a good correlation, the penetration of the oxide into the porous layer around the steel and open cracks needs to be taken into account. For the set of input parameters used herein to reasonably reproduce experimental data the thickness of this porous layer appears to be between 10-50μm, while the threshold crack width should be set between 25-50μm. For a different set of input parameters (E_O and β), somewhat different values would be obtained. It is, however, clear that the presence of these two mechanisms cannot be neglected in numerical simulations.

In case of non-uniform (pitting) corrosion, no experimental data is available. The assumed pitting scenarios [211] seem reasonable when compared to experimental observations [139, 219]. For both loading scenarios, three different microstructures were tested for each geometry. As is the case with uniform corrosion, a major crack appears first at the surface nearest to the rebar in all simulations (Figures 7.14 and 7.15). However, this is not accompanied by significant microcracking penetrating to the interior, but several larger cracks which penetrate to the sides, even for case 1. Since the appearance of a surface crack is usually a first visible sign of ongoing corrosion, this implies that in case of pitting corrosion much more damage has occurred in the interior of the

concrete element at that moment than in case of uniform corrosion. This has to be taken into account when extrapolating accelerated corrosion tests done in the laboratory, and trying to use the findings to assess deterioration in the field. Attempts to relate the surface crack width to degree of corrosion (i.e. determining the degree of corrosion from the known crack widths) [218] may therefore lead to wrong conclusions on site, when external chloride attack is the cause of damage. Thus, any condition assessment which relies on outwardly visible signs of deterioration must be performed with caution, if chloride induced corrosion is a possible cause of damage [217].

When it comes to cracking pressures, some interesting observations can be made. There is a variation of cracking pressures for different microstructures, stressing the influence of local mechanical properties on the corrosion crack propagation. Due to material heterogeneity of concrete, it is difficult to define a deterministic value of the internal pressure which leads to cover cracking. Instead, it would be more appropriate to deal with it in a stochastic manner [213]. In case of uniform corrosion, the following behavior occurred: the least amount of pressure is needed in case of the corner rebar – case 1 (on average 7.25 MPa), followed by case 2 (8.89 MPa) and case 3 (11.52 MPa). This behavior was expected [10, 211]. In cases of pitting, it is clear that the total internal pressure needed for cracking is significantly lower: for geometry 1, the average amount of pressure is 3.28 ($\alpha = 4$) and 4.33 ($\alpha = 8$) times lower than in the uniform corrosion case. For geometry 2, these values are 4.05 and 4.41 for $\alpha = 4$ and $\alpha = 8$, respectively. For geometry 3, values of 4.09 and 5.37 are observed. A similar trend of decrease in cracking pressure in case of pitting was reported by Jang and Oh [211]. Other factors influencing this trend in their study included the concrete strength and cover-to-diameter ratio. It is important to note, again, that the amount of pressure generated is directly proportional to the amount of oxide generated. In other words, a significantly lower quantity of corrosion product in case of pitting corrosion can cause the same amount of visible damage, and more interior damage, as higher quantity in case of uniform corrosion. This further underlines a statement by Angst et al.[217] that, in case of chloride induced (i.e. pitting) corrosion, models assuming uniform expansion may not be considered useful.

It has to be noted that the model presented here is limited to two spatial dimensions. Three-dimensional simulations of pitting corrosion would be more challenging, as the size of the pit would need to be known also in the direction perpendicular to the specimen cross section. Therefore, the internal pressure which results in cover cracking could be different than that obtained from a 2D analysis.

7.5. CONCLUSIONS

A model for corrosion induced cracking of the concrete cover was introduced, based on the Delft lattice model. With aid of the available literature, a procedure was developed for relating the rebar section loss due to corrosion and the internal pressure which the expansive corrosion reaction generates on the surrounding concrete. Even though certain parameters in the model have to be assumed (e.g. β and E_O), the presented procedure provides a sound basis for the numerical analysis. Current development in advanced experimental methods should provide more reliable input data in the future, especially regarding mechanical properties of the rust layer.

The numerical fracture analysis was performed within the framework of the two dimensional lattice model. In the meso-scale model, concrete was considered as a composite material, consisting of gravel, mortar, and the interface. The meso-scale analysis provides useful insights in the cracking process, which could be overlooked if concrete was considered as a quasi-homogeneous material. Since every analysis case was performed for three different (randomly generated) microstructures, it is possible to see that the local variations in mechanical properties are responsible for differences in cracking pressure and cracking patterns. As this is mostly ignored in current models, it is proposed that the determination of time-to-cracking should be done in a stochastic, rather than deterministic, way. That way, more realistic results would be obtained.
The proposed model was verified by comparing the results with well-documented results from the literature. In order to see good correlation between simulations and experimental data, it was necessary to include two effects: (1) transport of corrosion products into open cracks; and (2) existence of a porous layer around the reinforcing steel, able to accommodate a portion of the formed products. The thickness of the porous layer was found to be between 10-50μm, and the threshold crack width for corrosion product migration into open cracks between 25-50μm. These numbers are, to a certain extent, dependent on the assumed rust parameters (β and E_O). Nevertheless, a tendency that both of these parameters have to be included in numerical simulations is clear.
Effects of pitting corrosion on the cracking were also covered in the presented work. This type of corrosion occurs as a consequence of external chloride attack. Two different pitting scenarios were tested. It was found that, when pitting corrosion occurs, significantly less total pressure is needed to crack the concrete cover compared to uniform corrosion. On top of that, pitting corrosion creates more extensive internal damage. This is not visible from the outside at the time of cracking, and could easily be unnoticed. As chloride induced reinforcement corrosion is often encountered in the field, one needs to be aware of this effect when performing condition assessment of such structures based only on visual inspection.

8

SUMMARY AND CONCLUSIONS

It's the job that's never started
as takes longest to finish.

J.R.R. Tolkien

In this chapter, a brief summary of the work presented in this PhD thesis is given. Furthermore, general conclusions and findings of this research are briefly presented and discussed. In the end, some recommendations for further work are given.

8.1. SUMMARY

CHLORIDE ingress into concrete is a complex phenomenon, dependent on a multitude of material and environmental parameters. Even though it has been studied for decades, it is still not fully understood. This is mainly due to the complex material structure of concrete (i.e. its multi-scale character) and the uncertainties related to the environmental parameters. Nevertheless, vast knowledge has been accumulated over the years, providing researchers and practitioners with mathematical tools for dealing with the problem. However, the influence of concrete cover cracking on chloride ingress is still not sufficiently understood. In this thesis, an attempt was made to contribute to the body of knowledge in this field.

In chapter 1, an introduction of the PhD work is given. First, basics of service life design with respect to chloride induced corrosion are given. Then, very basic theory of chloride induced steel corrosion is presented. Critical chloride content is defined, and main sources of chloride ions are given. Then, mechanisms of chloride transport in concrete are described. This is followed by a brief review of cracking and cracks in concrete, their origin and characteristics. Their relation to durability of reinforced concrete is then given. In the last part of chapter 1, a literature review of chloride ingress in cracked concrete is given. Methods for specimen preparation, exposure, main influencing factors, and mitigating mechanisms are described. Finally, the outline of the thesis is given, and its relationship with a related PhD work is explained.

Chapters 2-4 deal with an experimental part of the research. Chapter 2 deals with experimental study of chloride ingress in cracked concrete under wet-dry cycles. Two concrete mixtures were used: a Portland cement mix, and a blast furnace slag mix. An innovative specimen geometry, based on the wedge-splitting test, was used. The effects of proposed modifications on the mechanical behavior of the specimens are studied using numerical simulation. After prolonged cyclic exposure to sodium chloride solution, cracked specimens were cut and examined using laser induced breakdown spectroscopy (LIBS). As a result, two-dimensional maps of both chloride and sodium across the cut surface were obtained. On top of that, LIBS was able to discard coarse aggregate locations based on their elemental composition. Afterwards, the specimens were vacuum impregnated with fluorescent low viscosity epoxy, and photographed under UV light. It was found that chloride ingress is, indeed, increased in specimens with larger cracks. Furthermore, the ingress profile was found to closely follow the cracks. This was especially interesting to observe in specimens with wider cracks, where debonding of the steel/concrete interface occurred. As expected, chloride ingress depth (both in the bulk material and around the crack) was much lower in the blast furnace slag mix, compared to the Portland cement mix. In the end, it was argued that advanced experimental techniques for determination of chloride ingress profiles (such as LIBS) should be given preference compared to standard wet chemical analysis, when high spatial resolution is sought. This seems especially important in the case of cracked concrete, where the ingress profile closely follows the cracks, whose geometry is not known a priori.

Chapter 3 studies the influence of autogeneous healing on chloride ingress in cracked concrete. The same concrete mixtures used in chapter 2 are used in this chapter. The wedge-splitting procedure (without modifications) was used to crack the specimens. Cylindrical cores were drilled, and the specimens exposed to a modified rapid chloride

migration test according to NT Build 492 [18]. Different curing (healing) regimes were tested for both mixes. The chloride penetration depth was measured, and maximum penetration depth was compared to the penetration depth in the uncracked part of each sample to characterize the effectiveness of autogeneous healing with respect to chloride ingress. It was found that healed specimens showed lower chloride penetration compared to the control series. It seems that cracks smaller than 60 μm were able to heal almost completely, while wider cracks showed partial healing.

Chapter 4 deals with a related phenomenon, cracking of the concrete cover *induced* by reinforcement corrosion. Two material mixtures were used: the so-called strain hardening cementitious composite (SHCC), which is a highly ductile fiber reinforced composite material; and a reference brittle material, which had the same mix proportions, but without fiber reinforcement. An accelerated corrosion setup was used, and formation of corrosion products and consequent cracks was monitored non-destructively using X-ray computed tomography (CT scanning). The SHCC specimen showed far more resistance to cracking, compared to the control specimen. After the accelerated test, mechanical and chemical properties of the corrosion product in both mixes were characterized using nanoindentation and EDS (Energy Dispersive X-ray Spectrometry), respectively. These properties were found to be dependent on the confinement level of the rust layer, i.e. on the amount of cracking. Part of the corrosion products was observed to leach out through open cracks. These findings could be of great use for numerical models.

Chapters 5-7 deal with the modeling part of the study. Chapter 5 presents a meso-scale model for chloride diffusion in cracked concrete based on the lattice modeling framework. For simplicity, a water-saturated state was assumed, with diffusion being the only transport mechanism for chloride ions. First, the procedure for spatial discretization of the domain is described. It is followed by the discretization of the governing differential equation and derivation of relevant element and system matrices. Then, transport properties of individual phases (i.e. mortar. interface, assuming impermeable aggregates) and cracks were determined based on data from the literature. For the mechanical analysis, the standard Delft lattice model was used. Finally, the proposed model is verified using suitable experimental data from the literature.

Chapter 6 expands this concept further by incorporating the effect of an external voltage on chloride ingress. As an external voltage is often applied to speed up the chloride ingress in cracked concrete, it is essential that this effect is studied. First, the governing diffusion-migration equation is discretized using the Characteristic Galerkin (CG) scheme, and the relevant element and system matrices are derived. Then, some numerical aspects of the model are tested with respect to the lattice element size and the so-called Peclét number. Then, the model is verified using several benchmark cases: meso-scale (heterogeneous concrete), micro-cracked concrete (cracked in uniaxial compression), notched concrete, and, finally, cracked concrete.

Chapter 7 deals with numerical modeling of concrete cover cracking due to reinforcing steel corrosion. A model which relates the cross section loss of reinforcing steel and the amount of expansion pressure exerted due to the rust confinement is proposed and implemented in the Delft lattice model. Also, two pressure relief mechanisms were included in the model: penetration of rust into the porous layer around the reinforcement (i.e. free rust expansion), and penetration of rust into open cracks. The existence of these

mechanisms has been widely recognized in the literature (although the first one was not observed in the experimental study in chapter 4, probably due to the very high corrosion rate). The heterogeneous material structure of concrete was implemented in the model, which was verified using well known accelerated-corrosion experiments from the literature. Furthermore, several cases of non-uniform (pitting) corrosion are tested. It is concluded that pitting corrosion could cause cover cracking at lower expansion pressure compared to uniform corrosion, and is therefore potentially more detrimental.

8.2. GENERAL CONCLUSIONS

IN every chapter of the thesis, conclusions related to that part of the work are drawn. Here, some general conclusions are given.

- *Cracking has a marked influence on chloride ingress in concrete*
  This effect was recognized in chapter 2. It was clearly shown that wider cracks allow for higher chloride penetration, as expected. However, all cracks are not created equal: it seems that cracks which are parallel to the reinforcement (i.e. those occurring due to debonding at the steel/concrete interface) are especially detrimental, as they expose a large surface of reinforcing steel to high chloride concentrations. Because chloride penetration seems to closely follow the cracks, it seems that the crack shape around the reinforcement bar is much more relevant than its surface width. This could be much more relevant for corrosion initiation and propagation than the surface crack width, as was found in a related study [103]. Similar findings were reported by Michel et al. [119]. Also, it was found that chloride penetration around cracks is dependent on the concrete material, as was expected. The implications of this for the corrosion behavior are to be seen in the corrosion behavior of the two tested mixtures: it seems that the locations where corrosion starts are not the same in Portland cement and blast furnace slag cement specimens [103]. Furthermore, use of experimental techniques with high spatial resolution (such as LIBS) is recommended for studying chloride distributions in highly heterogeneous areas, such as those around discrete cracks.

- *Autogeneous healing has potential to slow down chloride ingress in cracks*
  In chapter 3 it was found that chloride penetration resistance of cracked concrete specimens can be partially or fully recovered after exposure to favorable conditions. Here, this recovery was observed for both specimens cured under water and in 95% relative humidity. Yet, it is still not known which "minimum" favorable conditions are needed for this to occur. Also, while autogeneous healing could be beneficial, it is still difficult to evaluate its practical implications. The question still remains: can we rely on autogeneous healing in service life design? Another question which arises is if this autogeneous healing also fills up cracks which occur at the steel/concrete interface, which seem to be very critical for chloride induced corrosion in cracked concrete.

- *Meso-scale modeling provides a step forward in understanding chloride ingress in concrete*

Even though concrete is a multi-scale material, when it comes to chloride ingress, it is the concrete cover that is the region of interest. This cover has a thickness of several cm, so the so-called meso-scale is an appropriate scale of observation. Coarse aggregate particles, porous interfaces, and cracks all cause a deviation from an ideal and uniform chloride profile. Locally higher chloride concentrations may cause depassivation of steel, even though the "average" chloride concentration at the level of the reinforcement is lower. Influence of different parameters can be studied using meso-scale models, enabling smart design of future experiments. In conjunction with experiments on the meso-scale, modeling of this scale can provide more insight on the process of chloride ingress and corrosion initiation, for example its variability.

- *Care has to be taken when using an external voltage for accelerating chloride ingress in concrete with discrete cracks*
  In chapter 6, a numerical model for rapid chloride migration in concrete is presented. It was found that the chloride penetration through the crack highly depends on the voltage applied (compare figures with 0 V 6.10 and 25 V 6.9). The applicability of accelerated tests of chloride penetration around cracks on real exposure conditions is, therefore, questionable. Nevertheless, such accelerated tests can be used for comparative purposes, as in chapter 3.

- *During the corrosion process, corrosion products migrate into large pores and open cracks*
  As seen in one of the specimens in chapter 2 and observed in accelerated corrosion experiments in chapter 4, corrosion products dissolve in water and migrate into large pores and open cracks. This could have several consequences: (1) rust can potentially clog up open cracks, and slow down the ingress of further chloride ions; (2) part of the rust will not accumulate at the steel/concrete interface, and will therefore not exert expansive pressure on the surrounding concrete; and (3) this fact might challenge the assumption that the rate of rust production decreases in time. Liu and Weyers [135] assumed that this happens because, as the rust layer increases in thickness, so does the iron ionic diffusion distance, and the rate of rust production decreases because diffusion is inversely proportional to the thickness of the rust layer. Therefore, as part of the rust might migrate away from the steel surface, this might not be the case.

- *Mechanical properties of the rust layer are complex and dependent on the confinement provided by the surrounding concrete*
  In chapter 4, nanondentation was performed to determine the elastic modulus of the rust layer. Two tested specimens showed two clearly different levels of damage to the mortar, and therefore the surrounding material provided different confinement levels to the rust layer in these cases. The average elastic modulus of the rust layer was found to be significantly lower when less confinement is provided to it.

- *During the reinforcement corrosion process, internal pressure needed to cause cracking of the concrete cover is not a deterministic value.*

Instead, it depends on the local micro (meso) structure of the concrete surrounding the corroding rebar. As this internal pressure is proportional to the thickness of the rust layer, the thickness which is needed to cause cracking is not a deterministic value. In service life life predictions, time to corrosion induced cracking should therefore be calculated in a stochastic, rather than deterministic way. Also, in case of pitting corrosion, lower internal pressure is needed to cause cracking, compared to the uniform corrosion case. This means that pitting corrosion is potentially more detrimental, as less pressure means less total amount of corrosion.

8.3. RECOMMENDATIONS FOR FUTURE WORK

IN this research work, an attempt was made to contribute to the body of knowledge related to chloride ingress in cracked concrete and related phenomena. Many issues were tackled, while others arose or were left untouched. In the future, the following could be done:

- Testing chloride ingress for other loading conditions and materials. In chapter 2, chloride ingress was tested for specimens cracked in a bending-like fashion, where a single crack develops. In case of uniaxial tension or compression, the results might be different. Furthermore, innovative materials such as SHCC and other materials might show markedly different cracking and chloride ingress behavior.
- Testing of coupled degradation. For example, chloride ingress coupled with loading and carbonation could be a case of practical interest which seems quite detrimental.
- Extending the lattice model for chloride ingress presented in chapter 5 to take into account non-saturated conditions and wetting and drying cycles. Numerous models for this already exist for sound concrete (e.g. models of Meijers [220] and Martín-Peréz [209]). Recently, even a model of chloride penetration into cracked concrete subject to drying–wetting cycles was presented by Ye et al. [221]. In a mathematical and computational sense, the extension of the present model to non-saturated conditions is straightforward. This would enable realistic simulations of experiments such as that presented in chapter 2. However, many of the parameters needed as input for such a model are still missing. For example, the drying behavior of a crack at different environmental conditions is still largely unknown.
- Extending the single species lattice model for rapid chloride migration, presented in chapter 6, to multiple ionic species. In this way, both the influence of ionic interactions and the non-uniformity of the electrical field could be taken into account. Such a model could further be used to study other phenomena, such as for example alkali transport during an alkali-silica reaction, or electrochemical chloride extraction.
- Studying chloride ingress in cracked concrete in a multi-scale modeling framework, using a so-called parameter passing scheme [173]. Starting from the level

of cement paste and using hydration models (e.g. HYMOSTRUC3D [222]), both mechanical and transport properties of each phase could be numerically determined. The information would be passed to the higher (i.e. mortar) scale, calculated again, and passed to the highest (i.e. concrete) scale. This would enable that the model has fully predictive capabilities, the only input being the material characteristics of used raw materials.

- Coupling the lattice fracture model for corrosion induced cracking, presented in chapter 7, with the chloride ingress model. Furthermore, a model which would include the corrosion kinetics [136] would enable more reliable modeling of the propagation phase, which could be considerably longer than the initiation phase in case of cracked structures.

A

LITERATURE OVERVIEW

In the appendix, a selection of most important papers related to chloride ingress in cracked concrete is given. Different experimental parameters, such as the material used (i.e. cement paste, mortar, or concrete), the cracking method, and the exposure condition, is given for each publication. Also, most important findings are stated for each publication. The intention is to give a brief overview of the currently available literature in the field, and to provide a shortcut to the most relevant literature for an interested reader. For further details, individual papers should be referred.

Reference	w/c	Material	Rebar	Shape	Cover depth (mm)	Dimensions (mm)	Cracking method	Width (mm)	Spacing (mm)	Exposure conditions	Self-healing/crack blocking	Critical crack width (mm)	Main observations
[12]	0.6	Concrete	ø16	Beam	20	200 × 250 × 2200	Bending	0.1-0.2	90-230	immersion, 3% $NaCl$ (30 days-2 years)	-	0.2	A two-dimensional chloride diffusion process should be considered, because chloride ingress can occur from the cracked plane, as well as from the free surface.
[223]	0.37	Cement paste	-	Disc	-	25, ø100	Brazilian splitting	-	-	Similar to RCPT test	-	-	Ion diffusion coefficient and electrical conductivity are strongly (approximately linearly) related to the volume fraction of cracks (for through cracks, as are here). Diffusivity and conductivity are not significantly influenced by crack width.
[48]	0.25, 0.31, 0.45	Concrete	-	Cylinder	-	50, ø100	Brazilian splitting	0.05-0.4	-	RCPT	-	0.2	Only for HSC with very low w/c ratio chloride permeability was sensitive with respect to cracking. Water permeability was significantly more sensitive than conductivity with the respect to the crack widths.
[75]	0.5	Concrete/FRC	-	Cylinder	-	-	Static or dynamic compression	microcracks	-	NT Build 492 (24h)	-	-	Under low static compressive loading, there is a reduction in the chloride penetration depending on the type of concrete. At higher static compressive loading, an increase in chloride penetration was found. Increase in the chloride penetration is more pronounced when the concrete is subjected to cyclic compressive loading. Small and insignificant damage in the concrete material could accumulate under cyclic loading and increase the chloride penetrability.
[66]	0.5	Concrete	-	Cylinder	-	-	Artificial	0.2-0.3	-	NT Build 492 (varied duration)	-	no influence	A higher penetration of chlorides is obtained at the notch tip than in the "uncracked" part of the test specimens. The penetration depth is increasing with an increasing notch depth. This effect is more pronounced for longer test durations. The total chloride distribution is not influenced by the notch width (in the range of 0.2-0.3 mm). By increasing the amount of cement from 300 kg/m3 (T1) to 400 kg/m3 (T2) at a constant w/c ratio, the maximum and mean penetration depths are decreasing. This could be explained by the higher amount of chlorides that is bound to the cement matrix.
[64]	0.5	Mortar	-	Prism	-	40 × 40 × 160	Artificial	0, 0.2, 0.3, 0.5	-	Permanent 10% CO_2 environment; Permanent 3.5% $NaCl$ solution; Cycle 1 week 10% CO_2/1 week 3.5% NaCl solution; Cycle 1 week 10% CO_2 environment/1 week water; Cycle 1 week water/1 week 3.5% $NaCl$ solution	-	-	From the analyzed data, it seems that the crack influence factor is significantly higher for chloride penetration than for carbonation.
[79]	0.32, 0.38, 0.50	Concrete	-	Cylinder	-	50, ø110	Brazilian	0.2-0.7	-	Steady state migration	-	0.08	The chloride diffusion coefficient of cracked samples increases with increasing crack width, the variation of D_e with crack widths presenting similar trends for all three investigated concretes. The time to penetrate through the specimen is reduced which is very important to evaluate the initiation of corrosion.

[40]	0.5	Concrete	Ø12, Ø16 and stirrups Ø8	Beam	10 and 40	150 × 280 × 3000	bending	0.05-0.5	varies	35 g/L salt fog wetting (15 days) and drying in natural conditions (15 days) (for 12 years)	-	not important (if less than 0.5)	it is possible to conclude that the development of the reinforcement corrosion is not influenced by the width of cracks (for widths less than 0.5 mm) or by existence of the crack itself. However, the results appear to indicate that the load applied to a reinforced concrete beam plays an important role in the penetration of aggressive agents and then in the corrosion of the reinforcement.When the concrete cover is small, the depassivation threshold is quickly reached in every part of the beams, even if the penetration is also faster in the tensile zone.
[3]	N.A.	Concrete	N.A.	Beam	10, 40	N.A.	Bending	N.A.	-	17 years	possible	-	Results show that the corrosion development has no correlation with the crack width or even the crack existence.
[62]	0.48	Mortar	Ø6 and Ø8	Disc	Reinforcement in the center of the mould.	Thickness 50, internal Ø50, external Ø150	Expansive core	0.019-0.658	not measured	35 g/L salt solution wetting (1 day) and drying in lab conditions (13 days) 500-800 days	-	-	Irrespective of the COD, the Cl ions reach the reinforcement quickly, at its interection with the crack. Corrosion starts at this stage and then propagates along the length of the steel/concrete interface in the zone which was damaged by the creation of the crack.The development of oxides in steel/concrete interface zone around the intersection between the crack and the rebar leads to the generation of the additional tensile stresses in the mortar which is already loaded in tension, thus logically creating corrosion cracks at the intrados of the sample, where mechanical tensile stresses are the highest. The quantity of oxides necessary to produce a crack is very low (roughly 2% of mass loss is enough).The creation of corrosion crack modifes the local environment at the steel/concrete interface by damaging it and also supports the chloride intrussion; it is then followed by a gradual generalization of corrosion along the bar.
[46]	0.6	Concrete	Ø8, 2Ø8	Prism	30	90 × 100 × 650	Bending	0.3	-	Immersion 3% $NaCl$ (300 days)	-	-	At the crack, salt water may fill the crack and diffusion may occur from the cracked plane. w_{cr}/C ratio can be a suitable parameter to consider in relation to the durability performance of cracked reinforced concrete. The D_a value in the tension zone was higher than in the compression zone.
[82]	0.6	Steel fiber reinforced concrete	-	Prism	-	100 × 100 × 500	Bending	0.5 (no stress), when open 0.8	At supports and midpoint	Salt fog (3.5% $NaCl$)- wetting 1 week, drying 1 week (for 1 year)	Not observed (visually)	-	No corrosion (of steel fibres) should be expected from the cracks thinner than about 0.1 mm.
[224]	0.35, 0.40, 0.45	Concrete	Ø8 with Ø8 stirrups for tension; prestressing strand for compression	Prism	-	100 × 100 × 400	Bending or compressive load	Applied stresses of 0.3 & 0.5 f_c and f_t	-	Immersion 3.5% $NaCl$; salt spray 5% $NaCl$ (30, 40, 60, and 90 days)	-	-	The lower the w/c ratio, the lower the chloride content. Lower compressive stress decreases the penetration of chloride. Tensile stress and high compressive stress increase the chloride ingress. Salt solution immersion produces greater Cl penetration than salt spray. The diffusion coefficient decreases with time and increases with w/c ratio.
[60]	-	Brick	-	Disc	-	Thickness 50, internal Ø50, external Ø150	Expansive core	0.021-0.128	-	Steady-state diffusion	-	0.053	The experimental results show that the diffusion processes of chloride perpendicular to the crack wall in relatively large cracks (width >0.06 mm) are similar to that of the surface. In the case of fine cracks (width <0.053 mm), the reduced diffusion capacity of chloride ions along such fine cracks could be explained by mechanical interaction between the fracture surfaces, tending to impede chloride diffusion.

[61]	0.48	Mortar	-	Disc	-	Thickness 50, internal ø50, external ø150	Expansive core	0.006-0.325	-	Steady state diffusion (14 days)	Reduces chloride diffusion along the crack path	0.2	The diffusion of chloride in the solution filling cracks with an opening greater than 200 µm is not a limiting factor controlling the diffusion process perpendicular to the crack wall, regardless of the age at which the mortar was cracked.The results obtained with 80-100 µm cracks indicate that the diffusion process still occurs, but at a much slower rate (reduction by a factor of 2, regardless of the age).The self-healing potential of the mortar matrix can impede the chloride diffusion along a crack path. When the crack openings are 60 µm or more, the age at which the cracks were induced appears to have no significant effect on the ability of self-healing to impede chloride diffusion along the crack path. In the case of fine cracks (<60 µm), the age at which the crack is induced influences the ability of self-healing to impede chloride diffusion. The effect is stronger in cracks induced in younger mortars (28 days).
[70]	0.4	Concrete (Air entrained / non air entrained)	-	Cylinder	-	Strength-ø101.6,h=203.2 Chloride migration-ø95	Freeze/ thaw damage	-	-	Whitings test (ASTM C1202)- Electrical conductivity	Reduces chloride permeability	-	Self-healing of cracked concrete specimens for three months in water led to a significant reduction in rate of chloride migration: 28-35%, compared to migration in newly cracked specimens.The air entrainment increased the chloride migration slightly.
[225]	0.33	Concrete	-	Dumbell shaped	Specimens to be exposed to Cl were cut out of the original specimen	-	Direct tension	Load 0.65, 0.75, and 0.85 f_t	-	Specimens dried to constant weight first. Capillary absorption (ISO 15148) with 3% $NaCl$ solution for 3 months.	-	-	Axial tensile load has significant influence on the internal porosity of high performance concrete. The total porosity increases with the stress. With the increase of the tensile load, chloride resistance is reduced due to the development of micro-cracks. Especially, when stress is higher than 65% f_t, the apparent chloride diffusion coefficient increased rapidly.
[53]	0.40, 0.53, 0.64	Concrete (15.68-34.3 MPa)	-	Cylinder	-	50, ø100	Brazilian splitting	0.015-0.2	-	Steady state migration (700 h)	-	0.08	The diffusion coefficients of concrete does not increase with increasing crack width up to a "threshold crack width", while, over this value, they start to increase. The diffusion coefficient decreases with an increase of concrete strength at lower crack widths. The addition of fly ash also decreases the diffusion coefficient. This value is found to be around 80 microns, which is a little bit larger than, but close to around 55 microns reported earlier.
[162]	0.4	Concrete	-	Cylinder	-	150, ø75	0, 0.40, 0.75, 0.90 of f_c	Microcracks	-	NT Build 492 (24 h)	-	-	For 40% of the max load, chloride penetration is similar to that of an uncracked sample. For load levels of 75% and 90%, higher penetration depths are obtained. Apparently, the chloride diffusivity of concrete under compression increases rapidly when the applied stress surpasses a certain threshold value.

[56]	0.5	Concrete	-	Prism	-	100 × 100 × 400	Direct tension	0, 0.3, and 0.6 of f_t	-	NT Build 492 (24 h)	-	-	The chloride penetration front into concrete under tensile loading does not progress evenly and there is a prominent special location point of penetration with the highest value of penetration depth. Based on that, it could be proposed that using these penetration depth values instead of the averaged ones would lead to more realistic results, and safety. Comparing the diffusion coefficients of plain and BFS concretes in the unloaded state, BFS concretes showed lower diffusivity on the whole. In the loaded state, depending on the replacement amount of BFS, the application of BFS could be used for significant control over chloride penetration.
[55]	0.35 & 0.5	Concrete	Centered Ø16	Prism	10, 20, 42	100 × 100 × 500	Tension in the rebar	-	-	Specimens were kept vertically in a closed container, in a saline and humid atmosphere subjected to wetting and drying cycles every 2 weeks (tested every 3 months for 12 months).	-	-	The concrete composition seems to be of the highest importance in chloride penetration. The chloride rate increases with concrete microcracking density.HSC, with a low w/c ratio and silica fume, reduces the chloride penetration.
[226]	N.A.	8 and 11 year old concrete in marine environment	N.A.	Cores	N.A.	N.A.	Early age crack	0, 0.1, 0.2, 0.3	One crack	Exposed to marine environment 8-11 years	-	-	The service life calculated from probabilistic method (probability of failure 7 or 10%) is evaluated to be shorter than those obtained from deterministic method.Service life significantly increases with an increase of the cover depth and the time-exponent parameter m.Compared to the field investigations, the allowable crack concept may underestimate the damage state induced by chloride attack.
[74]	0.46	Concrete	-	Cylinder	-	200, Ø100	0.3-0.95 f_c	-	-	ASTM C1202	-	-	It appears that the influence of microcracks on mass transport in concrete cannot be described by its crack length only. Depending on the stress level to which the concrete was subjected, microcracks can close back partially or completely upon unloading. The ability of microcracks to "open" and "close" may suggest that the specific crack area is more sensitive parameter to consider than its crack length, when relating permeability to stresses in concrete.The chloride permeability of concrete (after it is unloaded) appears to be influenced by the occurrence of the critical stress. When the critical stress is exceeded in a concrete specimen, a comparatively large electrical charge is measured. Where the critical stress in a specimen is not exceeded, the increase in the charge passed is marginal in spite of the large increase in microcracks. The chloride permeability of concrete may be influenced by the test condition, i.e. whether the test was carried out under loading condition or after removal of load.
[81]	0.25, 0.27	High performance concrete	N.A.	Prism	-	100 × 100 × 500	Bending	0.3	-	Immersed in simulated sea water, in accordance with ASTM D1141	Crack blocking by corrosion products	-	The corrosion products that formed in the HPC/10%SF were entirely different from the products in the HPC/0SF. In addition, the former were confined to the space provided by the induced crack and the steel/concrete interface, while the latter were more uniformly spread throughout the concrete cover and not confined to either the steel/concrete interface or the main crack. Any corrosion products that form in the silica fume concrete would plug the crack, effectively barring further direct chloride and oxygen exposure to the surface of the steel. However, the more uniform, superficial damage to the steel within the HPC/0SF may be preferable to the localized damage resulting from the presence of silica fume in HPC/10%SF.

[65]	0.5	Concrete	-	Cylinder	-	50, ø100	Artificial crack	0.2, 0.3, 0.5	-	NT Build 492 (varied duration)	-	Influence not pronounced	A higher penetration of chlorides is obtained at the notch tip in comparison with the "un-cracked" part of the test specimens. The penetration depth is increasing with an increasing notch depth. The effect is more pronounced for longer test durations. The influence of the notch width is not clear.
[83]	0.4	Concrete	D19	Beam	Rebar in the middle of the specimen	150 × 200 × 900	Bending	0.16-0.33	-	Cyclic exposure 3%$NaCl$ salt rain (1 day wet 40C,95%RH, 6 days dry 40C, 60% RH) for 45, 95, 144 cycles	-	-	Chloride distribution along the crack surface was uneven under salty-rain and dry cyclic condition. And it was indicated by the result of slight variations of electrical resistances at the middle level zone, that middle level zone is rather humid than those of others just before raining. Chloride contents adjacent to steel bar were remarkably larger than chloride contents in concrete at the same depth but not adjacent to steel bar. This resulted from the presence of conical cracks that exist near the crack surface around the steel bar, in addition to gaps under the horizontally oriented steel bars due to bleeding.
[227]	0.45	Self compacting concrete	-	Cylinder	-	50, ø100	Artificial crack	0.3	-	NT Build 492	-	-	The influence of crack depth on chloride concentration under non-steady state migration is significant for the concrete zone deeper than 20 mm from the surface. The influental zone caused by the crack is limited to the distance of 10 mm at both sides from the crack. The existing equation of Cl transport is not applicable to cracked concrete.
[86]	0.4, 0.55	Concrete	ø10	Beam	40	100 × 100 × 400	Bending	Incipient crack, 0.4, 0.7 (after reloading 0.2, 0.6, 1.0)	-	Weekly cycle of 3 days ponding with 5%$NaCl$ solution followed by 4 days of air drying (32 weeks)	Could affect the corrosion of steel, especially if the crack width is small (less than 0,4 mm). However, it was not measured.	Not possible to set threshold crack width, without taking binder type, w/c, and cover depth into account	Concrete quality (represented by binder type and w/c ratio) may be used to control corrosion in cracked (and uncracked) concrete. Corex slag concretes (where corrosion rate tends to be governed by the (high) concrete resistivity) are less sensitive to the effects of cracking compared to OPC concretes (with low concrete resistivity). Corex slag concretes are considerably less sensitive to changes in w/b ratio compared to OPC concretes.It is not possible to obtain a universal threshold crack width for all concretes below which corrosion proceeds in a similar way to uncracked concrete. Reloading (crack reopening) of corroding RC structures accelerates corrosion by reactivating (reopening) self-healed cracks, widening the existing ones, increasing the load level (i.e. stress in the steel), damaging the concrete/steel and/or aggregate/paste interfaces or a combination thereof. However, the effect of reloading is more significant if the RC structure was actively corroding before reloading.

[63]	0.4	Concrete	-	Cylinder	-	40, ø100	Brazillian splitting + artificial cracks	0.08-0.68	-	NT Build 443 (40 days)	-	-	Chloride diffusion in concrete containing transecting, parallel wall cracks of the considered widths is independent of either the crack width or the crack roughness. Transecting, parallel wall cracks in the range of widths studied in this project behave like free concrete surfaces, greatly contributing to lateral chloride diffusion.Lateral diffusion of chlorides from the crack walls into the bulk of the concrete sample is fairly uniform along the crack length.Chloride diffusion in concrete containing the transcending crack becomes a case of two-dimensional diffusion.At equal w/cm ratio (0.4), concrete containing 25% replacement of cement by blast furnace slag possesses a better ability to resist the ingress of chloride ions than 100% OPC concrete.
[84]	0.485	Mortar	3 levels of steel mesh reinforcement	Prism	-	355.6× 50.8× 76.2	Bending	0.029-0.39	-	AASHTO T259-80 (3% NaCl ponding) 30 and 90 days	Observed for w less than 0.05 mm (formation of calcite). Transport of Cl ions is considerably slower.	0.135	As crack width increased, the effective diffusion coefficient also increased, thus reducing the initiation period of corrosion process. For crack widths lower than 0.135 mm, the effect of crack width on the effective diffusion coefficient was found to be marginal, whereas for cracks wider than 0.135 mm the effective diffusion coefficient increased rapidly. For crack width lower than 0.05 mm, a significant amount of self-healing was observed within the cracks subjected to 30 days sodium chloride solution. The formation of self-healing products slows down the rate of chloride penetration through the crack zone, and further reduces the effective diffusion coefficient of cracked mortar specimens.
[73]	0.22, 0.31, 0.43, 0.46, 0.53	Concrete, mortar	-	Cylinder slices	-	-	-	Specimens were subjected to compressive loads 0.0-1.0 fc	-	AASHTO T 277-83	-	-	Microcracks caused by non-cyclic compressive loading did not affect mass transport properties at load levels below roughly 75% of the maximum capacity of the concrete. However, when the load was increased beyond that point, the concrete became 15 to 20% less resistant to fluid and ion movement. The proportion of aggregate in the mix has a significant effect on the RCPT results; higher volume fractions of aggregate caused a reduction in cell currents. Mortar extracted from the concrete was 2 to 3 times as permeable as its parent concrete when measured by RCPT.The compressive strength and resistance of concrete to mass transport are independent properties.No correlation between the two was found.
[228]	0.38	Concrete	-	Beam	-	100 × 100 × 400	Bending	0, 0.3, and 0.5 of max flexural load	-	Tidal zone: 3.5%$NaCl$ and 12h wet/dry cycles; Spray: 5%$NaCl$ spray for 8h a day, followed by 16 hour drying (full cycle 24 h) (for 35, 70, 120, and 180 days)	-	-	Tensile stress promotes chloride diffusion, while compressive stress inhibits it. The greater the tensile stress, the higher the chloride concentration. Opposite is true for compressed area. Chloride concentration profiles are larger in tidal than in salt spray zone.Diffusion coefficient decreases non-linearly with time. This should be taken into account in service life predictions.

[41]	0.25, 0.45, 0.65	Concrete	2ø10 plain (single crack) and deformed (multicrack)	Prism	25, 45	100 × 100 × 400	Bending	0.1, 0.2, 0.3, 0.5	Single/ multi cracks	3%, 5%, 8%$NaCl$ solution (submerged) (for 7 days and 1 month)	-	-	Specimens with low w/c ratio (0.25) showed lower concentration profile and penetration depth both from exposed surface and around the crack (compared with w/c ratios of 0.45 and 0.65).The penetration depth from the surface of the crack is equal to or slightly higher than that from exposed surface in higher w/c mixes of 0.45 and 0.65. Capillary suction (when it is taking place) has great influence on the movement of ions along with the bulk solution. This fact has great influence, one that is greater than diffusion mechanism, and should not be ignored for real structures.
[229]	0.53	Concrete	-	Prism	-	150 × 75 × 400	Bending	0.05, 0.10, 0.15, 0.20	-	5% NaCl solution immersion (30 and 60 days)	-	-	For both OPC and GGBFS concrete, the larger the surface crack width, the higher the Cl concentration at crack surface. Based on EPMA tests, the influence of ITZ at cracked zone is not as detrimental as in sound concrete. However, aggregates embedded at both cracked zone and crack surface play an important role on Cl concentration distribution. Hence, the effect of concrete mixes cannot be ignored, even for cracked concrete. GGBFS concrete appears to be much more sensitive to cracking compared to OPC concrete, which is probably caused by a large difference in material porosity and binding capacity of chloride ions.
[58]	0.5	Concrete	-	Cylinder	-	50, ø100	Wedge splitting	0.012-0.13	-	NT Build 492	-	0. 012	If the cracks are wider than the critical crack width (in this case, that seems to be 0.012mm), then the crack depth has to be calculated. The part of the crack length where the crack is wider than the critical crack width is the zone where there is rapid chloride ingress. This part of the crack can be defined as Rapid Chloride Ingress Crack Part (RCICP). In designing concrete structures for certain durability, the cover depth which is usually determined for the un-cracked concrete should be increased by this RCICP.
[88]	0.5	Concrete	-	Cylinder	-	50, ø100	Wedge splitting	0.012-0.13	-	Short term: NT Build 492; Long term: immersion in chloride solution with $NaCl$ and $MgCl_2$ (472 days)	Noticed in the long term test. Should not be ingored!	0.012 (short term); 0.05 (long term)	The chloride penetration through cracks is directly proportional to CMOD in both the long term and the short term experiment.Experimental results clearly show that the chloride penetration through cracks in the long term test is much slower than in the short term test. This can most probably partly be explained by crack-healing.
[230]	0.35	Concrete	-	Disc	-	10, ø95	Compressive 5 times repeated static loading (40% and 80% of f_c)	-	-	Chloride migration test (180 h)	-	-	A SF addition of 5 and 10% results in a higher cylinder compressive strength and lower diffusion coefficient at 28 days. Repeated loading does affect D, with highets increases recorded for OPC>5%SF>10%SF. Remarkably, even at 80% loading, 10% SF shows significantly lower D than unloaded OPC.
[231]	0.3, 0.35, 0.4, 0.45	Concrete	-	Disc	-	10, ø95	Compressive 5 times repeated static loading (40% and 80% of f_c)	-	-	Chloride migration test (180 h)	-	-	In chloride laden environment, higher w/c ratio will considerably decrease the service life predicted by the Life-365 model. Loading 5 times to 40% and 80% of the compressive strength decreases the service life for all mixes, especially for concrete with a higher w/c ratio.

REFERENCES

[1] B. Šavija and E. Schlangen, *Chloride ingress in cracked concrete-a literature review,* in *Advances in Modeling Concrete Service Life* (Springer, 2012) pp. 133–142.

[2] K. Tutti, *Corrosion of steel in concrete. Swedish Cement and Concrete Institute*, Tech. Rep. (CIB, Research Report, 1982).

[3] R. François, A. Castel, T. Vidal, and N.-A. Vu, *Long term corrosion behavior of reinforced concrete structures in chloride environment,* Journal de Physique IV France **136**, 285 (2006).

[4] M. G. Richardson, *Fundamentals of durable reinforced concrete* (CRC Press, 2003).

[5] L. Bertolini, B. Elsener, P. Pedeferri, and R. Polder, *Corrosion of steel in concrete: prevention, diagnosis, repair* (Wiley-VCH Verlag GMBH & Co., Weinheim, Germany, 2004).

[6] A. Neville, *Chloride attack of reinforced concrete: an overview,* Mater Struct **28**, 63 (1995).

[7] S. Ahmad, *Reinforcement corrosion in concrete structures, its monitoring and service life prediction—-a review,* Cement Concrete Comp **25**, 459 (2003).

[8] S. Jaffer and C. Hansson, *Chloride-induced corrosion products of steel in cracked-concrete subjected to different loading conditions,* Cement Concrete Res **39**, 116 (2009).

[9] C. Andrade, C. Alonso, and F. Molina, *Cover cracking as a function of bar corrosion: Part 1-experimental test,* Mater Struct **26**, 453 (1993).

[10] C. Alonso, C. Andrade, J. Rodriguez, and J. Diez, *Factors controlling cracking of concrete affected by reinforcement corrosion,* Mater Struct **31**, 435 (1998).

[11] U. Angst, B. Elsener, C. K. Larsen, and Ø. Vennesland, *Critical chloride content in reinforced concrete—a review,* Cement Concrete Res **39**, 1122 (2009).

[12] S. Adiyastuti, *Influence of cracks on chloride induced corrosion in reinforced concrete structural members,* Ph.D. thesis, The University of New South Wales (2005).

[13] *BS 8110 -1. Structural use of concrete. Part 1: Code of practice for design and construction* (British Standards Institution, 1997).

[14] *Corrosion of metals in concrete,* (ACI Committee and American Concrete Institute and International Organization for Standardization, 1994).

[15] *Eurocode 2. Design of Concrete Structures. Part 1: General Rules and Rules for Buildings* (European Committee for Standardisation, 1992).

[16] E. Poulsen and L. Mejlbro, *Diffusion of chloride in concrete: theory and application* (Taylor & Francis, 2005).

[17] A. Küter, M. Geiker, J. Olesen, H. Stang, C. Dauberschmidt, and M. Raupach, *Chloride ingress in concrete cracks under cyclic loading,* in *Proceedings of ConMat '05, Vancouver, Canada*, edited by N. Banthia (2005).

[18] *Chloride migration coefficient from non-steady-state migration experiments* (Nord Test Build 492, 1999).

[19] A. Fick, *On liquid diffusion,* The London, Edinburgh, and Dublin Philosophical Magazine and Journal of Science **10**, 30 (1855).

[20] J. Crank, *The mathematics of diffusion* (Oxford university press, 1979).

[21] R. E. Weyers, *Service life model for concrete structures in chloride laden environments,* ACI Mater J **95** (1998).

[22] G. Glass and N. Buenfeld, *The influence of chloride binding on the chloride induced corrosion risk in reinforced concrete,* Corros Sci **24**, 329 (2000).

[23] Q. Yuan, C. Shi, G. De Schutter, K. Audenaert, and D. Deng, *Chloride binding of cement-based materials subjected to external chloride environment- a review,* Constr Build Mater **23**, 1 (2009).

[24] T. U. Mohammed, T. Yamaji, and H. Hamada, *Chloride diffusion, microstructure, and mineralogy of concrete after 15 years of exposure in tidal environment,* ACI Mater Jl **99** (2002).

[25] A. Guerrero, S. Goni, and V. Allegro, *Durability of class c fly ash belite cement in simulated sodium chloride radioactive liquid waste: Influence of temperature,* J Hazard Mater **162**, 1099 (2009).

[26] H. Justnes, *A review of chloride binding in cementitious systems,* Nordic Concrete Research **21**, 1 (1998).

[27] L. Tang and L.-O. Nilsson, *Chloride binding capacity and binding isotherms of opc pastes and mortars,* Cement Concrete Res **23**, 247 (1993).

[28] C. Arya, N. Buenfeld, and J. Newman, *Factors influencing chloride-binding in concrete,* Cement Concrete Res **20**, 291 (1990).

[29] P. Sandberg, *Studies of chloride binding in concrete exposed in a marine environment,* Cement Concrete Res **29**, 473 (1999).

[30] T. Mohammed and H. Hamada, *Relationship between free chloride and total chloride contents in concrete,* Cement Concrete Res **33**, 1487 (2003).

[31] B. Martín-Peréz, H. Zibara, R. Hooton, and M. Thomas, *A study of the effect of chloride binding on service life predictions,* Cement Concrete Res **30**, 1215 (2000).

[32] *Model code for service life design*, Vol. 34 (Fédération internationale du béton (fib), 2006).

[33] T. Siemes and C. Edvardsen, *Duracrete: service life design for concrete structures.* in *Eighth International Conference on Durability of Building Materials and Components, 8 dbmc* (1999) pp. 1343–1356.

[34] B. Oh and S. Jang, *Effects of material and environmental parameters on chloride penetration profiles in concrete structures,* Cement Concrete Res **37**, 47 (2007).

[35] L. Tang, *Engineering expression of the clinconc model for prediction of free and total chloride ingress in submerged marine concrete,* Cement Concrete Res **38**, 1092 (2008).

[36] J. van Mier, *Fracture processes of concrete: assessment of material parameters for fracture models* (CRC Press, Inc., 1997).

[37] *Non-structural cracks in concrete. Report of a Concrete Society Working Party* (Concrete Society London, 1992).

[38] *Control of cracking in concrete* (Transportation Research Board, 2006).

[39] *Concrete repair manual*, 3rd ed., Vol. 1 (American Concrete Institute, 2007).

[40] R. François and G. Arliguie, *Influence of service cracking on reinforcement corrosion,* J Mater Civil Eng **10**, 14 (1998).

[41] P. Win, M. Watanabe, and A. Machida, *Penetration profile of chloride ion in cracked reinforced concrete,* Cement Concrete Res **34**, 1073 (2004).

[42] B. Pease, *Influence of concrete cracking on ingress and reinforcement corrosion,* Ph.D. thesis, Technical University of Denmark (2010).

[43] *Control of Cracking in Concrete Structures (ACI 224R-01)* (American Concrete Institute, 2001).

[44] *Design of concrete structures. ceb-fip-model-code 1990,* Comite Euro-International du Beton (CEB-fip) (1990).

[45] K. Tammo and T. Thelandersson, *Crack behavior near reinforcing bars in concrete structures,* ACI Struct J **106**, 259 (2009).

[46] N. Gowripalan, A. Sirivivatnon, and C. Lim, *Chloride diffusivity of concrete cracked in flexure,* Cement Concrete Res **30**, 725 (2000).

[47] P. Witherspoon, J. Wang, K. Iwai, and J. Gale, *Validity of cubic law for fluid flow in a deformable rock fracture,* Water Resour Res **16**, 1016 (1980).

[48] C. Aldea, S. Shah, and A. Karr, *Effect of cracking on water and chloride permeability of concrete,* J Mater Civil Eng **11**, 181 (1999).

[49] N. Otsuki, S. Miyazato, N. Diola, and H. Suzuki, *Influences of bending crack and water-cement ratio on chloride-induced corrosion of main reinforcing bars and stirrups,* ACI Mater J **97**, 454 (2000).

[50] M. Şahmaran and I. Yaman, *Influence of transverse crack width on reinforcement corrosion initiation and propagation in mortar beams,* Can J Civil Eng **35**, 236 (2008).

[51] P. Schießl and M. Raupach, *Laboratory studies and calculations on the influence of crack width on chloride-induced corrosion of steel in concrete,* ACI Mater J **94**, 56 (1997).

[52] K. Wang, D. Jansen, and S. Shah, *Permeability study of cracked concrete,* Cement Concrete Res **27**, 381 (1997).

[53] S. Jang, B. Kim, and B. Oh, *Effect of crack width on chloride diffusion coefficients of concrete by steady-state migration tests,* Cement Concrete Res **41**, 9 (2011).

[54] B. Gérard, D. Breysse, A. Ammouche, O. Houdusse, and O. Didry, *Cracking and permeability of concrete under tension,* Mater Struct **29**, 141 (1996).

[55] A. Konin, R. François, and G. Arliguie, *Penetration of chlorides in relation to the microcracking state into reinforced ordinary and high strength concrete,* Mater Struct **31**, 310 (1998).

[56] D. Kim, K. Shimura, and T. Horiguchi, *Effect of tensile loading on chloride penetration of concrete mixed with granulated blast furnace slag,* J Adv Concr Technol **8**, 27 (2010).

[57] E. Brühwiler and F. Wittmann, *The wedge splitting test, a new method of performing stable fracture mechanics tests,* Eng Fract Mech **35**, 117 (1990).

[58] I. Yoon, E. Schlangen, M. de Rooij, and K. van Breugel, *The effect of cracks on chloride penetration into concrete,* Key Eng Mat **348-349**, 769 (2007).

[59] S.-T. Yi, T.-Y. Hyun, and J.-K. Kim, *The effects of hydraulic pressure and crack width on water permeability of penetration crack-induced concrete,* Constr Build Mater **25**, 2576 (2011).

[60] M. Ismail, A. Toumi, R. François, and R. Gagne, *Effect of crack opening on the local diffusion of chloride in inert materials,* Cement Concrete Res **34**, 711 (2004).

[61] M. Ismail, A. Toumi, R. François, and R. Gagne, *Effect of crack opening on the local diffusion of chloride in cracked mortar samples,* Cement Concrete Res **38**, 1106 (2008).

[62] R. François, I. Khan, H. Mercado, and A. Castel, *Influence of mechanical cracks on the development of corrosion mechanicsm,* in *Proceedings of the International Conference on Advances in Construction Materials through Science and Engineering, Hong Kong, China*, edited by C. Leung and K. Wan (2011).

[63] O. Garces Rodriguez and R. Hooton, *Influence of cracks on chloride ingress into concrete,* ACI Mater J **100**, 120 (2003).

[64] G. De Schutter, *Quantification of the influence of cracks in concrete structures on carbonation and chloride penetration,* Mag Concrete Res **51**, 427 (1999).

[65] L. Marsavina, K. Audenaert, G. De Schutter, N. Faur, and D. Marsavina, *Experimental and numerical determination of the chloride penetration in cracked concrete,* Constr Build Mater **23**, 264 (2009).

[66] K. Audenaert, L. Marsavina, and G. De Schutter, *Influence of cracks on the service life of concrete structures in a marine environment,* Key Eng Mat **399**, 153 (2009).

[67] S. Mu, G. De Schutter, and B.-g. Ma, *Non-steady state chloride diffusion in concrete with different crack densities,* Mater Struct **46**, 123 (2013).

[68] P. Van den Heede, M. Maes, and N. De Belie, *Influence of active crack width control on the chloride penetration resistance and global warming potential of slabs made with fly ash+ silica fume concrete,* Const Build Mater (2013).

[69] N. ter Heide, *Crack healing in hydrating concrete*, Master's thesis, Delft University of Technology (2005).

[70] S. Jacobsen, J. Marchand, and L. Boisvert, *Effect of cracking and healing on chloride transport in concrete,* Cement Concrete Res **26**, 869 (1996).

[71] A. Litorowicz, *Identification and quantification of cracks in concrete by optical fluorescent microscopy,* Cement Concrete Res **36**, 1508 (2006).

[72] A. Taheri-Motlagh, *Durability of reinforced concrete structures in aggressive marine environment*, Ph.D. thesis, Delft University of Technology (1998).

[73] H. Samaha and K. Hover, *Influence of microcracking on the mass transport properties of concrete,* ACI Mater J **89**, 416 (1992).

[74] C. Lim, N. Gowripalan, and V. Sirivivatnon, *Microcracking and chloride permeability of concrete under uniaxial compression,* Cement Concrete Comp **22**, 353 (2000).

[75] T. H. Antoni and N. Saeki, *Chloride penetration into fiber reinforced concrete under static and cyclic compressive loading,* in *Proceedings of the Tenth International Conference on Durability of Building Materials and Components, Lyon, France* (2005) pp. 52–59.

[76] C. Aldea, S. Shah, and A. Karr, *Permeability of cracked concrete,* Mater Struct **32**, 370 (1999).

[77] C. Aldea, W.-J. Song, J. Popovics, and S. Shah, *Extent of healing of cracked normal strength concrete,* J Mater Civil Eng **12**, 92 (2000).

[78] J. Rapoport, C. Aldea, S. Shah, B. Ankenman, and A. Karr, *Permeability of cracked steel fiber-reinforced concrete,* J Mater Civil Eng **14**, 355 (2002).

[79] A. Djerbi, S. Bonnet, A. Khelidj, and V. Baroghel-Bouny, *Influence of traversing crack on chloride diffusion into concrete,* Cement Concrete Res **38**, 877 (2008).

[80] T. Mohammed, N. Otsuki, M. Hisada, and T. Shibata, *Effect of crack width and bar types on corrosion of steel in concrete,* J Mater Civil Eng **13**, 194 (2001).

[81] T. Marcotte and C. Hansson, *The influence of silica fume on the corrosion resistance of steel in high performance concrete exposed to simulated sea water,* J Mater Sci **38**, 4765 (2003).

[82] J.-L. Granju and S. Ullah Balouch, *Corrosion of steel fibre reinforced concrete from the cracks,* Cement Concrete Res **35**, 572 (2005).

[83] I. Maruyama, K. Tanaka, and P. Sato, *Distribution of chloride ion in cracked reinforced concrete prism transported by cyclic rain with chloride ion,* in *Seminar on Durability and Lifecycle Evaluation of Concrete Structures, Hiroshima, Japan*, edited by P. e. a. Sato (2006).

[84] M. Şahmaran, *Effect of flexure induced transverse crack and self-healing on chloride diffusivity of reinforced mortar,* J Mater Sci **42**, 9131 (2007).

[85] M. Şahmaran, M. Li, and V. Li, *Transport properties of engineered cementitious composites under chloride exposure,* ACI Mater J **104**, 303 (2007).

[86] M. Otieno, M. Alexander, and H.-D. Beushausen, *Corrosion in cracked and uncracked concrete- influence of crack width, concrete quality and crack reopening,* Mag Concrete Res **62**, 393 (2010).

[87] H.-W. Reinhardt, M. Sosoro, and X.-f. Zhu, *Cracked and repaired concrete subject to fluid penetration,* Mater Struct **31**, 74 (1998).

[88] I. Yoon and E. Schlangen, *Long/short term experimental study on chloride penetration in cracked concrete,* Key Eng Mat **417-418**, 765 (2010).

[89] K. Stanish, R. Hooton, and M. Thomas, *Testing chloride penetration resistence of concrete: a literature review*, Tech. Rep. (Department of Civil Engineering, University of Toronto, 1997).

[90] *Concrete, hardened: accelerated chloride penetration* (Nord Test Build 443, 1995).

[91] *Standard Test Method for Electrical Indication of Concrete's Ability to Resist Chloride Ion Penetration (C1202-97)* (1997).

[92] F.-x. Jiang, F. Wittmann, and T.-J. Zhao, *Influence of sustained compressive load on penetration of chloride ions into neat and water repellent concrete,* in *Proceedings of the First International Conference on Performance-based and Life-cycle Structural Engineering, Hong Kong, China*, edited by J. Teng, J. Dai, S. Law, Y. Xia, and S. Zhu (2012) pp. 992–997.

[93] C. Wang, J. Jiang, G. Sun, J. Han, and Y. Qiao, *The research of the effect of dynamic load and temperature on the diffusion performance of chloride ion in concrete,* Adv Mat Res **163-167**, 3167 (2011).

[94] M. R. de Rooij, K. Van Tittelboom, N. De Belie, and E. Schlangen, *Self-healing Phenomena in Cement-based Materials: State-of-the-Art Report of RILEM Technical Committee 221-SHC: Self-Healing Phenomena in Cement-Based Materials* (Springer, 2013).

[95] C. Edvardsen, *Water permeability and autogenous healing of cracks in concrete,* ACI Mater J **96**, 448 (1999).

[96] T. U. Mohammed, N. Otsuki, and H. Hamada, *Corrosion of steel bars in cracked concrete under marine environment,* J Mater Civil Eng **15**, 460 (2003).

[97] N. Hearn, *Self-sealing, autogenous healing and continued hydration: What is the difference?* Mater Struct **31**, 563 (1998).

[98] W. Ramm and M. Biscoping, *Autogenous healing and reinforcement corrosion of water-penetrated separation cracks in reinforced concrete,* Nucl Eng Des **179**, 191 (1998).

[99] Y. Yang, M. Lepech, E.-H. Yang, and V. Li, *Autogenous healing of engineered cementitious composites under wet-dry cycles,* Cement Concrete Res **39**, 382 (2009).

[100] Y. Yang, E.-H. Yang, and V. C. Li, *Autogenous healing of engineered cementitious composites at early age,* Cement Concrete Res **41**, 176 (2011).

[101] M. Li and V. C. Li, *Cracking and healing of engineered cementitious composites under chloride environment,* ACI Mater J **108** (2011).

[102] L. Tang, L. Nilsson, and P. Basheer, *Resistance of Concrete to Chloride Ingress–Testing and Modelling* (Taylor & Francis Group, 2011).

[103] J. Pacheco, *Corrosion of steel in cracked concrete*, Ph.D. thesis, Delft University of Technology (In preparation).

[104] Y. Goto, *Cracks formed in concrete around deformed tension bars,* in *ACI Journal Proceedings*, Vol. 68 (ACI, 1971).

[105] F. Wittmann, P. Zhang, and T. Zhao, *Application of neutron radiography to study moisture movement in cracked and uncracked concrete,* in *Proceedings of the International Conference on Advances in Construction Materials through Science and Engineering, Hong Kong, China*, edited by C. Leung and K. Wan (2011).

[106] B. Pease, J. Couch, M. Geiker, H. Stang, and W. Weiss, *Assessing the portion of the crack length contributing to water sorption using x-ray absorption measurements on concrete wedge splitting specimens,* ConcreteLife'09: Second International RILEM Workshop on Concrete Durability and Service Life Planning, Haifa, Israel.

[107] E. Schlangen, *Experimental and numerical analysis of fracture processes in concrete*, Ph.D. thesis, Delft University of Technology (1993).

[108] N. Silva, T. Luping, and S. Rauch, *Application of la-icp-ms for meso-scale chloride profiling in concrete,* Mater Struct **46**, 1369 (2013).

[109] G. Wilsch, F. Weritz, D. Schaurich, and H. Wiggenhauser, *Determination of chloride content in concrete structures with laser-induced breakdown spectroscopy,* Constr Build Mater **19**, 724 (2005).

[110] F. Weritz, D. Schaurich, A. Taffe, and G. Wilsch, *Effect of heterogeneity on the quantitative determination of trace elements in concrete,* Anal Bioanal Chem **385**, 248 (2006).

[111] C. Arya and F. Ofori-Darko, *Influence of crack frequency on reinforcement corrosion in concrete,* Cement Concrete Res **26**, 345 (1996).

[112] J. Bolander and S. Saito, *Fracture analyses using spring networks with random geometry,* Eng Fract Mech **61**, 569 (1998).

[113] E. Schlangen and Z. Qian, *3d modeling of fracture in cement-based materials,* Journal of Multiscale Modell **1**, 245 (2009).

[114] P. Grassl and T. Davies, *Lattice modelling of corrosion induced cracking and bond in reinforced concrete,* Cement Concrete Comp **33**, 918 (2011).

[115] M. Gondal, A. Dastageer, M. Maslehuddin, A. Alnehmi, and O. Al-Amoudi, *Sensitivity enhancement at 594.8 nm atomic transition of cl i for chloride detection in the reinforced concrete using libs,* J Environ Sci Heal A **46**, 198 (2011).

[116] C. D. Gehlen, E. Wiens, R. Noll, G. Wilsch, and K. Reichling, *Chlorine detection in cement with laser-induced breakdown spectroscopy in the infrared and ultraviolet spectral range,* Spectroch Acta B **64**, 1135 (2009).

[117] K. Sugiyama, T. Fujii, T. Matsumura, Y. Shiogama, M. Yamaguchi, and K. Nemoto, *Detection of chlorine with concentration of 0.18 kg/m^3 in concrete by laser-induced breakdown spectroscopy,* Appl Optics **49**, 181 (2010).

[118] J. Pacheco, B. Šavija, E. Schlangen, and R. B. Polder, *Assessment of cracks in reinforced concrete by means of electrical resistance and image analysis,* Constr Build Mater **65**, 417 (2014).

[119] A. Michel, A. O. S. Solgaard, B. J. Pease, M. R. Geiker, H. Stang, and J. F. Olesen, *Experimental investigation of the relation between damage at the concrete-steel interface and initiation of reinforcement corrosion in plain and fibre reinforced concrete,* Corros Sci **77**, 308 (2013).

[120] H. Yu and W. Hartt, *Modeling corrosion initiation of reinforcing steel in concrete: effect of non-diffusive coarse aggregate,* J Comp Mater **45**, 153 (2011).

[121] U. M. Angst and R. B. Polder, *Spatial variability of chloride in concrete within homogeneously exposed areas,* Cement Concrete Res **56**, 40 (2014).

[122] J. Pacheco, O. Çopuroğlu, B. Šavija, E. Schlangen, and R. Polder, *Assessment of critical chloride content in reinforced concrete by energy dispersive spectrometry (eds) revisited,* in *Proceedings of the Third International Conference on Concrete Repair, Rehabilitation, and Retrofitting (ICCRRR), Cape Town, South Africa*, edited by M. Alexander, H.-D. Beushausen, F. Dehn, and P. Moyo (2012).

[123] H. M. Jonkers, A. Thijssen, G. Muyzer, O. Copuroglu, and E. Schlangen, *Application of bacteria as self-healing agent for the development of sustainable concrete,* Ecol Eng **36**, 230 (2010).

[124] V. Wiktor and H. M. Jonkers, *Quantification of crack-healing in novel bacteria-based self-healing concrete,* Cement Concrete Comp **33**, 763 (2011).

[125] S. Sangadji and E. Schlangen, *Self healing of concrete structures-novel approach using porous network concrete,* J Adv Concr Technol **10**, 185 (2012).

[126] D. Snoeck, K. Van Tittelboom, S. Steuperaert, P. Dubruel, and N. De Belie, *Self-healing cementitious materials by the combination of microfibres and superabsorbent polymers,* J Intel Mat Syst Struct (2012).

[127] H.-W. Reinhardt and M. Jooss, *Permeability and self-healing of cracked concrete as a function of temperature and crack width,* Cement Concrete Res **33**, 981 (2003).

[128] I.-S. Yoon and E. Schlangen, *Experimental examination on chloride penetration through micro-crack in concrete,* KSCE J Civ Eng **18**, 188 (2014).

[129] L. Ferrara, V. Krelani, M. Geminiani, and R. Gorlezza, *High performance fiber reinforced cementitious composites: autogenously self healing materials,* in *Proceedings of The First Concrete Innovation Conference (CIC), Trondheim, Norway*, edited by H. Justnes (2014).

[130] H. Huang, G. Ye, and D. Damidot, *Characterization and quantification of self-healing behaviors of microcracks due to further hydration in cement paste,* Cement Concrete Res **52**, 71 (2013).

[131] H. Huang, G. Ye, and D. Damidot, *Effect of blast furnace slag on self-healing of microcracks in cementitious materials,* Cement Concrete Res **60**, 68 (2014).

[132] B. Šavija, M. Luković, S. A. S. Hosseini, J. Pacheco, and E. Schlangen, *Corrosion induced cover cracking studied by x-ray computed tomography, nanoindentation, and energy dispersive x-ray spectrometry (eds),* Mater Struct .

[133] Z. Bažant, *Physical model for steel corrosion in concrete sea structures - theory,* J Struct Div-ASCE **105**, 1137 (1979).

[134] J. Molina, C. Alonso, and C. Andrade, *Cover cracking as a function of rebar corrosion: Part 2- numerical model,* Mater Struct **26**, 532 (1993).

[135] Y. Liu and R. Weyers, *Modeling the time-to-corrosion cracking in chloride contaminated reinforced concrete structures,* ACI Mater J **95**, 675 (1998).

[136] J. Ožbolt, F. Oršanić, G. Balabanić, and M. Kušter, *Modeling damage in concrete caused by corrosion of reinforcement: coupled 3d fe model,* Int J Fracture (2012).

[137] B. Šavija, M. Luković, J. Pacheco, and E. Schlangen, *Cracking of the concrete cover due to reinforcement corrosion: A two-dimensional lattice model study,* Constr Build Mater **44**, 626 (2013).

[138] A. Michel, B. Pease, M. Geiker, H. Stang, and J. Olesen, *Monitoring reinforcement corrosion and corrosion-induced cracking using non-destructive x-ray attenuation measurements,* Cement Concrete Res **41**, 1085 (2011).

[139] H. Wong, Y. Zhao, A. Karimi, N. Buenfeld, and W. Jin, *On the penetration of corrosion products from reinforcing steel into concrete due to chloride-induced corrosion,* Corros Sci **52**, 2469 (2010).

[140] A. Michel, B. J. Pease, A. Peterová, M. R. Geiker, H. Stang, and A. E. A. Thybo, *Penetration of corrosion products and corrosion-induced cracking in reinforced cementitious materials: Experimental investigations and numerical simulations,* Cement Concrete Comp **47**, 75 (2014).

[141] I. Balafas and C. Burgoyne, *Modeling the structural effects of rust in concrete cover,* J Eng Mech-ASCE **137**, 175 (2011).

[142] M. Ohtsu and F. Uddin, *Mechanisms of corrosion-induced cracks in concrete at meso- and macro-scales,* J Adv Concr Technol **6**, 419 (2008).

[143] K. J. Trainor, B. W. Foust, and E. N. Landis, *Measurement of energy dissipation mechanisms in the fracture of fiber reinforced ultra high strength cement-based composites,* J Eng Mech-ASCE (2012).

[144] M. Beck, J. Goebbels, and A. Burkert, *Application of x ray tomography for the verification of corrosion processes in chloride contaminated mortar,* Mater Corros **58**, 207 (2007).

[145] A. Česen, T. Kosec, and A. Legat, *Characterization of steel corrosion in mortar by various electrochemical and physical techniques,* Corros Sci (2013).

[146] H. E. Martz, D. J. Scheberk, G. P. Roberson, and P. J. Monteiro, *Computerized tomography analysis of reinforced concrete,* ACI Mater J **90** (1993).

[147] K. Wan, Q. Xu, L. Li, and W. Sun, *3d porosity distribution of partly calcium leached cement paste,* Constr Build Mater **48**, 11 (2013).

[148] K. Lundgren, *Modelling the effect of corrosion on bond in reinforced concrete,* Mag Concrete Res **54**, 165 (2002).

[149] Y. Zhao, H. Dai, and W. Jin, *A study of the elastic moduli of corrosion products using nano-indentation techniques,* Corros Sci **65**, 163 (2012).

[150] G. Constantinides, F.-J. Ulm, and K. Van Vliet, *On the use of nanoindentation for cementitious materials,* Mater Struct **36**, 191 (2003).

[151] M. Luković, B. Šavija, E. Schlangen, and G. Ye, *Micromechanical study of the interface properties of concrete repair systems,* in *Concrete Under Severe Conditions,* edited by Z. Li, W. Sun, C. Miao, K. Sakai, O. Gjørv, and N. Banthia (2013).

[152] X. H. Wang, S. Jacobsen, J. Y. He, Z. L. Zhang, S. F. Lee, and H. L. Lein, *Application of nanoindentation testing to study of the interfacial transition zone in steel fiber reinforced mortar,* Cement Concrete Res **39**, 701 (2009).

[153] V. C. Li, H. Horii, P. Kabele, T. Kanda, and Y. Lim, *Repair and retrofit with engineered cementitious composites,* Eng Fract Mech **65**, 317 (2000).

[154] M. Şahmaran, V. Li, and C. Andrade, *Corrosion resistance performance of steel-reinforced engineered cementitious composite beams,* ACI Mater J **105**, 243 (2008).

[155] J. Zhou, S. Qian, M. G. S. Beltran, G. Ye, K. van Breugel, and V. C. Li, *Development of engineered cementitious composites with limestone powder and blast furnace slag,* Mater Struct **43**, 803 (2010).

[156] G. T. Herman, *Fundamentals of computerized tomography: image reconstruction from projections* (Springer, 2009).

[157] J. F. Barrett and N. Keat, *Artifacts in ct: Recognition and avoidance,* Radiographics **24**, 1679 (2004).

[158] W. C. Oliver and G. M. Pharr, *Measurement of hardness and elastic modulus by instrumented indentation: Advances in understanding and refinements to methodology,* J Mater Res **19**, 3 (2004).

[159] I. S. Darma, T. Sugiyama, and M. A. B. Promentilla, *Application of x-ray ct to study diffusivity in cracked concrete through the observation of tracer transport,* J Adv Concr Technol **11**, 266 (2013).

[160] Z. Yang, W. Ren, M. Mostafavi, S. A. McDonald, and T. J. Marrow, *Characterisation of 3d fracture evolution in concrete using in-situ x-ray computed tomography and digital volume correlation,* in *Proceedings of theEighth International Conference on Fracture Mechanics of Concrete and Concrete Structures, Toledo, Spain*, edited by J. van Mier, G. Ruiz, C. Andrade, R. Yu, and X. Zhang (2013).

[161] B. Šavija, J. Pacheco, and E. Schlangen, *Lattice modeling of chloride diffusion in sound and cracked concrete,* Cement Concrete Comp **42**, 30 (2013).

[162] M. Rahman, W. Al-Kutti, M. Shazali, and M. Baluch, *Simulation of chloride migration in compression-induced damage in concrete,* J Mater Civil Eng **24**, 789 (2012).

[163] M. Boulfiza, K. Sakai, N. Banthia, and H. Yoshida, *Prediction of chloride ions ingress in uncracked and cracked concrete,* ACI Mater J **100**, 38 (2003).

[164] J. Ožbolt, G. Balabanić, G. Periškić, and M. Kušter, *Modelling the effect of damage on transport processes in concrete,* Constr Build Mater **24**, 1638 (2010).

[165] L. Wang and T. Ueda, *Mesoscale modelling of the chloride diffusion in cracks and cracked concrete,* J Adv Concr Technol **9**, 241 (2011).

[166] H. Sadouki and J. van Mier, *Meso-level analysis of moisture flow in cement composites using a lattice-type approach,* Mater Struct **30**, 579 (1997).

[167] J. Bolander and S. Berton, *Simulation of shrinkage induced cracking in cement composite overlays,* Cement Concrete Comp **26**, 861 (2004).

[168] P. Grassl, *A lattice approach to model flow in cracked concrete,* Cement Concrete Comp **31**, 454 (2009).

[169] P. Grassl, C. Fahy, D. Gallipoli, and J. Bolander, *A lattice model for fracture and mass transport in concrete,* in *Proceedings of the Second International Conference on Microstructural-related Durability of Cementitious Composites, Amsterdam, Netherlands*, edited by G. Ye, K. van Breugel, and C. Miao (2012).

[170] H. Nakamura, W. Srisoros, R. Yashiro, and M. Kunieda, *Time-dependent structural analyisis considering mass transfer to evaluate deterioration process of rc structures,* J Adv Concr Technol **4**, 147 (2006).

[171] Wikipedia, *Voronoi diagram,* http:/http://en.wikipedia.org/wiki/Voronoi_diagram (Accessed: 16-09-2014).

[172] M. Yip, J. Mohle, and J. Bolander, *Automated modeling of three-dimensional structural components using irregular lattices,* Comput-Aided Civ Inf **20**, 393 (2005).

[173] Z. Qian, *Multiscale modeling of fracture processes in cementitious materials*, Ph.D. thesis, Delft University of Technology (2012).

[174] E. Landis and J. Bolander, *Understanding material behavior by integrating numerical simulation with 3d microstructural imaging,* in *Proceedings of the International Conference on Advances in Construction Materials through Science and Engineering, Hong Kong, China*, edited by C. Leung and K. Wan (2011).

[175] A. Delagrave, J. Bigas, J. Ollivier, J. Marchand, and M. Pigeon, *Influence of the interfacial zone on the chloride diffusivity of mortars,* Adv Cem Based Mater **5**, 86 (1997).

[176] C. Moukarzel and H. Herrmann, *A vectorizable random lattice,* J Stat Phys **68**, 911 (1992).

[177] S. Vasić, I. Smith, and E. Landis, *Finite element techniques and models for wood fracture mechanics,* Wood Sci Technol **39**, 3 (2005).

[178] E. Schlangen, P. Flewitt, G. Smith, A. Crocker, and A. Hodgkins, *Computer modelling of crack propagation in porous reactor core graphite,* Key Eng Mat **452-453**, 729 (2011).

[179] E. Schlangen and E. Garboczi, *Fracture simulations of concrete using lattice models: computational aspects,* Eng Fract Mech **57**, 319 (1997).

[180] G. Lilliu, *3D analysis of fracture processes in concrete,* Ph.D. thesis, Delft University of Technology (2007).

[181] J. Bolander and N. Sukumar, *Irregular lattice model for quasistatic crack propagation,* Phys Rev B **71** (2005).

[182] P. Grassl and M. Jirásek, *Meso-scale approach to modelling the fracture process zone of concrete subjected to uniaxial tension,* Int J Solids Struct **47**, 957 (2010).

[183] R. Lewis, P. Nithiarasu, and K. Seetharamu, *Fundamentals of the finite element method for heat and fluid flow* (John Wiley & Sons, Ltd, 2004) p. 341.

[184] S. Caré and E. Hervé, *Application of a n-phase model to the diffusion coefficient of chloride in mortar,* Transport Porous Med **56**, 119 (2004).

[185] B. Oh and S. Jang, *Prediction of diffusivity of concrete based on simple analytic equations,* Cement Concrete Res **34**, 463 (2004).

[186] L. Tang *et al.*, *Guideline for practical use of methods for testing the resistance of concrete to chloride ingress,* EU-Project CHLORTEST, Project No: G6RD-CT-2002 **855** (2005).

[187] C. Yang and L. Wang, *The diffusion characteristic of concrete with mineral admixtures between salt ponding test and accelerated chloride migration test,* Mater Chem Phys **85**, 266 (2004).

[188] R. Parsons, *Handbook of electrochemical constants* (Butterworths, 1959).

[189] D. Hill, *Diffusion coefficients of nitrate, chloride, sulphate and water in cracked and uncracked chalk,* J Soil Sci **35**, 27 (1984).

[190] A. Soive and V. Baroghel-Bouny, *Influence of gravel distribution on the variability of chloride penetration front in saturated uncracked concrete,* Constr Build Mater **34**, 63 (2012).

[191] B. Šavija, M. Luković, and E. Schlangen, *Lattice modeling of rapid chloride migration in concrete,* Cement Concrete Res **61**, 49 (2014).

[192] M. De Rooij, R. Polder, and H. Van Oosten, *Validation of service life performance of in situ concrete by tem and rcm measurements,* HERON **52**, 225 (2007).

[193] Z. Yu and G. Ye, *New perspective of service life prediction of fly ash concrete,* Constr Build Mater **48**, 764 (2013).

[194] E. Samson and J. Marchand, *Numerical solution of the extended nernst-planck model,* J Colloid Interf Sci **215**, 1 (1999).

[195] O. Truc, J.-P. Ollivier, and L. Nilsson, *Numerical solution of multi-species transport trough saturated concrete during a migration test - msdiff code,* Cement Concr Res **30**, 1581 (2000).

[196] K. Krabbenhøft and J. Krabbenhøft, *Application of the poisson-nernst-planck equations to the migration test,* Cement Concr Res **38**, 77 (2008).

[197] Q. Liu, L. Li, D. Easterbrook, and J. Yang, *Multi-phase modelling of ionic transport in concrete when subjected to an externally applied electric field,* Eng Struct **42**, 201 (2012).

[198] L. Tang and L. Nilsson, *Rapid determination of the chloride diffusivity in concrete by applying an electric field,* ACI Mater J **89** (1993).

[199] *Resistance of concrete to chloride ion penetration,* AASHTO 259 (1980).

[200] M. Sillanpää, *The effect of cracking on chloride diffusion in concrete,* Master's thesis, Aalto University (2010).

[201] P. Spiesz, M. Ballari, and H. Brouwers, *Rcm: A new model accounting for the non-linear chloride binding isotherm and the non-equilibrium conditions between the free-and bound-chloride concentrations,* Constr Build Mater **27**, 293 (2012).

[202] F. Nilenius, F. Larsson, K. Lundgren, and K. Runesson, *A 3d/2d comparison between heterogeneous mesoscale models of concrete,* in *Multi-Scale Modeling and Characterization of Infrastructure Materials* (Springer, 2013) pp. 249–259.

[203] S. Yoon, K. Wang, W. Weiss, and S. Shah, *Interaction between loading, corrosion, and serviceability of reinforced concrete,* ACI Mater J **97**, 637 (2000).

[204] J. Cabrera, *Deterioration of concrete due to reinforcement steel corrosion,* Cement Concrete Comp **18**, 47 (1996).

[205] H.-S. Lee, T. Noguchi, and F. Tomosawa, *Evaluation of the bond properties between concrete and reinforcement as a function of the degree of reinforcement corrosion,* Cement Concrete Res **32**, 1313 (2002).

[206] R. François, I. Khan, and V. Dang, *Impact of corrosion on mechanical properties of steel embedded in 27-year-old corroded reinforced concrete beams,* Mater Struct **46**, 899 (2013).

[207] K. Toongoenthong and K. Maekawa, *Simulation of coupled corrosive product formation, migration into crack and propagation in reinforced concrete,* J Adv Concr Technol **3**, 253 (2005).

[208] K. Tran, H. Nakamura, K. Kawamura, and M. Kunieda, *Analysis of crack propagation due to rebar corrosion using rbsm,* Cement Concrete Comp **33**, 906 (2011).

[209] Martín-Peréz, *Service life modelling of R.C. highway srtuctures exposed to chlorides,* Ph.D. thesis, University of Toronto (1999).

[210] S. Pantazopoulou and K. Papoulia, *Modeling cover-cracking due to reinforcement corrosion in rc structures,* J Eng Mech-ASCE **127**, 342 (2001).

[211] B. Jang and B. Oh, *Effects of non-uniform corrosion on the cracking and service life of reinforced concrete structures,* Cement Concrete Res **40**, 1441 (2010).

[212] S. Guzmán, J. Gálvez, and J. Sancho, *Modelling of corrosion-induced cover cracking in reinforced concrete by an embedded cohesive crack finite element,* Eng Fract Mech **93**, 92 (2012).

[213] T. Pan and Y. Lu, *Stochastic modeling of reinforced concrete cracking due to nonuniform corrosion: Fem-based cross-scale analysis,* J Mater Civil Eng **24**, 698 (2012).

[214] E. Schlangen, E. Koenders, and K. van Breugel, *Influence of internal dilation on the fracture behavior of multi-phase materials,* Eng Fract Mech **74**, 18 (2007).

[215] L. Liu, G. Ye, E. Schlangen, H. Chen, Z. Qian, W. Sun, and K. van Breugel, *Modeling of the internal damage of saturated cement paste due to ice crystallization pressure during freezing,* Cement Concrete Comp **33**, 562 (2011).

[216] C. Anaç, E. Schlangen, and O. Çopuroğlu, *Lattice model implementation on alkali silica reaction gel expansion in a reacted concrete medium,* in *Proceedings of the Third International Conference on Concrete Repair, Rehabilitation, and Retrofitting (ICCRRR), Cape Town, South Africa*, edited by M. Alexander, H.-D. Beushausen, F. Dehn, and P. Moyo (2012).

[217] U. Angst, B. Elsener, A. Jamali, and B. Adey, *Concrete cover cracking owing to reinforcement corrosion - theoretical considerations and practical experience,* Mater Corros **63**, 1069 (2012).

[218] L. Chernin, D. Val, and M. Stewart, *Prediction of cover crack propagation in rc structures caused by corrosion,* Mag Concrete Res **64**, 95 (2012).

[219] J. González, C. Andrade, C. Alonso, and S. Feliu, *Comparison of rates of general corrosion and maximum pitting penetration on concrete embedded steel reinforcement,* Cement Concrete Res **25**, 257 (1995).

[220] S. Meijers, *Computational modelling of chloride ingress in concrete,* Ph.D. thesis, Delft University of Technology (2003).

[221] H. Ye, N. Jin, X. Jin, and C. Fu, *Model of chloride penetration into cracked concrete subject to drying–wetting cycles,* Constr Build Mater **36**, 259 (2012).

[222] K. Van Breugel, *Simulation of hydration and formation of structure in hardening cement-based materials,* Ph.D. thesis, Delft University of Technology (1991).

[223] A. Akhavan and F. Rajabipour, *Evaluating ion diffusivity of cracked cement paste using electrical impedance spectroscopy,* Mater Struct **46**, 697 (2013).

[224] L. Guoping, H. Fangjian, and W. Yongxian, *Chloride ion penetration in stressed concrete,* J Mater Civil Eng **23**, 1145 (2011).

[225] F.-x. Jiang, I. Xin, T.-j. Zhao, and W. X-m, *Inner damage and anti-chloride penetration of high-performance concrete under axial tensile load,* Adv Mat Res **261-263**, 1210 (2011).

[226] S. Kwon, U. Na, S. Park, and S. Jung, *Service life prediction of concrete wharves with early-aged crack: Probabilistic approach for chloride diffusion,* Struct Saf **31**, 75 (2009).

[227] S. Mu, G. De Schutter, and B. Ma, *Influence of crack depth on chloride transport of cracked self-compacting concrete under non-steady state migration test,* Adv Mat Res **328**, 1331 (2011).

[228] Y. Wang, C. Lin, and Y. Cui, *Experiments of chloride ingression in loaded concrete members under the marine environment,* J Mater Civil Eng (2013).

[229] H. Ye, Y. Tian, N. Jin, and C. Fu, *Influence of cracking on chloride diffusivity and moisture influential depth in concrete subjected to simulated environmental conditions,* Constr Build Mater **47**, 66 (2013).

[230] W.-m. Zhang and H.-j. Ba, *Effect of silica fume addition and repeated loading on chloride diffusion coefficient of concrete,* Mater Struct **46**, 1183 (2013).

[231] W.-M. Zhang, Y.-Z. Liu, H.-Z. Xu, and H.-J. Ba, *Chloride diffusion coefficient and service life prediction of concrete subjected to repeated loadings,* Mag Concrete Res (2012).

SUMMARY

Chloride induced corrosion of reinforcing steel is recognized as the most common deterioration mechanism affecting reinforced concrete structures. As such, it has been in focus of research for more than thirty years. Numerous studies of chloride ingress, corrosion initiation, and corrosion propagation have been conducted. Most studies of chloride ingress focused on sound (uncracked) concrete. In reality, however, concrete is almost never crack free. Cracks form either in the construction phase (early age cracks, for example shrinkage cracks), or during the use of a structure (e.g. cracks caused by mechanical loads). While these cracks are usually not detrimental to the load bearing capacity of a structure, they are potentially a threat to its durability.

Cracks occurring in the concrete cover diminish its protective capabilities, and present fast routes for ingress of deleterious species (e.g. chloride ions). While national and international design codes provide guidelines and limits for maximum crack widths in aggressive environmental conditions, these are often empirical and based on rules of thumb. As a result, only the surface crack width is considered. However, recent findings seem to indicate that an even more important factor could be the zone of debonding which occurs at the steel/concrete interface due to cracking of the cover.

In this thesis, an attempt is made to increase the body of knowledge related to chloride ingress in cracked concrete. Laboratory experiments and numerical simulations were used during the study.

Experimental data available in the literature is, at the moment, inconclusive. For years researchers have been trying to find a so-called "threshold" crack width for chloride (or water) transport, below which concrete can be treated as sound (uncracked). In this quest, mostly plain concrete specimens were used. While this approach resulted in increased understanding of chloride transport in cracks, it failed to address an important mechanism which affects *only* reinforced concrete - debonding occurring at the steel/concrete interface. Only recently have researchers focused their attention on the effect of damage at the steel/concrete interface on transport behavior and corrosion of reinforcement in concrete. In this thesis, compact reinforced specimen geometry is adopted, which mimics (with respect to crack geometry) the behavior of reinforced concrete beams. Cracked specimens were subjected to weekly cycles of salt water wetting and drying for a prolonged period of time. After the exposure, two-dimensional chloride maps were obtained by means of LIBS (Laser Induced Breakdown Spectroscopy), in collaboration with BAM Federal Institute for Materials Research and Testing in Berlin, Germany. The results showed that, once damage occurs at the steel/concrete interface, chloride ions penetrate parallel to the reinforcement, which could possibly be very harmful with respect to reinforcement corrosion.

It has been frequently reported in the literature that autogeneous healing of cracks can reduce chloride ingress in concrete. To examine this, experiments were performed to investigate the influence of the curing ("healing") regimen on chloride penetration depth in cracked specimens. Two regimens (submerged in water and in 95% relative humidity) both enabled the tested specimens to reduce chloride ingress in cracks, compared to the control series. It was found that, under favorable conditions, autogeneous crack healing does have a positive effect on chloride penetration resistance.

Corrosion induced cover cracking has been extensively studied in recent years. When reinforcing steel corrodes, it causes expansive pressure on the surrounding concrete. As a consequence, concrete cover cracks. In the thesis, cracking induced by accelerated corrosion was studied using X-ray computed tomography. Mechanical properties of the rust layer were determined using the nanoindentation technique. Valuable insights were obtained, especially for fine tuning of numerical models.

Numerical models can be of use in understanding complex problems. In this thesis, a model for chloride ingress in cracked concrete, based on the lattice modeling approach, was developed. Concrete is discretized as a set of one dimensional "pipe" elements through which the transport takes place. The model is coupled to the lattice fracture model, which enabled simulating chloride penetration around cracks in concrete. The model was validated using experimental results from the literature.

Numerous experiments make use of external electrical field to accelerate chloride ingress. Therefore, the developed model was extended to enable modeling chloride ingress in accelerated experiments. Based on the lattice modeling approach and utilizing the Characteristic Galerkin scheme, the approach enables using smaller elements compared to the conventional Galerkin approach. Apart from its computational efficiency, it showed that the, under accelerated conditions, chloride front ahead of a crack may be much more sharp

compared to the natural (i.e. diffusion) conditions. Therefore, it is questionable if findings from accelerated experiments on cracked specimens can be directly applied to "real" exposure conditions.

Cracking of the concrete cover caused by reinforcement corrosion is also frequently modeled. In this thesis, the two-dimensional Delft lattice model was used to model it. First, the developed model was validated using a set of well-documented experiments from the literature. It was found that penetration of corrosion products into pores and open cracks needs to be considered in order to obtain good match with the experiments. Furthermore, it was observed that the internal pressure which causes cracking is not a deterministic value, but that it depends on local mechanical properties inside the concrete. Also, two hypothetical pitting scenarios were tested and compared to then uniform corrosion case. It appears (according to the 2D model) that pitting is more detrimental for the concrete cover than uniform corrosion. This means that cover cracking will occur at lower internal pressure compared to the uniform corrosion case.

Techniques employed in this thesis (such as LIBS, X-ray computed tomography, and nanoindentation) can be used in the same or similar way for studying other deterioration mechanisms. Also, the chloride transport model can be easily modified to model other transport processes, such as moisture transport, sulfate transport, or carbon dioxide ingress. Employing a staggered scheme used in this thesis, these transport processes can be coupled with the mechanical analysis to model the influence of combined actions on reinforced concrete structures.

SAMENVATTING

Corrosie, veroorzaakt door chlorideindringing, is een van de meest voorkomende oorzaken van verslechtering van gewapende betonconstructies. Er wordt al ruim dertig jaar onderzoek verricht naar dit onderwerp. Talrijke studies van chlorideindringing, initiatie van corrosie, en propagatie van corrosie zijn gepubliceerd. De meerderheid van deze studies zijn gericht op scheurvrij beton. Beton is vrijwel niet scheurvrij. Scheuren vormen tijdens de verharding van het beton (bijvoorbeeld krimpscheuren) of gedurende het gebruik van de constructie (bijvoorbeeld scheuren die ontstaan zijn door belasting). Hoewel deze scheuren niet schadelijk zijn voor de draagcapaciteit van de constructie, kunnen ze wel een bedreiging vormen voor de duurzaamheid.

Scheuren die ontstaan in de dekkingslaag zijn snelle routes voor chlorideindringing. Hoewel er nationale en internationale richtlijnen gelden om de scheurwijdte in agressieve milieuklassen beperkt te houden, worden deze meestal gebaseerd op vuistregels en ervaring. Daardoor komt alleen de scheurwijdte op het oppervlak in aanmerking. Uit recent onderzoek is echter gebleken dat de schade die aan het grensvlak tussen wapening en beton ontstaat door het scheuren van de dekkingslaag belangrijker kan zijn dan de scheurwijdte op het oppervlak zelf.

Dit proefschrift is geschreven met het doel om de kennis over chlorideindringing te vergroten. Zowel experimenten als rekenmodellen zijn toegepast in dit onderzoek.

Gegevens uit de literatuur zijn momenteel niet maatgevend. Jarenlang probeerden de onderzoekers een zogeheten "drempel"scheurwijdte voor chloride- of watertransport te vinden, waaronder geen invloed van de scheur op het transport bestaat. Hiervoor zijn meestal betonnen proefstukken zonder wapening gebruikt. Hoewel de kennis over chlorideindringing in gescheurd beton enorm gegroeid is, ontbrak echter een belangrijk fenomeen dat *alleen* waarneembaar was bij gewapend beton - namelijk het onthechten van de wapening in het beton. De laatste tijd zijn de onderzoeken verricht op de invloed van het onthechten van de wapening in het beton op het transport van chloriden en wapeningscorrosie. In dit proefschrift zijn compacte proefstukken van gewapend beton gebruikt om het gedrag van balken van gewapend beton te simuleren (vergelijkbaar scheurmechanisme). Gescheurde proefstukken zijn blootgesteld aan wekelijkse cycli van bevochtigen met zout water en drogen, voor een lange tijdsperiode. Na het blootstellen van deze proefstukken zijn twee-dimensionele chlorideprofielen in kaart gebracht met behulp van LIBS (Laser Induced Breakdown Spectroscopy), in samenwerking met BAM Federal Institute for Materials Research and Testing in Berlijn, Duitsland. Uit de resultaten blijkt dat, als er schade ontstaat aan het grensvlak tussen wapening en beton, chlorideindringing parallel met het wapeningsstaal voorkomt, wat mogelijk kan leiden tot schadelijke effecten met betrekking tot de wapeningscorrosie.

In de literatuur werd altijd gesproken over de invloed van het zelfherstel van scheuren op chlorideindringing. Om dit te onderzoeken, werden experimenten uitgevoerd om de invloed van type nabehandeling (herstelbevordering) op de chlorideindringingsdiepte in gescheurde proefstukken te bepalen. Twee regimes (ondergedompeld in water en in 95% luchtvochtigheid) waren beide bevordelijk voor de vermindering van chlorideindringing in scheuren, in vergelijking met de controleserie. Het blijkt dat, onder gunstige voorwaarden, zelfherstel van scheuren een positief effect heeft op chlorideindringing.

Recent is veel onderzoek verricht op het gebied van scheurvorming van de betonnen deklaag veroorzaakt door corrosie. Als wapeningsstaal corrodeert, wordt omliggend beton onder druk gezet. Dit leidt tot scheurvorming in de betonnen deklaag. In dit proefschrift is dit onderzocht door middel van X-ray computed tomography (CT). Mechanische eigenschappen van de roest werden onderzocht door middel van nanoindentatie. Dit onderzoek heeft geleid tot waardevolle resultaten, vooral op het gebied van de optimalisatie van rekenmodellen.

Rekenmodellen zijn nuttig om complexe problemen op te vatten. In dit proefschrift is op basis van het lattice model, een numeriek model voor chloride indringing in gescheurd beton ontwikkeld. Het beton werd gediscretiseerd als reeks van eendimensionale "buis" elementen door welke transport plaatsvindt. Het model is gekoppeld aan het lattice scheurmodel, waardoor het mogelijk werd om chlorideindringing in gescheurd beton te simuleren. Het model werd met experimentele gegevens uit de literatuur gevalideerd.

Talrijke experimenten gebruiken een extern elektrisch veld om chlorideindringing te versnellen. En om chloride indringing in versnelde experimenten te kunnen simuleren werd dit model uitgebreid. Gebaseerd op het lattice model en gebruik makend van het Characteristic Galerkin schema, is het mogelijk om in dit

model kleinere elementen te gebruiken, in vergelijking met de conventionele Galerkin benadering. Naast de computationele efficiëntie, werd aangetoond dat, onder versnelde omstandigheden, het chloridefront voor de scheur veel scherper is in vergelijking met de natuurlijke (diffusie) conditie. Daarom is het twijfelachtig of de resultaten van versnelde experimenten op gescheurde proefstukken direct verbonden kunnen worden met "realistische" condities.

Tevens zijn de scheurvormingen van de betonnen deklaag, door corrosie, gesimuleerd. In dit proefschrift is voor deze simulaties gebruik gemaakt van het 2D Delft lattice model. Allereerst werd het model gevalideerd door een reeks goed gedocumenteerde experimenten uit de literatuur. Hieruit bleek dat de indringing van roest in poriën en scheuren in de gaten gehouden moet worden om goede resultaten te verkrijgen. Bovendien werd gevonden dat de druk die scheuren creëert niet als deterministisch gezien kan worden, maar dit hangt af van de lokale mechanische eigenschappen van het beton rondom het staal. Ook zijn twee hypothetische scenario's van putcorrosie onderzocht en vergeleken met de uniforme corrosie. Het blijkt (uit het 2D model) dat putcorrosie veel schadelijker is in vergelijking met uniforme corrosie. Dit heeft als gevolg dat de scheur reeds vormt bij lagere interne druk.

Technieken die in dit proefschrift zijn toegepast (zoals LIBS, X-ray computed tomography, en nanoindentatie) kunnen op dezelfde of soortgelijke manier voor de studie van andere verslechteringsmechanismen worden gebruikt. Het chlorideindringing model kan gemakkelijk gemodificeerd worden om andere transportprocessen te kunnen simuleren, zoals watertransport, sulfaattransport of kooldioxide-indringing. Door gebruik te maken van het schema ontwikkeld in dit proefschrift, kunnen deze processen gekoppeld worden aan de mechanische analyse om de invloed van gecombineerde belasting op gewapend beton te simuleren.

CURRICULUM VITÆ

Branko ŠAVIJA

06-11-1985	Born in Belgrade, Serbia.

EDUCATION AND WORK EXPERIENCE

2000–2004	10^{th} Belgrade Gymnasium "Mihajlo Pupin", Belgrade, Serbia
2004–2009	Student Faculty of Civil Engineering, University of Belgrade, Serbia
2010–2014	PhD student Delft University of Technology, the Netherlands *Thesis:* Experimental and numerical investigation of chloride ingress in cracked concrete *Promotor:* Prof. dr. ir. E. Schlangen
Sep 2014 –	Post-doc researcher Delft University of Technology, the Netherlands
e-mail	shavijabranko@yahoo.com

LIST OF PUBLICATIONS

JOURNAL PUBLICATIONS

1. **B. Šavija**, M. Luković, and E. Schlangen *Lattice modeling of rapid chloride migration in concrete*, Cement and Concrete Research **61**:49-63 (2014).
2. **B. Šavija**, M. Luković, S.A.S. Hosseini, J. Pacheco, and E. Schlangen *Corrosion induced cover cracking studied by X-ray computed tomography, nanoindentation, and energy dispersive X-ray spectrometry (EDS)*, Materials and Structures, (April 2014).
3. **B. Šavija**, M. Luković, J. Pacheco, and E. Schlangen *Cracking of the concrete cover due to reinforcement corrosion: A two-dimensional lattice model study*, Construction and Building Materials **44**:626-638 (2013).
4. **B. Šavija**, J. Pacheco, and E. Schlangen *Lattice modeling of chloride diffusion in sound and cracked concrete*, Cement and Concrete Composites **42**:30-40 (2013).
5. M. Luković, **B. Šavija**, H. Dong, E. Schlangen, and G. Ye *Micromechanical study of the interface properties in concrete repair systems*, Journal of Advanced Concrete Technology **12**:320-339 (2014).
6. M. Luković, H. Dong, **B. Šavija**, E. Schlangen, G. Ye, and K. van Breugel *Tailoring strain-hardening cementitious composite repair systems through numerical experimentation*, Cement and Concrete Composites **53**:200-213 (2014).
7. J. Pacheco, **B. Šavija**, E. Schlangen, and R.B. Polder *Assessment of cracks in reinforced concrete by means of electrical resistance and image analysis*, Construction and Building Materials **65**:417-426 (2014).
8. M. Nefovska-Danilović, M. Petronijević, and **B. Šavija** *Traffic-induced vibrations of frame structures*, Canadian Journal of Civil Engineering **40**:158-171 (2013).

CONFERENCE PROCEEDINGS

1. **B. Šavija**, J. Pacheco, E. Schlangen, S. Millar, T. Eichler, and G. Wilsch *Chloride ingress in cracked concrete studied using Laser Induced Breakdown Spectroscopy*, In: K. van Breugel and E.A.B. Koenders, editors, Proceedings of the 1st Ageing of Materials & Structures Conference, Delft, The Netherlands, 26-28 May 2014.
2. **B. Šavija**, M. Luković, and E. Schlangen *Modeling the rapid chloride migration test for concrete using the lattice model and characteristic Galerkin approach*, In: R. de Borst, H. Mang, G. Meschke, and N. Bićanić, editors, Proceedings of Computational Modelling of Concrete Structures (EURO-C), pages 629-638, CRC Press, 2014.
3. **B. Šavija**, M. Luković, and E. Schlangen, *Lattice modeling of cover cracking due to reinforcement corrosion*, In: Z.J. Li, W. Sun, C.W. Miao, K. Sakai, and O.E. Gjørv, editors, Proceedings of the Seventh International Conference on Concrete Under Severe Conditions - Environment and Loading, pages 1151-1163, RILEM publications S.A.R.L., 2013.
4. **B. Šavija**, J. Pacheco, and E. Schlangen *Lattice based simulation of chloride ingress in uncracked and cracked concrete: Model validation*, In: J.G.M. van Mier, G. Ruiz, C. Andrade,

R.C. Yu, and X. Zhang, editors, Proceedings of the VIII International conference on fracture mechanics of concrete and concrete structures, pages 1941-1952, 2013.

5. **B. Šavija**, J. Pacheco, E. Schlangen, and R.B. Polder *Modified wedge splitting test (MWST)—a simple tool for durability investigations of reinforcement corrosion in cracked concrete*, In: M.G. Alexander, H.D. Beushausen, F. Dehn, and P. Moyo, editors, Proceedings of the Third International Conference on Concrete repair, rehabilitation and retrofitting (ICCRRR-3), CRC Press, 2012.

6. **B. Šavija**, J. Pacheco, E. Schlangen, and R.B. Polder *Meso-scale simulation of chloride ingress in cracked concrete*, In: G. Ye, K. van Breugel, W. Sun, and C. Miao, editors, Proceedings of the Second International Conference on Microstructural-related Durability of cementitious composites, RILEM publications S.A.R.L., 2012.

7. **B. Šavija** and E. Schlangen *Modelling chloride diffusion in cracked concrete: A lattice approach*, In: R.M. Ferreira, J. Gulikers, and C. Andrade, editors, Proceedings of the International PhD student workshop on durability of reinforced concrete: From composition to service life design, pages 40-49, VTT Technical Research Center, 2012.

8. **B. Šavija**, J. Pacheco, R.B. Polder, and E. Schlangen *Lattice model as a tool for modelling transport phenomena in cement based composites*, In: P. Rossi and J.L. Tailhan, editors, Proceedings of the Numerical modeling strategies for sustainable concrete structures, 2012.

9. **B. Šavija** and E. Schlangen *Chloride ingress in cracked concrete - a literature review*, In: C. Andrade and J. Gulikers, editors, Proceedings of the 4^{th} International RILEM PhD workshop - Advances in Modeling Concrete Service Life, pages 133-142, Springer, 2010.

10. J. Pacheco, **B. Šavija**, E. Schlangen, and R.B. Polder *Corrosion of steel in cracked concrete: a microscale study*, In: M. Grantham, P.A.M. Basheer, B. Magee, and M. Soutsos, editors, Proceedings of Concrete Solutions, the 5^{th} International Conference on Concrete Repair, pages 551-557, Taylor & Francis Group, 2014.

11. M. Luković, **B. Šavija**, E. Schlangen, G. Ye, and K. van Breugel *A modelling study of drying shrinkage damage in concrete repair systems*, In: M.C. Forde, editor, Proceedings of the Structural faults and repair conference, 2014.

12. J. Pacheco, **B. Šavija**, E. Schlangen, and R.B. Polder *Performance assessment of cracks in reinforced concrete: from crack width to crack volume*, In: D. Bjegović, H.D. Beushausen, and M. Serdar, editors, Proceedings of the RILEM International workshop on performance-based specification and control of concrete durability, pages 419-426, RILEM publications S.A.R.L., 2014.

13. M. Luković, E. Schlangen, **B. Šavija**, G. Ye, and K. van Breugel *Numerical study of a strain hardening cementitious composite overlay system for durable concrete repair*, In: R. de Borst, H. Mang, G. Meschke, and N. Bićanić, editors, Proceedings of Computational Modelling of Concrete Structures (EURO-C), pages 827-836, CRC Press, 2014.

14. M. Luković, **B. Šavija**, E. Schlangen, G. Ye *Micromechanical study of the interface properties of concrete repair systems*, In: Z.J. Li, W. Sun, C.W. Miao, K. Sakai, and O.E. Gjørv, editors, Proceedings of the Seventh International Conference on Concrete Under Severe Conditions - Environment and Loading, pages 1685-1698, RILEM publications S.A.R.L., 2013.

15. M. Luković, E. Schlangen, G. Ye, **B. Šavija** *Impact of surface roughness on the debonding mechanism in concrete repairs*, In: J.G.M. van Mier, G. Ruiz, C. Andrade, R.C. Yu, and X. Zhang, editors, Proceedings of the VIII International conference on fracture mechanics of concrete and concrete structures, pages 611-621, 2013.

16. J. Pacheco, O. Çopuroğlu, **B. Šavija**, E. Schlangen, and R.B. Polder *Assessment of critical chloride content in reinforced concrete by Energy Dispersive Spectrometry (EDS) revisited*, In: M.G. Alexander, H.D. Beushausen, F. Dehn, and P. Moyo, editors, Proceedings of the Third International Conference on Concrete repair, rehabilitation and retrofitting (ICCRRR-3), CRC Press, 2012.
17. M. Luković, **B. Šavija**, G. Ye, and J. Zhou *Modeling water absorption of the concrete substrate in concrete repairs* In: M.G. Alexander, H.D. Beushausen, F. Dehn, and P. Moyo, editors, Proceedings of the Third International Conference on Concrete repair, rehabilitation and retrofitting (ICCRRR-3), CRC Press, 2012.
18. J. Pacheco, **B. Šavija**, E. Schlangen, and R.B. Polder *Relationship between cracking and electrical resistance in reinforced and unreinforced concrete*,In: G. Ye, K. van Breugel, W. Sun, and C. Miao, editors, Proceedings of the Second International Conference on Microstructural-related Durability of cementitious composites, RILEM publications S.A.R.L., 2012.